

Submitted by
Hubert Mitterhofer

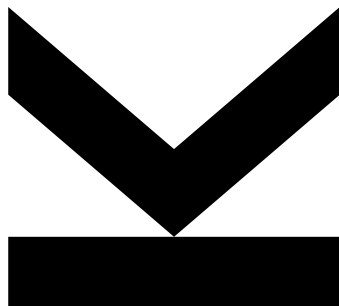
Submitted at
**Institute of Electrical Drives
and Power Electronics**

Supervisor and
First Examiner
**o. Univ. - Prof. DI Dr.
Wolfgang Amrhein**

Second Examiner
Prof. Eric H. Maslen

April, 2017

Towards high-speed bearingless disk drives



Doctoral Thesis

to obtain the academic degree of

Doktor der technischen Wissenschaften

in the Doctoral Program

Doctoral Program in Engineering Sciences

STATUTORY DECLARATION

I hereby declare that the thesis submitted is my own unaided work, that I have not used other than the sources indicated, and that all direct and indirect sources are acknowledged as references.

This printed thesis is identical with the electronic version submitted.

EIDESSTÄTTLICHE ERKLÄRUNG

Ich erkläre an Eides statt, dass ich die vorliegende Dissertation selbstständig und ohne fremde Hilfe verfasst, andere als die angegebenen Quellen und Hilfsmittel nicht benutzt bzw. die wörtlich oder sinngemäß entnommenen Stellen als solche kenntlich gemacht habe.

Die vorliegende Dissertation ist mit dem elektronisch übermittelten Textdokument identisch.

Linz, April 12th, 2017

Hubert Mitterhofer

Acknowledgment

The research work described in this thesis started at the *Institute for Electrical Drives and Power Electronics* (EAL) of *Johannes Kepler University Linz* (JKU) in 2009 in the framework of the K2 center *Austrian Center of Competence in Mechatronics* (ACCM) which was part of the *COMET* research grant of the Austrian and Upper Austrian Government. After approximately four years, the ACCM was integrated into the *Linz Center of Mechatronics GmbH* (LCM) where this work was continued and finally completed. Some parts of the work have been developed within the research project *Sustainable and resource saving electrical drives through high energy and material efficiency* sponsored through the program *Regionale Wettbewerbsfähigkeit OÖe 2007-2013 (Regio 13)* by the European Regional Development Fund and the Province of Upper Austria. I want to express my honest gratitude for the strategic research possibility that was provided to me through these grants.

In his role as both the head of EAL and the supervisor of this work, I would like to warmly thank Prof. Wolfgang Amrhein for his inspiring initial idea of bringing bearingless drives to high rotational speeds and for his ongoing support ever since. The numerous joint publications, conference visits, research grant and patent applications, and the countless discussions with him in a both friendly and personally appreciating atmosphere have helped me to grow as a research scientist and have allowed developing this work into a comprehensive study with a broad, mechatronic perspective.

I would equally like to express my sincere gratitude to Prof. Eric Maslen from *James Madison University, Virginia, USA*, for so quickly accepting my request to act as the second examiner of my work. His thorough revision, his valuable comments and his straightforward approach towards the end of this work were extremely helpful.

For welcoming me as a guest researcher in his lab at *Eidgenössischer Technischer Hochschule Zürich* (ETHZ) in 2009, I want to thank Prof. Johann Walter Kolar and the members of his group. Also Reto Schöb and Thomas Nussbaumer from *Levitronix* in Switzerland who helped me with their insightful knowledge on the industrial application and development perspectives for magnetic bearings shall be gratefully mentioned here. Equally, I want to thank Christof Zwyssig from *Celeroton*, for his initial advice during my time in Zurich and for the numerous follow-up discussions over the past years.

In the framework of a European Marie Curie project, I had the opportunity of joining the research team of *Rieter CZ s.r.o.* in Ústí nad Orlicí, Czech Republic for three months. Milan Moravec, Vladimír Klusoň, Miroslav Štusák, and Jiří Sloupenský warmly welcomed me in their research teams and made my stay instructive and personally rewarding - děkuju moc!

My sincere gratitude goes out to Lars-Olov Pennander from *Höganäs AB* in Sweden, for so openly discussing the material characteristics and loss data of SMC.

Last but not least on the international list, I want to thank Prof. Mikhail Rakov, last associated with the *University of California, Santa Barbara*, for turning our rather incidental acquaintance into an ongoing scientific correspondence resulting in a joint publication, and for becoming a dear friend.

Unsurprisingly, this work could not have been possible without the help of so many of my lab mates and friends at LCM and EAL and, despite their great number, I will not summarize all of their contributions in a single sentence but want to give their respective contributions the adequate space: First of all, I want to thank Siegfried Silber, head of the LCM area drives, for his strong backing in technical and administrative issues. Prof. Wolfgang Gruber, Herbert Grabner, Martin Reisinger and Peter Dirnberger gave me extremely valuable support, especially in the beginning of this work, when it came to dimensioning the first prototype, setting up the control, and dealing with all issues of power electronics. Gerald Jungmayr provided invaluable guidance during the modeling process of the tilt stabilization coil and was, together with Edmund Marth and Gerd Bramerdorfer, a valued discussion partner in many other theoretical issues. When problems with simulation or control software plagued me, Werner Koppelstätter, Günther Weidenholzer, Markus Aigner, Herbert Herzog and Stefan Fragner always offered a helping hand. Also, I want to mention Dietmar Andessner who supported me with his material characterization knowledge and Alexander Dorninger who provided help with the mechanical rotor simulations. Very special thanks also go to our team of technicians at EAL and LCM, Peter Heinetzberger, Martin Köck, Reinhold Wartecker, Willi Hopfinger, and Günther Seiberl for helping me during the construction of the different prototypes and to one of my master students, Elisabeth Göbl, for putting the 6-phase prototype into operation. Eventually, let me thank my long-time colleagues of office 11, Josef Passenbrunner, Sebastian Außerwöger, and Ralf Kobler, for making our office one better.

After so many years of school, university, and scientific research, I want to thank my parents for never having restricted my path but for having encouraged and supported me throughout these years. Together with my brother Stefan, they provided the non-technical but steady, invisible support of just being there for me. Since writing and, especially, finishing this work alongside regular project work often resulted in long office hours, I finally want to thank my dear Helena for her caring patience and her emotional support.

Abstract

Bearingless disk drives unite the functionality of magnetic bearings with electrical drives in a highly compact form with reduced mechanical complexity. The rotor field of a permanent magnet synchronous machine is used for passive stabilization in axial and tilt directions and, additionally, serves for the active creation of radial forces.

This special magnetic levitation topology is being used in high-purity pumps in the pharmaceutical, medical, and the semiconductor industry which operate at low speeds. The research activities leading to this work proposed the use of bearingless disk drives for high rotational speeds for the first time. Many aspects of high-speed operation such as increased winding and stator core losses, or the special challenges in mechanical rotor design due to the high centrifugal forces are, therefore, being considered in this work. Equally, the ability to provide sufficient active radial forces and drive torque independently in an efficient fashion is a key specification for the bearingless operation.

The design process includes the definition of suitable criteria which reflect the above-mentioned drive properties and demonstrates the advantageous application of multi-objective numerical optimization to the problem. Special attention is also given to the problem of tilting motion in a dedicated chapter since many possible applications involve high-speed impellers or turbines with tight housing tolerances. As tilt-triggered gyroscopic whirl can lead to the destruction of the system, a novel electrodynamic stabilization coil is proposed and documented based on a corresponding experiment.

As a result of the design process, several prototypes have been constructed, each realizing either a 5-phase double coil or a 6-phase single coil toroid winding concept using litz-wire and a low-loss slotless stator core. The prototype rotors comprise diametrically magnetized, ring-shaped rotors with high-strength support bandages and have a total outer rotor diameter between 30 mm and 32 mm.

The developed radial position and rotational speed control loop with an underlying current controller features several non-linear extensions for reducing either losses, undesired rotor motion, or computation time. Different experiments for demonstrating the operational behavior, including rotor orbits during run-up and input power measurements have been conducted using this control scheme which was implemented at a standard DSP which controls a 10 half-bridge power electronic module. The maximum rotational speed reached during these experiments was 115 000 rpm which corresponds to a surface speed of 192.6 m/s. To the knowledge of the author, this surface speed constitutes a world record for magnetically levitated disk drives.

A detailed analysis of the losses provides analytic models for the iron losses, the eddy current winding losses, and the windage losses. Existing models have been matched to the loss measurements conducted at a customized test rig in order to allow an extrapolation of the expected losses at a speed of 200 000 rpm.

Kurzfassung

Lagerlose Scheibenläuferantriebe vereinen die Funktionalität von Magnetlagerung und elektrischer Maschine in einer hochkompakten, die mechanische Komplexität reduzierenden Form. Das Rotormagnetfeld einer permanentenregten Synchronmaschine wird für die passive Stabilisierung von axialen und Kippauslenkungen mitverwendet und dient zusätzlich der Erzeugung von aktiven Radialkräften.

Diese spezielle Magnetlagertopologie wird in hochreinen Pumpen in der pharmazeutischen, medizinischen und der Halbleiterindustrie, mit Drehzahlen von 5000 U/min bis 15 000 U/min eingesetzt. Im Rahmen der hier beschriebenen Forschungsarbeit wurde zum ersten Mal die Hochgeschwindigkeitseignung lagerloser Antriebe untersucht. Daher behandelt diese Arbeit Aspekte wie etwa Wicklungswirbelstrom- und Statorverluste oder spezielle Herausforderungen im mechanischen Rotordesign zufolge der auftretenden Zentrifugalkräfte. Gleichmaßen sind die ausreichende, effiziente und voneinander unabhängige Erzeugung von Radialkräften und Antriebsmoment wichtige Designvorgaben.

Der Designprozess inkludiert die Definition von geeigneten Kriterien, die oben genannte Anforderungen widerspiegeln und demonstriert die Möglichkeiten von mehrkriterieller, numerischer Optimierung. Besonderes Augenmerk wird in einem eigenen Kapitel auch dem Problem des Rotorkippens gewidmet, da Verdichter oder Turbinen mit engen Gehäusespalten mögliche Anwendungen darstellen. Da solche Systeme durch gyroskopische Taumelbewegungen zerstört werden können, wird eine neuartige Stabilisierungsspule vorgestellt und ihr Einfluss anhand eines Experiments dokumentiert.

Infolge des Designprozesses wurden mehrere Prototypen aufgebaut, die über nutenlose Statoren, Litzendraht-Toroidwicklungen und ein 5-strängiges Doppelspulen- oder ein 6-strängiges Einfachspulenkonzent verfügen. Die bandagierten Rotoren mit Außendurchmessern von 30–32 mm sind diametral magnetisiert.

Zum Betrieb wurde eine Drehzahl- und eine Radialpositionsregelschleife mit unterlagertem Stromregelkreis und einigen nichtlinearen Erweiterungen umgesetzt, die einer Reduktion von Verlustleistung, unerwünschter Rotorbewegung oder benötigter Rechenzeit dienen. Unterschiedliche Messungen, etwa des Rotororbits oder der aufgenommenen Leistung beim Hochlauf wurden unter Einsatz dieses Regelschemas durchgeführt, das auf dem digitalen Signalprozessor der 10-Halbbrücken-Leistungselektronik implementiert wurde. Die bei diesen Versuchen erreichte Maximaldrehzahl von 115 000 rpm entspricht einer Oberflächengeschwindigkeit von 192.6 m/s , welche nach bestem Wissen des Autors einen Weltrekord für lagerlose Scheibenläufer darstellt.

Eine detaillierte Verlustanalyse mündet in analytische Modelle für Eisen-, Luftreibungs- und Wicklungswirbelstromverluste. Dafür wurden bestehenden Modelle an die an einem speziellen Prüfstand gemessenen Verluste angepasst, um eine Verlustvorhersage bei einer Zieldrehzahl von 200 000 U/min zu ermöglichen.

Contents

1. Introduction	1
1.1. The need for speed	2
1.2. Terminology of magnetic levitation principles	3
1.2.1. Passive magnetic bearing (PMB)	3
1.2.2. Active magnetic bearing (AMB)	4
1.2.3. Bearingless drives	5
1.2.3.1. Origin	5
1.2.3.2. Naming variations	6
1.2.3.3. History of bearingless drives	6
1.3. State of the art in bearingless disk drives	7
1.4. Content structure	9
2. System design	13
2.1. Rotor topology	14
2.1.1. Radial stiffness anisotropy	14
2.1.1.1. 2-pole rotor	14
2.1.1.2. 4-pole rotor	16
2.1.2. Tilt stiffness anisotropy	17
2.1.2.1. 2-pole rotor	17
2.1.2.2. 4-pole rotor	18
2.1.3. Rotor selection	19
2.2. Winding topology	19
2.2.1. Connection topology: separated vs. combined windings	19
2.2.1.1. Back-EMF sensitivity for separated windings	20
2.2.1.2. Back-EMF sensitivity for combined windings	22
2.2.1.3. Back-EMF sensitivity for DPNV windings	23
2.2.1.4. Selection of connection topology	25
2.2.2. Coil form	26
2.2.2.1. Air gap vs. toroid coil	26
2.2.2.2. Single coil vs. double coil	28
2.3. Evaluation criteria	29
2.3.1. Torque and radial forces	29
2.3.1.1. Direct criterion	30
2.3.1.2. Inverse criterion	30
2.3.1.3. Mean torque criterion	32
2.3.1.4. Start-up criterion and minimum force	32
2.3.2. Passive stabilization forces and torques	33
2.3.2.1. Axial stiffness criterion	33
2.3.2.2. Tilt stiffness criterion	35
2.4. Design optimization	35
2.4.1. Validation of simulation approach through measurement	35

2.4.2.	Topology selection	37
2.4.2.1.	Evaluated designs	37
2.4.2.2.	Torque comparison	37
2.4.2.3.	Force comparison	38
2.4.2.4.	Comparison of power electronics requirements	38
2.4.2.5.	Selected topology	39
2.4.3.	Geometry selection	41
2.4.3.1.	Optimization setup	41
2.4.3.2.	Optimization procedure	43
2.4.3.3.	Analysis of the optimization result	44
2.5.	Conclusion	45
3.	Tilt stabilization	47
3.1.	Passive tilt damping	48
3.1.1.	Problem description	48
3.1.2.	Additional damping	51
3.1.3.	Tilt stabilization coil (TSC)	52
3.1.4.	Stabilization model	54
3.1.4.1.	Derivation of the tilt torque	54
3.1.4.2.	Coupling term	56
3.1.4.3.	TSC current	57
3.1.4.4.	Simplified model	58
3.1.4.5.	Stability analysis of the simplified model	60
3.1.4.6.	Extended differential equation system	62
3.1.4.7.	Stability and design guidelines	63
3.1.5.	Numerical simulation and model comparison	64
3.1.6.	Measurement	66
3.2.	Active influence	70
3.2.1.	Active tilting - 1 coil	70
3.2.2.	Active axial force - 2 coils	70
3.2.3.	Active tilting - 4 coils	71
3.2.4.	Simulation results	73
3.3.	Conclusion	73
4.	Mechanical rotor stability	75
4.1.	Mechanical properties	76
4.1.1.	Surface mounted magnets	77
4.1.2.	Buried magnets	77
4.1.3.	Bandaging	78
4.2.	Analytic stress calculation of the rotor	78
4.2.1.	Unsupported rotor	78
4.2.2.	Bandaged rotor	80
4.2.3.	Mechanical effects of an inner back iron	83
4.2.4.	Dimensioning of the interference fit	84
4.2.4.1.	VON MISES - criterion	85
4.2.4.2.	Principal normal stress hypothesis	86
4.3.	Comparison of the analytical model with a finite element (FE) simulation	87
4.3.1.	Simulation setup	87
4.3.2.	Validation of the method	88

4.3.3.	Stress simulation result with ring structure	89
4.3.4.	Flexible body modes	89
4.4.	Rotor segmentation	91
4.4.1.	Single-sided cut	91
4.4.2.	Double-sided cut	92
4.4.3.	Four-sided cut	92
4.5.	Conclusion	95
5.	Prototypes	97
5.1.	Motivation	98
5.2.	Bearingless machine	98
5.2.1.	Component description	98
5.2.1.1.	Stator core	98
5.2.1.2.	Windings	98
5.2.1.3.	Touchdown bearing	99
5.2.1.4.	Rotor components	100
5.2.1.5.	Sensors	101
5.2.1.6.	Housing and in-machine PCBs	101
5.2.2.	Prototype data	103
5.3.	Control	104
5.3.1.	Power electronics unit	104
5.3.2.	Control software	104
5.3.2.1.	Radial position signal treatment	105
5.3.2.2.	Rotor angle and speed signal treatment	107
5.3.2.3.	Position and speed control	108
5.3.2.4.	Speed dependent transformation and current control	108
5.4.	Prototype test results	109
5.4.1.	Control verification tests	109
5.4.2.	Turbine and compressor tests	111
5.4.3.	High-speed test	113
5.5.	Conclusion	116
6.	Drive losses	119
6.1.	Introduction	120
6.2.	Measurement setup and results	120
6.2.1.	Measurement system	120
6.2.2.	Loss measurement results	122
6.3.	Loss component description	123
6.3.1.	Analytical rotor field description	123
6.3.2.	Comparison of FE and analytical calculation	125
6.3.3.	Armature reaction field	127
6.3.4.	Stator losses	127
6.3.5.	Copper losses	131
6.3.5.1.	Skin effect	131
6.3.5.2.	Proximity effect	132
6.3.5.3.	Comparison to measurement	133
6.3.5.4.	Losses due to permanent magnet field	134
6.3.6.	Air drag losses	135
6.3.6.1.	Rotor disk friction	135

6.3.6.2. Air gap friction	136
6.3.6.3. Combined air drag losses	137
6.3.7. Thermal measurement	138
6.3.8. Efficiency measurement	140
6.4. Design variation	141
6.4.1. Increased speed	141
6.4.2. Wire selection	143
6.4.3. Variation of the radial air gap	146
6.4.4. Increased pole number	147
6.5. Conclusion and criticism	148
7. Conclusion and outlook	149
A. Appendix	153
A.1. Analytical magnetic field calculation	153
A.2. Rotating field iron loss model	156
A.3. Skin and proximity effect related loss coefficients	157
A.4. External field due to neighboring wire bundles	158
B. Index of symbols	161
Bibliography	165
Curriculum Vitae	177

1. Introduction

Contents

1.1. The need for speed	2
1.2. Terminology of magnetic levitation principles	3
1.2.1. Passive magnetic bearing (PMB)	3
1.2.2. Active magnetic bearing (AMB)	4
1.2.3. Bearingless drives	5
1.3. State of the art in bearingless disk drives	7
1.4. Content structure	9

1.1. The need for speed

Before investing a considerable effort into researching and developing a high-speed bearingless disk drive, we should verify the motivation for this work. Why push such machines towards higher speeds and what is this *craving for speed* about, anyway? These are generally valid questions, so we should start at the very basis, at electrical machines with conventional bearings. Looking into the development in the past decades, we can find some answers.

- The technically simplest and yet strongest argument for high-speed drives can be expressed by three variables

$$P = T \cdot \omega. \quad (1.1)$$

When we want to increase the power P of a drive, we can either increase its torque T or its rotor speed ω . Higher torque capacity of a drive can be achieved by increasing the diameter or length, using more or stronger permanent magnets or providing higher copper volume. We can summarize these changes as making the drive bigger, heavier and, potentially, more expensive. It is evident that these properties are undesirable for most applications.

Pushing for higher speed capacity instead of higher torque may also raise the overall system costs due to increased efforts for power electronics and manufacturing, however, it does *not* automatically increase the size and weight of the machine itself. While certain measures such as rotor bandaging or larger permanent magnets may be necessary, the gain in weight and size is significantly lower than for increased torque capacity. At the first glance, it is, thus, the more elegant path to increase the power of a drive.

- A certain range of applications can benefit from high-speed machines combined with a gearing mechanism. If the necessary torque and speed transmission ratio is low enough, the combination of high-speed machine and gear may be preferable over a low-speed machine with higher torque despite the additional constraints by the gear (life time, lubrication, backlash, etc.). However, very high-speed motors are not a remedy to all applications, especially when the necessary rotational speed is *significantly* below the machine output speed. Mechanical gears are limited in their tolerable input speeds and the benefits of smaller, more lightweight machines may be taken away when large and heavy multi-stage gears are necessary. It would, e.g., make little sense to drive a kitchen blender with a tiny 100 000 rpm motor and an enormous multi-stage mechanical gear which transforms the speed down to the necessary few hundred rpm and the output torque up to the required values. In applications such as compressors, vacuum pumps, turbines, flywheels, or high-speed mills, there is an actual need for high rotational speeds. Here, higher rotational speeds increase efficiency, storage capacity or productivity. It is, therefore, such types of applications that we need to keep in mind when talking about high-speed operation.
- There is an interesting chain of problems and solutions which unfolded over the last few decades.
 - As high machine speeds cause increased bearing wear and lifetime problems, conventional mechanical bearings have been pushed to their limits concerning rotational speeds.

- Magnetic levitation technology can solve these problems as a magnetic bearing works without contact between rotor and stator. It also introduces new features which, for mechanical bearings, are hard to achieve or cannot be provided at all. However, magnetic bearings usually consume more space than the mechanical bearings they replace, thus raising the necessary drive volume and often also increasing the rotor length.
- Long and thin rotors are very prone to resonance frequencies including flexural modes which can be excited at high rotor speeds, potentially causing severe mechanical instability issues. Especially when the driven element, e.g., an impeller wheel or a machining tool has to be mounted at the very end of the rotor shaft, the axial length consumed by the magnetic bearing and its winding heads is a critical parameter.
- Bearingless drives integrate the magnetic bearing function into the electrical machine, thus reducing the axial length of the drive. This creates a mechanically compact and simple unit with most of the complexity being shifted to the electrical and control systems. Especially bearingless *disk* drives, using both, passive and active magnetic stabilization, offer highest degrees of integration and mechanical compactness. This compactness can be the key to pushing the structural resonance frequencies far beyond the occurring vibration frequencies and, thus, allowing stable drive operation. Despite the significant technological efforts and adaptations necessary for this integration, all crucial features of conventional magnetic bearings are preserved.

From a research perspective, the mentioned potentials and developments appear like an assembled puzzle with a missing piece, since, up to the point in time when this research work started, bearingless drives were operated for low speeds, only.

1.2. Terminology of magnetic levitation principles

In the following sections, the term *bearingless* is explained in detail, but for doing so, we also need to look at the two other main principles of magnetic levitation and at how they compare to each other. Since the following explanations aim at being generally comprehensible, several passages of this section have also been chosen for publication at the magnetic bearings technology website www.magneticbearings.org.

1.2.1. Passive magnetic bearing (PMB)

A PMB achieves contact-free levitation of an object by using the attractive or repulsive reluctance forces of permanent magnets. Depending on the configuration, stabilization in the radial, axial or tilt degree of freedom (DOF) is possible. The concerned parts of the bearing system are usually maintenance-free due to the absence of mechanical friction. It is, however, not possible, to stabilize all degrees of freedom of a body by passive magnetic levitation only¹.

The stiffness values of a PMB are determined by the geometrical bearing configuration and its material properties. Several classical examples for such PMB arrangements are

¹Diamagnetic materials such as superconductors are explicitly not considered in this statement. This has been shown by Werner Braunbeck [18] who, 100 years later, interpreted the findings of Samuel Earnshaw [29] on the stability conditions in static force fields, for magnetic levitation.

1. Introduction

shown in Figure 1.1. The PMB itself provides close to zero damping which is why it is typically accompanied by external damping elements such as suspension with visco-elastic materials, or electrodynamic dampers.

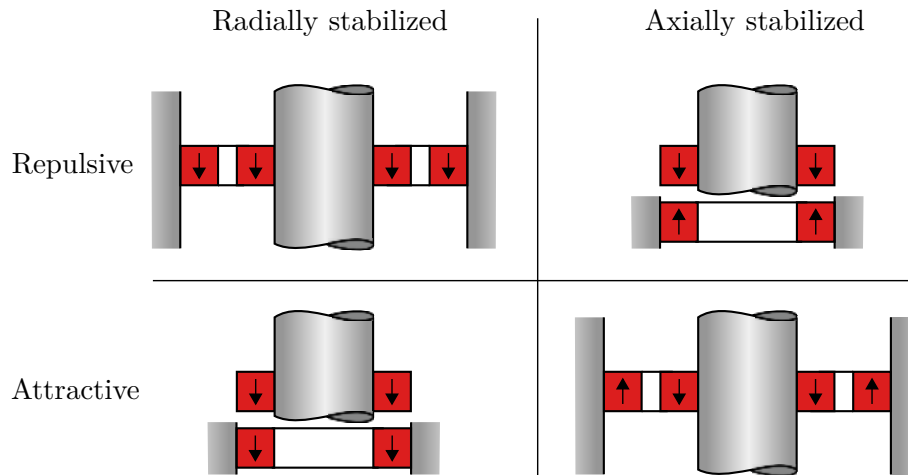


Figure 1.1.: Examples for possible PMB arrangements, the arrows indicate the magnetization direction of the permanent magnet rings

No active components such as actuators, coils or power electronics are needed in a PMB which makes it a cheap, small and mechanically simple magnetic bearing. Nevertheless, this form is only rarely used in industry up to now but research interest has grown over the past years in theoretical research [128, 67] and for applications with PMBs and additional support by electrodynamic structures [4], active magnetic bearings [31, 48, 56], or visco-elastic materials [66].

1.2.2. Active magnetic bearing (AMB)

An AMB uses electromagnetic actuators in order to control the position of the rotor or the levitated object. Any degree of freedom can be stabilized using an AMB and in contrast to PMBs, full and stable levitation is possible using only AMBs. Each bearing can be implemented as a separate unit, typically consisting of an iron core, bearing windings, optional permanent magnets for efficiency increasing bias-magnetization, and attached sensors² for determining the rotor position which shall be controlled. With these additional components and the power electronics necessary for driving AMBs, the overall system complexity increases. Due to the additional iron cores, copper windings, and, optionally, permanent magnets, also the production costs and the required space grow. The demand for installation space often leads to higher rotor lengths and, thus, to higher mechanical complexity because of lowered critical bending frequencies.

AMBs allow controlling the stiffness and damping coefficients of the bearing and can, therefore, influence the object's rotordynamic behavior by changing the respective control parameters. The vast majority of industrial applications using magnetic levitation rely on active bearings. Figure 1.2 illustrates the special characteristics of AMBs and their consequential application scope. Even though PMBs also provide many of the listed aspects, the full spectrum can only be covered by AMBs.

²*Sensorless* or *self-sensing* operation of magnetic bearing systems has been reported in scientific research (e.g. [101] or [52]) but most commercially available systems seem to use position sensors.

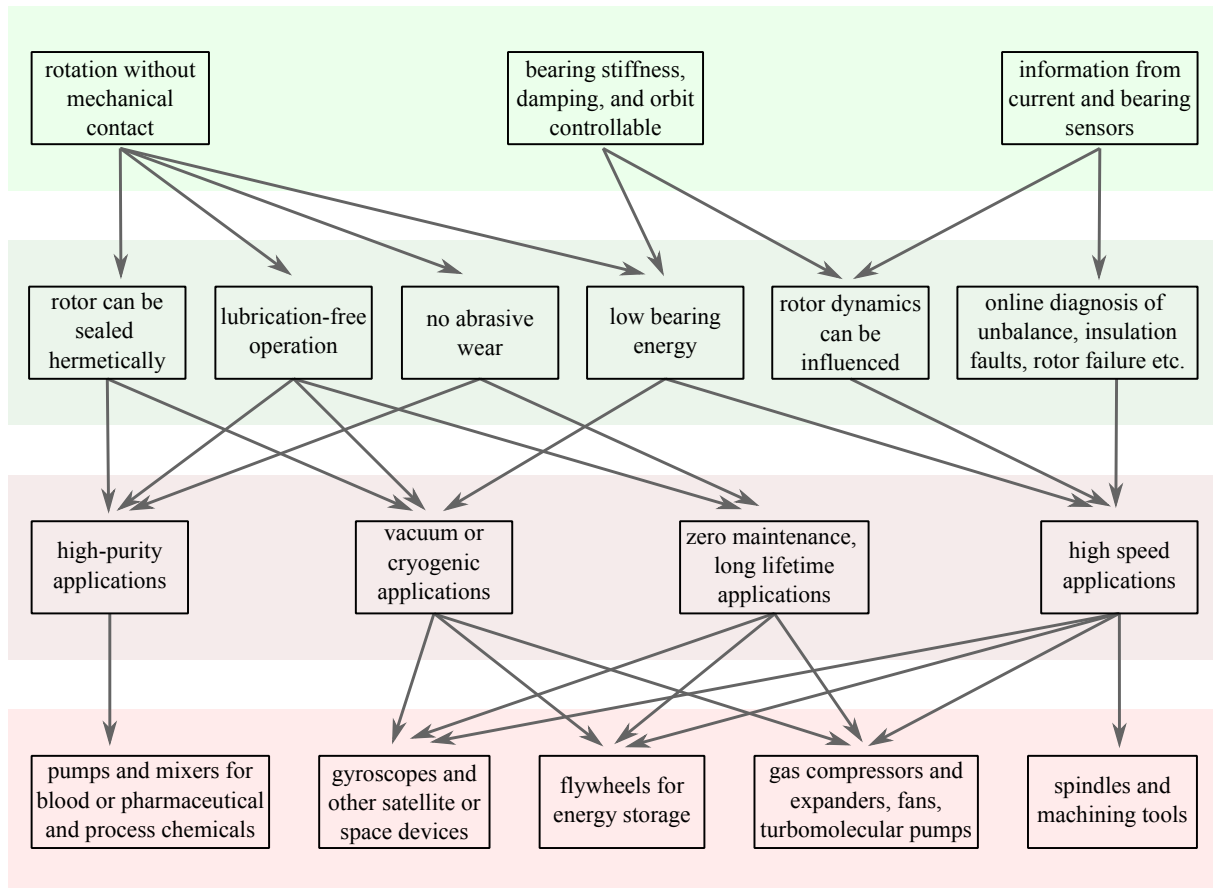


Figure 1.2.: AMB technological map. Horizontally, from top downwards: Basic characteristics, resulting special bearing features, possible application types and realized application examples

1.2.3. Bearingless drives

1.2.3.1. Origin

A bearingless drive is a special form of an AMB. CHIBA gives two definitions of a bearingless drive [21]:

A motor with a magnetically integrated bearing function.

and

A magnetic bearing with a magnetically integrated motor function.

While the etymology of the term *bearingless*, which first surfaced in a publication by RICARD BOSCH at UPC Barcelona [16], seems to be unknown, it is frequently explained as being derived from the word *brushless*, since similar to the brushes in a DC drive, mechanical bearings are eliminated as a source of failure. However, it also seems plausible to the author that the term *sensorless* is the name source. In a *sensorless* drive, there are no *distinct* sensor units for measuring the rotor angle but the sensor functionality is *integrated* in the motor winding. In a *bearingless* drive, the same is true for the bearing. There is no *distinct* bearing unit (except for possible touchdown bearings) but the bearing functionality is *integrated* in the motor unit.

1.2.3.2. Naming variations

Even though it is the most common expression for denoting this special motor type, the term *bearingless* is not the only one used in the literature. In several international publications on this subject, the terms *self-bearing* and *combined motor-bearing* are used instead. Table 1.1 gives an estimation of the usage rate of the three terms by comparing the hits when running a title search in the *IEEE Xplore Search Engine*³ tool.

<i>Term in title</i>	<i>Number of hits</i>	<i>Time span of found publications</i>
<i>bearingless</i> or <i>bearing-less</i>	428	1991-2015
<i>self bearing</i> or <i>self-bearing</i>	41	1999-2015
<i>combined motor-bearing</i>	2	1999-2000

Table 1.1.: Result of cumulative title-search in *IEEE-Xplore*

1.2.3.3. History of bearingless drives

The history of bearingless drives is a rather young one since research activities started only in the late 1980s despite the fact that the original idea of uniting magnetic bearing and electrical drive dates back to a patent by HERMANN in 1974 [50]. Early research on the subject, also bringing forth first prototypes, was conducted by BICHSEL and SCHOEB in the group of professor HUGEL [11] at ETH Zurich and, at the same time, was taken up by researchers in Japan [20], [89], Brazil [100], and the US.

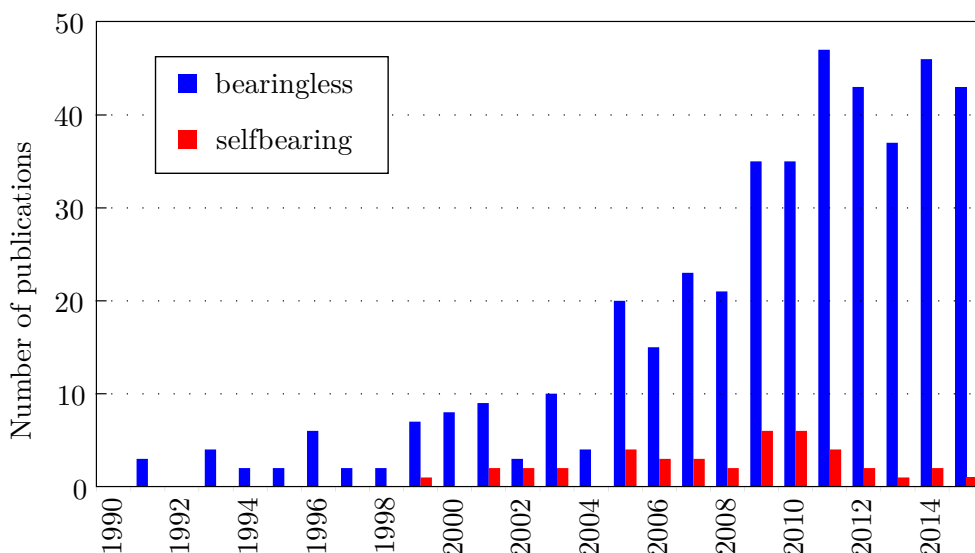


Figure 1.3.: Publication statistics from searches in *IEEE-Xplore* according to title search including the terms *bearingless* and *self bearing* given in Table 1.1

All of the early bearingless drives used conventional stator and rotor topologies with additional or modified windings. With the exception of [16], where torque and axial forces

³The IEEE Xplore repository was chosen as one of the major online databases for scientific publications in this area. There are, of course, also many other online publication repositories. The search was conducted in May, 2015.

were exerted on a flat rotor, the produced bearing forces were used to stabilize radial rotor deflections in motors with elongated rotors. In all of the cited cases, this meant that additional active magnetic or mechanical bearing units were required to completely stabilize the rotor movement. Also, rotordynamic issues as in conventionally supported elongated shafts had to be dealt with. The development of bearingless drives started to expand in the beginning of the 1990s and touched all major types of electrical machines – from induction to permanent magnet, homopolar or switched reluctance type machines⁴. The increasing interest in research was answered with the creation of the International Symposium on Magnetic Bearings (ISMB), held every second year since 1988. As shown in Figure 1.3, also the number of publications outside this special symposium has significantly increased over the past years.

1.3. State of the art in bearingless disk drives

Disk-shaped rotors in a bearingless drive or a magnetic bearing system can be designed to have a unique property in comparison to elongated shafts. It is possible to fully stabilize a flat disk using active and passive magnetic bearings in one common bearing layer. This concept was proposed by BLEULER in [14] with electromagnetic excitation and later adapted to include permanent magnet excitation in [5] and [105] for a bearingless motor unit which creates active radial bearing forces and passive rotor stabilization in axial and both tilt directions as illustrated in Figure 1.4. The principle allows the use of a single bearingless unit to provide stable levitation without having to add further bearings.

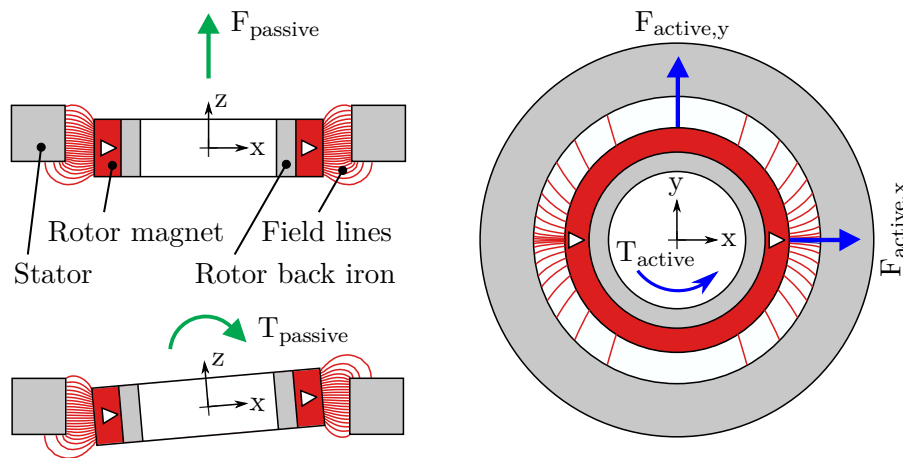


Figure 1.4.: Passive and active forces (F) and torques (T) stabilizing all degrees of freedom in a bearingless disk drive

The flat disk or ring form of the rotor yields a rotordynamic situation which is very different from the elongated shafts in conventional machines. Many critical issues connected to the bending and torsion flexibility of elongated rotors which typically occur in high speed regions can be avoided with this rotor form. Despite this advantage, most of the research efforts in bearingless disk drives have targeted applications for rather low speeds of up to approximately 20 000 rpm and for surface speeds which typically do not exceed 50 m/s.

⁴An excellent overview of this early phase of research is given by SALAZAR in [99].

1. Introduction

Early application-specific patents of bearingless disk drives date back to 1996 [105] and the technology was first commercialized by the Swiss company *Levitronix* for producing pumps for blood or sensitive chemical process fluids [104]. The main advantage of bearingless motors in this field is the lubrication-free, abrasion-free and hermetically sealed operation, fulfilling highest purity demands and applying a minimum of mechanical shear stress to the pumped fluids. Since, however, these high-purity process fluids typically are liquids, high-speed rotation of the pump head is neither necessary nor reasonable.

The development of bearingless disk motors continued, mainly driven by developments for blood pumps and other pump systems but also several other different application targets such as mixers or process handling machines emerged. Most research works in the area of bearingless disk drives revolve around the questions of

- which rotor topology and stator form to apply,
- how many phases to use and how to structure and place the windings,
- which technology to use for the position sensors and how to place them,
- which power electronics and control method to apply, and
- how to best simulate and model all of the above.

Of course, along all of this research work, a lot of prototypes were manufactured and put into operation. Figure 1.5 illustrates the bearingless disk drives which the author has found in the literature [7, 103, 41, 132, 92, 95, 114, 37, 17, 44, 123, 91, 96, 124, 131, 116, 108, 2]. The overview exclusively includes concepts which were actually realized and tested according to the respective publication. Even though considerable effort has been made for creating this overview, the author cannot and does not claim that it is complete. To identify the drives which are marked in Figure 1.5, they are linked to the corresponding publication in Table 1.2.

This map shows that most of the bearingless disk drive designs presented in the literature have small diameters of up to 100 mm and maximum speeds of below 20 000 rpm. These developments usually target pump applications or constitute prototypes for proving the feasibility of a bearingless disk drive technique without mentioning a certain target application.

Two other groups of drives were designed to function in bioreactors and chemical process chambers, respectively. These drives typically feature quite large diameters of up to 370 mm, rotating slowly at up to 2500 rpm. Due to their big circumference, the surface speeds reached by these drives may surpass those of the pump group.

Two entries in the diagram should be mentioned separately because they represent bearingless motors with relatively high rotational speeds and surface speeds of 91.1 m/s and 106.8 m/s, respectively. In case of the first publication ([7]), this speed was achieved by tuning a pump motor in order to fulfill the specification for a hydrogen blower. However, running into several difficulties of mechanical nature, it turned out that for a true high-speed drive, a fundamentally different design is necessary. The second drive was published in late 2013 ([116]), presenting a high-speed demonstrator for high-purity applications.

The last area marked in Figure 1.5 is denoted as *Target area* because this constitutes the remaining blank area on the map that this thesis is aiming at: The development of a high-speed bearingless disk drive.

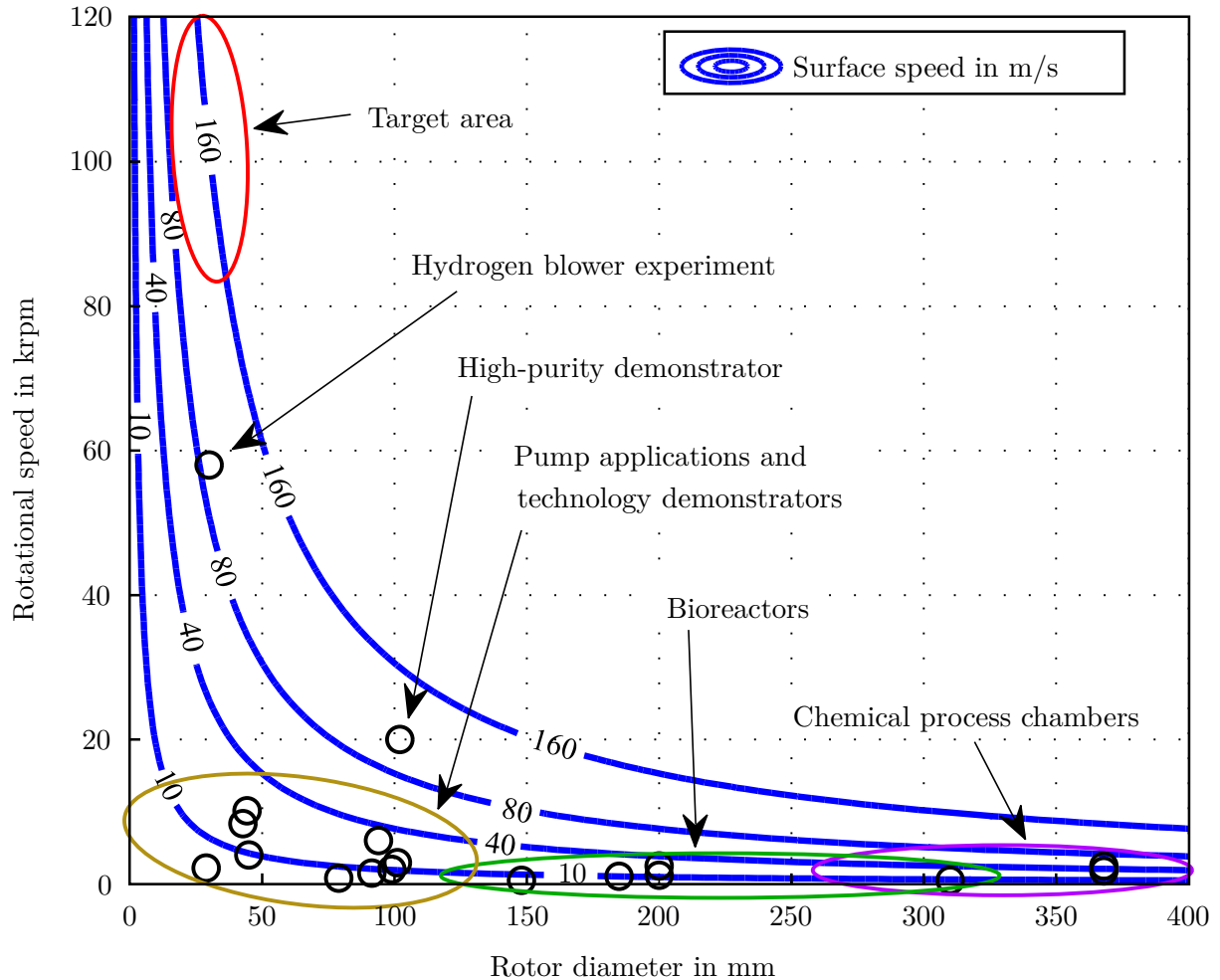


Figure 1.5.: Map of bearingless disk drives found in the literature, placed according to outer rotor diameter and documented rotor speed, also showing the resulting surface speed. The ellipses mark the respective application areas.

1.4. Content structure

While the past sections try to answer the question *why* it is interesting from a scientific point of view to develop a bearingless high-speed drive, the following one will give the structure of *how* this is achieved.

Chapter 2 first describes the starting point for the conducted research by fixing certain design decisions such as the disk shape of the rotor and some of the basic geometric dimensions including the justifications for these predeterminations. In the further course of that chapter, some effort was dedicated to choosing an appropriate winding system. This concerns the number of phases as well as the winding form by establishing means for evaluating the different possible solutions. Furthermore, the criteria and motivation for choosing the magnetic properties and geometric dimensions of the motor parts are presented. The evaluation methods include the calculation of bearing forces and motor torque. The underlying theory, which has been presented in detail in [108] and [36], is briefly introduced. Eventually, the process of design parameter selection through numerical optimization is presented using the optimization suite MagOpt which is being developed at LCM.

Following the system design for high-speed bearingless disk drives, *Chapter 3* is dedi-

1. Introduction

Publication	Outer rotor diameter	Rotational speed	Surface speed
[108]	106 mm	3 krpm	16.65 m/s
[7]	30 mm	58 krpm	91.11 m/s
[103]	200 mm	1.2 krpm	12.57 m/s
[41]	99 mm	2 krpm	10.37 m/s
[132]	368 mm	1.8 krpm	34.68 m/s
[92]	28.9 mm	2.2 krpm	3.33 m/s
[95]	35 mm	14 krpm	25.66 m/s
[114]	79 mm	0.8 krpm	3.31 m/s
[37]	46 mm	10 krpm	24.09 m/s
[17]	94 mm	6 krpm	29.53 m/s
[44]	368 mm	2.5 krpm	48.17 m/s
[123]	91.5 mm	1.5 krpm	7.19 m/s
[91]	185 mm	2.8 krpm	26.93 m/s
[96]	148 mm	0.5 krpm	3.87 m/s
[124]	310 mm	0.5 krpm	8.12 m/s
[131]	200 mm	2.5 krpm	26.18 m/s
[116]	102 mm	20 krpm	106.81 m/s
[2]	45 mm	4 krpm	9.42 m/s

Table 1.2.: Data of the bearingless disk drives used for creating the map in Figure 1.5

cated to a novel tilt stabilization technique which can be added to the design by placing an additional coil in the stator. The passive stabilization effect and the active torque and force creation capacities of this new component are investigated analytically, through simulation and in experiment.

Chapter 4 is dedicated to the mechanical requirements of the high-speed rotor. As it will become clear later in this work, the mechanical stability is of critical importance because the centrifugal forces that act on the rotor determine the maximum speed for the drive. The necessary calculations and design steps have been formed as a separate chapter since this is an atypical issue for the design of bearingless drives which, as mentioned above, were formerly constructed for low rotational speeds only.

The design decisions from Chapter 2 and Chapter 4 have been used to construct several prototype drives of which two are presented in Chapter 5. The description also includes the power electronics circuit, the speed dependent control structures which have been added specifically for the high-speed operation of the drive as well as the experimental results obtained with the prototype drives.

Experimental data on the constructed 5-phase disk drive is partly presented in Chapter 5 in order to directly present the effects of the proposed control mechanisms. Addi-

tional data can be found in Chapter 6 which also gives the analytical description of the loss components including an extrapolation to yet higher rotational speeds. This projection eventually leads to proposed improvements for future designs.

As a closure remark, Chapter 7 tries to give an outlook on future reasearch activities and the necessary steps towards industrial application.

Significant parts of the findings included in this documentation are included in journals, conference papers, and a patent application [69]-[82].

2. System design

Contents

2.1. Rotor topology	14
2.1.1. Radial stiffness anisotropy	14
2.1.2. Tilt stiffness anisotropy	17
2.1.3. Rotor selection	19
2.2. Winding topology	19
2.2.1. Connection topology: separated vs. combined windings	19
2.2.2. Coil form	26
2.3. Evaluation criteria	29
2.3.1. Torque and radial forces	29
2.3.2. Passive stabilization forces and torques	33
2.4. Design optimization	35
2.4.1. Validation of simulation approach through measurement	35
2.4.2. Topology selection	37
2.4.3. Geometry selection	41
2.5. Conclusion	45

The intention to fill a blank area in the map shown at the end of Chapter 1 determines that the target of this development is a bearingless drive with a disk shaped rotor. However, there are several other design decisions to make, entailing specific consequences which are not evident and which need to be discussed. These decisions concern the rotor topology and the winding design regarding the choice between combined and separated windings, between air gap and toroid winding form, and between single coil or double coil arrangement. Furthermore, the actual number of phases and, finally, the geometric dimensions and adequate material selection will be presented.

2.1. Rotor topology

In order to provide a smooth, sinusoidal air gap flux density distribution, a 2-pole rotor magnet needs to have diametric magnetization. Higher pole number rotors bring certain advantages and disadvantages which are discussed in the following section. In order to allow an adequate comparison, however, higher pole number rotors need to be magnetized with a so-called HALBACH-¹magnetization which also produces a sinusoidal air gap flux density distribution.

At a rotor pole number of two, the mechanical angular rotation frequency Ω is equal to ω which denotes the electrical angular frequency. Higher pole numbers do not only demand higher electrical frequencies for the fundamental wave of the motor currents but also higher sampling rate of the current and angle sensor and a higher cycle frequency for the entire control loop. A comparison of a 2-pole and 4-pole rotor for the high-speed disk drive project was presented in [72]. The results of the cited work rely on a limited choice of phase numbers and coil configurations, making the comparison incomplete. Especially when it comes to the presented torque and force capacities, which were calculated for double coil² arrangements only, the cited work must be substantially supplemented with the conclusions of Section 2.2.2.2. However, the most stringent conclusions of [72] concerning the stiffness anisotropy remain fully valid and are briefly outlined in the following paragraph.

2.1.1. Radial stiffness anisotropy

Moving the permanent magnet rotor out of the ideal stator center causes destabilizing radial forces

$$\mathbf{F}_r = \begin{bmatrix} F_{r,x} \\ F_{r,y} \end{bmatrix}. \quad (2.1)$$

The force per deflection distance is referred to as the radial stiffness c_r in analogy to a mechanical spring³. This stiffness varies strongly with the air gap, the axial length, the air gap flux density and also, the pole number. While the influence of the mentioned geometric dimensions is detailed in Section 2.4.3, the pole dependent stiffness characteristic is examined here.

2.1.1.1. 2-pole rotor

Unlike in passive magnetic bearings where, usually, axially magnetized permanent magnets are used, the radial stiffness is angle-dependent in a bearingless drive using a 2-pole rotor. As shown in Figure 2.1, a rotor movement in the direction of the magnetization axis provokes the maximum destabilizing radial force while the minimum value is produced when it is being moved perpendicular to this axis. A mean radial stiffness value can be

¹KLAUS HALBACH, * 1925 in Wuppertal, Germany, † 2000

²For the definition and detailed comparison of double coil and single coil arrangements, see Section 2.2.2.2.

³It shall be noted here that the stiffness is defined as c in the standard equation of motion $m\ddot{x} + d\dot{x} + cx = F_{external}$ with m and d denoting the mass and the damping parameter. This means that for the unstable radial degrees of freedom, the stiffness is negative because, e.g., in an equilibrium situation ($\ddot{x} = \dot{x} = 0$), a constant positive deflection in x demands a negative external stabilization force $-F_{external}$.

calculated according to

$$\bar{c}_r = \frac{{}_R C_x + {}_R C_y}{2} \quad (2.2)$$

when the maximum and minimum stiffness values, ${}_R C_x$ and ${}_R C_y$, are defined in the rotor-bound coordinate system (subscript R in front of the variable) according to the magnetization direction shown in Figure 2.1.

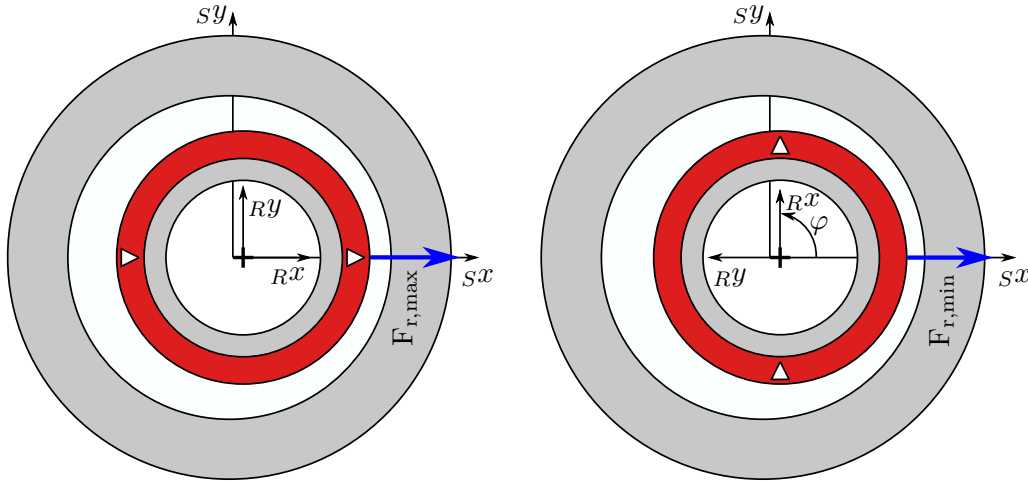


Figure 2.1.: Maximum and minimum radial reluctance forces at radial rotor deflection.

Additionally, the variation ratio

$$\hat{c}_r = \frac{{}_R C_r}{\bar{c}_r} - 1 \quad (2.3)$$

can be introduced. With these variables, the rotor-bound forces due to the passive radial stiffness can be written as

$${}_R \mathbf{F}_r = {}_R \mathbf{C}_r \cdot {}_R \mathbf{q}_r = \begin{bmatrix} \bar{c}_r (1 + \hat{c}_r) & 0 \\ 0 & \bar{c}_r (1 - \hat{c}_r) \end{bmatrix} \begin{bmatrix} {}_R x \\ {}_R y \end{bmatrix} \quad (2.4)$$

with ${}_R \mathbf{q}_r$ being the vector of radial rotor deflections (${}_R x$ defines the deflection in the direction of magnetization) and ${}_R \mathbf{C}_r$ denoting the stiffness matrix. The off-diagonal terms are non-zero when the stiffness in an eccentric rotor position is regarded, however, for small deflections from the center and for large air gaps, these terms can be neglected. Transforming ${}_R \mathbf{C}_r$ from the rotor coordinate system to the stationary stator system using the angle displacement $\varphi = \Omega t$ and the transformation matrix

$$\mathbf{A}_{SR} = \begin{bmatrix} \cos(\Omega t) & -\sin(\Omega t) \\ \sin(\Omega t) & \cos(\Omega t) \end{bmatrix} \quad (2.5)$$

according to

$${}_S \mathbf{C}_r = \mathbf{A}_{SR} \cdot {}_R \mathbf{C}_r \cdot (\mathbf{A}_{SR})^{-1} \quad (2.6)$$

allows calculating

$${}_S \mathbf{F}_r = {}_S \mathbf{C}_r {}_S \mathbf{q}_r \quad (2.7)$$

with

2. System design

$${}_S\mathbf{C}_r = \begin{bmatrix} \bar{c}_r (1 + \hat{c}_r \cdot \cos(2\Omega t)) & \bar{c}_r \hat{c}_r \cdot \sin(2\Omega t) \\ \bar{c}_r \hat{c}_r \cdot \sin(2\Omega t) & \bar{c}_r (1 - \hat{c}_r \cdot \cos(2\Omega t)) \end{bmatrix}. \quad (2.8)$$

The radial degrees of freedom are unstable by nature which means that a displacement-proportional controller with its control parameter P fulfilling

$$P > |\bar{c}_r (1 + \hat{c}_r)| \quad (2.9)$$

needs to be put in place in order to overcome the destabilizing reluctance effect, e.g. when lifting the rotor out of the touchdown bearing. For high rotational speeds, the theoretical requirement is reduced to

$$P > |\bar{c}_r| \quad (2.10)$$

due to the rotor's inertia.

2.1.1.2. 4-pole rotor

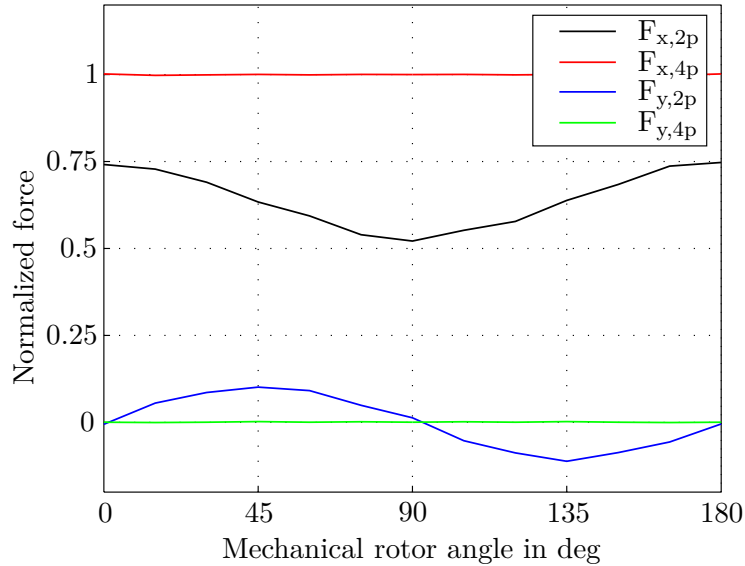


Figure 2.2.: Normalized, numerically simulated radial forces on a 2-pole and a 4-pole rotor due to a positive radial x-shift in stator-bound coordinates while the rotor turns about its rotational axis. At an angle of $\varphi = 0^\circ$, the magnetization direction of the rotor magnet coincides with the stator x-axis.

As clearly visible in Figure 2.2, and as explained in [36], the problem of anisotropic radial stiffness only occurs within the 2-pole rotor. Given a truly sinusoidal air gap flux distribution and a slotless, i.e., cylindrical, stator core, the stiffness with a higher pole number in the rotor is constant and independent of the direction of deflection. In contrast to (2.8), the stiffness matrix of the centered 4-pole system

$${}_R\mathbf{C}_{r,4p} = {}_S\mathbf{C}_{r,4p} = \begin{bmatrix} c_{r,4p} & 0 \\ 0 & c_{r,4p} \end{bmatrix} \quad (2.11)$$

is much simpler because there is no angle dependency and no stiffness coupling. Of course, the constant stiffness and, therefore, the linear force to displacement relationship is only valid for small deflections.

The fact that the variation term \hat{c}_r is missing in this case must not mislead to the conclusion that the stiffness is generally smaller. On the contrary, for a given rotor and stator geometry, the passive radial stiffness is higher with the 4-pole Halbach magnet than with the diametrically magnetized one. This means that, even though the radial stiffness is isotropic, the minimum necessary proportional gain P is higher for the 4-pole rotor at identical geometric dimensions.

2.1.2. Tilt stiffness anisotropy

The stiffness values for the tilt axes can be defined in analogy to the radial stiffness values⁴. Again, two cases shall be investigated.

2.1.2.1. 2-pole rotor

Starting out in the rotor-bound coordinate system, we can define a mean stiffness value (now with the index \mathcal{T} for the tilting degrees of freedom)

$$\bar{c}_{\mathcal{T}} = \frac{{}_R C_{\mathcal{T},\beta} + {}_R C_{\mathcal{T},\alpha}}{2} \quad (2.12)$$

between the smaller tilt stiffness ${}_R C_{\mathcal{T},\alpha}$ for tilt movements about the axis of magnetization and the larger one, ${}_R C_{\mathcal{T},\beta}$, for tilting about the axis perpendicular to it. The stiffness variation ratio then is

$$\hat{c}_{\mathcal{T}} = \frac{{}_R C_{\mathcal{T},\beta}}{\bar{c}_{\mathcal{T}}} - 1 \quad (2.13)$$

and the reluctance torques due to the positive stiffnesses can be written as

$${}_R \mathbf{T}_{c,\mathcal{T}} = \begin{bmatrix} {}_R T_{c,\alpha} \\ {}_R T_{c,\beta} \end{bmatrix} = {}_R \mathbf{C}_{\mathcal{T}} \cdot {}_R \mathbf{q}_{\mathcal{T}} \quad (2.14)$$

with

$${}_R \mathbf{C}_{\mathcal{T}} = \begin{bmatrix} \bar{c}_{\mathcal{T}}(1 - \hat{c}_{\mathcal{T}}) & 0 \\ 0 & \bar{c}_{\mathcal{T}}(1 + \hat{c}_{\mathcal{T}}) \end{bmatrix} \quad (2.15)$$

and

$${}_R \mathbf{q}_{\mathcal{T}} = \begin{bmatrix} R\alpha \\ R\beta \end{bmatrix} \quad (2.16)$$

denoting the stiffness matrix and the state variable vector, respectively, for the tilt degrees of freedom, expressed in the rotor coordinate system. As the radial stiffness matrix, also ${}_R \mathbf{C}_{\mathcal{T}}$ has non-zero off-diagonal terms when a tilted rotor situation is regarded, however, for small deflections from the non-tilted rotor position and for large air gaps, these terms can be neglected. We can now transform ${}_R \mathbf{C}_{\mathcal{T}}$ from the rotor coordinate system to the stationary stator system using the same transformation matrix \mathbf{A}_{SR} as above for deriving the radial stiffness according to

$${}_S \mathbf{C}_{\mathcal{T}} = \mathbf{A}_{SR} \cdot {}_R \mathbf{C}_{\mathcal{T}} \cdot (\mathbf{A}_{SR})^{-1} \quad (2.17)$$

⁴In contrast to the radial deflections, the tilt degrees of freedom are stable and, thus, exhibit positive stiffness values. This becomes clear as, e.g., in an equilibrium situation ($\ddot{\alpha} = \dot{\alpha} = 0$), a positive external torque $T_{external}$ is necessary in order to maintain a tilted position $\alpha = 0$.

2. System design

and further substitute into (2.14) to obtain the reluctance torques

$${}^s\mathbf{T}_{c,\mathcal{T}} = {}^s\mathbf{C}_{\mathcal{T}} \cdot {}^s\mathbf{q}_{\mathcal{T}} \quad (2.18)$$

in the stator-fixed coordinate system with

$${}^s\mathbf{C}_{\mathcal{T}} = \begin{bmatrix} \bar{c}_{\mathcal{T}} (1 - \hat{c}_{\mathcal{T}} \cdot \cos(2\Omega t)) & \bar{c}_{\mathcal{T}} \hat{c}_{\mathcal{T}} \cdot \sin(2\Omega t) \\ \bar{c}_{\mathcal{T}} \hat{c}_{\mathcal{T}} \cdot \sin(2\Omega t) & \bar{c}_{\mathcal{T}} (1 + \hat{c}_{\mathcal{T}} \cdot \cos(2\Omega t)) \end{bmatrix} \quad (2.19)$$

and

$$\mathbf{q}_{\mathcal{T}} = \begin{bmatrix} \alpha \\ \beta \end{bmatrix} \quad (2.20)$$

in the stationary stator coordinate system.

2.1.2.2. 4-pole rotor

The tilt stiffness anisotropy is, as with the radial stiffness, limited to the 2-pole rotor. As depicted for the radial reluctance forces above, Figure 2.3 displays the restoring reluctance torques. While we can see the same cross coupling and anisotropy for the 2-pole rotor, the 4-pole rotor shows constant tilt stiffness $c_{\mathcal{T},4p}$ and exerts no cross coupling as it rotates about its principle axis so that we can state

$${}^R\mathbf{C}_{\mathcal{T},4p} = {}^s\mathbf{C}_{\mathcal{T},4p} = \begin{bmatrix} c_{\mathcal{T},4p} & 0 \\ 0 & c_{\mathcal{T},4p} \end{bmatrix} \quad (2.21)$$

as a concluding expression for the 4-pole rotor.

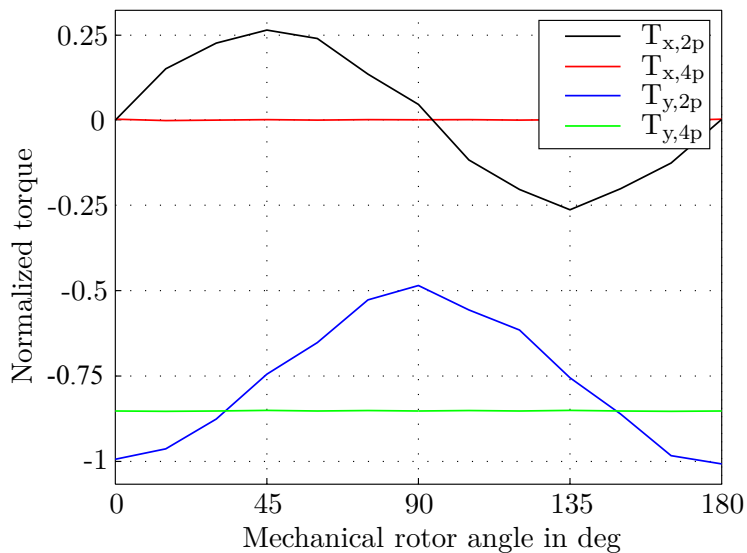


Figure 2.3.: Normalized, numerically simulated torque on a 2-pole and a 4-pole rotor due to a positive tilt about the y-axis in stator-bound coordinates while the rotor turns about its rotational axis. At an angle of 0° , the magnetization direction of the rotor magnet coincides with the stator x-axis.

2.1.3. Rotor selection

Summarizing the above argumentation, the following facts lead to the decision to use a 2-pole rotor for the further design process.

- While it may be a very disturbing property for low-speed drives, the radial and tilt stiffness anisotropy of the 2-pole rotor are not much of a concern for high-speed applications. This is simply due to the fact that the main frequency of the radial reluctance force and tilt reluctance torque acting on a deflected rotor which is equal to twice the mechanical rotor speed Ω quickly surpasses the rigid body modes of the stabilized radial and tilt rotor movement.
- The same is true for the cross coupling between the deflections in radial and tilt directions to the axes which are perpendicular to the deflection axis. While critical for low-speed drives, this behavior is not relevant for high-speed drives.
- In comparison to the 2-pole rotor, the control of a drive with a 4-pole rotor requires the double values for minimum PWM-frequency, minimum sampling frequency for angle and current signals, and control loop calculation frequency. This increases switching losses in the active power electronic elements and, for the current project, also pushes the requirements beyond the capabilities of the available control hardware.
- As reported in [72], a 4-pole rotor causes significantly higher iron losses per mass unit of stator iron. Due to the shorter flux path and the reduced flux density in case of the 4-pole rotor, however, the necessary stator yoke can be thinner which, in total, reduces the losses to a value close to the 2-pole rotor. Of course, this verdict heavily depends on the loss characteristic of the applied stator material.
- High energy density permanent magnets are made of sintered NdFeB which is anisotropic due to its manufacturing process. While technically feasible, permanent magnet rings in suitable dimensions with 4-pole HALBACH-magnetization were not available for prototyping. The 2-pole diametrically magnetized version does not pose any availability problems.

2.2. Winding topology

2.2.1. Connection topology: separated vs. combined windings

It is possible to differentiate between the following winding configurations within a bearingless drive:

- When multiple sets of windings are used, i.e., one which is responsible for creating torque and another one for producing the necessary bearing forces, then the term *separate winding system* is applied. In this case, the necessary currents and voltages for the motor and bearing function are calculated, applied and controlled separately for each winding set. Since it poses a very intuitive approach to the problem of parallel torque and force creation, this is a common design which is scientifically documented in numerous publications, e.g. [20, 22, 90, 85, 57, 19, 125].

2. System design

- For a further step of mechanical simplification in a bearingless drive, the reduction to only one back iron core with one single set of windings is possible. The current components generating torque and forces now have to be superposed in the control circuit before being applied to the bearingless motor. In this case, the term *combined winding system* is used. Such a combined winding system allows a simplification of the mechanical setup but increases the control complexity. Many studies have dealt with this type of winding [1, 111, 38, 40, 43, 42, 96, 74, 80].
- A third winding topology has appeared recently ([23, 88, 107]) which partly mixes the properties of the separated and the combined winding technology. It provides combined windings with different coil terminals for torque and force current connections by tapping the respective coils. This is termed *parallel motor winding* or *bridge winding*⁵ and can, more generally be found in the literature as *dual-purpose no-voltage (DPNV)* windings. However, this topology can increase the required number of power switches and current sensors significantly as shown by the authors of [107].

All three configurations have advantages and disadvantages and there have been lively discussions about whether one should be preferred over the others. The authors of [94] have compared separated and combined winding systems for a disk shaped bearingless radial pump. Another work [106] discusses the differences between the two available DPNV winding configurations and eventually gives their common advantages and disadvantages compared to a separated winding system. All these discussions have come to the conclusion that no general verdict can be given but that the correct choice is application-dependent. One of the most significant differences between the mentioned winding types is the sensitivity to the induced voltage or *back-EMF*⁶ which shall be discussed in the following passages.

2.2.1.1. Back-EMF sensitivity for separated windings

Depending on how the individual coils within an electric machine are connected and which winding pitch they span, the back-EMF plays an important role. This is first demonstrated with a separated winding system. Figure 2.4 shows 2 coils which are wound around a slotless stator core in a toroid winding manner⁷, connected in order to produce bearing forces (identical winding sense, Figure 2.4a) and motor torque (opposing winding sense, Figure 2.4b), respectively. Coil 1 and Coil 2 have an identical number of winding turns and, thus, identical values for their resistance

$$R = R_1 = R_2 \quad (2.22)$$

and individual inductance

$$L = L_1 = L_2. \quad (2.23)$$

Also the linked rotor flux amplitudes in the coils

$$\hat{\Psi} = \hat{\Psi}_1 = \hat{\Psi}_2 \quad (2.24)$$

⁵In this work, the terms '*parallel motor, serial bearing winding*' and '*serial motor, parallel bearing winding*' are applied in order to express key difference in the terminology itself.

⁶Internationally, the term back-EMF (*back Electro Motive Force*) is dominant.

⁷The toroid winding topology is discussed in Section 2.2.2.1.

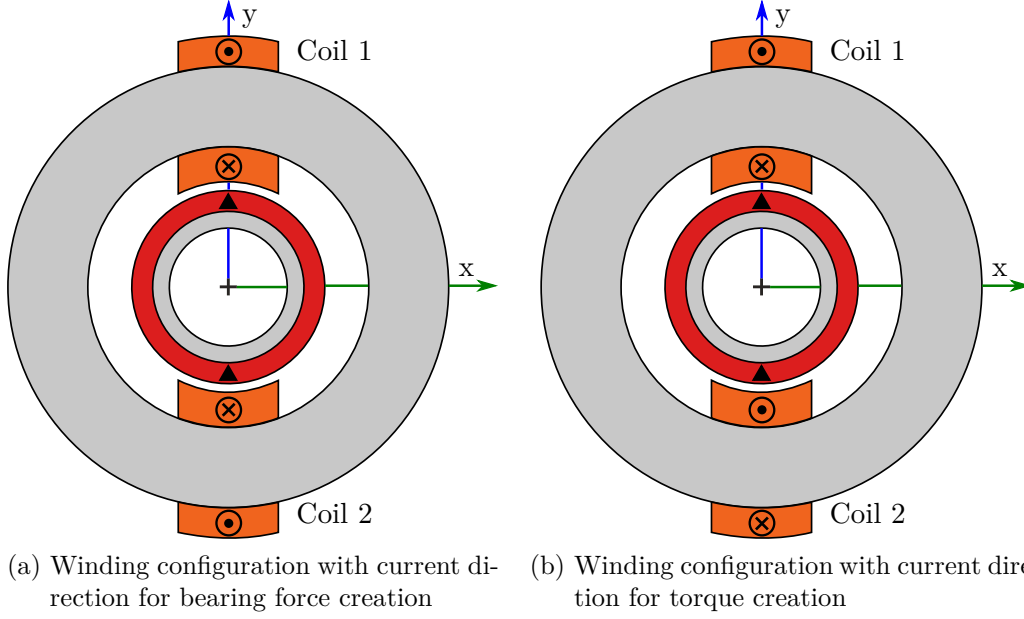


Figure 2.4.: Cross section through a 2-pole rotor and a stator with an exemplary toroid coil pair

are equal but due to the geometrically opposing placement, the linked flux in coil 1 is

$$\Psi_1 = \hat{\Psi} \sin(\omega t) \quad (2.25)$$

while the flux in coil 2 is

$$\Psi_2 = \hat{\Psi} \sin(\omega t + \pi) \quad (2.26)$$

in the case of a diametrically magnetized rotor where the mechanical angular speed Ω is equal to the electrical angular frequency ω . This means that the back-EMF voltages due to the rotor speed in the coils can be written as

$$V_{bEMF,1} = -\frac{d\Psi_1}{dt} = -\hat{\Psi} \cos(\omega t) \omega \quad (2.27)$$

and

$$V_{bEMF,2} = -\frac{d\Psi_2}{dt} = -\hat{\Psi} \cos(\omega t + \pi) \omega = +\hat{\Psi} \cos(\omega t) \omega. \quad (2.28)$$

For the sake of clarity, only one back-EMF component,

$$V_{bEMF} = \hat{\Psi} \cos(\omega t) \omega = -V_{bEMF,1} = V_{bEMF,2} \quad (2.29)$$

will be used in the following circuit diagrams. The difference in sign will be expressed by the direction of the voltage arrow.

When looking at Figure 2.4a, it becomes clear that by connecting the two coils, the back-EMF components of coil 1 and coil 2 cancel out. The equivalent circuit in Figure 2.5a shows the relevant electrical components for bearing force creation.

Closing the loop by connecting the top and bottom of the circuit with the two center points of a full bridge of the bearing inverter stage gives the voltage equation

$$V_{bridge,F} = i_F 2R + 2L \frac{di_F}{dt} \quad (2.30)$$

2. System design

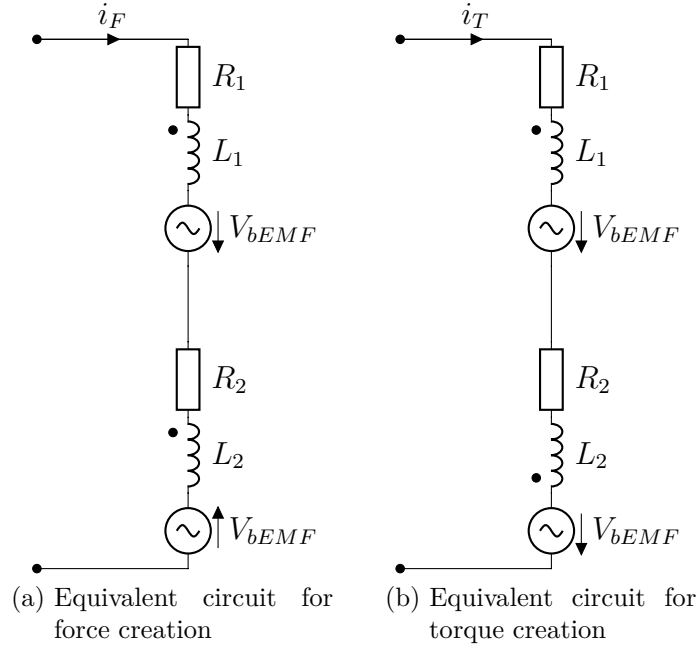


Figure 2.5.: Equivalent circuits for the coil configurations shown in Figure 2.4

which only holds the ohmic and inductive voltage drops caused by the bearing force current i_F .

The same coils could be used for creating motor torque when the coil connections are carried out differently so the torque-creating current i_T flows in opposite winding direction through one of the coils as shown in Figure 2.4b. The equivalent circuit is given in Figure 2.5b. The opposed sense for coil 2 changes (2.30) to

$$V_{bridge,T} = i_T 2R + 2\hat{\Psi} \cos(\omega t) \omega \quad (2.31)$$

for the bridge connection voltage of the motor inverter stage. The first interesting observation about (2.31) is that for the special topology of a toroid winding and for the case of a non-saturated, ideal stator core, the inductive voltage drops of coil 1 and coil 2 cancel out as a consequence of the opposed winding directions. The second notable point is the back-EMF which now adds up the two voltages of Figure 2.5b so the maximum speed for the separated coil system is limited to

$$\omega_{max,sep} = \frac{V_{DC} - i_T 2R}{2\hat{\Psi}} \quad (2.32)$$

when the peak full DC-link voltage

$$\hat{V}_{bridge,T} = V_{DC} \quad (2.33)$$

is applied to the full bridge of the motor inverter.

2.2.1.2. Back-EMF sensitivity for combined windings

In a combined winding scheme, each of the opposingly placed coils in Figure 2.4 needs to be controlled individually which results in a corresponding circuit diagram shown in Figure 2.6.

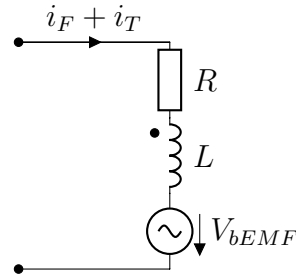


Figure 2.6.: Equivalent circuit for one of the coils shown in Figure 2.4 in a combined winding system

Consequently, the closed loop voltage equation for, e.g., coil 1 evolves into

$$V_{bridge} = (i_F + i_T) R + L \frac{d(i_F + i_T)}{dt} + \hat{\Psi} \cos(\omega t) \omega \quad (2.34)$$

and (2.32) is rewritten for the combined coil as

$$\omega_{max,comb} = \frac{V_{DC} - (i_F + i_T) R - L \frac{d(i_F + i_T)}{dt}}{\hat{\Psi}} \quad (2.35)$$

when a full bridge is available for controlling the coil voltage. If, however, all coils are star-connected in a symmetric system, the maximum speed equation (2.35) turns into

$$\omega_{max,comb,star} = \frac{\frac{V_{DC}}{2} - (i_F + i_T) R - L \frac{d(i_F + i_T)}{dt}}{\hat{\Psi}}. \quad (2.36)$$

Equation (2.34) reveals that the back-EMF component will be relevant not only for the torque creation but also for the bearing forces since these two systems are merged into one. The maximum speed is no longer determined by the necessary torque-related current i_T alone. In addition to that component which is speed-dependent in many applications and which, therefore, would allow quantifying ω_{max} , now the bearing force current i_F also needs to be taken into account. Since the bearing currents typically pose the system's reaction to a certain unknown disturbance force, they cannot be calculated *a priori* and thus, (2.36) is undetermined. Consequently, in order to be able to apply the necessary bearing currents even at maximum speed, a certain supply voltage reserve needs to be respected.

2.2.1.3. Back-EMF sensitivity for DPNV windings

The idea of the separated winding system is to use physically separated coils for force and torque creation. The combined winding system uses superposition of bearing and motor currents for energizing one common coil. The dual-purpose no-voltage windings do change the physical arrangement of the combined winding system by providing additional coil terminals but they do not completely decouple the two systems and, thus, they do not limit the coil volume available for either force or torque production. In the ensuing section, the two arrangements discussed in the literature [23, 106] shall be applied to the example of the two opposing coils shown in Figure 2.4.

Serial motor, parallel bearing coil connection Coil 1 and Coil 2 can be connected as for the motor winding in the separated winding topology shown in the right image of Figure 2.4b. In order to also provide bearing forces, the connection point between the two coils can be tapped and modulated by a terminal of the bearing inverter stage (Figure 2.7). This means that when the bearing inverter injects $2i_F$ in this connection

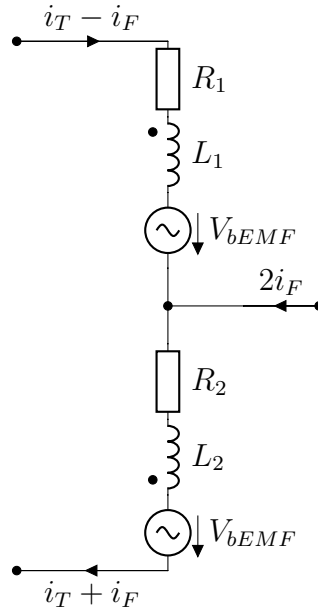


Figure 2.7.: Equivalent circuit for the coils shown in Figure 2.4 being connected for serial motor, parallel bearing DPNV configuration.

point, the current in coil 1 must be $i_T - i_F$ and that in coil 2 must be $i_T + i_F$. This topology has the disadvantage of summing up the two back-EMF components to $2V_{bEMF}$ due to the serial connection of coil 1 and coil 2 when seen from the motor inverter clamp. Concerning the necessary supply voltage for a given rotor speed, this is equal to the separated winding design. Other than with the combined winding topology, the back-EMF components cancel out when seen from the bearing inverter clamp and thus, no supply voltage reserve needs to be respected for force creation.

Parallel motor, serial bearing coil connection Connecting coil 1 and coil 2 in parallel and connecting the bearing inverter to one coil terminal also provides the feature of using both coils and, thus, the entire copper volume, for both force and torque creation (Figure 2.8). In contrast to the serial motor, parallel bearing coil connection shown above, the motor inverter terminal now experiences only V_{bEMF} instead of $2V_{bEMF}$. Of course, the inverter needs to drive a current of $2i_T$ in order to create the same torque as above. The bearing inverter now sees a serial connection of coils which means that a current of only i_F is necessary while the voltage which needs to be overcome is the sum of both coil paths. This, however, is not much of a problem because, as in the bearing coil system of the separated winding topology or in the serial motor, parallel bearing coil connection shown above, the back-EMF voltage cancels out for the bearing force creation.

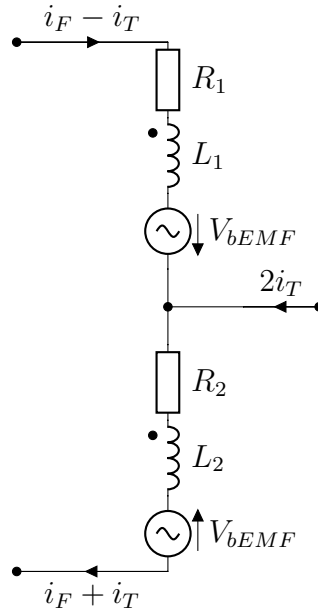


Figure 2.8.: Equivalent circuit for the coils shown in Figure 2.4 being connected for parallel motor, serial bearing DPNV configuration.

2.2.1.4. Selection of connection topology

With all the specific advantages and disadvantages given above, the combined winding system is chosen for the presented work. The central arguments for this decision are listed below.

- Separated windings and DPNV windings offer a more straight forward approach to controlling the bearingless motor with physically separated coils or at least coil terminals, currents, and control structures. In a scientific project, however, this argument should be null and void.
- As stated in the preceding parts of Section 2.2.1, the combined winding topology demands a supply voltage reserve for bearing force creation at maximum speed. However, only one coil and, thus, only one back-EMF component is connected to the power supply. Let aside the parallel motor, serial bearing DPNV winding, the available source voltage is twice as high for the combined winding as for all other systems when the same connection type (full bridges or half bridges with star-connected phases) is chosen. This means that either ω_{max} is higher or, at equal ω_{max} , sufficient voltage reserve is provided since V_{bEMF} reaches only half of the supply voltage when resistive and inductive losses are not considered.
- As with the DPNV winding, a combined winding system always uses the entire conductor cross section. This means that the copper volume is well utilized and the conductive losses are reduced, no matter if high torque and low radial forces or low torque and high radial forces are required.
- The part count and the required winding space is obviously reduced compared to the separated winding topology.

2. System design

- Many features of the parallel motor, serial bearing DPNV winding are similar to the ones of a combined winding system, making it the most probable replacement candidate in the case that, for some reason, a combined winding is not applicable.

2.2.2. Coil form

The reduction of iron losses is a critical factor for the successful design of a high-speed drive. An analysis of the analytical calculation for this matter, as well as experimental data can be found in Chapter 6. One of the key measures which can be taken on the geometric design side is the use of a slotless stator. Slotted stators dispose of stator teeth which represent zones of high flux density concentration. Additionally, the flux modulation by these teeth adds higher harmonics to the magnetic field and it has been pointed out in the literature (e.g. in [6] and [10]) that this is why slotted stator designs entail high iron losses and, therefore, should be avoided in a high-speed drive. The basic differences of a slotted and a slotless stator core are demonstrated in Figure 2.9.

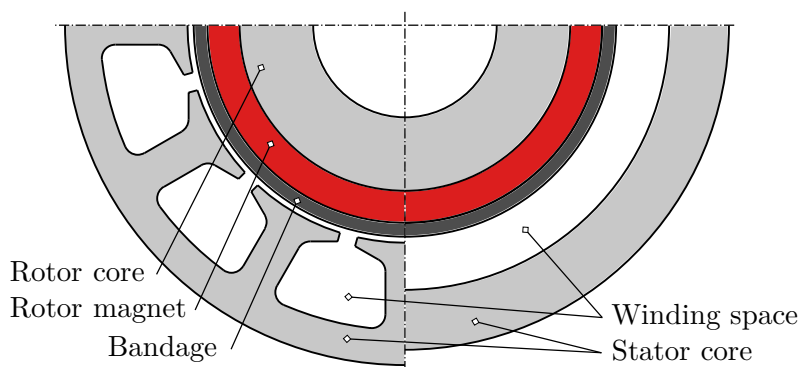


Figure 2.9.: Slotted stator (left) and slotless stator (right) topology.

The use of a slotless stator core opens the question of how to manufacture the coils for the stator winding since there are no teeth to wind the conductors around. A so-called *air gap coil* as shown in Figure 2.10 usually is made of self-bonding wire or by applying some other form-stabilizing technique such as epoxy pouring or dribbling of the conductors. These rather demanding manufacturing processes, together with the fact that the winding heads in a flat stator dominate the necessary wire length, encourage consideration of alternative methods for placing the conductors on the stator core.

2.2.2.1. Air gap vs. toroid coil

Of the entire air gap coil, only the axial conductor sections constitute the active part, the tangential sections do not contribute to the torque or force production. The same active sections can be provided by a so-called *toroid coil* which is depicted in Figure 2.11 and which has been analyzed in [72] for the use in the present drive topology. This topology eliminates the winding head which is produced by traversing back and forth from one slot⁸ to the other but instead creates an inactive wire section where it is wound around the stator core. The question of which coil form is beneficial regarding wire length l_{Cu} and, thus, resistive losses, is decided by the axial length of the stator l_S , its radial height

⁸The term *slot* actually refers to a *virtual slot* which is used to define the the circumferential position of a coil while ignoring the fact that there are no actual teeth or slots in a slotless core.

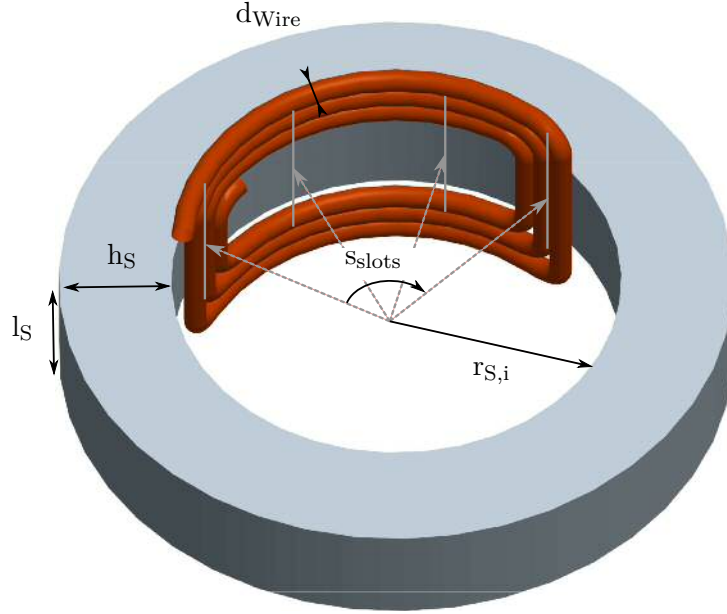


Figure 2.10.: Air gap winding with basic geometric parameters

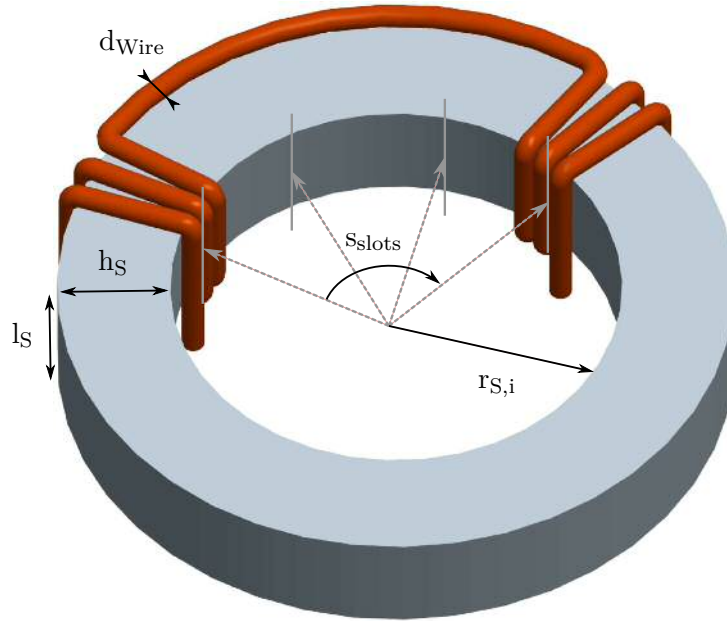


Figure 2.11.: Toroid winding with basic geometric parameters

h_S , and the angle between the two coil sides which is expressed as the slot step s_{slots} . A numerical comparison for a certain design can be drawn by evaluating

$$l_{Cu,Airgap} = 2N \left(l_S + h_S + d_{wire} + 2\pi \cdot \left(r_{i,S} + \frac{h_S}{2} \right) \frac{s_{slots}}{n_{slots}} \right) \quad (2.37)$$

and

$$l_{Cu,Toroid} = 2N (2h_S + 2l_S + 4d_{wire}) + 2\pi \cdot \left(r_{i,S} + \frac{h_S}{2} \right) \frac{s_{slots}}{n_{slots}} \quad (2.38)$$

where, in addition to the given geometric parameters, N , d_{wire} , and n_{slots} specify the number of winding turns, the wire diameter and the total number of slots, respectively.

2. System design

It needs to be remarked that the radius of the air gap winding head and of the connection wire in the toroid winding was enlarged by $\frac{h_S}{2}$ in order to reflect the necessity of crossing the heads and connections of different overlapping phases.

Table 2.1.: Influencing parameters for the winding topology decision

Air gap winding	Parameter	Toroid winding
← <i>short</i> →	Slot step s_{slots}	← <i>wide</i> →
← <i>low</i> →	Number of winding turns N	← <i>high</i> →
← <i>long</i> →	Axial stator length l_S	← <i>short</i> →
← <i>small</i> →	Radial stator height h_S	← <i>large</i> →

Apart from a possible advantage regarding the necessary wire length, the toroid winding offers simple prototype manufacturing, a very compact and robust mechanic configuration, and good cooling properties as the winding head does not protrude axially into the ambient air but is fully wound around the stator. This, additionally, makes both, the stator core and the winding available to cooling measures at the outer stator surface. It has to be mentioned here that the real winding does not cover the entire outer stator core surface as suggested in the winding scheme in Figure 2.12 but is concentrated as later shown in Figure 2.15. Manufacturing in an automated process may be more complex than for the air gap winding unless a segmented stator core is used where pre-manufactured coils can be slid onto the stator segments.

Overall, the toroid winding seems advantageous and will, therefore, be used in the further design process.

2.2.2.2. Single coil vs. double coil

In Section 2.2.2.1, the toroid winding form is presented as an alternative to the air gap winding which in turn was deduced from a standard winding design in a slotted motor. Therefore, the toroid winding shown in Figure 2.11 consists of two coil halves which, together, are electrically equivalent to the air gap winding. This way of statically connecting the two winding halves will be called a *double coil* arrangement in this work. It is, however, also possible to use only one half of the depicted toroid winding per phase which will be called a *single coil* arrangement. Figure 2.12 shows an example of both arrangements.

The single coil arrangement was applied to bearingless disk drives in [115] and [116]. Since the drive topology used in these cited works has been adopted from preceding publications of the current project, a comparison of the single coil and double coil arrangement was drawn in [80]. The most essential findings of this work will be reflected and extended in Sections 2.3 and 2.4.

In the further course of this work, an abbreviation terminology will be used which specifies the number of phases and the coil topology. For example, the terms *5ps*, *6ps*, and *8pd* stand for a *5-phase single coil* design, a *6-phase single coil* design, and an *8-phase double coil* design, respectively.

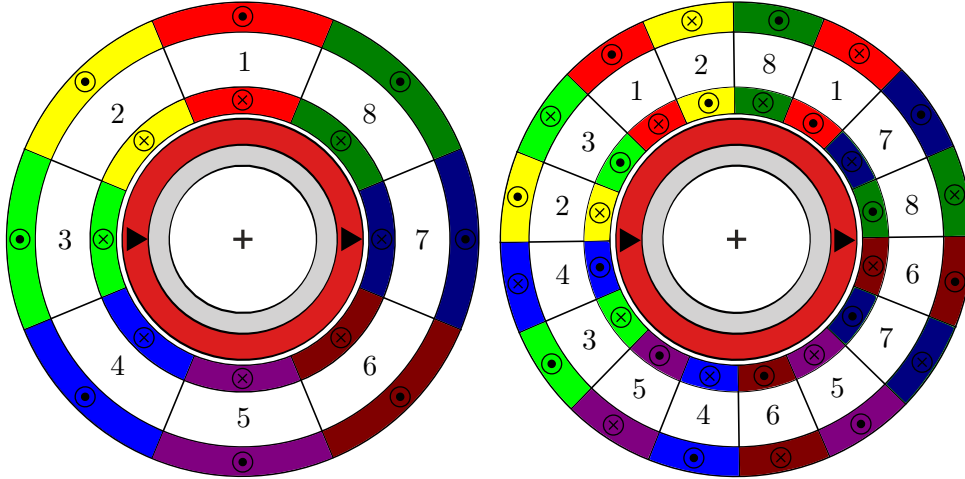


Figure 2.12.: Winding scheme of 8-phase single coil (left) and 8-phase double coil (right) including the rotor showing the diametric magnetization direction

2.3. Evaluation criteria

The previously presented topological possibilities offer a wide pool of feasible winding designs. In order to allow an optimization, this section will discuss which evaluation criteria are suitable for bearingless drives.

2.3.1. Torque and radial forces

As shown in Figure 1.4, a disk drive with passive stabilization in the axial and tilt directions needs to generate the motor torque and the active bearing forces in the two radial degrees of freedom. Therefore, the torque and radial force capacity of the different designs constitute the main comparison values. However, there is no standard definition of these values for bearingless drives as, e.g., the torque coefficients for conventional electrical drives. This is due to the fact that, here, forces and torque have to be created simultaneously and that certain winding properties have quite different effects on the torque and force capacity. One way of obtaining a suitable evaluation criterion can be to consider the achievable radial force values F_r for *one* distinct direction (e.g. either F_x or F_y) while producing *no* force in the other direction and also *no* torque T_z . Therefore, the rotor angle dependent matrix $\mathbf{T}_m(\varphi)$ has to be found, defining the relationship between the vector of phase currents for the m phases

$$\mathbf{i}(\varphi) = \begin{bmatrix} i_1(\varphi) \\ \vdots \\ i_m(\varphi) \end{bmatrix} \quad (2.39)$$

and the radial force and torque vector

$$\mathbf{Q}(\varphi) = \begin{bmatrix} F_x(\varphi) \\ F_y(\varphi) \\ T_z(\varphi) \end{bmatrix} \quad (2.40)$$

as

$$\mathbf{Q}(\varphi) = \mathbf{T}_m(\varphi) \mathbf{i}(\varphi). \quad (2.41)$$

2. System design

For reasons of simplicity, we assume in these general torque and force analysis matters, that each winding consists of 1 winding turn, making the value for the magneto-motive force in Atturns equal to the phase currents in A. The j -th column of $\mathbf{T}_m(\varphi)$ holds the angle dependent force and torque value which is created when only the j -th phase is powered with a constant current value while the rotor rotates about φ . Knowledge of producible torque and radial forces for *one* energized coil over the entire rotor angle is sufficient in order to describe the complete machine behavior. This has been presented in detail in [111], [108], and [38].

2.3.1.1. Direct criterion

It may seem tempting to use the relationship given in (2.41) to create a bearing force evaluation criterion

$$t_F = \frac{\sum_{i=1}^2 \sum_{j=1}^m rms(\mathbf{T}_m(\varphi)_{i,j})}{2m} \quad (2.42)$$

and a torque evaluation criterion

$$t_T = \frac{\sum_{j=1}^m rms(\mathbf{T}_m(\varphi)_{3,j})}{m} \quad (2.43)$$

by taking the mean value of the grouped matrix components for forces or torques. Unfortunately, the two terms mentioned above would not yield a good basis for comparison since it is not guaranteed in that case that only one of the components of $\mathbf{Q}(\varphi)$ is created exclusively. This however, is one of the key features of a bearingless drive as we want to be able to produce torque and forces independent of each other and we also want the force and torque comparison values to reflect this property.

2.3.1.2. Inverse criterion

For controlling a bearingless drive, the relationship between the force and torque vector and the currents, given in (2.41), needs to be inverted in order to form the relationship

$$\mathbf{i}(\varphi) = \mathbf{K}_m(\varphi) \mathbf{Q}(\varphi) \quad (2.44)$$

which links the demanded output $\mathbf{Q}(\varphi)$ to the necessary currents $\mathbf{i}(\varphi)$. The matrix $\mathbf{K}_m(\varphi)$ is calculated by inversion of $\mathbf{T}_m(\varphi)$. For this inversion, additional criteria such as the star-connection of the motor phases or a minimum winding loss criterion are necessary since usually, $\mathbf{T}_m(\varphi)$ is not a square matrix. A detailed mathematical description of this inversion procedure is given in [109].

Applying the current vectors

$$\mathbf{i}_{F_x}(\varphi) = \mathbf{K}_m(\varphi) \begin{bmatrix} 1\text{N} \\ 0 \\ 0 \end{bmatrix} \quad (2.45)$$

$$\mathbf{i}_{F_y}(\varphi) = \mathbf{K}_m(\varphi) \begin{bmatrix} 0 \\ 1\text{N} \\ 0 \end{bmatrix} \quad (2.46)$$

$$\mathbf{i}_{T_z}(\varphi) = \mathbf{K}_m(\varphi) \begin{bmatrix} 0 \\ 0 \\ 1\text{Nm} \end{bmatrix} \quad (2.47)$$

ensures that, in the respective situation, only the demanded force or torque component is produced without exciting any other component. Applying the currents in the appropriate ratios according to (2.45)-(2.47), with the highest current not exceeding the phase current limit, gives the mentioned maximum exclusive force in one distinct direction or maximum exclusive torque. Calculating the rms-values of $\mathbf{i}_{F_x}(\varphi)$, $\mathbf{i}_{F_y}(\varphi)$ and $\mathbf{i}_{T_z}(\varphi)$ and then taking the mean value over all phases leads to more suitable comparison values for bearingless drives than the ones given in (2.42) and (2.43). The new criteria were introduced in [110] as the force and torque constants

$$k_F = \frac{2m}{\sum_{i=1}^m \sum_{j=1}^2 \text{rms}(\mathbf{K}_m(\varphi)_{i,j})} \quad (2.48)$$

and

$$k_T = \frac{m}{\sum_{i=1}^m \text{rms}(\mathbf{K}_m(\varphi)_{i,3})}, \quad (2.49)$$

respectively. The constants k_F and k_T can be interpreted as the reciprocal mean value of the minimum rms current necessary to create 1 N of F_x or F_y force or 1 Nm of T_z torque. These constants, therefore, have the units N/A and Nm/A, respectively. They provide a more adequate comparison value for the different designs, yet for k_F , there is a potential flaw. The forces and torques used for the calculation of $\mathbf{T}_m(\varphi)$ and, by inversion, of $\mathbf{K}_m(\varphi)$, are divided by the phase current⁹ applied in the simulation or measurement. This is necessary in order to obtain the factors in N/A and Nm/A which constitute $\mathbf{T}_m(\varphi)$. However, this also eliminates the link to the available copper cross section of a respective design. Therefore, comparing k_F and k_T for designs with different phase number or different coil number per phase and, thus, different winding space per phase is misleading.

⁹It shall be reminded here, that, as stated in the beginning of Section 2.3.1, we assume all windings to have 1 winding turn, making the phase currents equal to the magneto-motive force.

2. System design

2.3.1.3. Mean torque criterion

The best comparison quantity is obtained by evaluating the mean value of the maximum torque while producing zero radial forces, defined as

$$\bar{T}_z = \frac{1}{2\pi} \int_0^{2\pi} \max \left(T_z(\varphi) \mid_{J_{1..m} \leq J_{max}, F_x = F_y = 0} \right) d\varphi \quad (2.50)$$

with J_{max} giving the maximum current density that shall be allowed in the conductor. The problem transforms to

$$\bar{T}_z = \frac{1}{n} \sum_{i=1}^n \max \left(T_z(\varphi_i) \mid_{J_{1..m} \leq J_{max}, F_x = F_y = 0} \right) \quad (2.51)$$

for n discrete simulation or measurement points. Using the current to forces and torque relationship given in (2.41), the maximum value can be found by solving the optimization problem

$$\max \left(\begin{bmatrix} 0 & 0 & 1 \end{bmatrix} \mathbf{T}_m(\varphi) \mathbf{i}(\varphi), \mathbf{i}(\varphi) \right) \quad (2.52)$$

for the vector of the phase currents while respecting the zero-radial-force requirement $F_x = F_y = 0$ which translates into

$$\begin{bmatrix} 1 & 0 & 0 \\ 0 & 1 & 0 \end{bmatrix} \mathbf{T}_m(\varphi) \mathbf{i}(\varphi) = \begin{bmatrix} 0 \\ 0 \end{bmatrix}, \quad (2.53)$$

the maximum current density specification $J_{1..m} \leq J_{max}$ which can be expressed as

$$i_{1..m} \leq i_{max}, \quad (2.54)$$

and the zero-sum-current requirement

$$\begin{bmatrix} 1 & \dots & 1 \end{bmatrix} \mathbf{i}(\varphi) = 0 \quad (2.55)$$

which reflects the star-connection. As the matrix $\mathbf{T}_m(\varphi)$ only holds the linear components for the force and torque calculation, equations (2.52)-(2.55) can be solved in a linear optimization algorithm.

2.3.1.4. Start-up criterion and minimum force

Another weakness of the inverse criterion above comes from the fact that in the first two columns of $\mathbf{K}_m(\varphi)$, only the distinct force directions F_x and F_y are regarded. The additional use of the rms value of $\mathbf{K}_m(\varphi)$ increases this selectivity and entails the problem that there may be certain rotor angles where only little forces or torques can be created but which, in this comparison, would stay unnoticed. This may become problematic for the start-up, when the rotor needs to be lifted into the center position. Forces of *any* direction may be required, since the resting position may be at *any* point around the stator surface, with, theoretically, *any* rotor orientation. Other than with the torque criterion, averaging is not possible, calling for a separate *start-up* criterion.

For successful startup, the active radial force needs to overcome the radial reluctance force $F_{r,rel}$ according to

$$F_r(\varphi, \varphi_F) > F_{r,rel}(\varphi, \varphi_\Delta) \quad (2.56)$$

for every rotor angle, every force angle φ_F , and every rotor deflection angle φ_Δ . The latter two are evidently related according to

$$\varphi_F = \varphi_\Delta + \pi \quad (2.57)$$

but are retained as separated variables to emphasize the active nature of F_r and the passive character of $F_{r,rel}$. For a general minimum force capacity, $F_r(\varphi, \varphi_F)$ can be maximized for the available current and minimized over the associated angles according to

$$F_{r,min} = \min \left(\max \left(F_r(\varphi, \varphi_F) \mid J_{1..m} \leq J_{startup}, T_z = 0 \right) \right) \forall \varphi, \varphi_F \in [0, 2\pi]. \quad (2.58)$$

Additionally, the independence from the torque creation needs to be retained by demanding that zero torque is produced when applying the start-up force. Similar as for the mean torque criterion, the maximum short-term current density, here specified for the start-up current density $J_{startup}$, needs to be respected. Again, a linear optimization problem can be defined, however, the cascaded optimization must be treated differently. A simple approach can be to evaluate the maximum possible F_x force while generating no F_y force or torque. This can be expressed as

$$\max \left(\begin{bmatrix} 1 & 0 & 0 \end{bmatrix} \mathbf{T}_m(\varphi) \mathbf{i}(\varphi), \mathbf{i}(\varphi) \right) \quad (2.59)$$

and

$$\begin{bmatrix} 0 & 1 & 0 \\ 0 & 0 & 1 \end{bmatrix} \mathbf{T}_m(\varphi) \mathbf{i}(\varphi) = \begin{bmatrix} 0 \\ 0 \end{bmatrix} \quad (2.60)$$

with (2.54) and (2.55) still being respected. Then, the coordinate system defining the x and y directions is rotated to the next value of φ_F and the linear optimization problem is repeated. As the resulting term is not simple to interpret, an intuitive graphic approach is shown in Section 2.4.2.3.

The start-up moment is also special when it comes to the rotor position. The deflection of the rotor is equal to the physically available air gap δ . This eccentricity does influence the force and torque characteristics of the drive but as the magnetic air gap δ_m is typically significantly wider than δ due to the slotless topology, the effect is negligible. Figure 2.13 shows the simulated active forces and the torque in a 6ps disk drive which are created when one coil is energized with a constant current density while the rotor is rotated about 360° . Both situations, the centered and the eccentric rotor position, are compared. In the latter case, the direction of the rotor deflection also changes with the rotor angle so one pole is always in contact with the touchdown bearing.

2.3.2. Passive stabilization forces and torques

2.3.2.1. Axial stiffness criterion

As depicted in Figure 1.4 in Chapter 1, the axial stiffness c_z of a rotor in a permanent magnet circuit is positive, i.e., stabilizing. Its value depends on the geometric dimensions of the rotor, the stator, and the air gap, as well as on the applied magnetic and ferromagnetic materials. It is thus clearly an objective for an optimization process which is presented in Section 2.4.3. The objective itself, however, is not clear *a priori* but must be decided depending on the application. On the one hand, an axially stiff system does not deflect as much under a certain axial load as a system with less stiffness. On the other

2. System design

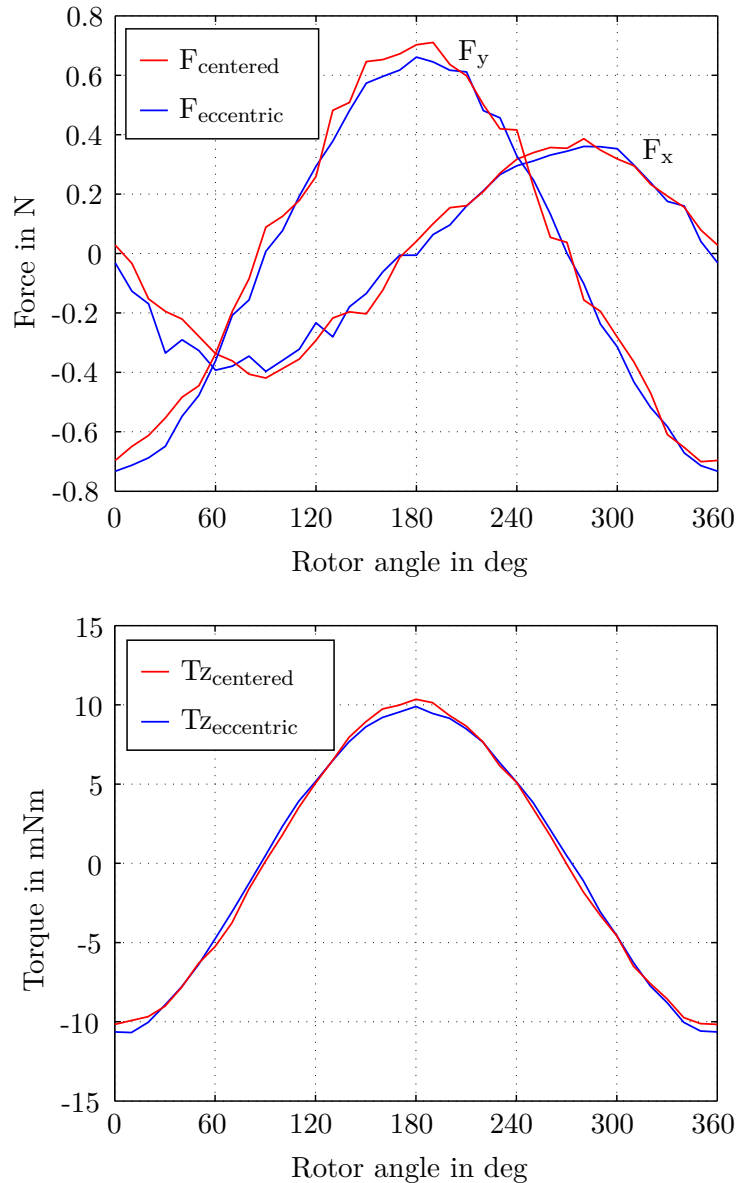


Figure 2.13.: Comparison of simulated x- and y- forces (top) and torque (bottom) with constant current in one coil over one rotor revolution with centered or 0.5 mm eccentric rotor, illustrating the start-up.

hand, low stiffness values bring the rigid body resonance frequency

$$\Omega_z = \sqrt{\frac{c_z}{m_R}} \quad (2.61)$$

down to low values where it can be passed-through quickly and without risking system damage if the rotor contacts the touchdown bearings. In this equation, m_R stands for the rotor mass. For disk drives with a slotless stator topology, the stiffness values are generally low because of the large magnetic air gap. It is, therefore, common to optimize the highest possible value for c_z .

2.3.2.2. Tilt stiffness criterion

The criteria for the rotor stiffness values for tilting about the axis of magnetization ($c_{\mathcal{T},\alpha}$) and the axis perpendicular to it ($c_{\mathcal{T},\beta}$) are not clear at all. On the one hand, high stiffness values ensure small angular rotor deflections due to disturbance torques. On the other hand, low stiffness values lower the critical tilting frequencies at standstill

$$\Omega_{\mathcal{T},\alpha} = \sqrt{\frac{c_{\mathcal{T},\alpha}}{I_d}}, \quad \Omega_{\mathcal{T},\beta} = \sqrt{\frac{c_{\mathcal{T},\beta}}{I_d}} \quad (2.62)$$

where I_d stands for the polar moment of inertia. Other than with the axial deflection, however, the gyroscopic behavior must also be considered in case of the tilting movement of a rotating body. This means that for defining a criterion for the stiffness in the tilt directions α and β , two situations need to be regarded:

1. At rotor stand-still, high tilt stiffness leads to small deflections when a certain disturbance torque acts on the rotor.
2. During rotation, high tilt stiffness leads to high resonance frequencies (2.62) and to high precession frequencies. More details on the tilting motion and the precession resonance frequencies are given in Chapter 3. The faster precession movements are damped quicker than the slow ones due to damping by, e.g., an external fluid. If, however, a tilt stabilization coil as presented in Chapter 3 is applied, not only the first derivatives of the tilt deflections themselves, but also the rotation about the main axis of rotation stabilizes the tilting degrees of freedom. With little or no external damping, low tilt stiffness may be desirable because this damping effect is equal and the precession frequency is lower.

Since, however, the more general case is the one without a tilt stabilization coil, the stiffness shall be maximized. Only the stability of the tilt movement, i.e., the positivity of the tilt stiffness, must be seen as a hard limitation for this objective.

2.4. Design optimization

2.4.1. Validation of simulation approach through measurement

As mentioned in Section 2.3, the angle dependent vector of producible forces and torque, $\mathbf{Q}(\varphi)$, can be obtained by either simulation or measurement. From an *a priori* design perspective, simulation is clearly the favorable way. All of the conducted simulations for the topology comparison use the same stator and rotor geometries, rely on the same nonlinear stator iron characteristics and also allow the same current density in the winding. Only the available copper cross section A_{Cu} per phase varies with the chosen phase number and coil topology due to the different number of insulation walls between the coils.

During the simulations, a single phase is energized with a constant current density of 6 A/mm^2 while the permanent magnet rotor is rotated in order to obtain the respective values of achievable forces and torque dependent on φ . The resulting vectors are normalized to 1 Aturn of magneto-motive force and are then used to calculate $\mathbf{T}_m(\varphi)$ and follow the calculation of evaluation criteria outlined in Section 2.3.

In order to evaluate the 3D finite element simulation method used here, the simulation results for a 5pd and 6ps motor type are compared to measurements with the available prototypes of these topologies. Figure 2.14 shows the comparison of the overall achievable

2. System design

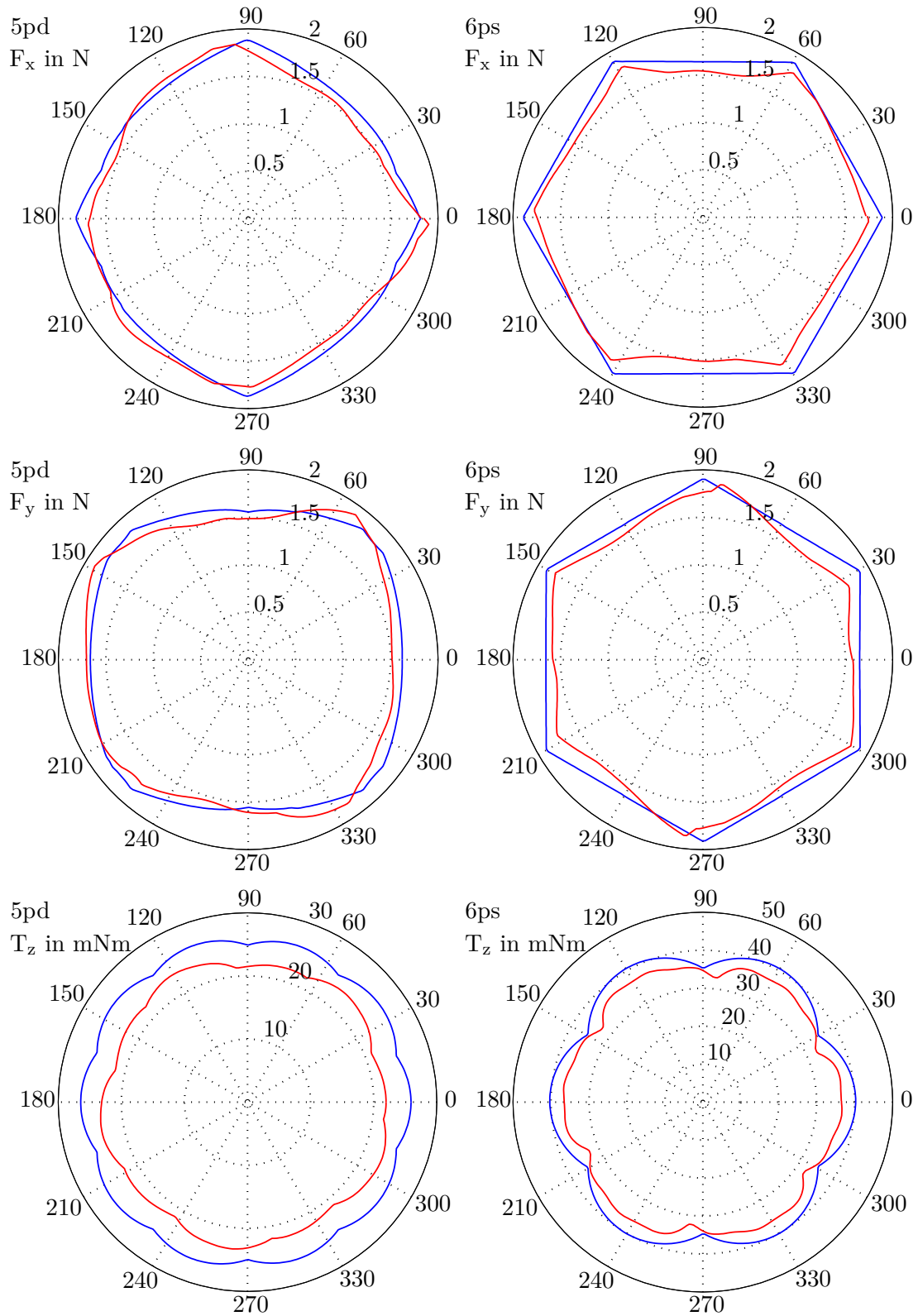


Figure 2.14.: Simulation based (blue) and measurement based (red) exclusive force and exclusive torque creation for the 5pd and 6ps topology.

F_x , F_y and T_z values when all phases can be optimally energized while respecting the limitation due to the maximum current density, the exclusiveness (no other force or torque created), and a star-connection of the phases. The quantitative mismatch between mea-

surement and simulation is within an acceptable range. Also, the notable phase shift of some points can be explained with imprecise angular placement of the coils and some error of setting the indexing head used for this measurement. This decent agreement justifies the further use of simulation results for the comparison of the investigated designs.

2.4.2. Topology selection

In the preceding sections, the topological decisions for a disk shaped, 2-pole permanent magnet inner rotor, bearingless drive with a combined toroid winding were taken. The choices of the phase number and the coil form regarding the single coil or double coil arrangement are made in this section.

2.4.2.1. Evaluated designs

The variations chosen for comparison feature a phase number of either five, six or eight phases with either single coil or double coil arrangement. These resulting six variations are hence called 5ps, 5pd, and further 6ps, 6pd, 8ps and 8pd. Figure 2.15 exemplarily show the 3D models and the winding schemes of the 5pd and 6ps topology.

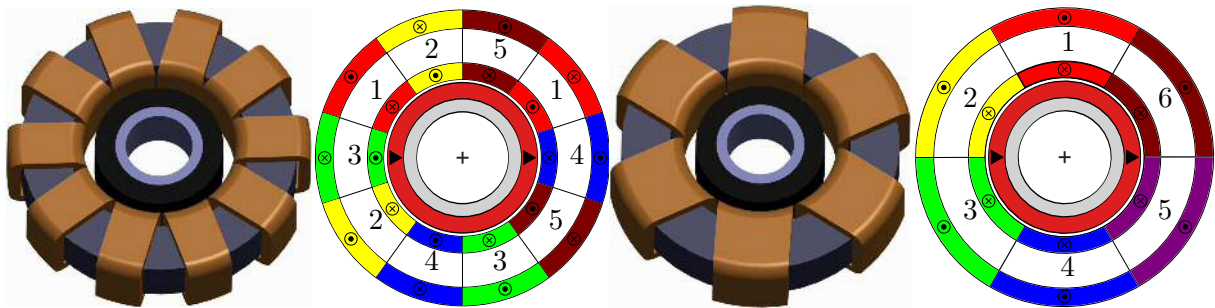


Figure 2.15.: 3D model and winding scheme of the exemplary 5-phase double coil (5pd) setup (left) and the 6-phase single coil (6ps) setup (right) with the rotor showing the diametric magnetization direction. The 6pd, and 8pd setups are structured accordingly.

2.4.2.2. Torque comparison

The maximum torque calculation which is introduced in Section 2.3.1.3 is now applied for comparing the six designs under consideration. Figure 2.16 gives the six torque curves where the single coil designs are displayed in dashed lines and the double coil designs are shown in solid lines. The single coil versions using six or eight phases are the best choices concerning torque capacity. Both have similar peak values whereas the torque ripple is more prominent in the 6-phase design. Next in line is the 5ps version and only then, the double coil variants follow. It is interesting that an increase in the number of phases is beneficial for the single coil but detrimental for the double coil designs. Both effects, the superiority of the single coil arrangements and the torque reduction with rising phase number in the double coil arrangements can be explained with a look at Figure 2.12 where the winding schemes of both 8-phase designs are given exemplarily. The 8ps design can emulate a full pitch coil, producing only torque and yielding an idealized winding factor of 1^{10} , by having, e.g., positive current in phase one and negative current in phase

¹⁰The actual winding factor is always lower when a distributed winding is applied.

2. System design

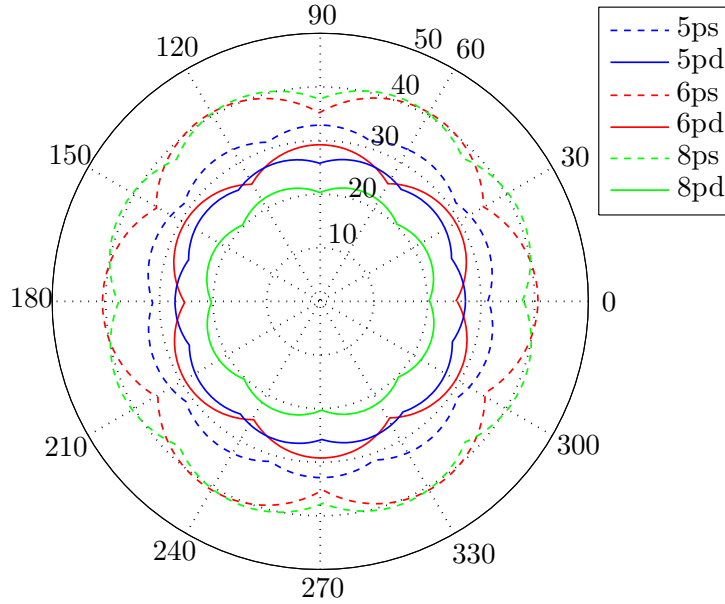


Figure 2.16.: Maximum torque in mNm over rotor angle in degree for all six topologies without creating radial forces.

five. In comparison, the two connected coils of each phase in the double coil design are short-pitched and thus have a very small winding factor for a diametrically magnetized rotor.

Table 2.2 lists the torque constant k_T , defined in (2.49), the mean torque value for a current density of 6 A/mm^2 over one rotor period, and the torque ripple peak to peak value relative to that mean torque.

2.4.2.3. Force comparison

As proposed in (2.48) and given in Table 2.2, a force constant k_F can be calculated for evaluating the different designs. Due to the mentioned potential flaw of these factors (cf. Section 2.3), Figure 2.17 considers the *minimum force* value mentioned in Section 2.3.1.4. The resulting values are plotted as one blue line per force angle φ_F . In this way, all force directions from a mechanical angle of 0° to 360° in steps of $10\text{--}15^\circ$ are evaluated. The overlay of all these blue lines allows drawing the red dashed in-circle at the minimum force which can be generated regardless of the rotor angle and the required force direction.

There are two main striking points about the comparison in Figure 2.17. The first one is that the fear of a “*dead spot*” - an angular position where significantly less radial force than in the principle x - and y -axes could be produced, was needless. Practically every blue line has the same radial minimum value as the resulting red in-circle.

The second finding is that even though the maximum force value is quite different for the six designs, the minimum producible force represented by the in-circle is very similar.

2.4.2.4. Comparison of power electronics requirements

For comparing a complete drive system, it is important to consider the power electronics requirements as well as the individual performance characteristics of the electric machine. The number of phases is a crucial parameter since, when considering a classical power

Table 2.2.: Comparison data

Topology	A_{Cu} per phase in mm^2	Torque constant k_T in mNm/Aturn	\bar{T}_z in mN m	Torque ripple pp in % of mean value	Force constant k_F in mN/Aturn	$F_{r,min}$ in N
5ps	21.67	0.339	32.32	4.9 %	18.9	1.73
5pd	21.18	0.286	26.6	4.9 %	18.2	1.63
6ps	17.98	0.399	38.8	14.0 %	21.6	1.65
6pd	17.48	0.295	27.9	14.0 %	23.4	1.74
8ps	13.36	0.550	39.7	7.8 %	31.0	1.76
8pd	12.87	0.307	21.4	7.8 %	28.9	1.57

electronics circuit with half bridges and a star-connected winding system, it directly gives the number of necessary semiconductors in the half bridges

$$n_{hb} = 2m$$

and of the required current sensors

$$n_{cs} = m - 1.$$

However, the real question for reaching a power electronics motivated design choice is rather if the circuit is a custom design for the drive or if standard off-the-shelf components are to be used. The customized solution is not unlikely since, depending on the application, it may be beneficial to have a compact circuit to go with the compact bearingless motor, integrating all system components such as the controller, the sensor signal treatment, and the power semiconductors. In this case, the cost for the additional semiconductors and current sensors in the designs with high phase number might be negligible.

In the second case when off-the-shelf products are used, the choice of an 8-phase design is very unlikely as the possible combination of two standard 3-phase inverters [39] is, of course, only applicable to designs with up to six phases.

2.4.2.5. Selected topology

Without the considerations of the above sections in mind, the choice for building a high-speed prototype was made for a 2-pole rotor with a combined winding system featuring a 5pd winding system. The 5-phase system was built in order to demonstrate the feasibility of a high-speed bearingless drive while at the same time minimizing the necessary phase number. The double coil arrangement was chosen since it constitutes the direct equivalent to the air gap or single-tooth windings which were applied in practically all preceding bearingless disk drives. When the comparison with higher phase number designs and the single-coil arrangements was made in a later stage when the 5pd prototype was already in operation, it quickly became clear that the single-coil designs offer significant advantages.

2. System design

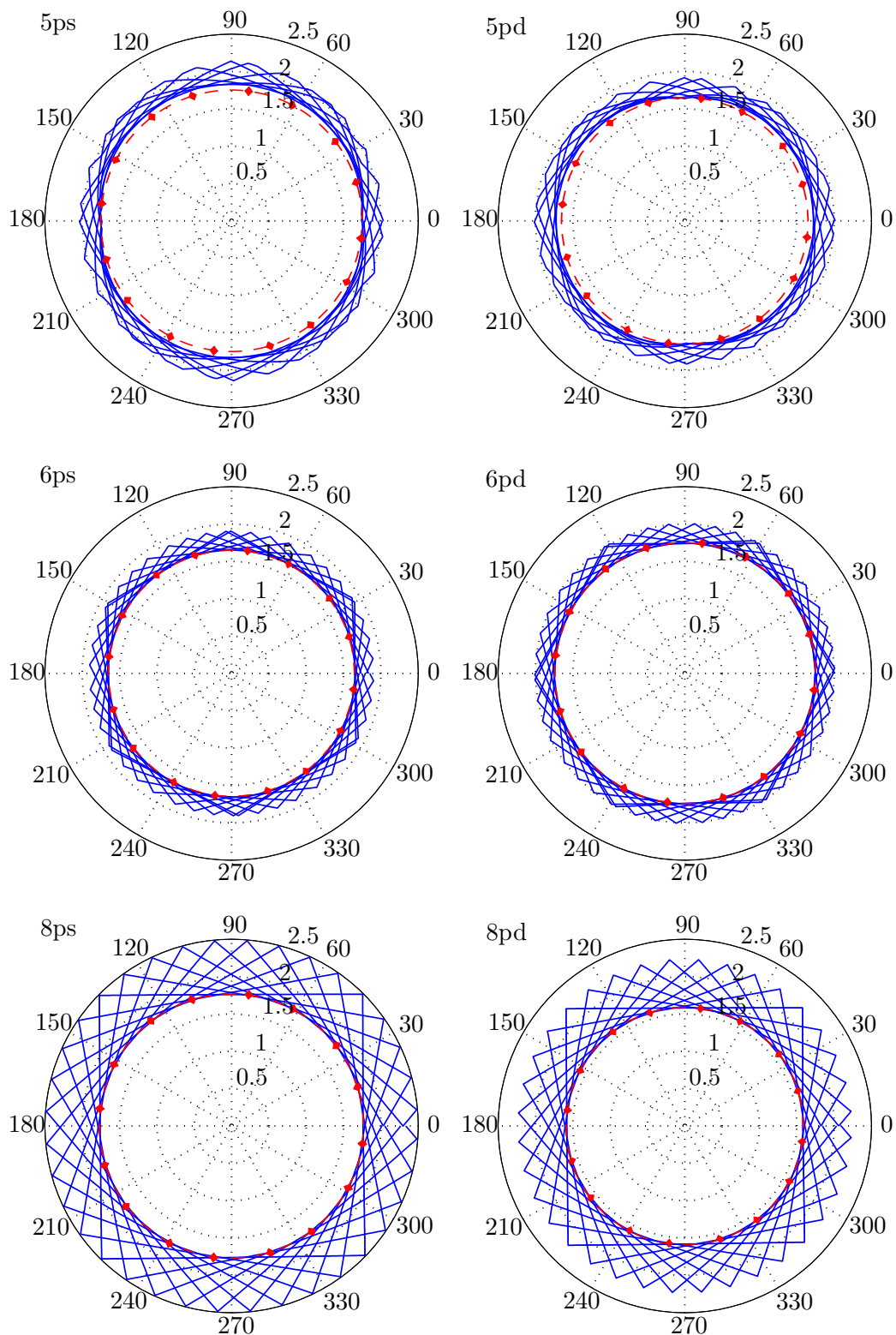


Figure 2.17.: Overlay of the polar force plots in N for evaluating of the *minimum force* value for all designs. Every blue line represents the maximum achievable force in one distinct direction, evaluated for all rotor angles φ . The resulting minimum producible force range is displayed with a red dashed line.

This was the reason for aiming at even higher speeds with a 6ps design for the second prototype. Again, the phase number played an important role as the potential use of two

off-the-shelf 3-phase inverters seemed tempting.

From a perspective at the end of the practical works connected to this project, also the 8ps system can be seriously considered. The reason lies in the thought mentioned at the end of Section 2.4.2.4. It is very likely that such an unusual machine topology also triggers the development of a suitable power electronics circuit, holding all the additional components in one electrical system, maybe even on one printed circuit board. The eight necessary phases should, therefore, not be regarded as a severe obstacle on the way to the promising properties of this topology.

2.4.3. Geometry selection

Following the course of this chapter, the rotor, stator, and winding topologies have been selected. The remaining design parameters to choose are the geometric dimensions which are not strictly defined for the current project. However, the following sections focus on their dependencies and show the setup and evaluation of a multi-objective optimization process using the optimization suite *MagOpt* in order to find suitable dimensions for a high-speed bearingless disk drive. Parts of this study have also been presented in [82].

2.4.3.1. Optimization setup

The outer diameter of the rotor magnet is fixed to 30 mm and the physical air gap width δ is set to 0.5 mm. The radial heights for the rotor bandage, the physical air gap, and the radial touchdown bearing need to be specified according to the allowed materials and application specific demands. They are, thus, not understood as variables in an optimization problem as it is assumed that they should be as small as possible.

This leaves the three geometric key dimensions

- radial coil height h_{coil} ,
- radial back iron yoke width h_Y
- axial length¹¹ l_S , and
- radial stator yoke width h_S

to be decided according to the demanded specifications. These specifications, however, are not uniformly defined for bearingless drives and need some closer consideration:

1. The clearest objective for successful operation of a magnetically levitated drive is the levitation capacity, expressed in (2.56). Substituting the stiffness definition according to (2.19) into (2.56) yields

$$F_r(\varphi, \varphi_F) > \bar{c}_r (1 + \hat{c}_r \cdot \cos(\varphi_\Delta - \varphi)) \delta \quad (2.63)$$

where the angle difference between the deflection angle and the rotor angle is the one relevant for calculating the respective radial stiffness and, thus, the radial reluctance

¹¹The axial length of the stator and rotor are set to be equal. Several publications have dealt with different lengths for rotor and stator, e.g., a patent [87] secures the right to a magnetic rotor length exceeding the magnetic stator length.

2. System design

force to overcome. Fulfilling (2.63) with F_r being maximized for the rated current and respecting the zero torque condition according to

$$F_{r,max}(\varphi, \varphi_F) = \max(F_r(\varphi, \varphi_F) |_{J_{1..m} \leq J_{max}, T_z=0}) \quad (2.64)$$

guarantees that the rotor can be lifted out of any resting position under any rotor angle. For a practical and meaningful value, the radial reluctance force can be set into relation to the maximum producible force for every angle combination. The worst case is then expressed as the startup-current coefficient

$$k_{startup} = \max\left(\frac{\bar{c}_r (1 + \hat{c}_r \cdot \cos(\varphi_\Delta - \varphi)) \delta}{F_{r,max}(\varphi, \varphi_\Delta + \pi)}, \forall \varphi, \varphi_\Delta \in [0, 2\pi]\right) \quad (2.65)$$

which, multiplied with the rated current density J_{max} , must not exceed $J_{startup}$. For the short rotor start-up process, a 100% current overload of $J_{startup} = 12 \text{ A/mm}^2$ shall be tolerable.

2. The mean achievable torque capacity \bar{T}_z defined in 2.3.1.3 shall be as high as possible, with an arbitrarily set minimum value of 42.9 mN m which amounts to a drive power of 150 W at a nominal speed of 100 krpm. For the evaluation of the present geometries, a nominal current density of $J_{max} = 6 \text{ A/mm}^2$ was set for each of the m phases due to thermal limits. For constant phase number and geometric topology in the sense that the decisions taken in the beginning of Section 2.4.2 are not overthrown, the result of the optimization problem in (2.51) can be expressed as

$$\bar{T}_z = \xi_{\bar{T}_z} \cdot \max(T_z(\varphi) |_{i_1=i_{max}, i_{2..m}=0}) \quad \forall \varphi \in [0, 2\pi] \quad (2.66)$$

with the constant factor $\xi_{\bar{T}_z}$. This simplifies the optimization procedure since the necessary torque distribution can be obtained directly from simulation or measurement when only one phase is energized and the linear optimization problem needs to be solved only once for each topology in order to obtain $\xi_{\bar{T}_z}$. With Figure 2.16 in mind, it is also possible to simulate only at distinct values of φ in order to obtain the maximum of T_z .

3. While the two aforementioned active drive characteristics have optima for the magnetic air gap width which, if increased, results in high available copper volume but reduced air gap flux density, the following passive stiffness demands push the optimization towards small air gaps and, thus, high air gap flux density values. In order to limit the gravitational rotor deflection to below half of the radial air gap and, therefore, to 0.25 mm, the rotor with a weight of approximately 50 g must experience a passive stiffness of at least $c_z = 1.96 \text{ N/mm}$.
4. In addition to this static deflection limit, the passive stiffness values are also constrained with an upper limit which confines the resonance frequencies Ω_z , $\Omega_{\mathcal{T},\alpha}$, and $\Omega_{\mathcal{T},\beta}$ to below 166 Hz which means that acceleration from 0 to 6000 rpm fast enough in order to prevent any of the resonances from provoking large deflections allows passing all rigid body modes. Depending on the actual rotor mass and the moment of inertia, these upper stiffness limits will vary but for an exemplary rotor with $m_R = 50 \text{ g}$ and $I_d = 4 \times 10^{-6} \text{ kg m}^2$, the maximum tolerable value for the axial stiffness is $c_{z,max} = 19.7 \text{ N/mm}$ which is safely out of reach. For the tilt stiff-

ness, a maximum of $c_{\mathcal{T},max} = 1.8 \text{ Nm/rad}$ can be given while an arbitrary minimum of $c_{\mathcal{T},min} = 0.8 \text{ Nm/rad}$ is also included.

2.4.3.2. Optimization procedure

To meet the specified optimization targets, a 3D-FE simulation is necessary. The optimization tool *MagOpt*, developed at the *Linz Center of Mechatronics* was used to set up the optimization process and to perform the post-processing. This tool simplifies the problem that for each parameter variation, multiple simulations are necessary. These include one for each passive stiffness as well as additional active current simulations at different rotor angles for calculating $k_{startup}$ and \bar{T}_z as described above. Figure 2.18 shows the optimization problem in *MagOpt* in a tree-structure which is then fed into a genetic optimization algorithm to create the individual parameter sets. These sets are sent to the FE solver, in this case *Ansys® Maxwell*, and the results are obtained from the simulation output. After processing the results in the genetic optimizer, the next data sets are created and sent to the solver.

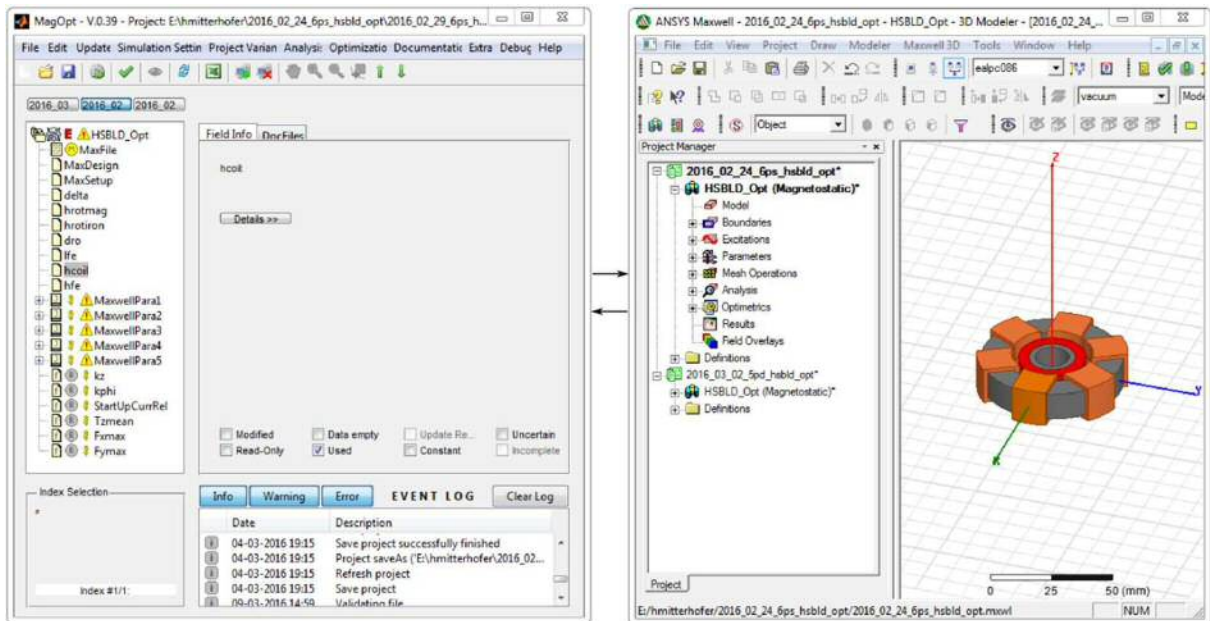


Figure 2.18.: Tool chain controlled by the optimizer *MagOpt* (left), sending each parameter set to the 3D-FE solver *Maxwell* (right), obtaining force and torque values for optimization target calculation and post processing of the data.

The actual optimization data gained from the decisions and findings in the above sections is displayed in Table 2.3. Three topologies, the 5pd, 6ps, and 8ps arrangements are optimized. In order to visualize the results properly, the Pareto¹² fronts are displayed in Figure 2.19. This Pareto front is made from all individuals which are optimal. This means that there is no other individual which does at least as good in every target criterion and better in at least one target criterion.

¹²VILFREDO PARETO, * 1848 in Paris, France, † 1923 in Celigny, Switzerland

2. System design

<i>Parameter</i>	<i>Type</i>	Value
Machine topology	fixed	Inner rotor PMSM
Winding topology	fixed	Combined winding
Magnetization	fixed	Diametral
Coil form	variable	5pd, 6ps, 8ps
Maximum current density	fixed	6 A/mm ²
Start up current density	fixed	12 A/mm ²
$d_{o,R}$	fixed	30 mm
h_M	fixed	4.5 mm
δ_m	fixed	1.5 mm
h_S	variable	9 - 13 mm
h_{coil}	variable	2 - 3.5 mm
h_Y	variable	2.5 - 3 mm
l_S	variable	10 - 14 mm
c_z	target	>2 N/mm
$c_{\mathcal{T}}$	target	0.8 - 1.8 N ^m /rad
$k_{startup}$	target	<2
\bar{T}_z	target	>45 mN m

Table 2.3.: Optimization parameters

2.4.3.3. Analysis of the optimization result

The automated optimization process is stopped when the resulting Pareto front shown in Figure 2.19 converges and no longer produces new individuals in the graph. The top left and the bottom right graphs which display the two passive stiffnesses and the two active torque or force targets, respectively, are not useful for finding the optimal individuals. In these two images, both displayed targets benefit from and are weakened by the same geometrical changes.

The remaining four graphs compare targets which show opposed reactions to a geometry variation. It is these graphs that the optimum needs to be selected from. It quickly becomes clear that the 5-phase, 6-phase, and 8-phase designs do not differ in the passive stiffness targets as these results do not depend on the winding characteristics. The most prominent difference appears in the torque capacity where the 6ps and 8ps designs dominate. This is the only feature where the topology choice is significantly more important than the geometric choice. After filtering the solution swarm according to the limit values given in Table 2.3, the parameter sets marked with red circles in Figure 2.19 remain. For each phase number, one individual is selected and displayed in Table 2.4.

While all three individuals fulfill the requested specification, the 6ps and 8ps designs

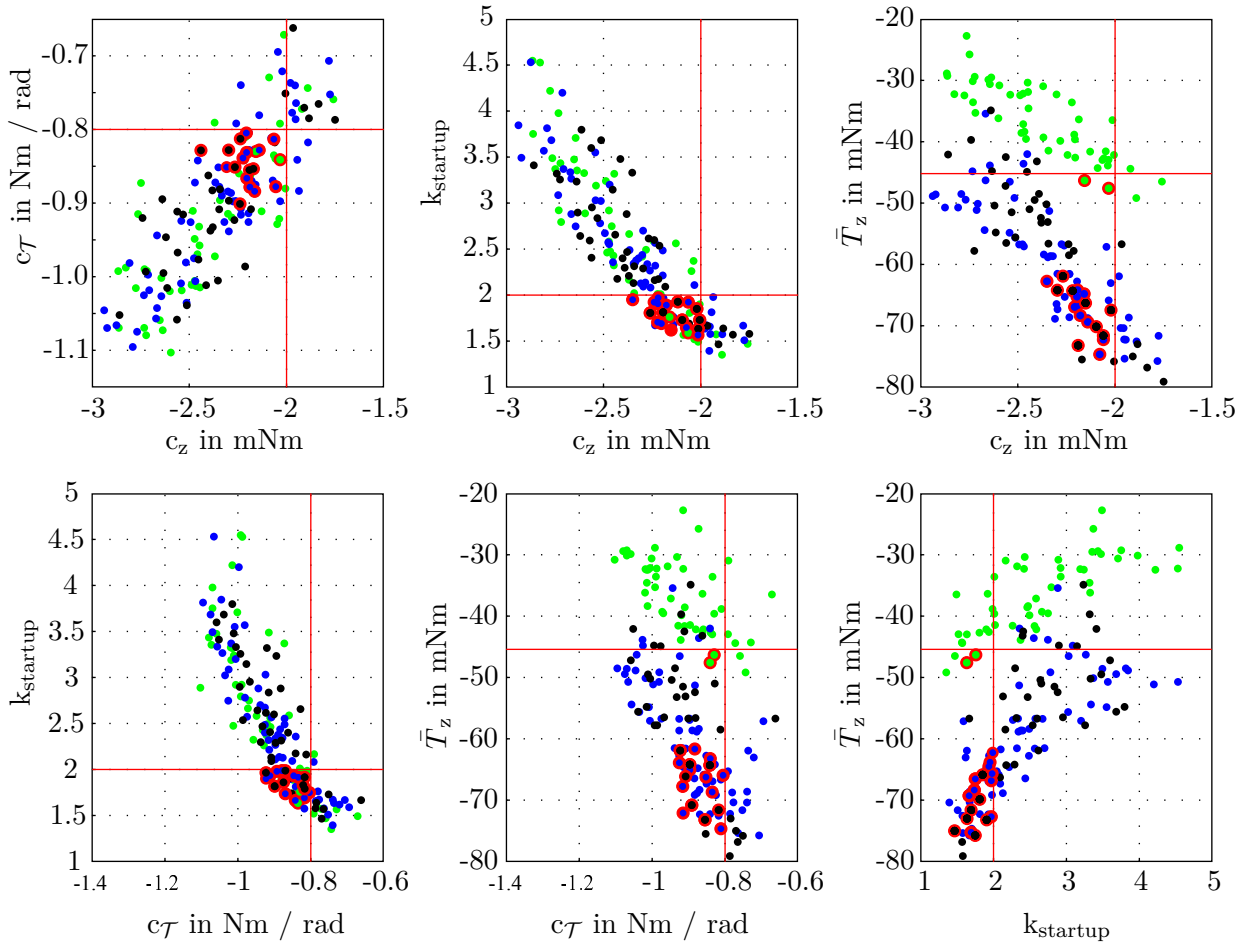


Figure 2.19.: Optimization output in form of Pareto fronts linking every target with every other one. 5pd variants are shown in green, 6ps in blue, 8ps in black. The individuals marked with a red circle fulfill all demanded limits which are depicted with red lines.

are clearly favorable because of their increased torque capacity. It has to be noted that these designs are the outcome of the first optimization process since the coupling of a 3D-FE solver with MagOpt was achieved only shortly before this work. The individuals show clearly that for reaching the proposed targets, the air gap can be much higher than it was chosen to be for the constructed prototype drives. In those past designs, the passive stiffness values were overrated which is why the magnetic air gap in the prototypes was kept to a smaller value, entailing higher torque but also difficulties of overcurrent at the startup moment.

2.5. Conclusion

The design of bearingless drives is a complex undertaking which is expressed by the plurality of topological decisions and the numerous geometric parameters influencing the drive performance. When reflecting upon the described design process, several interesting conclusions can be reached.

- Characteristic requirements such as very high speed, high torque demands, high compactness, or high drive efficiency need to be respected in every design step and

2. System design

<i>Parameter</i>	5pd	6ps	8ps
h_S	9.6 mm	9.8 mm	10.5 mm
h_{coil}	3.3 mm	3.21 mm	3.27 mm
h_Y	2.91 mm	2.94 mm	2.96 mm
l_S	13.4 mm	12.7 mm	13.95 mm
<i>Target</i>	5pd	6ps	8ps
c_z	2.03 N/mm	2.14 N/mm	2.17 N/mm
$c_{\mathcal{T},max}$	0.84 N m/rad	0.82 N m/rad	0.85 N m/rad
$k_{startup}$	1.63	1.68	1.73
\bar{T}_z	47.6 mN m	69.2 mN m	76.4 mN m

Table 2.4.: Exemplary selection of three individuals

cannot be left to an optimization process alone. This is especially true for the proper selection of the winding topology and the phase number which heavily influence the necessary power electronics circuit.

- However, even if certain topological decisions are made in advance, a multi-criteria optimization is necessary due to the large number of influential geometric dimensions and their cross coupled relationships.
- The definition of optimization targets is significantly more complex than with a conventional electric machine and their number is higher since active and passive magnetic forces need to be considered. Even if the optimizing tool used in this work does not restrict the number of variable parameters or targets, a large number of either one of them will make the optimization process extremely lengthy and the results become hard to interpret. Therefore, it is important to specify which targets must absolutely be met for the drive to function properly (e.g., the startup criterion) and which ones are nice-to-have (in this example, e.g. the tilt stiffness).
- Even though the optimization domain can be enlarged to also include, e.g., a thermal simulation or a function for the production cost of machine and power electronics, the geometric optimization alone shows that significant gains in drive performance would be lost by, instead, intuitively choosing geometric dimensions as whole numbers out of convenience.

3. Tilt stabilization

Contents

3.1. Passive tilt damping	48
3.1.1. Problem description	48
3.1.2. Additional damping	51
3.1.3. Tilt stabilization coil (TSC)	52
3.1.4. Stabilization model	54
3.1.5. Numerical simulation and model comparison	64
3.1.6. Measurement	66
3.2. Active influence	70
3.2.1. Active tilting - 1 coil	70
3.2.2. Active axial force - 2 coils	70
3.2.3. Active tilting - 4 coils	71
3.2.4. Simulation results	73
3.3. Conclusion	73

One of the central ideas of the bearingless disk drive topology, which is also the reason for its mechanical compactness, is the distribution of passively and actively stabilized degrees of freedom. The axial and the tilt deflections are stabilized passively via the reluctance forces of the rotor. Figure 1.4 illustrates that only the two radial degrees of freedom need to be stabilized actively - a fact that allows concentrating this bearing function into the combined winding system presented in Chapter 2, Section 2.2.1. One of the key flaws of this concept, however, also flows from this distribution since the passive magnetic bearings provide little to no damping and cannot be controlled in any way. What sounds annoying when looking at the axial degree of freedom may virtually become a knock-out criterion for many applications when the tilt deflections are considered as they can easily excite gyroscopic movements of the rotor. This is especially true for applications with high rotational speeds, non-static motor suspensions introducing disturbance forces and torques in all degrees of freedom, or a combination of both. Typical examples are, e.g., magnetically levitated turbo chargers, pumps or compressors for vehicles.

To the knowledge of the author, there is no existing solution to this tilting problem in the literature except for adding external damping via fluids surrounding the rotor. This kind of external damping, however, would seriously hamper many possible applications where the rotor is supposed to work in a low-viscous medium.

This chapter presents a novel, structurally simple approach for stabilizing the tilt degree of freedom and proposes additional operation modes for additional active influence on the rotor movement. Parts of this chapter have been presented in a conference publication [77].

3.1. Passive tilt damping

3.1.1. Problem description

Moving the axis of rotation of a spinning body is problematic, especially if this movement does not lead to a parallel axis deflection. A common example for such a non-parallel movement is the tipping of a spinning top, shown in Figure 3.1. The top has an angular momentum vector \mathbf{L} pointing in the direction of the axis of rotation with a magnitude of

$$|\mathbf{L}| = I_p \Omega \quad (3.1)$$

and I_p standing for the polar moment of inertia. The gravitational force vector \mathbf{F}_g acts on its center of mass. If the top is tipped over - here in a negative sense about the y-axis - the gravitational force vector does not go through the point of contact with the ground (root point) and, thus, creates an external torque \mathbf{T}_{ex} . For a constant spinning speed, this external torque vector is equal to the change of the angular momentum since

$$\sum \mathbf{T}_{ex} = \frac{d\mathbf{L}}{dt} = \mathbf{I} \frac{d\boldsymbol{\Omega}}{dt} \quad (3.2)$$

with \mathbf{I} and $\boldsymbol{\Omega}$ standing for the momentum of inertia matrix and the angular velocity vector, respectively. This means that the entire top tilts in a counterclockwise direction, thus also rotating the external torque vector \mathbf{T}_{ex} and, consequently, the vector $\frac{d\mathbf{L}}{dt}$. With the top in Figure 3.1 spinning in a counterclockwise direction, the described tilting results in an equally counterclockwise, and thus, *forward* whirl movement.

The same principle can be applied to the magnetically levitated disk rotor with passive tilt stabilization, depicted in Figure 3.2. The main difference, however, is that for a negative tilt around a certain horizontal axis, the *external* reaction torque \mathbf{T}_{ex} is the reluctance torque $\mathbf{T}_{\mathcal{T}}$ described in Section 2.1.2 acting in the positive direction of that very axis. Consequently, the vector $\frac{d\mathbf{L}}{dt}$ also points in that negative direction which means that, other than in the case of a top under the influence of an external torque due to gravity, the whirl occurs in *backward* direction. This description shows that the spinning, magnetically levitated disk is subjected to gyroscopic effects when an external torque is applied. However, the actual description of a tilting, spinning object needs to take the time dependencies of the problem parameters into account by setting up a differential equation.

This more precise model of the tilting, spinning disk at constant circumstances is well known in the literature as the JEFFCOTT¹ or LAVAL² rotor with a massless, flexible axis and a centrally placed massive disk. Other than with the spinning top, the tilted disk depicted in Figure 3.3 experiences the same restoring torque due to the spring constant of the axis as the magnetically levitated disk due to the reluctance torque. Equal to the JEFFCOTT rotor, the tilt equation of motion for $\alpha(t)$ and $\beta(t)$ which indicate the tilting angles of the rotor about two stator-fixed axes x and y , respectively, can be written as

$$\begin{aligned} I_d \ddot{\alpha}(t) + I_p \dot{\beta}(t) \Omega + c_{\mathcal{T}} \alpha(t) &= 0 \\ I_d \ddot{\beta}(t) - I_p \dot{\alpha}(t) \Omega + c_{\mathcal{T}} \beta(t) &= 0 \end{aligned} \quad (3.3)$$

¹HENRY HOMAN JEFFCOTT, * 1877 in Co. Donegal, Ireland, † 1937 in Walton on Thames, England

²GUSTAF DE LAVAL, * 1845 in Orsa, Sweden, † 1913 in Stockholm, Sweden

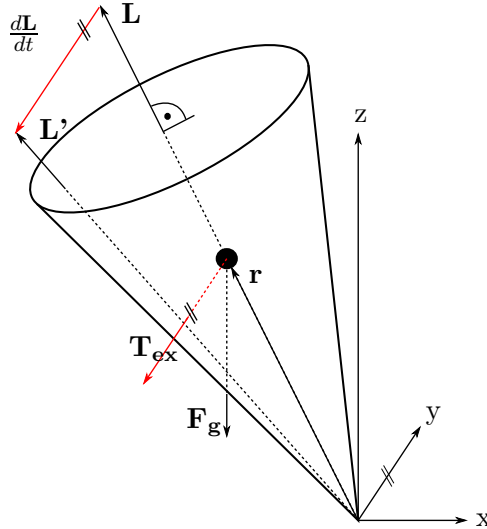


Figure 3.1.: Gyroscopic situation of a spinning top due to an external torque \mathbf{T}_{ex} due to the gravitational force \mathbf{F}_g . The external torque provokes a whirl movement in the sense of rotation (forward whirl).

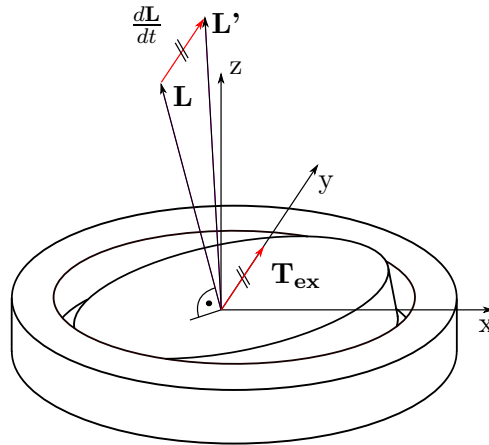


Figure 3.2.: Gyroscopic situation of a spinning magnet rotor disk due to an external torque $\mathbf{T}_{ex} = \mathbf{T}_{\mathcal{T}}$ due to passive stabilization. The stabilization torque provokes a whirl movement opposite to the sense of rotation (backward whirl).

with I_d giving the diametral moment of inertia and $c_{\mathcal{T}}$ denoting the tilt stiffness coefficient which is the analogon to the spring constant of the JEFFCOTT rotor's axis. The roots of this differential equation system are

$$\Omega_{c,\mathcal{T},f} = \frac{I_p\Omega + \sqrt{(I_p\Omega)^2 + 4c_{\mathcal{T}}I_d}}{2I_d} \quad (3.4)$$

$$\Omega_{c,\mathcal{T},b} = \frac{I_p\Omega - \sqrt{(I_p\Omega)^2 + 4c_{\mathcal{T}}I_d}}{2I_d} \quad (3.5)$$

where the indices f and b denote the forward and backward tilt whirling mode, respectively. These modes are frequently also referred to as *nutation* and *precession*, respectively. The two frequency dependent resonance frequencies are plotted in Figure 3.4 in solid lines. Equation (3.5) yields negative values which need to be interpreted as backward whirling

3. Tilt stabilization

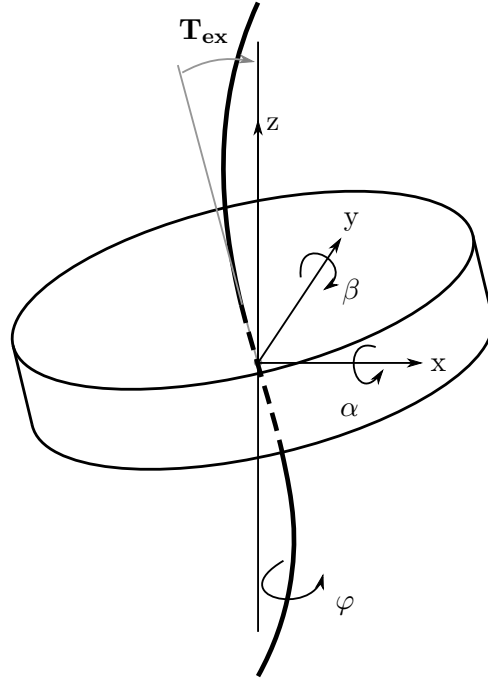


Figure 3.3.: Equivalent gyroscopic situation in the JEFFCOTT rotor with massless axis

motion. In order to clearly display the relation to the unbalance excitation which is synchronous with the rotational frequency, the backward whirl curve is plotted with inversed sign.

The given resonance frequencies, however, are based on the assumption that the tilt stiffness defined in Chapter 2, $c_{\mathcal{T}} = \bar{c}_{\mathcal{T}}$ correctly describes the tilt stiffness of the rotor. While uniform for the JEFFCOTT rotor, a two-pole magnetic rotor needs a more detailed description with $c_{\mathcal{T},\alpha}$ and $c_{\mathcal{T},\beta}$ for the individual tilt axes as described in Section 2.1.2. This stiffness anisotropy leads to a significantly more complex description of the resonance frequencies. Without further discussion, their definition

$$\Omega_{c,\tilde{\mathcal{T}},f} = \Omega + \sqrt{\Omega_{c,\mathcal{T}}^2 + \Omega^2 \left(1 + \frac{1}{2}\xi^2 - \xi\right) - \sqrt{\Omega^4 \xi^2 \left(1 - \frac{1}{2}\xi\right)^2 + \Omega_{c,\mathcal{T}}^2 \Omega^2 (2 - \xi)^2 + \Omega_{c,\mathcal{T}}^4 \hat{c}_{\mathcal{T}}^2}} \quad (3.6)$$

$$\Omega_{c,\tilde{\mathcal{T}},b} = \Omega - \sqrt{\Omega_{c,\mathcal{T}}^2 + \Omega^2 \left(1 + \frac{1}{2}\xi^2 - \xi\right) + \sqrt{\Omega^4 \xi^2 \left(1 - \frac{1}{2}\xi\right)^2 + \Omega_{c,\mathcal{T}}^2 \Omega^2 (2 - \xi)^2 + \Omega_{c,\mathcal{T}}^4 \hat{c}_{\mathcal{T}}^2}} \quad (3.7)$$

shall be adopted from [36] with

$$\Omega_{c,\mathcal{T}(\Omega=0)} = \sqrt{\frac{\bar{c}_{\mathcal{T}}}{I_d}} \quad (3.8)$$

which gives the critical tilt frequency at standstill for the mean stiffness value and with

$$\xi = \frac{I_p}{I_d} \quad (3.9)$$

giving the moment of inertia ratio. In the same work, a detailed analysis of the rotor-dynamic behavior of a magnetically levitated disk can be found. Figure 3.4 shows two

additional resonance frequency traces in dashed lines of which again one exhibits a forward whirl and one a backward whirl. The depicted curves assume $1 < \xi < 2$ and $\hat{c}_{\mathcal{T}} = 0.5$. At the limit of $\xi = 1$ which marks an elongated rotor, $\Omega_{c,\tilde{\mathcal{T}},f}$ asymptotically approaches the rotational frequency trace, leading to a critical frequency. It can be seen that the influence of the anisotropic magnetization is strong at standstill where it splits the resonance frequencies into $\Omega_{c,\mathcal{T}}\sqrt{1 \mp \hat{c}_{\mathcal{T}}}$ but at speeds of $\Omega = \Omega_{c,\mathcal{T}}$ or above, the result is nearly identical to the standard JEFFCOTT model using the mean tilt stiffness value $\bar{c}_{\mathcal{T}}$. In the further course of this work, the anisotropy is, therefore, not taken into account.

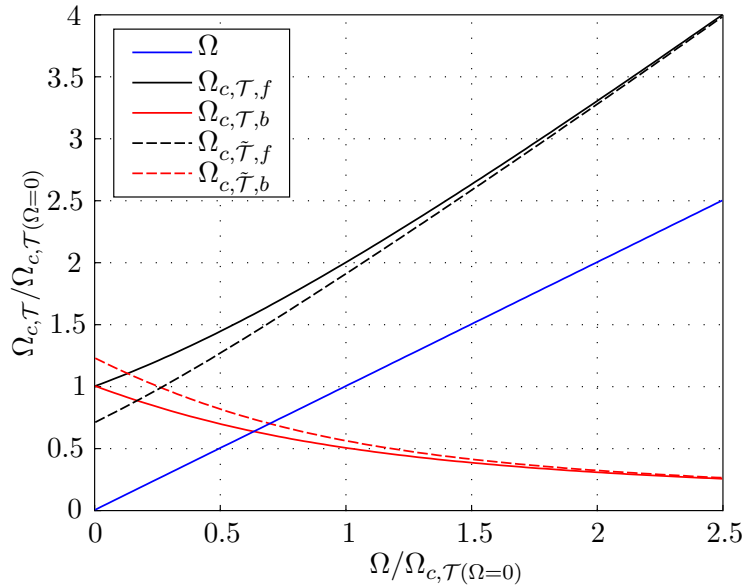


Figure 3.4.: Normalized resonances for the tilting axes for the standard JEFFCOTT rotor (solid lines) and the anisotropic stiffness model (dashed lines) [36]. The backward whirl curves have been inversed in sign.

Regardless of the stiffness values, Figure 3.4 clearly shows that the backward whirl motion is sensitive to very low excitation frequencies as the rotational speed increases. Unfortunately, the passive tilt stabilization of a bearingless disk drive usually provides very little inherent damping, which means that this backward whirl movement can easily become large if excited. The precessing rotor can either contact a housing part or lead to chaotic movement which causes the rotor to fall into the touchdown bearings, potentially damaging the drive.

3.1.2. Additional damping

Only a few methods can be considered for adding damping to a magnetically passively stabilized degree of freedom.

One of them is to provide an appropriate support of the stator, e.g., in form of visco-elastic damping elements. The authors of [66], for instance, have demonstrated the effectiveness of this method for suppressing radial vibrations of a magnetically levitated shaft. This work, however, focused on rotor translations with notable amplitudes and frequencies, while the tilt precession movement in the present disk drive exerts torques which may be very small in amplitude and frequency but yet cause severe problems. Additionally, a visco-elastic stator support is very demanding for the damping materials concerning

3. Tilt stabilization

life time, temperature, aging, precision, and stiffness and may not be suitable in many applications.

A second source of damping can be a medium, surrounding the rotor, which has a significantly higher viscosity than air. This is relevant for most magnetically levitated pump applications as, e.g., in the disk drives used as blood pumps [86], [95] or for blenders and mixers for the pharmaceutical industry [124, 96] which operate in liquids. However, this sort of damping can usually not be added arbitrarily to a drive - dependent on the application it is either present or it is not.

Apart from the mentioned methods, an electrodynamic damper can be applied. The principle of electrodynamic force generation is based on Lenz' law. Changing magnetic flux in an electric conductor loop will induce a voltage which, in turn, will offset currents in this conductor. These currents will produce a magnetic field which opposes the inducing field change, in other words, they tend to maintain that field constant. The principle of electrodynamic dampers appeared in the 1970's, usually connected to the support of railway vehicles [3]³ and surfaced again after the turn of the millennium, this time focused on the stabilization of rotors [25, 27, 59]. Two very extensive works [63, 54] describe many different forms and design criteria for such electrodynamic bearing and damping elements. However, they mostly focus on bearings or dampers with homopolar permanent magnetic fields and rotor-bound electric conductors where stabilization currents are induced. This creates the problem that the *non-rotating* damping necessary for the stability of the electrodynamic levitation must be added externally. Additional works of DAVEY and FILATOV [26, 25, 34] propose so-called *null flux bearings* which employ rotor coils within a magnetic field that only experience a net linked flux if the rotor is spinning while being displaced radially or axially from its central position. An equal effect can be achieved by using the symmetry of a heteropolar rotating field to cancel the induction effects in opposingly placed coils as long as the rotor is not deflected.

The principle of these *null flux bearings* which are able to provide stiffness and damping when arranged correctly will be applied to the tilt degrees of freedom in the following sections. Unlike in the works cited above, the effect presented in this chapter does not require additional magnetic means but instead utilizes the permanent magnetic rotor field of the bearingless drive. In contrast to most principles shown in the literature, the null flux coil is, therefore, not placed on the rotor but on the stator. Additionally, the physical union with an electric drive also means that the null flux coil is embedded in a magnetically conductive part. Due to these differences, the theoretical findings of the cited works cannot simply be assumed to be equally true for the present case but will rather be used as a guidance for the following modelling process.

3.1.3. Tilt stabilization coil (TSC)

The proposed stabilization uses the rotating diametric permanent magnet field of the present bearingless disk rotor and just requires an additional short-circuited *null flux* winding in the stator, placed as shown in Figure 3.5. In the centered and non-tilted rotor position, the newly introduced tilt stabilization coil (TSC) does not experience an induced voltage. About half of the permanent magnet flux is conducted in the upper half of the

³In December 2007, the Japanese Railway Company announced the planned construction of a 286 km long track, linking the cities of Tokyo and Nagoya, for magnetically levitated trains using an electrodynamic suspension principle. Starting from the year 2026, the track is supposed to allow travel at a speed of above 500^{km}/h and is the first part of a longer railway link from Tokyo to Osaka.

stator iron, the other half is conducted in the lower half.

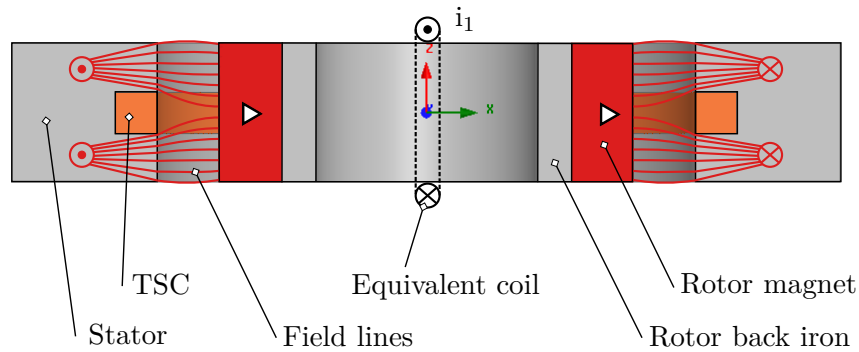


Figure 3.5.: Flux lines in motor cross section with TSC when rotor is in aligned position

If the diametrically magnetized rotor is tilted, the flux at the magnet poles is not equally distributed vertically over the inner stator surface but is more concentrated in the upper or lower half, respectively. This is schematically demonstrated in Figure 3.6. The largest share of the magnetic flux still leaves the stator core in the same half that it has entered (red flux lines). However, we also see a part of the flux (green flux lines) crossing from one axial half to the other - leaving the magnet, crossing the air gap, entering the stator (here: in the lower half of the stator), flowing through the stator to the opposite side, leaving the stator (here: from the upper stator half), again crossing the air gap and entering back into the magnet. This means that there is a net flux closing through the TSC. This is illustrated in an equivalent flux path in the lower part of Figure 3.6.

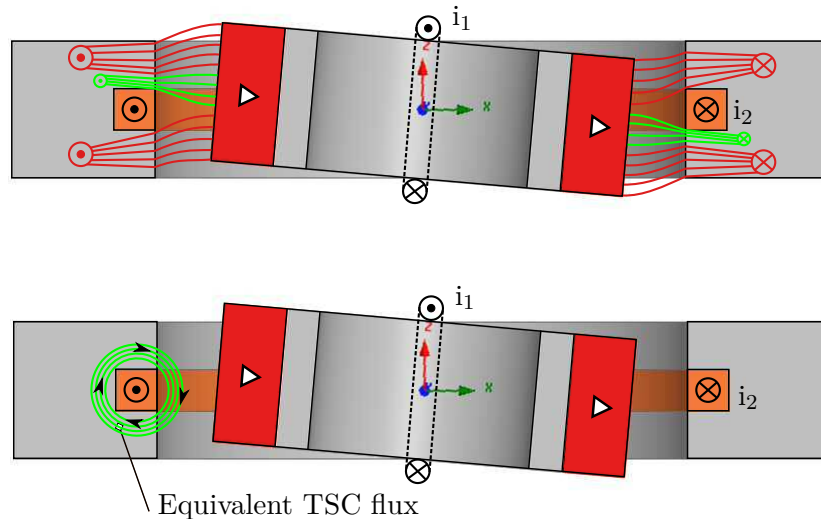


Figure 3.6.: Motor cross section with tilted rotor causing unequally distributed flux lines (top) and an equivalent flux consideration (bottom)

The described flux path changes when the non-rotating rotor tilts back and forth about one axis but the frequency of this movement is relatively low. A low frequency of the flux linked to the coil would also result in low induced voltage and thus, low values of the short-circuit current i_2 . However, the presented arrangement is also sensitive to the high-frequency rotation when it is linked to the tilting. As the rotor rotates with a quasi-static tilt inclination of the axis of rotation, the pole orientation changes and so does the direction of the flux through the TSC. The quasi-static consideration seems legitimate

3. Tilt stabilization

when the rotational frequency is far above the tilting frequency. The mentioned flux change, of course, induces a voltage which now depends on both, the rotational speed and the tilt angle. Since the coil is short-circuited, that voltage will drive the current i_2 through the coil. Due to the high frequency of rotation compared to the frequency of pure tilting movement, the induced voltage and the current i_2 are significantly larger in this case. The resulting effect on the precession movement was confirmed by introducing a TSC, similar to the one shown here, into an existing disk drive.

The described effect is based on two assumptions:

- The rotor does not spin about its main rotational axis with the same speed and in the same direction as the precession movement. For this special case, the vertical positions of the poles would not change and no voltage would be induced.
- Depending on the magnetic field frequency and the TSC placement, eddy current effects in the TSC conductors have to be minimized by using thinly stranded wire. Otherwise the TSC would resemble an eddy current brake which operates independently of the rotor eccentricity or its tilt angle.

3.1.4. Stabilization model

The effects that can be observed when the spinning rotor tilts inside the stator which holds the TSC are complex. In order to analyze them, the induction of currents in the short-circuited TSC and their effect on the tilting angles need to be modeled. For this analytical model, the following assumptions shall be used:

- The rotor will be regarded as a solid permanent magnet disk, the actual ring-shape and the inner back iron ring will be neglected.
- The permanent magnet will be replaced by an equivalent coil shown in Figure 3.5, conducting the magnetization current i_1 , producing a purely sinusoidal air gap field.
- At a rotational angle of $\varphi = 0^\circ$, the tilt axis for α coincides with the rotor's axis of magnetization.
- The variables $\alpha(t)$, $\beta(t)$, $\varphi(t)$, and $i_2(t)$ are time-dependent. For the sake of readability, they will be written as α , β , φ , and i_2 .
- The rotational speed Ω is constant, no acceleration or deceleration shall be taken into account. Therefore, the rotational angle can always be expressed as $\varphi = \Omega t$.

3.1.4.1. Derivation of the tilt torque

For finding a valid equation of motion, we assume an initial situation of a radially centered rotor which is tilted about the stator-fixed x- and y-axis (cf. Figure 3.7). The system shall be analyzed for its magnetic co-energy in order to obtain the electromagnetic contribution to the equation of motion. Generally, the magnetic co-energy $W_{m,co}$ of a conservative, electromagnetic system with one coil is

$$W_{m,co} = \int \Psi di \quad (3.10)$$

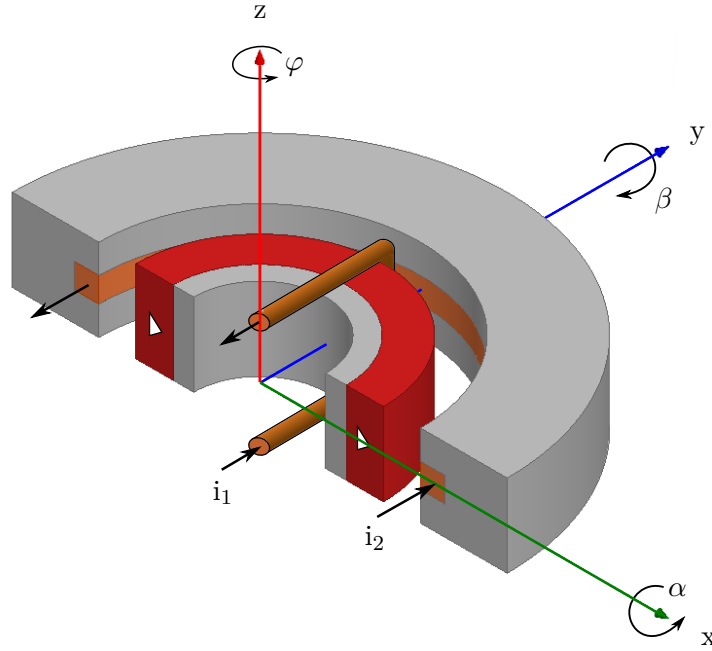


Figure 3.7.: Stator coordinate system, relevant angles and current variables for the stabilization model. The magnetization of the replaced permanent magnet (indicated by the white flashes) is provided by the equivalent current i_1 . It needs to be kept in mind that the equivalent coil which conducts i_1 is merely a virtual coil, whereas the TSC which conducts i_2 is embedded in the actual stator in the prototype.

where Ψ is the linked coil flux due to the current i . For the general case of n phases, the equation can quite simply be extended to

$$W_{m,co} = \sum_{j=1}^n \int \Psi_j di_j \quad (3.11)$$

but an important remark needs to be made here. Since we need to integrate over the current but due to the fact that not only one but n currents are involved, the currents of those coils that have not yet been considered in the sum, need to be set to zero. When putting the coil flux for n coils into matrix form

$$\begin{bmatrix} \Psi_1 \\ \Psi_2 \\ \vdots \\ \Psi_n \end{bmatrix} = \begin{bmatrix} L_{11} & L_{12} & \cdots & L_{1n} \\ L_{21} & L_{22} & \cdots & L_{2n} \\ \vdots & \vdots & \cdots & \vdots \\ L_{n1} & L_{n2} & \cdots & L_{nn} \end{bmatrix} \begin{bmatrix} i_1 \\ i_2 \\ \vdots \\ i_n \end{bmatrix} \quad (3.12)$$

the integration of (3.11) will thus only consider the coupling and self inductances in and below the main diagonal. Rewritten as one equation, this can be expressed as

$$W_{m,co} = \sum_{j=1}^n \int \Psi_j (i_1, i_2, \dots, i_j, i_{j+1} = 0, \dots, i_n = 0) di_j \quad (3.13)$$

for an arbitrary number of coils. For the present case of a two coil system (coil 1 with current i_1 is the equivalent coil, replacing the permanent magnet, coil 2 with current i_2 is

3. Tilt stabilization

the TSC in the stator), (3.13) will evaluate to

$$W_{m,co} = \frac{1}{2}L_{11}i_1^2 + L_{12}i_1i_2 + \frac{1}{2}L_{22}i_2^2 \quad (3.14)$$

where the inductance values L_{11} and L_{12} depend on the angles α , β and, additionally, on φ since α and β are stator-bound. All angles are marked in Figure 3.7. The self-inductance value L_{22} is constant since a position change of the permanent magnet does not influence the inductance of the TSC⁴. The current i_1 is also constant whereas i_2 , circulating in the TSC, is coupled with the angles α , β and φ . Differentiating the magnetic co-energy with respect to the tilt angles yields the resulting tilt torques

$$\begin{aligned} T_\alpha &= \frac{\partial W_{m,co}}{\partial \alpha} = \frac{\partial}{\partial \alpha} \left[\frac{L_{11}i_1^2}{2} + \cancel{\frac{L_{22}i_2^2}{2}} + L_{12}i_1i_2 \right] \\ T_\beta &= \frac{\partial W_{m,co}}{\partial \beta} = \frac{\partial}{\partial \beta} \left[\frac{L_{11}i_1^2}{2} + \cancel{\frac{L_{22}i_2^2}{2}} + L_{12}i_1i_2 \right] \end{aligned} \quad (3.15)$$

which can be decomposed into the coupling torque terms

$$\begin{aligned} T_{TSC,\alpha} &= \frac{\partial L_{12}i_1i_2}{\partial \alpha} \\ T_{TSC,\beta} &= \frac{\partial L_{12}i_1i_2}{\partial \beta} \end{aligned} \quad (3.16)$$

due to the newly introduced TSC and into the reluctance terms

$$\begin{aligned} T_{\mathcal{T},\alpha} &= \frac{1}{2} \frac{\partial L_{11}i_1^2}{\partial \alpha} \\ T_{\mathcal{T},\beta} &= \frac{1}{2} \frac{\partial L_{11}i_1^2}{\partial \beta} \end{aligned} \quad (3.17)$$

which may equally be expressed as

$$\begin{aligned} T_{\mathcal{T},\alpha} &= \bar{c}_{\mathcal{T}} (1 - \hat{c}_{\mathcal{T}} \cdot \cos(2\Omega t)) \alpha + \bar{c}_{\mathcal{T}} \hat{c}_{\mathcal{T}} \cdot \sin(2\Omega t) \beta \\ T_{\mathcal{T},\beta} &= \bar{c}_{\mathcal{T}} \hat{c}_{\mathcal{T}} \cdot \sin(2\Omega t) \alpha + \bar{c}_{\mathcal{T}} (1 + \hat{c}_{\mathcal{T}} \cdot \cos(2\Omega t)) \beta \end{aligned} \quad (3.18)$$

according to the tilt stiffness anisotropy definition stated in Section 2.1.2.

3.1.4.2. Coupling term

When we take a closer look at the coupling inductance L_{12} , it is important to keep in mind that α and β are defined in a stationary coordinate system.

The component \hat{L}_{12} is the peak coupling inductance value between the TSC and the equivalent coil when the two are collocated in the same plane. This would, however, only be the case when the magnet is tilted upright, with the vector of magnetization pointing

⁴In addition to neglecting the back iron ring, we tacitly assume a perfect permeability of the permanent magnet of $\mu_{PM} = 1$.

up or downwards. Generally, L_{12} can be described as

$$L_{12} = -\hat{L}_{12} \sin(\beta) \cos(\Omega t) + \hat{L}_{12} \sin(\alpha) \sin(\Omega t) \quad (3.19)$$

where all angles are time dependent. It is also important to notice that the coupling does not only depend on α and β but additionally also on the rotational angle. The tilt angles change slowly compared to the rotational angle and also, they are relatively small in amplitude. This means that a linearization of these tilt angles, yielding

$$L_{12} = -\hat{L}_{12} \cdot \beta \cos(\Omega t) + \hat{L}_{12} \cdot \alpha \sin(\Omega t) \quad (3.20)$$

is possible for small deviations. Substituting into (3.16), the coupling torque components can be written as

$$\begin{aligned} T_{TSC,\alpha} &= \frac{\partial}{\partial \alpha} \left[\hat{L}_{12} (\alpha \sin(\Omega t) - \beta \cos(\Omega t)) i_1 i_2 \right] \\ T_{TSC,\beta} &= \frac{\partial}{\partial \beta} \left[\hat{L}_{12} (\alpha \sin(\Omega t) - \beta \cos(\Omega t)) i_1 i_2 \right], \end{aligned} \quad (3.21)$$

showing the influence of the tilt angles but also of the unknown TSC-current i_2 .

3.1.4.3. TSC current

The voltage equation for the short-circuited coil

$$V_2 = i_2 R_2 + \frac{d\Psi_2}{dt} = 0 \quad (3.22)$$

can be combined with the linear relationship between the linked coil flux value Ψ_2 and the coupling and self inductance

$$\Psi_2 = L_{12} i_1 + L_{22} i_2. \quad (3.23)$$

After deriving Ψ_2 with respect to time⁵, we obtain an additional differential equation for the TSC current

$$L_{22} \frac{di_2}{dt} + i_2 R_2 + \hat{L}_{12} i_1 \cdot (\alpha \cos(\Omega t) \Omega + \dot{\alpha} \sin(\Omega t) + \beta \sin(\Omega t) \Omega - \dot{\beta} \cos(\Omega t)) = 0 \quad (3.24)$$

which needs to be coupled with the differential equations for the tilting angles for forming the complete differential equation system. This means, however, that the classical approaches for stability analysis in linear time invariant systems (Routh-Hurwitz stability criterion, Nyquist stability criterion etc.) are not applicable due to the periodically time dependent coefficients. For a first step, this problem can be circumnavigated when the inductive voltage in the TSC and, therefore, the influence of the self-inductance L_{22} is neglected. This is only legitimate if the electrical cut-off frequency of the TSC

$$\omega_{c,TSC} = \frac{R_2}{L_{22}} \quad (3.25)$$

⁵As mentioned in the modeling assumptions in the beginning of Section 3.1.4, the rotational angle will be replaced by $\varphi = \Omega t$ for improved clarity in the calculation process.

3. Tilt stabilization

is significantly above the expected angular current frequency

$$\omega(i_2) = \Omega \quad (3.26)$$

or, in other words, when the rotational speed is low enough. This simplification is critical for high-speed drives as will be demonstrated in Section 3.1.4.6 but for the moment, it eliminates the differential equation in i_2 and we can then express the current in the TSC as

$$i_2 = \frac{\hat{L}_{12}i_1}{R_2} \left(\dot{\beta} \cos(\Omega t) - \beta \sin(\Omega t) \Omega - \dot{\alpha} \sin(\Omega t) - \alpha \cos(\Omega t) \Omega \right). \quad (3.27)$$

3.1.4.4. Simplified model

The TSC current (3.27) can be substituted into (3.21), yielding

$$\begin{aligned} T_{TSC,\alpha} &= \chi \frac{\partial}{\partial \alpha} \left[(\alpha \sin(\Omega t) - \beta \cos(\Omega t)) \cdot \left((\dot{\beta} - \alpha \Omega) \cos(\Omega t) - (\dot{\alpha} + \beta \Omega) \sin(\Omega t) \right) \right] \\ T_{TSC,\beta} &= \chi \frac{\partial}{\partial \beta} \left[(\alpha \sin(\Omega t) - \beta \cos(\Omega t)) \cdot \left((\dot{\beta} - \alpha \Omega) \cos(\Omega t) - (\dot{\alpha} + \beta \Omega) \sin(\Omega t) \right) \right] \end{aligned} \quad (3.28)$$

where

$$\chi = \frac{\hat{L}_{12}^2 i_1^2}{R_2}. \quad (3.29)$$

After deriving with respect to the tilt angles and by additionally applying the trigonometric equalities of

$$\begin{aligned} \sin(\Omega t) \cos(\Omega t) &= \frac{1}{2} \sin(2\Omega t) \\ \sin^2(\Omega t) &= \frac{1}{2} (1 - \cos(2\Omega t)) \\ \cos^2(\Omega t) &= \frac{1}{2} (1 + \cos(2\Omega t)) \end{aligned} \quad (3.30)$$

the torque due to the TSC yields

$$\begin{aligned} T_{TSC,\alpha} &= \chi \left[-\frac{\dot{\alpha}}{2} + \frac{\dot{\beta} - 2\alpha\Omega}{2} \sin(2\Omega t) + \frac{2\beta\Omega + \dot{\alpha}}{2} \cos(2\Omega t) \right] \\ T_{TSC,\beta} &= \chi \left[-\frac{\dot{\beta}}{2} + \frac{2\alpha\Omega - \dot{\beta}}{2} \cos(2\Omega t) + \frac{2\beta\Omega + \dot{\alpha}}{2} \sin(2\Omega t) \right] \end{aligned} \quad (3.31)$$

The torque expressions in (3.31) contain several trigonometric dependencies on the rotational angle. Since the resonance frequency for the tilting movement, $\Omega_{c,\mathcal{T}}$, given in (3.8), is significantly lower than the rotational speeds of a high-speed drive, we can expect an averaging of the torques which actually influence the rotor dynamic behavior. Eliminating the summands of $T_{TSC,\alpha}$ and $T_{TSC,\beta}$ which contain a time dependent sinusoidal term, however, adds a second blind spot to the model. In addition to

neglecting the influence of the self-inductance L_{22} which makes the model invalid for current frequencies approaching or surpassing the TSC cut-off frequency, the mentioned averaging eliminates the system's response to those components in the angles α and β or in the angular speeds $\dot{\alpha}$ and $\dot{\beta}$ which oscillate with a frequency of 2Ω . This is due to the fact that a multiplication of such components with the sinusoidal factors in (3.31) results in a constant offset which will, thus, not disappear due to the averaging. In order to stay on the path towards a linear time-invariant system, however, this additional weakness of the simplified model will be accepted for the moment.

This means that for setting up the equation of motion, we will only consider the tilt torques (3.15) after averaging them over the rotational angle φ . Equation (3.31) hence becomes

$$\begin{aligned}\overline{T_{TSC,\alpha}} &= -\frac{\chi\dot{\alpha}}{2} \\ \overline{T_{TSC,\beta}} &= -\frac{\chi\dot{\beta}}{2}\end{aligned}\quad (3.32)$$

and (3.18) becomes

$$\begin{aligned}\overline{T_{\mathcal{T},\alpha}} &= \bar{c}_{\mathcal{T}}\alpha \\ \overline{T_{\mathcal{T},\beta}} &= \bar{c}_{\mathcal{T}}\beta\end{aligned}\quad (3.33)$$

which allows assembling these torque values into a state space model for the state vector $\mathbf{q}_{\mathcal{T}}$ for the equation of motion

$$\mathbf{I} \cdot \ddot{\mathbf{q}}_{\mathcal{T}} = \sum \mathbf{T}. \quad (3.34)$$

Starting with the formulation of the standard model for the JEFFCOTT rotor

$$\mathbf{I} \cdot \ddot{\mathbf{q}}_{\mathcal{T}} + (\mathbf{G} + \mathbf{D}) \cdot \dot{\mathbf{q}}_{\mathcal{T}} + \mathbf{C} \cdot \mathbf{q}_{\mathcal{T}} = \mathbf{T}_{TSC} \quad (3.35)$$

with the inertia matrix

$$\mathbf{I} = \begin{bmatrix} I_d & 0 \\ 0 & I_d \end{bmatrix}, \quad (3.36)$$

the gyroscopic matrix

$$\mathbf{G} = \begin{bmatrix} 0 & I_p\Omega \\ -I_p\Omega & 0 \end{bmatrix}, \quad (3.37)$$

which reflects the gyroscopic coupling between the two tilting axes, the damping matrix with the external tilt damping coefficient⁶ $D_{\mathcal{T}}$

$$\mathbf{D} = \begin{bmatrix} D_{\mathcal{T}} & 0 \\ 0 & D_{\mathcal{T}} \end{bmatrix}, \quad (3.38)$$

and the stiffness matrix

$$\mathbf{C} = \begin{bmatrix} \bar{c}_{\mathcal{T}} & 0 \\ 0 & \bar{c}_{\mathcal{T}} \end{bmatrix}. \quad (3.39)$$

⁶The damping in the passively stabilized tilt degrees of freedom is very weak and consists mainly of iron losses in the stator core. Additional damping due to a surrounding fluid can also be included in this coefficient.

3. Tilt stabilization

The additional influence of the TSC is, not yet included in the standard JEFFCOTT rotor model which is why these terms are included in

$$\mathbf{T}_{TSC} = \begin{bmatrix} -\frac{\chi}{2}\dot{\alpha} \\ -\frac{\chi}{2}\dot{\beta} \end{bmatrix} + \mathbf{T}_{external}. \quad (3.40)$$

Assuming the external torque $\mathbf{T}_{external}$ on the disc to be zero for the moment, the terms of \mathbf{T}_{TSC} can also be brought to the left side of the equation of motion with an extended damping matrix, leaving

$$\mathbf{I} \cdot \ddot{\mathbf{q}}_{\mathcal{T}} + (\mathbf{G} + \mathbf{D}') \cdot \dot{\mathbf{q}}_{\mathcal{T}} + \mathbf{C} \cdot \mathbf{q}_{\mathcal{T}} = \mathbf{0} \quad (3.41)$$

with

$$\mathbf{D}' = \begin{bmatrix} D_{\mathcal{T}} + \frac{\chi}{2} & 0 \\ 0 & D_{\mathcal{T}} + \frac{\chi}{2} \end{bmatrix}. \quad (3.42)$$

3.1.4.5. Stability analysis of the simplified model

In the following passage, the stability of the simplified system (3.41) is investigated. Since the system is a linear time-invariant differential equation system, the stability criterion of Routh-Hurwitz which is well described in the literature can be applied. Asymptotic stability can be shown for the system, when all principal minors of the Hurwitz matrix H are positive. In the present case, the principal minors are

$$\begin{aligned} H_{m1} &= I_d^2 \\ H_{m2} &= I_d(\chi + 2D_{\mathcal{T}}) \end{aligned} \quad (3.43)$$

$$H_{m3} = I_p^2\Omega^2 + \frac{\chi^2}{4} + D_{\mathcal{T}}\chi + I_d\bar{c}_{\mathcal{T}} + D_{\mathcal{T}}^2 \quad (3.44)$$

$$H_{m4} = \frac{\bar{c}_{\mathcal{T}}(\chi + 2D_{\mathcal{T}})(I_p^2\Omega^2 + \frac{\chi^2}{4} + D_{\mathcal{T}}\chi + D_{\mathcal{T}}^2)}{I_p^2\Omega^2 + \frac{\chi^2}{4} + D_{\mathcal{T}}\chi + I_d\bar{c}_{\mathcal{T}} + D_{\mathcal{T}}^2} \quad (3.45)$$

$$H_{m5} = \bar{c}_{\mathcal{T}} \quad (3.46)$$

which allow a simple verdict since all used variables are positive and, therefore, all the principal minors are positive. This asymptotic behavior does not come unexpected when we note that the present disk drive model considers a positive, stabilizing tilt damping $D_{\mathcal{T}}$ and that the only terms of the equation of motion which were contributed by the TSC add to this damping value.

In order to quantify the prediction of increased damping due to the TSC influence, Figures 3.8 and 3.9 show the tilt angle α when a torque impulse impinges the rotor. Compared to the system without TSC, the oscillations of the angular deflection and of the angular speed are quickly damped. Especially in the top image which shows the angle deflection, the slower precession movement and the faster oscillating nutation movement can be identified clearly. The nutation amplitude is quickly reduced, leaving the deflection due to precession which experiences weaker damping due to its slower frequency. The same behavior can be observed in the lower image where the fast angular speed components of the nutation movement decrease quickly.

The simplified model was numerically evaluated at a fixed rotational speed of 3000 rpm.

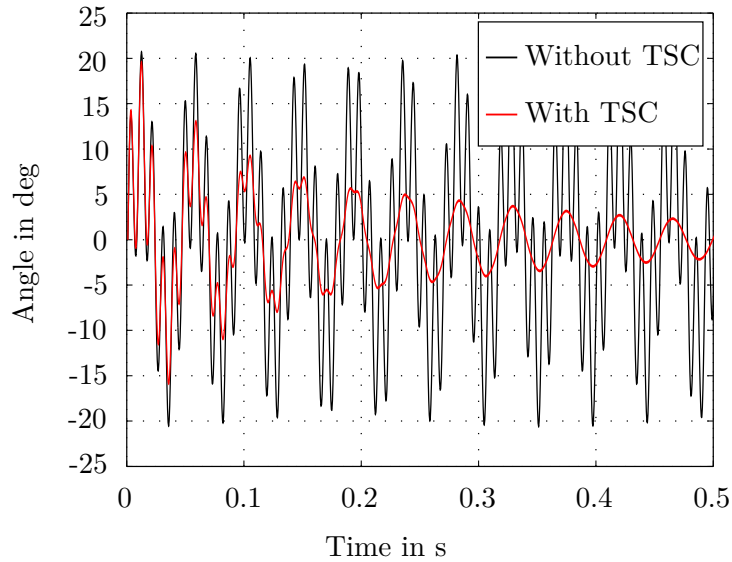


Figure 3.8.: Response of the tilt angle α in the simplified system due to a torque impulse in direction α when the external tilt damping $D_{\mathcal{T}}$ is set to 0. Except for the expected phase shift, the angle β reacts likewise.

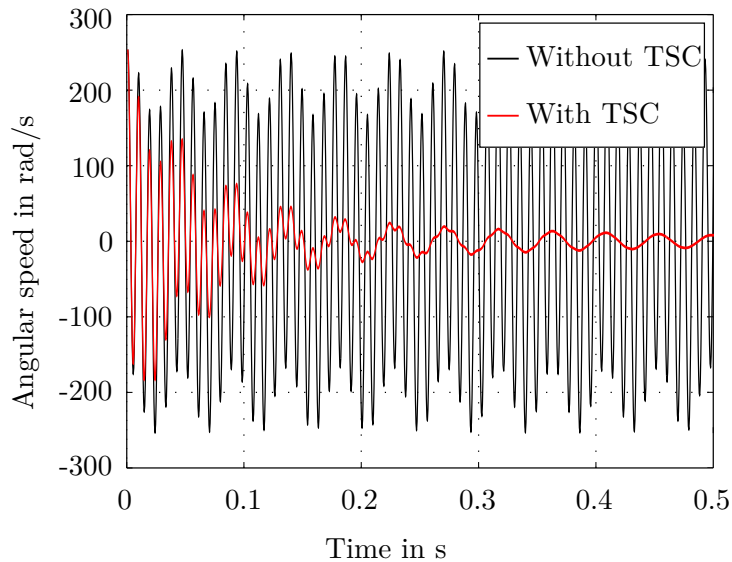


Figure 3.9.: Response of the angular speed $\dot{\alpha}$ in the simplified system due to a torque impulse in the direction of α when the external tilt damping $D_{\mathcal{T}}$ is set to 0. Except for the expectable phase shift, the angular speed $\dot{\beta}$ reacts likewise.

This relatively low speed was chosen in order to present a result which is certainly within the restricted domain which was defined in the derivation of the analytical model. Even though the model yields comparable results for much higher rotational speeds, these results cannot be used for a general verdict on the system stability as the cut-off frequency of the TSC due to the measured resistance and inductance values lies at about 5500 rad/s , equivalent to 47750 rpm . This means that the simplified analytical model will be significantly influenced when the rotational speed approaches this speed. Additionally, the averaging of (3.31) distorts the presented results to an unknown degree. Therefore, an approach which takes the inductance of the TSC into account and which does not resort to averaging will be carried out in the following.

3.1.4.6. Extended differential equation system

The simplification which neglected the self-inductance L_{22} of the TSC in Section 3.1.4.3 leads to the model becoming invalid at rotational speeds, and thus, TSC-current frequencies, which approach the cut-off frequency $\omega_{c,TSC}$. In order to allow a statement about the rotor's motion behavior at and above these speeds, the current will be modeled using the differential equation (3.24). This extends the state vector to

$$\tilde{\mathbf{q}} = \begin{bmatrix} \alpha \\ \beta \\ i_2 \end{bmatrix} \quad (3.47)$$

and makes the redefinition of the state matrices used in (3.41) necessary. Additionally, the fact that i_2 cannot be eliminated from the coupling torque expression (3.21) but instead, is present as a state variable, changes these torque components to

$$\begin{aligned} T_{TSC,\alpha} &= \hat{L}_{12} i_1 i_2 \sin(\Omega t) \\ T_{TSC,\beta} &= -\hat{L}_{12} i_1 i_2 \cos(\Omega t). \end{aligned} \quad (3.48)$$

With this relationship, the electric and the mechanic system can be coupled in a system of the three differential equations

$$\begin{aligned} \ddot{\alpha} I_d + \dot{\alpha} D_{\mathcal{T}} + \dot{\beta} \Omega I_p + (\bar{c}_{\mathcal{T}} + \bar{c}_{\mathcal{T}} \hat{c}_{\mathcal{T}} \cos(2\Omega t)) \alpha + (\bar{c}_{\mathcal{T}} \hat{c}_{\mathcal{T}} \sin(2\Omega t)) \beta \\ - \hat{L}_{12} i_1 \sin(\Omega t) i_2 &= 0 \\ \ddot{\beta} I_d + \dot{\beta} D_{\mathcal{T}} - \dot{\alpha} \Omega I_p + (\bar{c}_{\mathcal{T}} \hat{c}_{\mathcal{T}} \sin(2\Omega t)) \alpha + (\bar{c}_{\mathcal{T}} - \bar{c}_{\mathcal{T}} \hat{c}_{\mathcal{T}} \cos(2\Omega t)) \beta \\ + \hat{L}_{12} i_1 \sin(\Omega t) i_2 &= 0 \\ L_{22} \dot{i}_2 + i_2 R_2 + \hat{L}_{12} i_1 \cdot (\alpha \cos(\Omega t) \Omega + \dot{\alpha} \sin(\Omega t) \\ + \beta \sin(\Omega t) \Omega - \dot{\beta} \cos(\Omega t)) &= 0 \end{aligned} \quad (3.49)$$

which can be written in matrix form

$$\tilde{\mathbf{I}} \cdot \ddot{\tilde{\mathbf{q}}} + (\tilde{\mathbf{G}} + \tilde{\mathbf{D}}) \cdot \dot{\tilde{\mathbf{q}}} + \tilde{\mathbf{C}} \cdot \tilde{\mathbf{q}} = \mathbf{0} \quad (3.50)$$

with

$$\tilde{\mathbf{I}} = \begin{bmatrix} I_d & 0 & 0 \\ 0 & I_d & 0 \\ 0 & 0 & 0 \end{bmatrix}, \quad (3.51)$$

$$\tilde{\mathbf{G}} = \begin{bmatrix} 0 & I_p \Omega & 0 \\ -I_p \Omega & 0 & 0 \\ 0 & 0 & 0 \end{bmatrix}, \quad \tilde{\mathbf{D}} = \begin{bmatrix} D_{\mathcal{T}} & 0 & 0 \\ 0 & D_{\mathcal{T}} & 0 \\ \hat{L}_{12} i_1 \sin(\Omega t) & -\hat{L}_{12} i_1 \cos(\Omega t) & L_{22} \end{bmatrix}, \quad (3.52)$$

$$\tilde{\mathbf{C}} = \begin{bmatrix} \bar{c}_{\mathcal{T}} (1 - \hat{c}_{\mathcal{T}} \cdot \cos(2\Omega t)) & \bar{c}_{\mathcal{T}} \hat{c}_{\mathcal{T}} \cdot \sin(2\Omega t) & -\hat{L}_{12} i_1 \sin(\Omega t) \\ \bar{c}_{\mathcal{T}} \hat{c}_{\mathcal{T}} \cdot \sin(2\Omega t) & \bar{c}_{\mathcal{T}} (1 + \hat{c}_{\mathcal{T}} \cdot \cos(2\Omega t)) & \hat{L}_{12} i_1 \cos(\Omega t) \\ \hat{L}_{12} i_1 \cos(\Omega t) \Omega & \hat{L}_{12} i_1 \sin(\Omega t) \Omega & R_2 \end{bmatrix}. \quad (3.53)$$

3.1.4.7. Stability and design guidelines

It can be seen that there are components of the current differential equation in matrix $\tilde{\mathbf{D}}$ which are multiplied with the angular speeds and, thus, influence the damping and that $\tilde{\mathbf{C}}$ holds two other components of the current equation being multiplied with the angles α and β which alter the stiffness of the system.

The averaging over the rotational angle cannot be carried out for the terms which originate from (3.28). Even though the involved components now are different from the ones in the simplified model, the basic flaw introduced by the averaging of the matrices in $\tilde{\mathbf{D}}$ or $\tilde{\mathbf{C}}$ would stay the same: Averaging eliminates the matrix components which are multiplied with a $\sin()$ – or $\cos()$ – expression. However, since the angles α and β as well as the current i_2 have significant components which oscillate with Ω , their multiplication with the sinusoidal components in, e.g., the last column of $\tilde{\mathbf{C}}$ results in a constant offset which would disappear when averaging is applied.

Regarding the stability of the presented model, a significant aspect can be adapted from [34] where a phase angle

$$\theta = \arctan\left(\frac{R_2}{\omega L_{22}}\right) \quad (3.54)$$

is used as a stability indicator for a radial null flux bearing. It may seem uncommon that θ is defined as the complementary angle to what is usually defined as the phase angle in an inductive circuit. However, the definition is plausible as it gives the angle between the two physically relevant quantities; the coil current i_2 and the linked flux Ψ_2 . The stability boundary of

$$\theta < \frac{\pi}{2} \quad (3.55)$$

given by the authors of [34] can be transferred to the present work: The physical interpretation of this boundary are either very high resistance R_2 which would prevent the flow of the stabilizing current i_2 or very low inductance L_{22} which would prevent the induction effect. In the numerical simulation, the effect of the TSC decreases more and more when θ approaches $\frac{\pi}{2}$ but does not destabilize the system.

Also very large values for L_{22} and very small values for R_2 may not result in an effective TSC design as the electrical cut-off frequency $\omega_{c,TSC}$ may be too low for the current to rise in the TSC at a given rotor speed. Very small values of θ lead to decreasing TSC current and decreasing stabilization effect. Again, the system remains stable for all examined rotational speeds and resistance and inductance values.

In addition to the mentioned stability limit, we can, therefore, add a minimum boundary for the ratio of cut-off frequency to rotational speed to the design guidelines. This requirement can be translated to the aforementioned phase angle since the argument of the arctan function is equal to this ratio. According to the numerical simulation, values of

$$\omega_{c,TSC} \sim \Omega \quad (3.56)$$

which correspond to

$$\theta \sim \frac{\pi}{4} \quad (3.57)$$

seem to be a reasonable orientation for a good TSC design. It shall be mentioned here that simply changing the number of winding turns does not change the characteristic of the TSC since both, L_{22} and R_2 depend quadratically on the number of winding turns

3. Tilt stabilization

when the available cross section and the possible copper fill factor are fixed. Possible options are, therefore, the change of that available cross section inside the stator or the connection to an external circuit. The latter possibility seems to be an interesting point for further research as this would allow adapting the coil characteristics to the rotational speed.

3.1.5. Numerical simulation and model comparison

In order to analyze the behavior of the complete extended differential equation system as given in (3.50), a numerical simulation was conducted. The model was implemented in Matlab/Simulink®, using the same parameter values as for the simplified analytical model. Their values have been obtained by measurement and identification and are given in Table 3.1 in Section 3.1.6. Figure 3.10 compares the impulse response of this numerically simulated extended differential equation system with the impulse response of the simplified, analytically calculated system (3.41) at three different rotational speeds. As mentioned at the end of the preceding section, the first difference between the two models is the consideration of the time-dependent components of the passive tilt stiffness. The second difference comes from the additional state variable i_2 , or rather, the inductance of the TSC which was neglected in the simplified model but which was taken into account in the extended model. Finally, the third difference is due to the averaging process in the simplified model which eliminates the stiffness contribution of the TSC.

In order to verify the simulation, the top figure considers a rotational speed of 3000 rpm which is far below the cut-off frequency of the TSC. However, even at that point, the behavior of the two models is not identical. Only if the components of the TSC-current equation which contribute to the stiffness were omitted in the extended model, the result would be identical. This verifies the basic identity of the two models concerning the damping values but also makes clear that the averaging process in the simplified model causes significant errors at low speeds. These additional components in the extended model cause the oscillation to be suppressed significantly faster than in the simplified model while the high-frequency nutation movement can be observed for a longer time.

The next comparison in the middle image of Figure 3.10 was carried out at a rotational speed of 50 000 rpm. Again, the angle oscillation is suppressed significantly faster in the extended model and also again, the high-frequency nutation movement can be recognized for a longer time than in the simplified model. The experiment of omitting the coupling components in the current equation in matrix $\tilde{\mathbf{C}}$ for the simulation of the extended model again gives nearly identical curves which demonstrates that also at speeds significantly above the cut-off frequency of the TSC, these stiffness related components still dominate the error between the two models. Generally, it needs to be noted that both, the oscillation amplitudes and the precession frequency are drastically decreased compared to the low-speed simulation. This low angular speed of the precession movement is the reason for its very low damping in the simplified analytical model.

The third simulation in the bottom image was carried out at 200 000 rpm, showing that all before seen effects are intensified. The oscillation amplitude and frequency of the precession movement are decreased and the high-frequency movement is damped so quickly that it cannot be recognized in neither one of the curves. Once again, it becomes clear, that only the stiffness contribution of the TSC in matrix $\tilde{\mathbf{C}}$ significantly suppresses the slow precession movement.

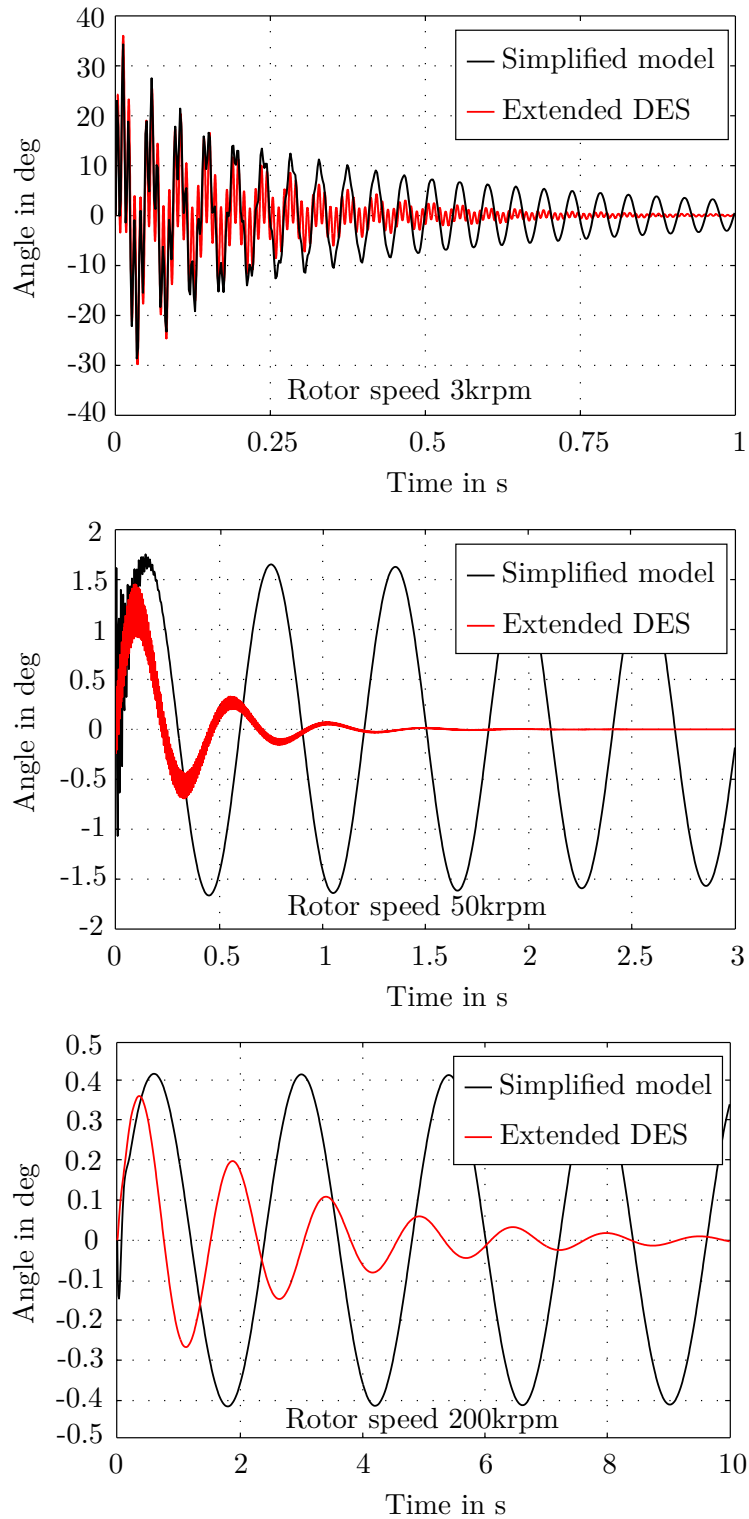


Figure 3.10.: Response of the angle α to a torque impulse in the direction of α when the rotor is spinning at 3000 rpm (top), 50 000 rpm (middle) and 200 000 rpm (bottom). All figures compare the simplified analytical model with the numerically simulated extended differential equation system (DES). Except for the expectable phase shift, the angle β reacts likewise.

3.1.6. Measurement

The TSC was implemented in the design of a bearingless disk drive by milling a notch in the inside wall of the stator hollow cylinder. The geometrical and electrical properties of the TSC and the necessary drive components are given in Table 3.1. In order to test the

Table 3.1.: Experimental TSC and demonstrator drive data

Parameter	Value
Winding space	2.5 mm x 2.5 mm
Winding turns	30
Wire diameter (copper)	0.33 mm
Copper cross section	2.56 mm ²
Coil resistance R_2	980 m Ω
Coil inductance L_{22}	180 μ H
Coupling inductance \hat{L}_{12}	0.44 μ H
Equivalent current i_1	20 200 A
Mean tilt stiffness $\bar{c}_{\mathcal{T}}$	0.35 N m/rad
Tilt stiffness variation ratio $\hat{c}_{\mathcal{T}}$	0.65
Tilt damping parameter $D_{\mathcal{T}}$	8×10^{-4} N m s
Diametric moment of inertia I_d	3.75×10^{-6} kg m ²
Polar moment of inertia I_p	6.40×10^{-6} kg m ²

functionality and behavior of the drive with this new feature, a torque impulse has to act on the spinning rotor. It is, however, a very difficult task to define such an impulse in reality because an impulse hammer which would normally be used in structural analysis cannot be used on a spinning rotor. Therefore, the following measuring procedure was defined for measuring the TSC effect with a measurement setup shown in Figure 3.11:

- Acceleration of the rotor to target speed
- Adjustment of optical distance sensors (a) and (b) in order to measure the axial deflection on two opposite positions of the rotor (c) at a radial distance of r_{sens} from the rotor center
- Zeroing of the distance sensors
- Slow tilting of the entire drive unit (d) to allow the placement of a defined spacer (e) on a defined position under the drive housing
- Triggering of measurement by sharply pulling spacer out from under the drive housing

As a result of the spacer being removed, the drive will tilt down and hit the table surface, bringing a certain tilting impulse on the spinning rotor. This impulse cannot be quantified easily but it is well reproducible with the described procedure.

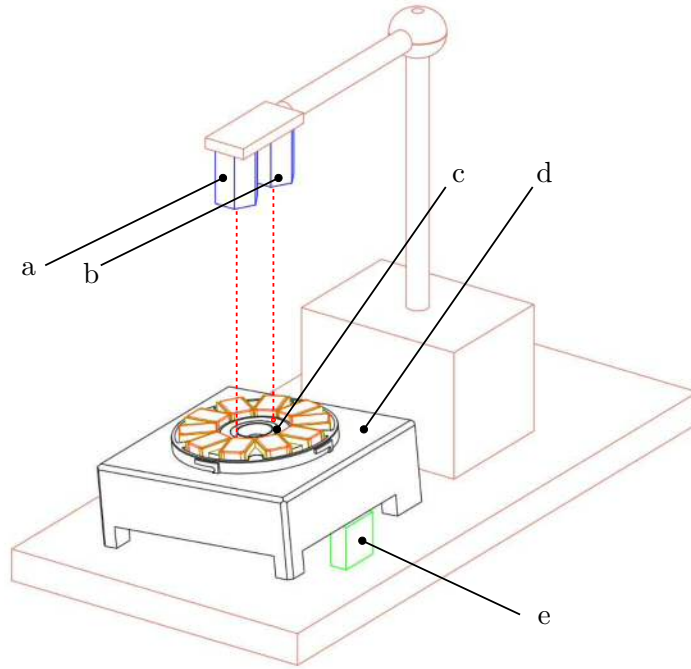


Figure 3.11.: Tilt measurement apparatus with two optical sensors (a) and (b), measuring the axial deflection of the spinning rotor (c) when the drive (d) is tilted by removing a spacer (e).

The resulting axial distance vectors z_a from sensor (a) and z_b from sensor (b) allow calculating the axial displacement of the rotor center

$$u_{center} = \frac{z_a + z_b}{2} \quad (3.58)$$

and the tilting angle

$$\alpha = \tan\left(\frac{z_a - z_b}{r_{sens}}\right). \quad (3.59)$$

The experiment was repeated for several rotational speeds, showing that the impulse is well reproducible since the measured signals were nearly identical in their amplitude. The phase angle, of course, depends on the rotor angle at which the spacer is pulled out from under the plate and which cannot be controlled. Figure 3.12 shows the axial oscillation of the rotor which is remarkably well tolerated by the spinning rotor as it never touches the touchdown bearing during the measurement. With the two curves being practically identical, the influence of the TSC on this axial degree of freedom can be neglected.

Figure 3.13 and Figure 3.14 compare the tilt angle of the measurement with the simulation of the extended differential equation system at a rotor speed of 25 000 rpm and 50 000 rpm, respectively.

As the real parameters such as damping due to the speed dependent eddy currents in the stator iron or the precise value of the tilt stiffness are extremely difficult to obtain by measurement, a different procedure must be chosen. First, the TSC is left open-ended and the resulting tilt movement due to the tilt impulse is measured. In a next step, the simulation parameters for tilt stiffness and damping are set in order to produce a fitting curve, cf. top image of Figure 3.13 and Figure 3.14. Then, the TSC is short-circuited, thus enabling its functionality, and the measurement is repeated. The simulation is then

3. Tilt stabilization

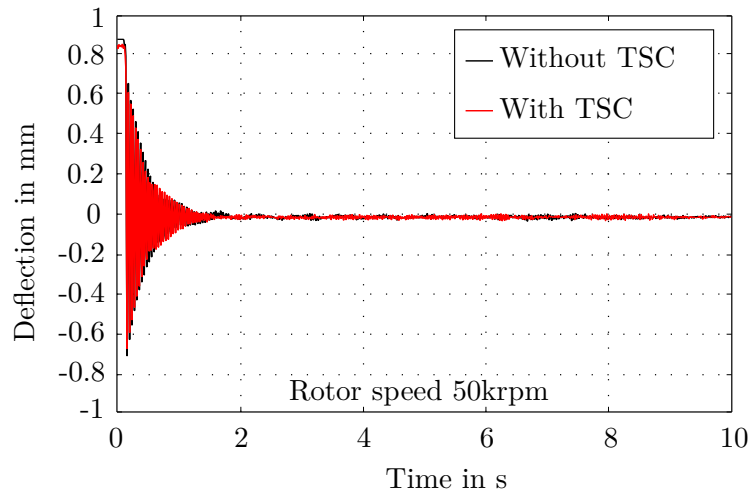


Figure 3.12.: Measurement of the axial deflection as a consequence of the sudden tilting of the measurement apparatus at a rotor speed of 50 000 rpm.

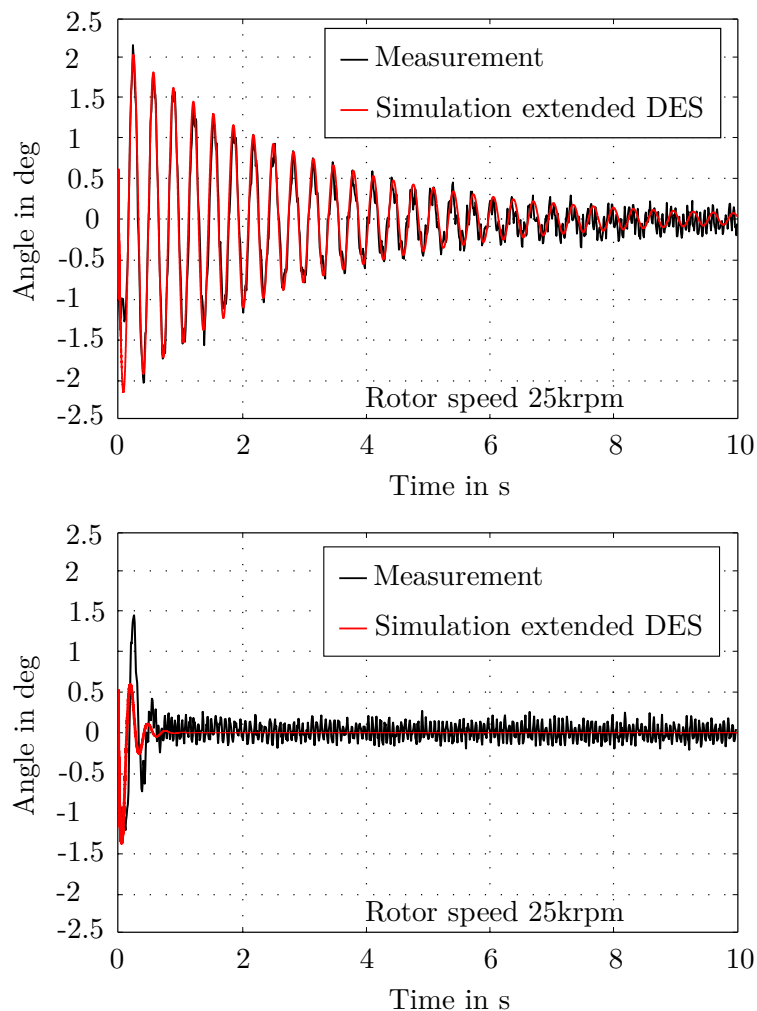


Figure 3.13.: Tilt angle α at a rotor speed of 25 000 rpm with open-ended (top) and short-circuited (bottom) TSC. Both figures show the behavior in the measurement and in the simulation of the extended differential equation system (DES).

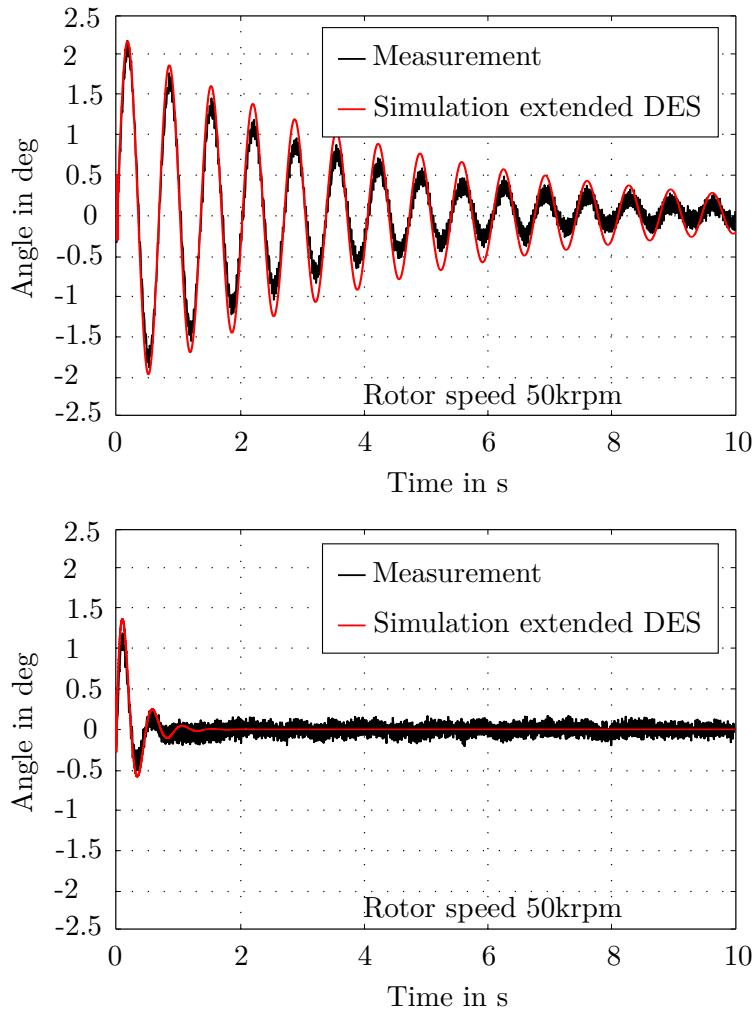


Figure 3.14.: Tilt angle α at a rotor speed of 50 000 rpm with open-ended (top) and short-circuited (bottom) TSC. Both figures show the behavior in the measurement and in the simulation of the extended differential equation system (DES).

carried out with the previously defined values and is compared to the measurement in the bottom image of the two figures. As mentioned above, only the phase of the tilt angle needs to be adapted since it is stochastically determined in the measurement.

Several conclusions can be drawn from the comparison:

- Even with the open-ended TSC, the tilting movement is damped by external effects such as the surrounding air and speed-dependent iron losses in the stator core.
- The damping effect of the short-circuited TSC is tremendous compared to the open-ended TSC.
- There is very good correlation between the measurement and the simulation when the actual external damping and the passive tilt stiffness are known.
- The constant amplitude which can be observed with the measured tilt angle signal is partly due to an uneven rotor surface and must partly also be attributed to some measurement noise. However, the overall signal quality is absolutely adequate for investigating the desired effects.

3.2. Active influence

In the previous Section 3.1, the passive tilt stabilization was introduced by short-circuiting the TSC. When the coil endings of the TSC or of slightly modified coil setups are connected to a power electronics circuit, it can also be used to exert active forces and torques on the rotor. The following passages give a brief explanation of the necessary adaptations and the resulting effects. There is, however, no detailed analysis since the effect is not used in the current prototype. This must rather be seen as complementary information to unveil the complete scope of possibilities given with these additional windings.

3.2.1. Active tilting - 1 coil

Considering the geometrical shape of the TSC as it was introduced in Section 3.1, active torque on the rotor can be created when the coil is not short-circuited but energized actively. The effect is shown in Figure 3.15 and can be understood by either considering the Lorentz forces on the winding or by examining the Maxwell forces on the radial slot walls. The axis about which the active torque is produced is always perpendicular to the axis of magnetization. Only the amplitude of this torque T^\perp and its sense (positive or negative) can be modulated by the amplitude and direction of the coil current.

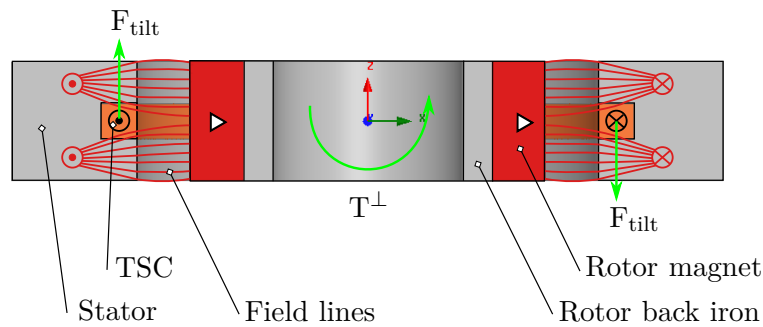


Figure 3.15.: Flux path in motor cross section with resulting force on the winding and reaction torque on rotor when coil is actively energized

3.2.2. Active axial force - 2 coils

So far, the difference in the presented effects on the rotor was due to the either passive or active use of the TSC. For the next active method of influencing the rotor, namely by creating axial forces, the coil geometry has to be modified, forming two electrically insulated and geometrically separated, “C”-shaped coils, as shown in Figure 3.16.

This modification to the stator reduces the effective iron volume but otherwise, it has similar characteristics as the ring-shaped TSC. Both previously presented effects, the passive tilt stabilization and the active tilting torque generation can be achieved with this winding set by either short-circuiting the “C”-shaped coils (for passive stabilization) or by energizing them in identical sense (for active tilting torque), respectively.

If the two coils, however, are energized with currents of opposing sense (cf. Figure 3.16), an axial force is actively created. Since the geometric setup is not rotationally symmetric anymore, the achievable axial force F_z depends on the rotor angle. With the rotor’s axis of magnetization being aligned with the x-axis at $\varphi = 0$, the achievable force can be

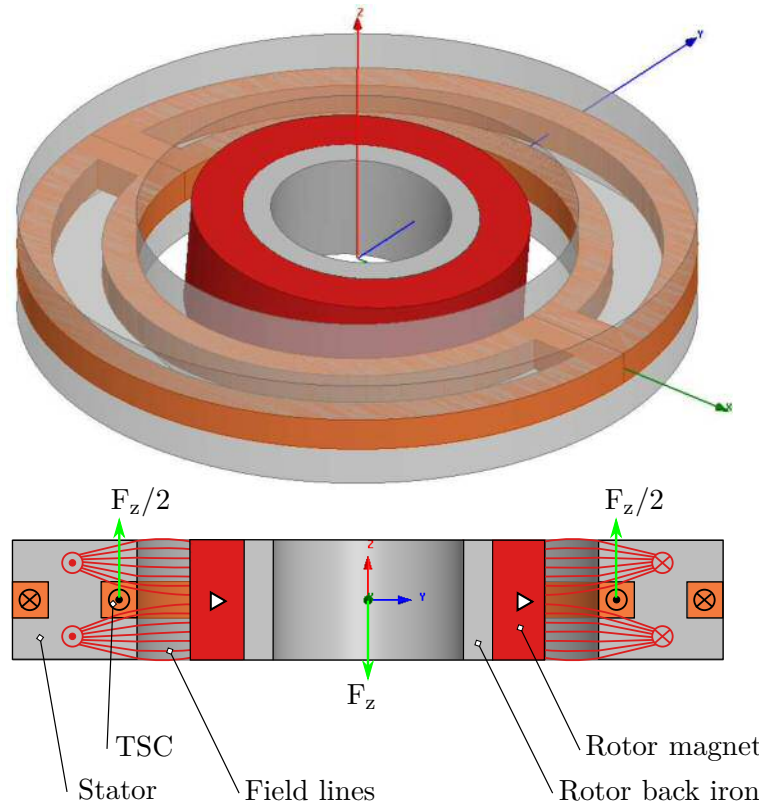


Figure 3.16.: 3D view of the drive with semi-transparent stator showing the modified coil shape (top) and vertical motor cross section with flux path and resulting force on stator and rotor when the “C”-shaped coils are energized in opposite sense (bottom)

expressed as

$$F_z(\varphi) = \chi_z i_2 \cdot \sin(\varphi) \quad (3.60)$$

with χ_z representing a force coefficient which relates the current to the maximum achievable force amplitude.

3.2.3. Active tilting - 4 coils

A last modification shall be mentioned even if the necessary number of separately controlled coils is considerably increased.

Axial force When segmenting the coil further into four electrically insulated coils as shown in Figure 3.17, a large variety of active force and torque components can be created. The passive stabilization characteristic can be provided by accordingly short-circuiting the 4 coils. Energizing all coils in the same current sense creates a situation equivalent to Figure 3.15, describing the creation of T^\perp . If two adjacent coils are chosen for one current direction and the other two for the opposite direction, the scenario is similar to Figure 3.16 with one main difference; The current direction can be changed every 90 deg, thus avoiding the angular rotor position where no active force F_z can be created. The resulting force capacity was evaluated through simulation and is displayed in Figure 3.18.

3. Tilt stabilization

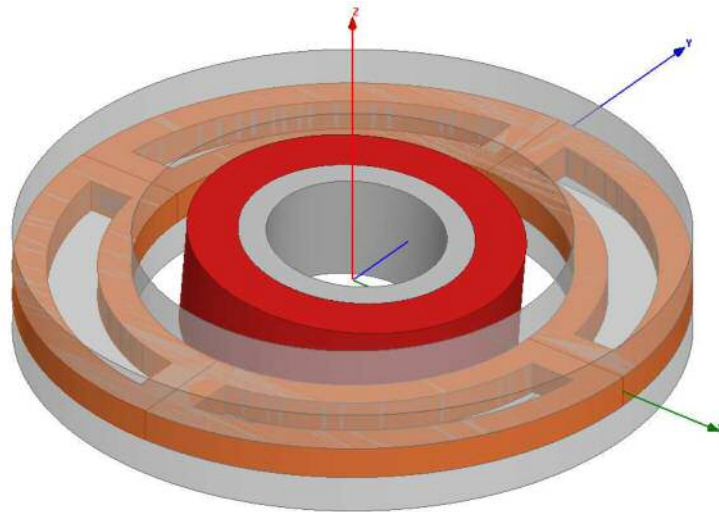


Figure 3.17.: Transparent 3D view of the drive showing the modified coil shape for four coils

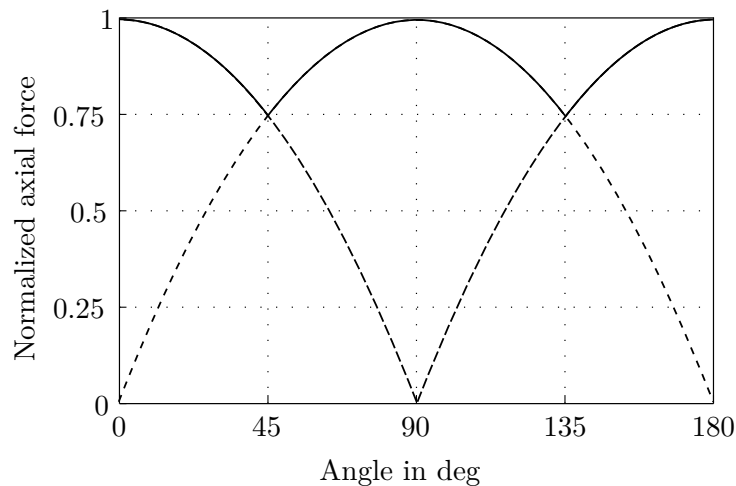


Figure 3.18.: Normalized axial force curves obtained by simulation of the 4-coil configuration over the rotor angle. The solid line represent the force capacity that can be achieved by switching the current directions according to the rotor angle.

Torque Only if the current configuration is chosen in such a way that each geometrically opposite coil pair is energized in the same current direction, the rotor can additionally be tilted actively about the axis parallel to its magnetization axis by producing a torque T^{\parallel} . However, there is an essential difference between the generation of T^{\perp} and T^{\parallel} . The torque component about the axis perpendicular to the magnetization axis due to constant coil currents turns out to be a rotating vector of constant amplitude. The new active torque component about the magnetization axis is sinusoidally dependent on the rotor angle just like the axial force component. In other words, constant coil currents will produce a rotating vector which additionally oscillates in amplitude. As a consequence, there are certain angular positions at which no torque T^{\parallel} can be created and at which the rotor cannot be tilted about its magnetization axis.

Apart from this deficit, the necessary effort for this solution is extensive, considering the necessary four independent coils with four independent power electronic circuits energizing

them and the increased loss of effective iron volume compared to all previous variations.

3.2.4. Simulation results

A concluding 3D-simulation of the proposed concepts has been conducted. For the determination of the active force and torque components, the stator coils have been designed to have a cross section of 3 mm x 3 mm. Apart from these new coils, the geometric dimensions and material parameters used in the simulation are identical to the referenced system described in [74]. The current density in the coils was set to constant value of 10 A/mm^2 and their direction in the individual coils was set accordingly to the requirements of the respective active component. Along with the achievable amplitudes of the active components, the passive tilt stiffness $c_{\mathcal{T},\beta}$ is given in Table 3.2 in order to give a comparison value and also, to show the negligible influence of the presented stator core modifications on this value.

Table 3.2.: Passive stiffness and active forces and torques produced with exemplary setups

Parameter	Original setup	1-coil setup	2-coil setup	4-coil setup
$c_{\mathcal{T},\beta}$	0.81 Nm/rad	0.78 Nm/rad	0.76 Nm/rad	0.76 Nm/rad
\hat{T}^\perp	-	31.6 mN m	30.2 mN m	30.1 mN m
\hat{F}_z	-	-	2.4 N	2.4 N
\hat{T}^\parallel	-	-	-	11.1 mN m

3.3. Conclusion

A novel *null flux* winding structure for adding damping and active torque and force capacities to the drive has been presented in this chapter.

The first part, Section 3.1, discusses the passive influence of the tilt stabilization coil (TSC). The individual parts of that section have shown that an analytical model is essential for understanding the effects of the newly introduced tilt stabilization coil. The first and most important lesson learned from the analysis of the aligned and tilted flux situations in Figure 3.5 and Figure 3.6 is that the tilt stabilization mechanism is not only triggered by the tilting movement. It is rather a consequence of the tilting combined with the rotation of the rotor. As mentioned in Section 3.1.3, this is the prime difference between the applied *null flux* arrangement and early homopolar electrodynamic bearings which exclusively depend on the movement in the one degree of freedom that they are supposed to stabilize. Especially for high rotational speeds as in the present case, this heteropolar setting is clearly advantageous.

The equation of motion can be obtained using the magnetic co-energy approach. Since the result is not a linear time-invariant system due to the angle dependent terms, several simplification steps have to be taken in order to obtain an LTI system. The comparison of the simulation results in the preceding section, however, clearly reveals that these simplifications in the derivation of the analytical model are unacceptable. In contrast to the non-simplified and numerically evaluated extended differential equation system model, the simplified model incorrectly suggests that the occurring slow angle oscillations cannot be suppressed sufficiently. The measurement results in Figure 3.13 and Figure 3.14,

3. Tilt stabilization

however, clearly prove this simplified model wrong. Therefore, the more detailed, extended differential equation system model must be used in order to better reflect the real circumstances.

The stabilization effect of the presented TSC depends on the rotational speed of the rotor. Section 3.1.4.7 gives a guideline for the coil design based on the cut-off frequency and the chosen design speed. It is evident that a strong coupling between the TSC and the equivalent coil, expressed in high values of the coupling inductance \hat{L}_{12} , increases the effect of the TSC.

The second part, Section 3.2, shows how the TSC can also serve to provide active influence in the form of active tilting torque and active axial forces. The necessary modifications are shown and some resulting side effects are mentioned. Finally, the effect of the additional windings is shown by simulation for the active force and torque generation. In contrast to the passive stabilization effect, the active influence of the TSC was not verified in an actual prototype as this feature is not the focus of the current development but rather a possible modification worth consideration in the future.

4. Mechanical rotor stability

Contents

4.1. Mechanical properties	76
4.1.1. Surface mounted magnets	77
4.1.2. Buried magnets	77
4.1.3. Bandaging	78
4.2. Analytic stress calculation of the rotor	78
4.2.1. Unsupported rotor	78
4.2.2. Bandaged rotor	80
4.2.3. Mechanical effects of an inner back iron	83
4.2.4. Dimensioning of the interference fit	84
4.3. Comparison of the analytical model with a finite element (FE) simulation	87
4.3.1. Simulation setup	87
4.3.2. Validation of the method	88
4.3.3. Stress simulation result with ring structure	89
4.3.4. Flexible body modes	89
4.4. Rotor segmentation	91
4.4.1. Single-sided cut	91
4.4.2. Double-sided cut	92
4.4.3. Four-sided cut	92
4.5. Conclusion	95

High-speed rotors demand special attention for their mechanical stability due to centrifugal forces. This chapter deals with the mechanical properties of the applied materials, discusses several different rotor construction techniques and then gives an analytical model for certain rotor configurations. The different cases highlight the mechanical effect of the rotor back iron, the rotor bandage, and the necessary interference fit for mounting the rotor components.

The third section of this chapter shows the setup and results of a finite element simulation for verifying the proposed analytic model. This finite element simulation is then used to calculate rotor configurations with segmented magnets which are not covered by the analytic model. Finally, the conclusion at the end of the chapter lists the necessary steps for safe operation of the 5pd rotor in the current motor and also in a design extrapolation for increased speeds.

4.1. Mechanical properties

Rotors in electrical machines are subject to different kinds of mechanical stress. Depending on the field of application and the demanded rotor speeds, either tensile stress due to the centrifugal forces or vibrations due to external disturbance forces or natural oscillation dominate. In the present case of a high-speed rotor, the material bound centrifugal forces

$$F_c = m_R r \Omega^2 \quad (4.1)$$

which depend linearly on the rotor mass m_R and the radial distance r between the mass center and the axis of rotation but quadratically on the rotor speed Ω . For cylindrical composite bodies consisting of multiple interleaved rings and an axial length l_R , F_c can be generalized as

$$F_c = \int_{r_i}^{r_o} \rho(r) r \Omega^2 2r \pi l_R dr \quad (4.2)$$

using a radius dependent density variable $\rho(r)$. For n cylinders, this can be written as

$$F_c = \sum_{j=1}^n \rho_j 2\Omega^2 \frac{(r_{o,j}^3 - r_{i,j}^3)}{3} \pi l_R \quad (4.3)$$

where ρ_j , $r_{o,j}$ and $r_{i,j}$ denote the density, the outer and the inner radius of the respective cylinder.

Depending on the rotor structure and the mechanical properties of the materials, these forces cause stresses in its components. In order to prevent plastic deformation or, worse, the destruction of the rotor, the stress values need to be kept below the tolerable yield stress of the respective material at all times. Table 4.1 lists the main mechanical characteristics of several typical materials for the construction of PMSM rotors. It is important to notice that the sintered permanent magnets have significantly lower yield strength and YOUNG's¹ modulus than the listed steel sheet material. Depending on the mounting method, this can lead to serious difficulties.

<i>Material</i>	<i>Density</i>	<i>Yield / tensile strength, typic.</i>	<i>YOUNG's modulus, typic.</i>
NdFeB	7400 kg/m ³	70 - 80 MPa	151 GPa
Sm2Co17	8100 - 8400 kg/m ³	35 - 50 MPa	100 - 110 GPa
Hard ferrite, sintered	4800 kg/m ³	50 - 60 MPa	150 GPa
Steel sheet M400-50A	7650 kg/m ³	265 - 380 MPa	200 - 210 GPa

Table 4.1.: Mechanical parameters of typical motor materials taken from [30, 118, 112]

¹THOMAS YOUNG, * 1773 in Milverton, Somerset, England, † 1829 in London, England

4.1.1. Surface mounted magnets

The most relevant stress component for surface mounted, glued segments is the radial tensile stress. The most critical issue, however, is not the tensile yield strength of the magnet material, but rather the mechanical strength and the reliability of the adhesive layer. The adhesive must, along with highest bond strength and long time stability, also provide sufficient elasticity in order to prevent brittle failure of the bond when the rotor is subject to externally imposed or resonance-caused vibrations - even at low rotational speed. Since these demands have to be fulfilled for the entire temperature range and over the full life time of the respective drive, the number of applicable adhesives will be strongly limited.

Another aspect regarding the tenacity of the bond is the choice of the magnet coating. Especially for sintered NdFeB permanent magnets, this coating is essential for preventing oxidation but regarding the adhesive mounting method, it needs to fulfill two additional demands. On the one hand, the thin layer of coating material must reliably stick to the magnet. A problem concerning this matter with the widely used nickel coatings has been reported and analyzed in [49]. During the coating process, hydrogen molecules can diffuse into the neodymium-rich border zone of the sintered material and form neodymium hydride. Due to the volume expansion caused by this reaction, micro-cracks occur in the sinter structure which can eventually lead to a breakaway of the coating including the surface sinter layer.

On the other hand, the surface of the coating needs to be suitable in terms of the mechanical strength of the adhesive connection.²

Even though modern adhesive systems can achieve remarkable strengths and reliability as, e.g., demonstrated in [97], this mounting method is not considered for high-speed rotors due to the described risks at high mechanical stress.

4.1.2. Buried magnets

This type of mounting typically requires the lowest mechanical stability from the permanent magnets, since the magnets are supported by the rotor iron in which they are fully embedded. The main stress component is, therefore, radial compressive stress or, if the steel in the pole area is deforming, bending stress. The mechanically critical region, however, is shifted to the saturation bars which now have to support the centrifugal forces of both the iron pole area and the permanent magnet. Even if an adhesive bonding is used in combination with a buried mounting form, the steel parts would have to be strong enough to support the full magnet-related centrifugal load in case of bond failure. The saturation bars are usually carried out as thin as possible in order to impede a magnetic short circuit. As a consequence, the demanded mechanical stability for this material needs to be increased dramatically at high speeds in order to prevent rotor failure.

This mounting concept was evaluated in [13] for a high-speed rotor (outer radius $r_o = 41.8$ mm, $\Omega_{max} = 48\,000$ rpm) and was found to be unsuitable due to the stress, exceeding the electric sheet material's yield strength by a factor of 4.

²No scientific reports have been found which compare the attainable bond quality when applying concrete adhesives to the different magnet coatings available. According to several statements from practical experience, however, the strongest adhesive bonds can be achieved with uncoated, passivated or epoxy coated magnets and the weakest ones with nickel or tin coatings.

4.1.3. Bandaging

A high strength material bandage can be used for surface mounted magnets instead of or in addition to the adhesive bond. This limits the tensile stress in the magnets and the maximum tolerable surface speed can be increased. Typically, high strength metals or fiber compound materials are applied for high-speed rotors as, e.g., demonstrated in [13] or [83]. This of course increases the magnetic air gap and lowers the resulting air gap flux density.

For non-segmented magnet rings, the above-mentioned stress situations according to the respective mounting method also apply but in addition, also tangential tensile stress occurs. In order to define a maximum tolerable speed for a selected rotor, these tangential and radial stress components need to be analyzed in detail.

4.2. Analytic stress calculation of the rotor

4.2.1. Unsupported rotor

Exact analytical solutions for the stress components in a cylinder due to radially symmetric forces as, e.g., the centrifugal forces exist in the literature [120]. For this calculation, the rotor is modeled as a flat solid or hollow cylinder magnet disposing of the outer diameter $r_{o,M}$, the inner diameter $r_{i,M}$ and the axial length l_M . The following assumptions are made:

- Only centrifugal forces acting exactly symmetrically are regarded.
- The cylindrical rotor is symmetric and consists of completely homogenous and isotropic material.
- The shear stress τ in the axial direction as described in [113] can be omitted due to the short axial rotor length. Together with the symmetry condition mentioned above, a flat stress distribution free of shear stress is assumed in the rotor. The general formulation of the stress tensor

$$S = \begin{bmatrix} \sigma_{xx} & \tau_{xy} & \tau_{xz} \\ \tau_{yx} & \sigma_{yy} & \tau_{yz} \\ \tau_{zx} & \tau_{zy} & \sigma_{zz} \end{bmatrix} \quad (4.4)$$

can always be transformed to a principal axis coordinate system where the tensor shows only entries in the main diagonal. Due to the above characteristics of the stress distribution, this coordinate system is the polar coordinate system with the radial and the tangential stress component σ_r and σ_φ .

- The rotor is operated in vacuum. Friction effects with surrounding media are not regarded.
- The rotor is operated at room temperature. Thermal expansion or contraction of any of the components is not considered.
- All changes in rotational speed happen sufficiently slow which means that acceleration effects can be neglected.

Under the cited conditions and at constant rotational speed, the radial and tangential stress components in the cylinder can be calculated as a function of the radius r as

$$\sigma_r(r) = C_0 + C_1 \frac{1}{r^2} - \frac{3 + \nu}{8} \rho \Omega^2 r^2 \quad (4.5)$$

$$\sigma_\varphi(r) = C_0 - C_1 \frac{1}{r^2} - \frac{1 + 3\nu}{8} \rho \Omega^2 r^2 \quad (4.6)$$

with the POISSON'S³ ration ν and the density ρ being constant. In order to eliminate the unknown variables C_0 and C_1 , additional constraints or boundary conditions need to be found. They can be derived from the fact that the radial stress components

$$\begin{aligned} \sigma_r(r_{i,M}) &= 0 \\ \sigma_r(r_{o,M}) &= 0 \end{aligned} \quad (4.7)$$

are zero at the inner and outer radius of the hollow cylinder. Using these conditions, the variables

$$C_0 = \frac{1}{8} \Omega^2 \rho (r_{o,M}^2 + r_{i,M}^2) (3 + \nu) \quad (4.8)$$

$$C_1 = -\frac{1}{8} \Omega^2 \rho r_{o,M}^2 r_{i,M}^2 (3 + \nu) \quad (4.9)$$

can be determined. This allows evaluating the stress distribution in the hollow cylinder as shown in Figure 4.1.

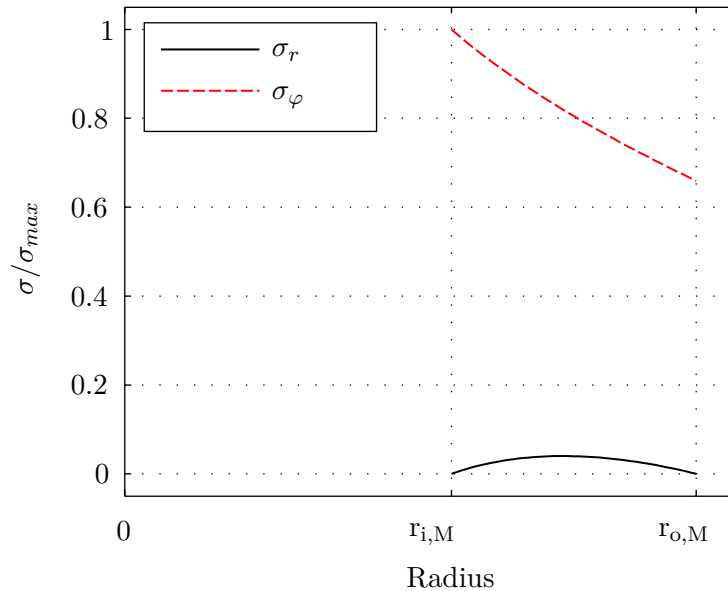


Figure 4.1.: Stress distribution in a magnet ring over the rotor radius

As stated in the additional conditions (4.7), the radial stress maximum is not located at the inner or outer edge but within the cylinder body. This is not the case for the tangential stress. Figure 4.1 clearly shows that the maximum value occurs at the inner surface of the hollow ring.

³SIMÉON DENIS POISSON, * 1781 in Pithiviers, France, † 1840 in Paris, France

4. Mechanical rotor stability

In order to calculate the tolerable rotor speed, the material's limit of elasticity is compared to a suitable equivalent stress value. One of these equivalent stress hypotheses being commonly used in steel construction and stress evaluation in other ductile media is the VON MISES⁴ hypothesis. For the flat, shear stress-free case it is defined as

$$\sigma_{Mises} = \sqrt{\sigma_r^2 + \sigma_\varphi^2 - \sigma_r \sigma_\varphi}. \quad (4.10)$$

For brittle structures such as powder metal or sintered materials, however, it does not yield reliable values [65]. The principal normal stress hypothesis is better suited for these kinds of material since it relies on the highest normal tensile stress component as a comparison value. In the present case, this is the tangential tensile stress component which will be used to formulate the simple constraint

$$\sigma_\varphi(\Omega_{max}) \cdot \zeta < R_{m,NdFeB} \quad (4.11)$$

where ζ stands for a safety coefficient yet to choose. For ductile media, the yield stress or elastic limit $R_{p0.2}$ is mostly used to characterize the mechanical strength of the material. For brittle materials, the definition of elasticity is difficult and, therefore, the tensile strength R_m is referred to as the main strength parameter.

The given stress constraint allows calculating the maximum rotor speed Ω_{max} after choosing the inner and outer radius as well as the material parameters and evaluating (4.6). A magnet ring with an outer and inner radius of $r_{o,M} = 15$ mm and $r_{i,M} = 10.5$ mm, respectively, can be spun to slightly above 60 000 rpm when a safety coefficient of $\zeta = 1.25$ is applied to the stress constraint (4.11). For further increasing the maximum rotor speed, additional measures have to be taken.

4.2.2. Bandaged rotor

As shown for the magnet ring in the last section, the stress distribution can also be calculated for a rotor bandage using (4.5) and (4.6) (index M is used for the magnet, B for the bandage). Together with the equations for the magnet, the resulting system of equations holds four entries and thus, four unknown parameters $C_{0,M}$, $C_{1,M}$, $C_{0,B}$ and $C_{1,B}$. Just as for the unsupported ring, suitable boundary conditions need to be found. Again, the radial stress component needs to be zero at the inner and outer rotor radius, yielding

$$\sigma_{r,M}(r_{i,M}) = 0 \quad (4.12)$$

$$\sigma_{r,B}(r_{o,B}) = 0. \quad (4.13)$$

Additionally, the radial stress components of the two bodies need to be equal at the contact layer, expressed as

$$\sigma_{r,M}(r_{o,M}) = \sigma_{r,B}(r_{i,B}). \quad (4.14)$$

A supplementary condition results from the forced contact between the magnet and the bandage, defined by the displacement

⁴RICHARD EDLER VON MISES, * 1883 in Lviv (Lemberg), Austria-Hungary, † 1953 in Boston, USA

$$u(r) = \frac{1}{E} \left((1 - \nu) C_0 r - (1 + \nu) C_1 \frac{1}{r} - \frac{1 - \nu^2}{8} \rho \Omega^2 r^3 \right) \quad (4.15)$$

of each body. This means that for a compressed body with a reduced radius compared to its resting state, the displacement is

$$u(r) < 0$$

whereas it is

$$u(r) > 0$$

for a stretched body with an enlarged radius. In addition to the already mentioned material parameters, knowledge of the YOUNG's modulus E is necessary for both components.

In order to guarantee contact between the resting magnet and its bandage, the displacement of the inner bandage radius needs to be superior to the displacement of the outer magnet radius. Generalizing this contact condition for all occurring speeds and load situations, the difference between the two displacements must additionally be constant, expressed by

$$u_B(r_{i,B}) - u_M(r_{o,M}) = \Delta_{r,MB} = \text{const.} \geq 0. \quad (4.16)$$

Being constant over the rotational speed, this difference $\Delta_{r,MB}$ is also the sum of the bandage undersize and the magnet oversize before mounting, better described as the value of the interference fit between the two bodies referred to the radius. In order to fulfill condition (4.16) also with rising loads, the bandage should have a higher YOUNG's modulus to density ratio, i.e., be stiffer than the magnet. Otherwise, the bandage would expand more than the magnet since the higher radius would cause higher centrifugal loads. For insufficiently prestressed assemblies, this will lead to a bandage lift-off which can be described by

$$u_B(r_{i,B}, \Omega_{limit}) - u_M(r_{o,M}, \Omega_{limit}) > \Delta_{r,MB} \quad (4.17)$$

with Ω_{limit} marking the critical speed where that lift-off occurs. Passing this speed will most likely lead to heavy damage or complete destruction of the rotor.

In order to push the critical speed beyond the targeted speed range, the interference fit needs to be designed. As mentioned before, the contact equation given in (4.16) can help since it relates the radius tolerances of bandage and magnet to the stress calculation and presents the fourth and last condition for solving the set of stress equations presented in the last section. Now (4.12), (4.13), (4.14) and (4.16) can be used to determine the four unknown parameters $C_{0,M}$, $C_{1,M}$, $C_{0,B}$ and $C_{1,B}$. Reinserting their values into (4.5) and (4.6) allows drawing the stress distributions in the magnet and its bandage for given material parameters, nominal dimensions, bandage gauge and interference fit. The curves plotted in Figure 4.2 and Figure 4.3 are related to the maximum stress σ_{max} in the unbandaged magnet ring scenario shown in Figure 4.1.

It has to be mentioned that the contact condition as modeled above is defined to be independent of the stress direction and, therefore, also allows tensile radial stress at the contact radius. This corresponds to a perfect adhesive bond between the two bodies and would mean that the inner body could hold back the outer body while expanding. Of course, this would also lead to higher stress values in the inner body as it is the case for the magnet ring in Figure 4.2 where the tangential stress at the inner surface is even

4. Mechanical rotor stability

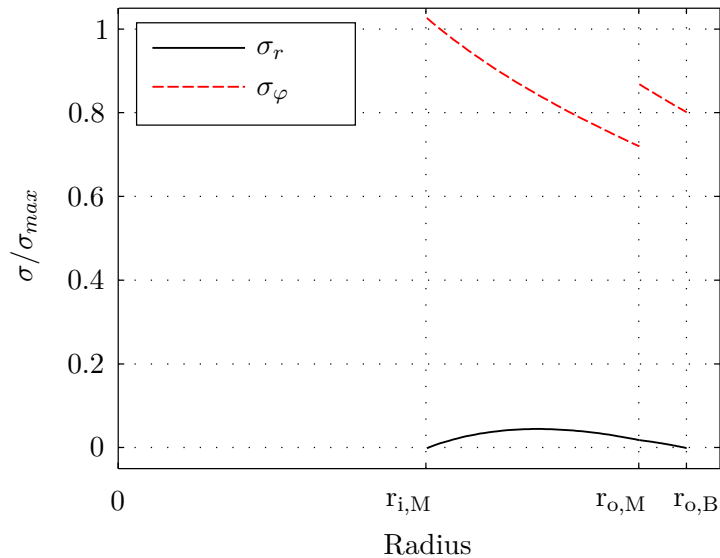


Figure 4.2.: Stress distribution in the magnet ring with a non-prestressed bandage relative to σ_{max} from Figure 4.1

higher than in the unbandaged rotor. In the chosen case, the bandage material is selected to have high density and low YOUNG's modulus in order to exhibit the described effect.

For modeling a pure force-fit between magnet and bandage which better represents the real conditions, the additional constraint

$$\sigma_{r,M}(r_{o,M}) = \sigma_{r,B}(r_{i,B}) < 0 \quad (4.18)$$

must be introduced, extending (4.14). It limits the radial stress at the boundary between magnet and bandage to compression stress only, excluding all situations where the bandage would lift-off without an adhesive bond.

Figure 4.2 further shows that the tangential stress in the magnet ring is higher than in the bandage which is not surprising given the non-prestressed fit of the two components. If the requirement (4.11) of maintaining the maximum normal stress component in the magnet below the yield strength of sintered NdFeB and the new radial stress condition (4.18) are to be fulfilled, the necessary press fit of the bandage can be determined analytically. The resulting stress distribution which is now shifted towards the bandage is shown in Figure 4.3. Since the bandage material is typically not brittle, the maximum stress values are compared to the material yield stress $R_{p0.2}$ according to the VON MISES criterion and need to comply to

$$\max(\sigma_{Mises,B}(\Omega_{max})) \cdot \zeta < R_{p0.2,B} . \quad (4.19)$$

for verifying the design.

As long as the tolerable material stress region of the bandage is not exceeded, the press fit value $\Delta_{r,MB}$ can be increased in order to reduce the maximum tensile stress arising in the magnet and thus, increase the maximum tolerable rotational speed of the rotor. Of course, the diameter difference needs to stay within a range where the bandage can actually be mounted onto the magnet. Heating up the bandage in order to benefit of the thermal expansion is possible, however, cooling off the magnet ring will not significantly make it shrink. This is due to the anomalous thermal expansion coefficients of magnetized NdFeB which were discovered in the early days of NdFeB research [98]. The material will

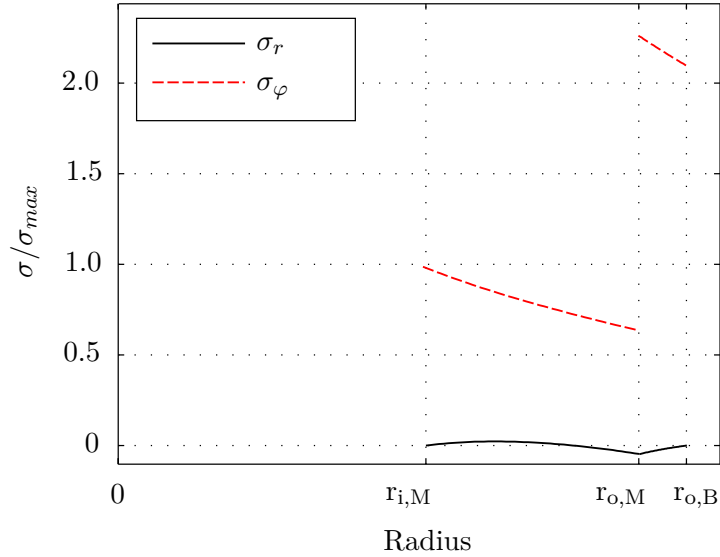


Figure 4.3.: Stress distribution in the magnet ring with a bandage prestressed by interference fit relative to σ_{max} from Figure 4.1.

expand in the direction of magnetization when heated but will behave oppositely for the direction perpendicular to it. Nevertheless, cooling the magnet during the fitting process of a heated bandage may be necessary in order to prevent demagnetization in the contact zones.

4.2.3. Mechanical effects of an inner back iron

An inner back iron or rotor yoke can be inserted into the diametrically magnetized permanent magnet ring in order to reduce the reluctance of the magnetic flux path. Since the back iron can be carried out as a hollow cylinder, the calculation of the mechanical stress previously used for the magnet and the bandage in Sections 4.2.1 and 4.2.2 can also be applied here.

Now, (4.5) and (4.6) for the radial and tangential stress as well as (4.15) for the displacement need to be written for all three bodies using the indices Y^5 , M and B for back iron, magnet and bandage, respectively. The set of equations is, therefore, again enlarged and now holds six unknown parameters $C_{0,Y}$, $C_{1,Y}$, $C_{0,M}$, $C_{1,M}$, $C_{0,B}$ and $C_{1,B}$, demanding six conditions for determining them. Just as for the unbandaged and bandaged rotor modeled above, four of these conditions can be extracted from the radial stress situations at the inner and outer boundary of the rotor as well as of the boundary surfaces of the connecting bodies. The definition of the interference fit, now not only for magnet and bandage but also for inner back iron and magnet provide the remaining conditions. The full set is expressed as

⁵The index Y is chosen for the analogy between the rotor back iron and the stator iron which is often called stator *yoke*.

4. Mechanical rotor stability

$$\begin{aligned}
 \sigma_{r,Y}(r_{i,Y}) &= 0 \\
 \sigma_{r,B}(r_{o,B}) &= 0 \\
 \sigma_{r,Y}(r_{o,Y}) &= \sigma_{r,M}(r_{i,M}) \\
 \sigma_{r,M}(r_{o,M}) &= \sigma_{r,B}(r_{i,B}) \\
 u_M(r_{i,M}) - u_Y(r_{o,Y}) &= \Delta_{r,YM} \\
 u_B(r_{i,B}) - u_M(r_{o,M}) &= \Delta_{r,MB}
 \end{aligned} \tag{4.20}$$

where $\Delta_{r,YM}$ and $\Delta_{r,MB}$ denote the mentioned interference fit values related to the radii of the concerned bodies. The press fits are necessary for a conservative analysis when no form-locking or elastic adhesive prevents the rotation and axial displacement of one element relative to the others. The contact condition, however, is separately extended by

$$\begin{aligned}
 \sigma_{r,Y}(r_{o,Y}) &= \sigma_{r,M}(r_{i,M}) < 0 \\
 \sigma_{r,M}(r_{o,M}) &= \sigma_{r,B}(r_{i,B}) < 0
 \end{aligned} \tag{4.21}$$

guaranteeing that only compressive stress and no tensile stress can be transmitted by the mechanical contact without a perfect adhesive bond.

Figure 4.4 shows the effect of the added back iron on the rotor stress distribution. In order to meet the magnet's material restrictions according to (4.11), the bandage must be pretensioned more than before, causing higher tensile stress values in its thin material.

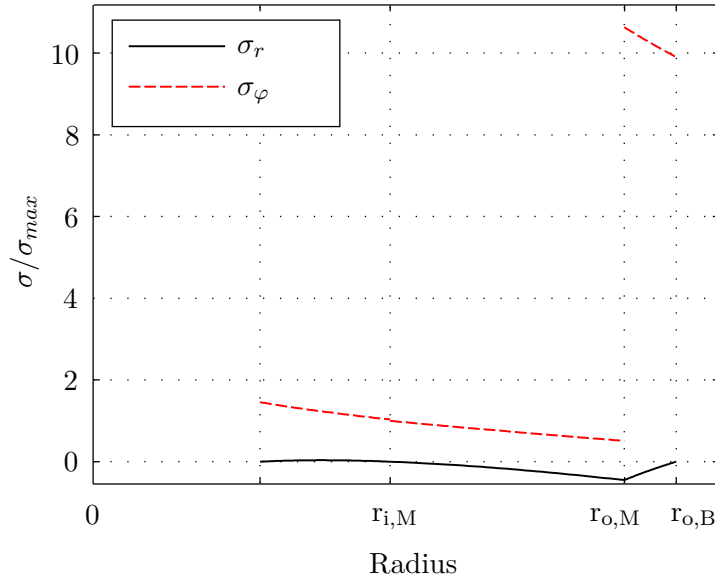


Figure 4.4.: Stress distribution in back iron, magnet ring and bandage. Stress values are related to the maximum stress in the unbandaged magnet ring shown in Figure 4.1.

4.2.4. Dimensioning of the interference fit

Unlike the fit of magnet ring and bandage which supports the brittle ring, the fit between the back iron and the magnet affects the stress levels in the latter in a very negative way.

Due to the oversized back iron, the magnet will be stretched, creating high tensile stress at this most critical point of the entire magnet. In order to prevent material failure, the press fit of the bandage further needs to be increased as the back iron diameter rises to create the interference fit. Even though the relationship between the two pressings depends strongly on the used materials, a qualitative analysis also shows the importance of the applied comparison stress criterion.

4.2.4.1. Von Mises - criterion

When the VON MISES stress value (4.10) multiplied by the safety coefficient is compared to the limiting tensile strength of the magnet material according to

$$\sigma_{Mises}(\Omega_{max}) \cdot \zeta < R_{m,NdFeB} \quad (4.22)$$

a region can be defined for the two interference fit values $\Delta_{r,YM}$ and $\Delta_{r,MB}$, shown in Figure 4.5. The abscissa gives the value of the inner, the ordinate the value of the outer matching, whereas both values are given relative to the maximum allowed value of $\Delta_{r,YM}$ which will be defined later in the following paragraph.

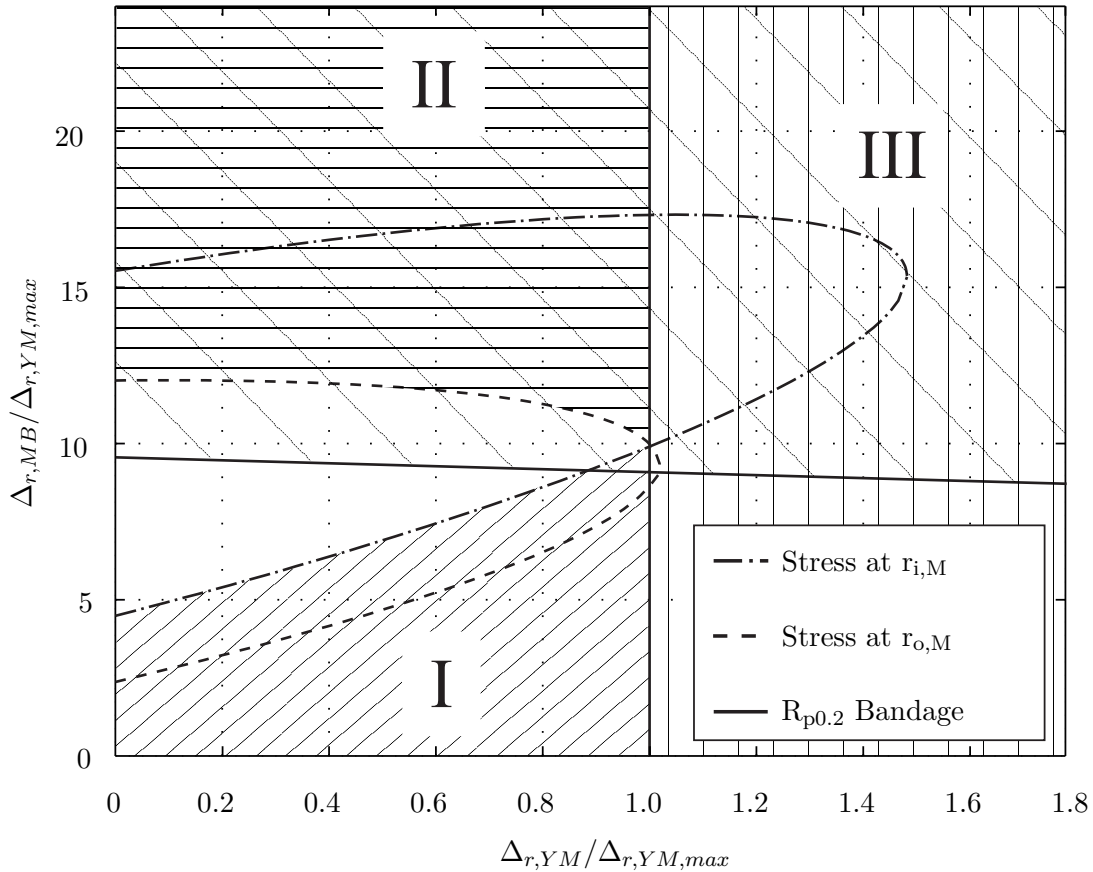


Figure 4.5.: Over-restricted region for the interference fit between back iron and magnet (abscissa) as well as magnet and bandage (ordinate) due to the stress estimation using the VON MISES stress hypothesis for the magnet and the bandage at a given target speed.

The dashed and dash-dotted curves in Figure 4.5 describe the sum of combinations of interference fits where the stress limit of the magnet is reached, once for the magnet's

inner surface, once for the outer one. In the area below the respective curve, the tensile stress is above the material strength, in the area above, the compression stress exceeds the limit. Combining the two curves, an area I (fine diagonal hatching) can be defined where the bandage press fit is not yet strong enough to sufficiently confine the tangential tensile stress at the inner magnet surface. Area II (horizontal hatching) describes the region where the bandage press fit is too strong, creating unacceptably high radial compression stress at the outer magnet surface according to (4.22). The intersection of the limiting curves of area I and II marks the point of the maximum value $\Delta_{r,YM,max}$ for the back iron interference fit. Above this value for $\Delta_{r,YM}$, no press fit combination can be found which would satisfy the stress limitations of the magnet for both, the radial compression stress as well as the tangential tensile stress. This area is marked as III (vertical hatching).

Up to now, only the constraints for the stress within the magnet have been regarded. The question which interference fit combination can be realized, however, also depends on the admissible stress levels of the bandage. Figure 4.5 therefore also shows the area where this stress level is surpassed (coarse diagonal hatching).

The described effects and the resulting constraints on the tolerable fit range of the respective components leave a blank area where all constraints are fulfilled. The presented graph describes a qualitative approach but it becomes quite clear that only a very small area is found to be admissible.

4.2.4.2. Principal normal stress hypothesis

Taking a closer look at the VON MISES stress hypothesis which was used to specify the borders and areas in Figure 4.5 reveals its unfitness for brittle materials. For the shear stress-free case and $sgn(\sigma_r) = sgn(\sigma_\varphi)$, (4.10) yields

$$\sigma_{Mises}(\sigma_r, \sigma_\varphi) = \sigma_{Mises}(-\sigma_r, -\sigma_\varphi) \quad (4.23)$$

showing that negative and positive stress values are treated equally. This equality does not correctly reflect the true strength of brittle materials which typically demonstrate low resistance against tensile loads but high durability when subjected to compressive loads. The given compressive strength exceeds the tensile strength by a factor of 10 for sintered NdFeB magnets. Thus, the given stress limits of Figure 4.5 unnecessarily constrain the interference fit region due to compression stresses.

As described previously in Section 4.2.1, the principal normal stress hypothesis provides a more adequate model. Figure 4.6 shows the tolerable fit regions for this stress hypothesis with the interference fit values again related to the maximum back iron fit $\Delta_{r,YM,max}$ from Figure 4.5 in order to allow a direct comparison. Areas I and II have the same meaning as before with the main difference that the bandage fit is now allowed to be much stronger, based on the true compressive strength of the sintered magnet material. For showing the characteristics properly, the ordinate was scale-shifted in the upper part of the diagram. Also, there is no area III visible in the plot since the intersection of the tensile and compressive stress borders is not within the given scope.

However, as shown in the previous section, the main limit when increasing the bandage press fit is the yield strength of its material. The coarse hatching again limits the allowed area, leaving a region similar to the one found when using the VON MISES comparison stress hypothesis.

The actually necessary fit values can now be calculated for a certain target speed by solving the equation system consisting of the stress limitation for the inner magnet radius

4.3. Comparison of the analytical model with a finite element (FE) simulation

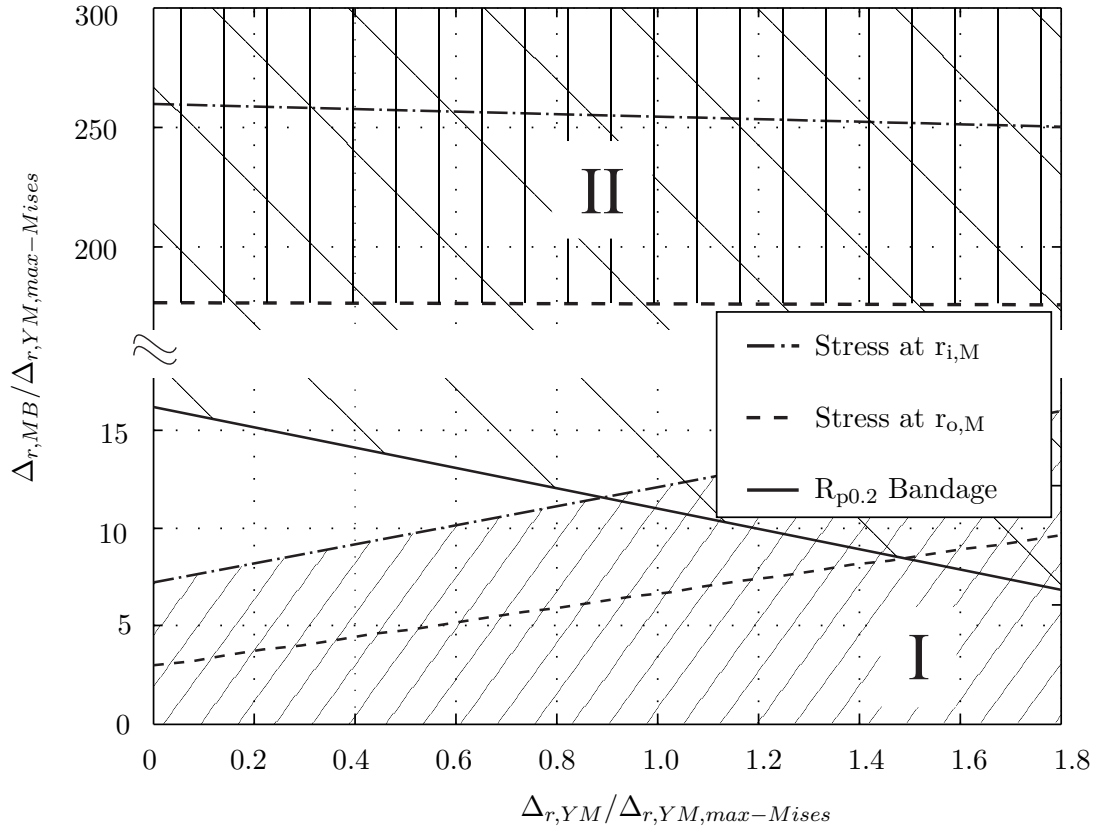


Figure 4.6.: Correctly restricted region for the normalized interference fit between back iron and magnet (abscissa) as well as magnet and bandage (ordinate) due to the stress estimation using the principal normal stress hypothesis for the magnet and the bandage.

according to (4.11) and a chosen radial tension requirement, fulfilling (4.21) for $\Delta_{r,YM}$ and $\Delta_{r,MB}$.

4.3. Comparison of the analytical model with a finite element (FE) simulation

The analytical model of the stresses in the spinning rotor as described in the above sections is based on the stress distribution in flat hollow cylinders. An FE simulation was conducted with *Ansys®Workbench 11.0* for a discrete rotor setup in order to allow a comparison. The applied dimensions and other simulation parameters are given in Table 4.2 for the back iron made of *9SMnPb36* standard machining steel, a sintered *N42 - NdFeB* magnet ring and a bandage made of magnetically non-conductive *T200* hot work steel. The simulations were carried out at 120 000 rpm in order to investigate a speed region not only up to the target nominal speed of 100 000 rpm.

4.3.1. Simulation setup

In order to come close to real life conditions, not only the rotor dimensions but also the connection conditions between the respective bodies need to be set correctly. The connection between magnet ring and bandage is not critical in this sense as a consequence

4. Mechanical rotor stability

<i>Nominal dimension or material parameter</i>	<i>Variable</i>	<i>Value</i>
Inner radius back iron	$r_{i,Y}$	7.5 mm
Outer radius back iron = inner radius magnet	$r_{o,Y} = r_{i,M}$	10.5 mm
Outer radius magnet = inner radius bandage	$r_{o,M} = r_{i,B}$	15 mm
Outer radius bandage	$r_{o,B}$	16 mm
Axial rotor length	l_R	10 mm
Density back iron	ρ_Y	7810 kg/m ³
Density magnet	ρ_M	7400 kg/m ³
Density bandage	ρ_B	7950 kg/m ³
YOUNG's modulus back iron	E_Y	210 GPa
YOUNG's modulus magnet	E_M	151 GPa
YOUNG's modulus bandage	E_B	201 GPa
Yield strength back iron	$R_{p0.2,Y}$	260 - 440 MPa
Tensile strength magnet	$R_{m,M}$	70 - 80 MPa
Yield strength bandage	$R_{p0.2,B}$	650 - 700 MPa
POISSON's ratio back iron	ν_Y	0.28
POISSON's ratio magnet	ν_M	0.20
POISSON's ratio bandage	ν_B	0.25
Nominal speed	Ω_N	12 566 rad/s $\hat{=} 120\,000$ rpm

Table 4.2.: Data of the rotor used for a comparison between analytical calculation and FE simulation

of the interference fit and the YOUNG's modulus to density ratio of the magnet being inferior to that of the bandage. As the rotor is subjected to centrifugal forces, contact is therefore maintained and the radial stress is limited to compression stress, only. For the second boundary, this is not automatically provided which means that the limitation of tensile stress transmission must be introduced in the FE simulation setup in order to fulfill condition (4.21).

4.3.2. Validation of the method

Figure 4.7 shows the comparison in the results of analytical calculation and FE simulation for the NdFeB ring magnet with a 1 mm T200 hot work steel bandage at 120 000 rpm. The maximum tangential stress value in the magnet can only be confined to below the allowed stress level considering the safety factor of $\zeta = 1.25$ with a bandage press fit of about 72 μm . This interference value, however, already creates intolerably high VON MISES stress in the bandage. The good match between the two calculation methods is due to

4.3. Comparison of the analytical model with a finite element (FE) simulation

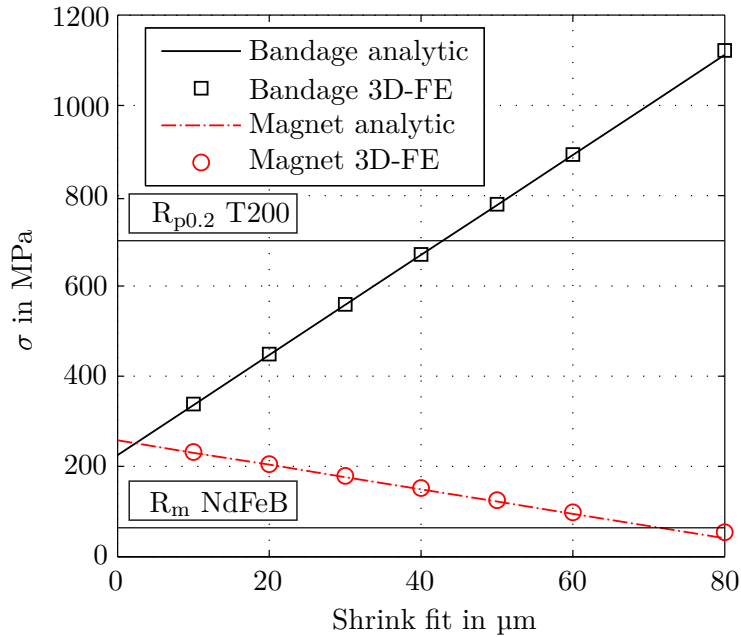


Figure 4.7.: Comparison of analytically and numerically obtained stress maxima in magnet and bandage, respectively, for a rotor with a 1mm T200 steel bandage at 120 000 rpm. The VON MISES stress is shown for the bandage, the maximum tangential stress for the permanent magnet.

the ideal geometries and allows an extension of the calculation in three ways. First, the design of similar rotors with a cylindrical, homogenous structure can rely on the analytic calculation for determining the overall dimensions and the interference fit values. Second, the numerical model can be used for the estimation of the flexible body modes in order to provide certainty to operate in the sub-critical region. Third, the stress distribution for complex but yet similar geometries such as segmented cylinder rings can be evaluated using the FE simulation. In the following, this method shall be applied for a changed construction strategy.

4.3.3. Stress simulation result with ring structure

The result of the FE simulation for the full ring rotor, depicted in Figure 4.8, shows that the stress maximum is located at the inner radius of the respective body. The tangential and VON MISES stress distributions have been evaluated for the magnet ring and the rotor bandage, respectively. Two different shrink fit configurations have been considered, showing that the maximum stress levels given in Table 4.2 are exceeded for the magnet in the first case shown in Figure 4.8a and for the rotor bandage in the second case, shown in Figure 4.8b.

4.3.4. Flexible body modes

The numerical simulation set up and explained earlier was also used to obtain the flexible body modes of the closed ring structure. This knowledge is important in order to assure that the operation range does not include the crossing of any of these frequencies. Figure 4.9 shows the calculated resonance shapes with the respective frequency values for a

4. Mechanical rotor stability

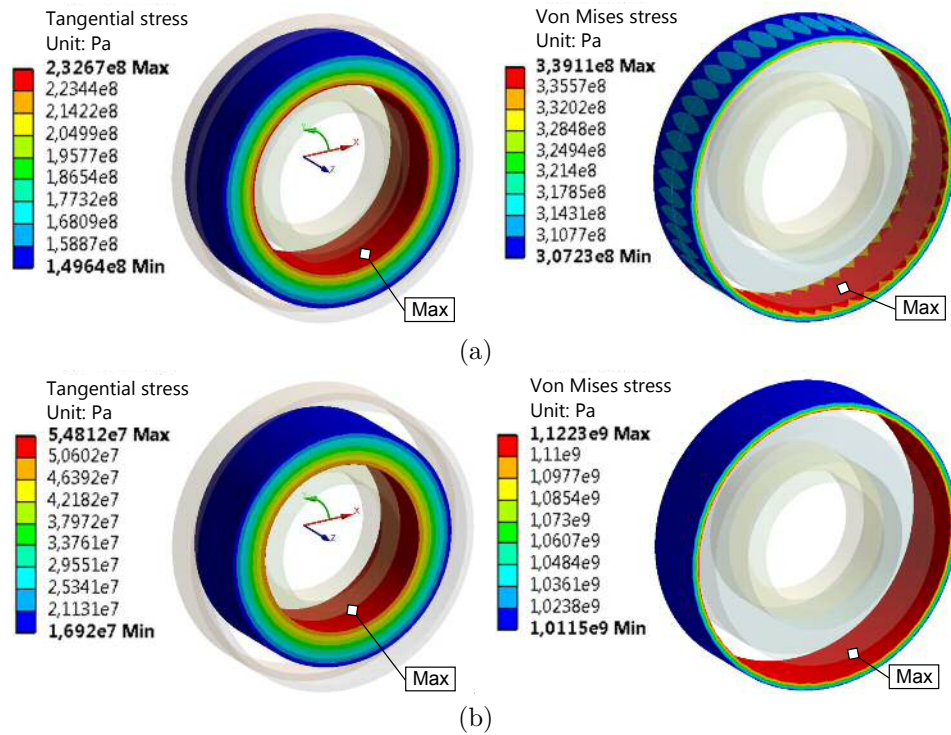


Figure 4.8.: Stress distribution in full magnet (left) and bandage (right) for (a) 10 μm and (b) 80 μm shrink fit

rotor with steel bandage. It can be seen that these frequencies are well out of the range of the rotational frequency.

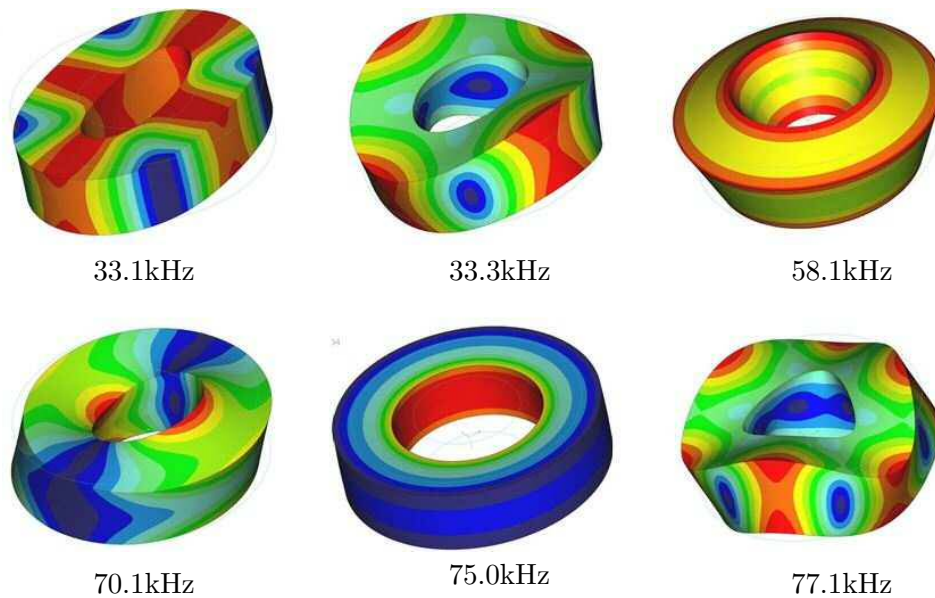


Figure 4.9.: Shapes of the first six flexible body modes from top left to bottom right.

4.4. Rotor segmentation

As Figure 4.1 already showed clearly, the tangential tensile stress at the inner surface of the magnet is the critical stress component threatening its mechanical stability. Figure 4.7 approves of the idea of applying a bandage around the magnet ring but also of the problem that the necessary pretensioning for high rotational speeds drives the bandage material into its stress limitation.

In an extended approach, a mechanical failure of the permanent magnet may be accepted on purpose since this does not dramatically alter its magnetic properties. For such a rotor, the bandage would require only weak pretension thus reducing the stress peaks in the steel and changing the stress scenario completely. Of course, a sudden cracking of the magnet during rotation causes highly disturbing unbalance forces due to both the mechanical as well as the magnetic unbalance. Furthermore, a cracked NdFeB magnet is no longer protected against corrosion at the cracked surface leading to long term instability of all its major characteristics. For the new geometry possibly caused by such a failure, the analytical methods no longer apply. Therefore, all following stress values originate from the FE simulation as mentioned above.

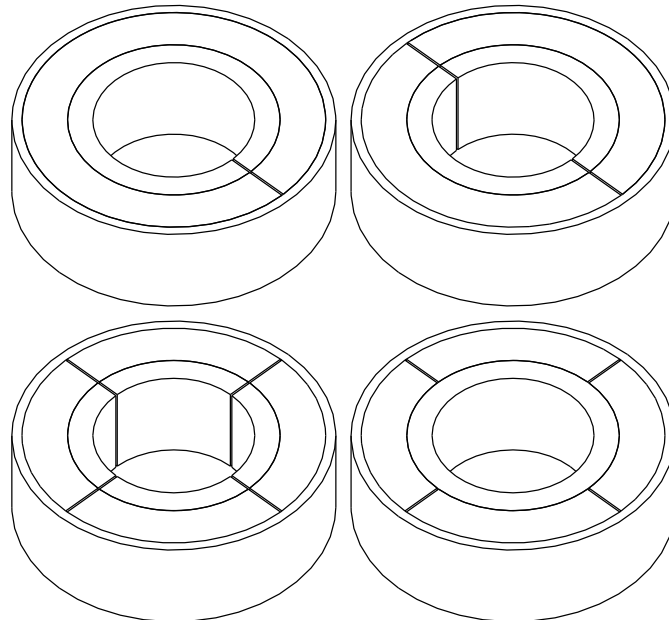


Figure 4.10.: Cutting strategies for reducing the tangential stress

4.4.1. Single-sided cut

The above mentioned problems may be eased with a preliminary cut through the magnet. This fine cut as shown in Figure 4.10 on the top left can be carried out at the middle position of the magnetic pole, thus creating minimum changes in the magnetic rotor field. Additionally, the thin slitting can be sealed which again provides protection against corrosion. In order to avoid losing contact between the two inner bodies, the back iron ring can be cut just like the magnet so it will also expand and be supported by the magnet.

Of course, a one-sided cut through a hollow cylinder considerably increases the stress values in the zones opposite of the slit and also adds a large mechanical unbalance to the system. Therefore, this concept was not further followed.

4. Mechanical rotor stability

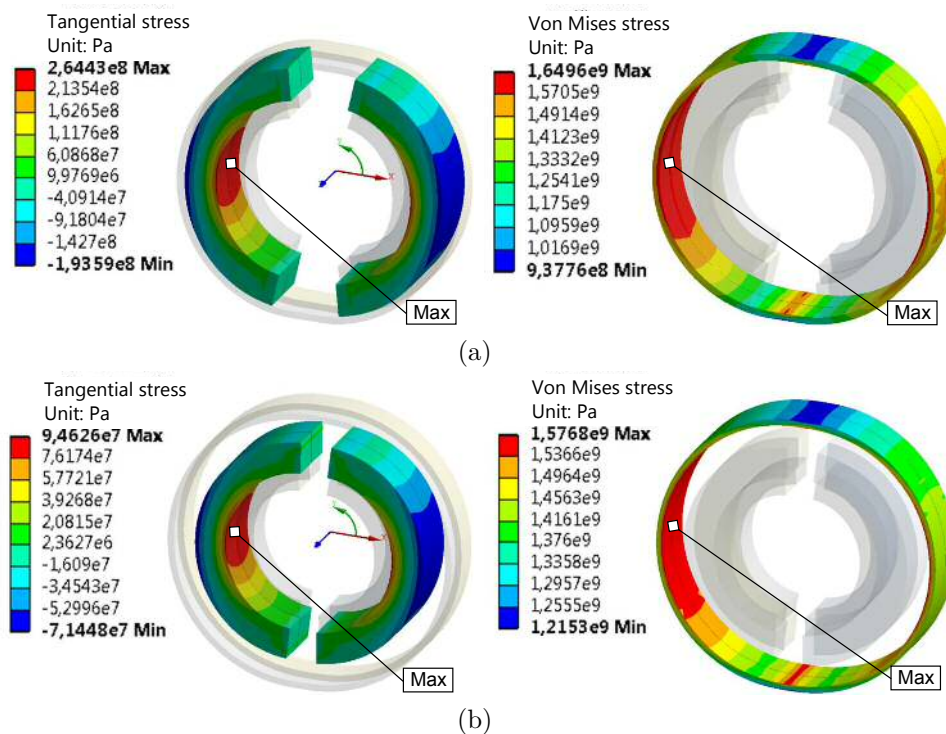


Figure 4.11.: Stress distribution in halved magnet and bandage for (a) 10 μm and (b) 80 μm shrink fit

4.4.2. Double-sided cut

If the magnet ring and the inner back iron are cut in two halves as shown in Figure 4.10 on the top right as well as in Figure 4.11, no additional unbalance is created. The zone of the increased stress values is shifted to the two areas in between the two cuts as the ring halves tend to open up when subjected to centrifugal forces. Even though the remaining zones of the magnet are relieved of most of the tangential stress, the mentioned area of increased tangential tensile stress greatly surpasses the values of the uncut version.

Contrary to the previous assumption that the bandage would be greatly relieved of the tangential stress since smaller interference fit values may be sufficient, the FE simulation reveals increased stresses. In addition to the area supporting the center of the segments, the area where the cut has been effectuated is concerned most. This increase due to the sharp edges quenching the bandage is known from bandages over surface mounted magnet segments in conventional motors. Still, especially with low interference fits (Figure 4.11a), the stress levels are astonishingly high. The reason why the maximum stress is lower with a higher press fit (Figure 4.11b) seems to be the smaller shift of the spreading segments and, therefore, bigger bandage surface in contact with the magnet.

4.4.3. Four-sided cut

The next variation to be regarded is a rotor cut into four segments. From a magnetic point of view, two of the sections may be neglected when they are placed exactly in the magnetic poles. The two additional sections, however, then need to be placed in the zone of the maximum flux and may no longer be generally neglected. Depending on the width of the cut as well as on the ratio of this additional air gap to the main air gap, the consequence on the flux distribution will vary making individual simulation of the

respective rotor design indispensable.

In Figure 4.12, the expected stress relief in the magnet can now be seen clearly as the maximum tangential stress value lies at approximately 10 % of both, the rotor with the double-sided cut and the full ring rotor. However, the bandage again experiences a severe increase of stress at the zones of the magnet sections, showing that this rotor modification is also not suitable for improving the overall mechanical rotor stability.

In a last attempt, the magnet is cut as before in four segments but the back iron left uncut. Figures 4.12c and 4.12d show that the stress in the magnets does not change significantly relative to Figures 4.12a and 4.12b but that the stress in the bandage is reduced.

4. Mechanical rotor stability

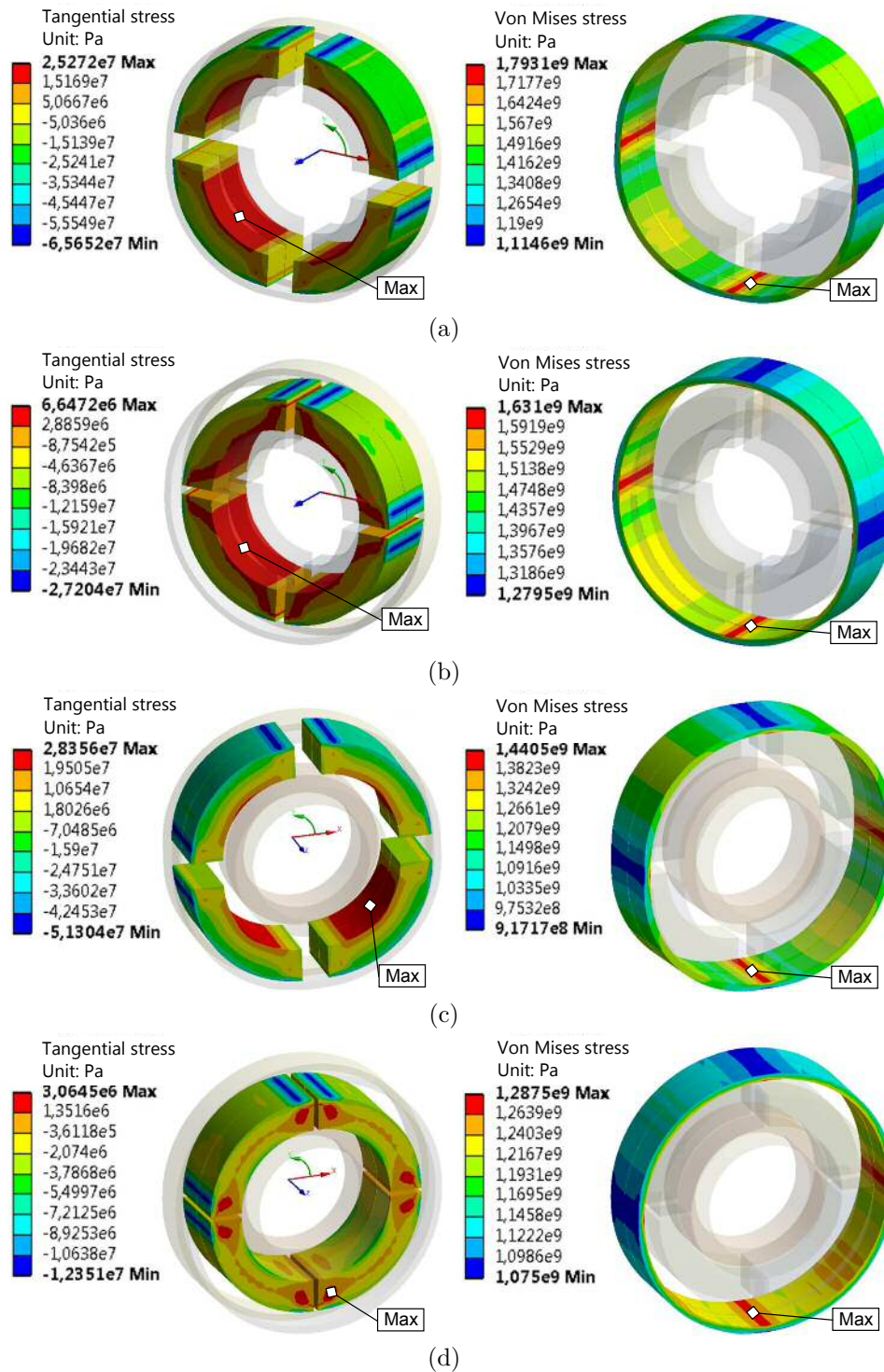


Figure 4.12.: Stress distribution in fourfold cut back iron, magnet and bandage for (a) 10 μm and (b) 80 μm shrink fit as well as with uncut back iron for (c) 10 μm and (d) 80 μm shrink fit

4.5. Conclusion

Before drawing a general conclusion, it has to be mentioned that for the segmented magnet versions, the stress in the bandage at the magnet cuts does depend on the influence of the sharp segment edges. This micro-geometry might be different in the real rotor and will influence the actual peak stress values. However, this does not significantly alter the maximum value since the stress in the region between the cuts is only a little less than in those spots. Apart from this effect, the FE simulation results allow the following conclusions:

- A reduction of the tangential stress as the main stress component in the magnet cylinder can be achieved by cutting it into four segments.
- Cutting the magnet into half is not helpful for the given setup since the new stress components due to the bending of the segments reach values similar to or even above the stress in the uncut cylinder.
- Not segmenting the back iron reduces tensions in the bandage. As with the uncut version, the pretensioning of the bandage needs to provide sufficient radial pressure in order to prevent axial movement of the rotor parts relative to each other.
- The maximum stress value in the bandage is not reduced by segmenting parts of the rotor. The idea that less pretension of the bandage is necessary in order to constrain the stress in the magnet is true, the conclusion that this would also reduce the peak stress in the bandage is not (due to the stress peaks where the magnet is cut).
- The best solution is provided by the uncut magnet assembly for which also analytic stress computation can be used. For guaranteeing the mechanic integrity, adaptations in the rotor design are necessary. The following sets of design changes each constrain the stresses at 120 000 rpm to the tolerable limits:
 - an increase of the bandage gauge from 1 mm to 2.4 mm *OR*
 - a reduction of the magnet outer radius from 15 mm to 14.5 mm, a reduction of the magnet height from 4.5 mm to 3 mm, an unmodified back iron height and a bandage gauge of 1.5 mm instead of 1 mm *OR*
 - a reduction of the magnet outer radius from 15 mm to 14 mm, a reduction of the magnet height from 4.5 mm to 4 mm, a reduction of the back iron height from 2.5 mm to 2 mm with a bandage gauge increased from 1 mm to 1.4 mm.
- As shown in (4.1) at the beginning of this chapter, the centrifugal force depends quadratically on the rotational speed. Therefore, more severe changes in the rotor dimensions would be necessary for a comparable system running at 200 000 rpm. The following possible sets of design changes shall give an idea of how dramatically the dimensions would need to be adapted:
 - a reduction of the magnet outer radius from 15 mm to 9.8 mm, a reduction of the magnet height from 4.5 mm to 2 mm, an unmodified back iron height and a bandage gauge of 2.4 mm instead of 1 mm *OR*
 - a reduction of the magnet outer radius from 15 mm to 11 mm, a reduction of the magnet height from 4.5 mm to 3 mm, an unmodified back iron height

4. Mechanical rotor stability

and the use of a Grade-5, *Ti6Al4V* titanium bandage with a gauge of 1.5 mm instead of 1 mm *OR*

- a reduction of the magnet outer radius from 15 mm to 12 mm, a reduction of the magnet height from 4.5 mm to 3.75 mm, an unmodified back iron height and the use of a Grade-5, *Ti6Al4V* titanium bandage with a gauge of 1.4 mm instead of 1 mm when using light-weight *SmFeN* permanent magnet material⁶ *OR*
- leave everything as it is and use standard, commercially available ultra-modulus strength (UMS) carbon fiber material for the bandage⁷.

⁶This only takes the lower density of *SmFeN* into account - the effects due to the lower remanence values of only up to $B_{max,SmFeN} = 0.81T$ are not considered.

⁷The extremely high tensile strength of more than 4500 MPa and Young's modulus values of more than 390 GPa theoretically allow using identical rotor dimensions as for the preceding 100 000 rpm motor. The main obstacle of such a solution, however, is the mounting procedure of such a bandage - prestressed winding of the fiber cannot achieve the demanded shrink fit values and simple pressing of the magnet into the bandage can easily destroy or weaken the bandage. Additionally, carbon fiber composites exhibit very poor friction coefficients and may melt locally when grinding over another surface.

5. Prototypes

Contents

5.1. Motivation	98
5.2. Bearingless machine	98
5.2.1. Component description	98
5.2.2. Prototype data	103
5.3. Control	104
5.3.1. Power electronics unit	104
5.3.2. Control software	104
5.4. Prototype test results	109
5.4.1. Control verification tests	109
5.4.2. Turbine and compressor tests	111
5.4.3. High-speed test	113
5.5. Conclusion	116

In the course of this work, several prototypes of two principle designs have been designed, constructed, and tested. This chapter gives a detailed description of the bearingless machine with all of its subcomponents and the dimensions of the latest prototypes realized. Furthermore, the power electronics circuit is specified and the control software is described. Eventually, the practical experience and test results of the prototypes are given at the end of the chapter.

5.1. Motivation

Before going straight to a system description, let's take a look at the question of why a prototype should be built in the first place. Many engineering companies tend to push computational methods to the point where an actual prototype needs to be built. This is a reasonable approach for gradual development and definitely a sound procedure for many producing industries which need to implement adaptations and modifications to a proven concept. This trend is recognized in the term *lot size one* which was coined for expressing ultimate flexibility in production through perfect simulation in order to avoid bad parts even without experimenting with production settings.

In basic research, however, the deep insights gained from a prototype are invaluable. Validation of newly deployed materials, effects of disturbances based on sensor noise or aerodynamic and rotordynamic behavior are just some of the lessons which can be intuitively learnt from a prototype but which are very difficult to grasp through simulation. Last but not least, actual handling of a prototype tends to inspire human creativity for further development and problem solution more than simulation models.

5.2. Bearingless machine

The most demanding design process concerns the bearingless machine as there were no examples of high-speed bearingless drives available in the literature before the start of this work. Of course, high-speed machines with conventional bearings give important clues on how to best design such a drive.

5.2.1. Component description

5.2.1.1. Stator core

To constrain the temperature inside the stator of a compact high-speed drive, the use of low-loss material is crucial. For this reason, the first prototypes were built using Megaperm®40L NiFe alloy sheets with a sheet thickness of 0.2 mm. This material combines very low hysteresis losses and relatively low eddy current losses with considerable permeability. For the prototype core which has the simple shape of a hollow cylinder, however, the manufacturing process consists of annealing, stack bonding and wire-cut EDM. Compared to the relatively straight forward milling process for an SMC prototype core, this is a rather time-consuming and expensive process. The later prototypes were, therefore, made of Somaloy®500 SMC. Further details on the loss characteristics can be found in Chapter 6 and a comparison of these two cores is given in [71].

5.2.1.2. Windings

Due to the chosen slotless stator topology, the permanent magnetic rotor field directly permeates the windings which fill the space between rotor and stator core. Therefore, it is necessary to use wires with thin, electrically insulated, strands in order to reduce the eddy current losses inside the conductors due to the changing magnetic rotor field. The chosen wire bundle dimensions, the applied number of winding turns and related data are given in Table 5.1. For insulation purposes, the coils are not directly wound onto the stator but, instead, on a coil carrier made from 0.5 mm thick rapid prototyping polyamide. In order to increase the heat transfer from stator with its winding system, the entire

stator is poured in epoxy resin once inserted into the aluminum housing. The resin must be chosen carefully since some very interesting products with high thermal conductivity contain ferromagnetic particles which could cause high losses or electric insulation failure. By inserting a negative form before the pouring, a smooth epoxy surface defines the inner stator air gap border.

Symbol	Parameter	5pd Value	6ps Value
m	Phase number	5	6
N	Winding turns	13	13
n_s	Number of strands per bundle	225	315
d_{strand}	Diameter of litz strand	0.071 mm	0.071 mm
d_{bundle}	Diameter of wire bundle	0.5 mm	0.5 mm
A_{Wire}	Copper section of wire bundle	0.91 mm ²	1.27 mm ²
A_{Cu}	Copper section per coil	11.81 mm ²	16.54 mm ²
R	Phase resistance	33 mΩ	16 mΩ
L	Phase inductance	19.5 μH	21 μH

Table 5.1.: Data of applied windings

5.2.1.3. Touchdown bearing

Two different materials for the touchdown bearing were applied. First, the high-performance plastic poly-ether-ether-ketone, better known as PEEK was used. While the material shows excellent behavior in practically all mechanical, chemical and thermal domains, the friction coefficient with steel is still higher by a factor of 4 to 5 ([68]) than that of polytetrafluoroethylene (PTFE). This is the reason why, despite its inferiority concerning mechanical resistance, creeping characteristic and thermal shape retention, PTFE is preferred. As shown in Figure 5.2, the touchdown bearing is realized as a thin sleeve, however, the mounting position for the two prototypes was quite different. In the 5pd prototype, the bearing is placed between the rotor and the stator coils. While mechanically separating the functionality of touchdown bearing and radial position sensors, this brings several difficulties:

- The width of the touchdown bearing enlarges the magnetic air gap without creating more coil space.
- Located directly at the stator windings, the ambient temperature for the touchdown bearing during normal operation is higher than in any other point of the drive. In the touchdown case, the energy dissipated in the touchdown bearing further heats the windings.
- The stator winding needs to be poured with epoxy or a similar electrically non-conductive material in order to provide an even, homogenous surface at the inner

5. Prototypes

radius of the stator winding. However, even with this pouring, the individual, very delicate strands of the litz wire are directly behind the touchdown bearing. In case of a touchdown event at high speeds, there is a considerable mechanical impact on these strands.

- The fact that the friction partner of the touchdown bearing is the rotor bandage limits the material choice for that part to reasonably good sliding partners such as steels, or smooth surface ceramics. The use of a carbon fiber bandage within an epoxy compound is practically excluded since the matrix material melts easily due to the friction heat generated in a touchdown event and the risk of carbon fiber failure due to the resulting grinding motion is high.
- With a contact point located at the outer rotor radius, the differential speed between bandage and touchdown bearing is at a maximum of 167.55 m/s for a touchdown event at $100\,000 \text{ rpm}$. At a maximum deformation for small loads, the expected deformation is $<0.5\%$ according to [28] which yields an approximate contact surface of 100 mm^2 between rotor and touchdown bearing. This means that the actual pressure for a radial passive stiffness of 8.37 N/mm is around 42 kPa . Depending on the applied touchdown bearing material, the reduced contact pressure at the price of higher contact speeds may be counterproductive since, e.g., for PTFE, friction coefficients become lower at increasing loads [28].

In the 6ps prototype, a different strategy was chosen in order to allow the use of a carbon fiber bandage. The touchdown bearing is located at the inner rotor radius which entails the following changes:

- The drive air gap is only slightly bigger than the mechanical air gap between the touchdown bearing and the inner rotor surface in order to avoid contact of bandage and coils.
- The windings do not come in direct or indirect contact with the rotor while it is running out. This is beneficial both from a thermal and a mechanical perspective.
- Due to the smaller radius of the touchdown bearing, the surface speed at a touchdown event at $100\,000 \text{ rpm}$ is reduced to 69.12 m/s . At the same time, the contact surface is reduced to 35 mm^2 under the same premise of deformation as applied above. With a radial passive stiffness of 7.56 N/mm , this results in an increased contact pressure of 108 kPa . As mentioned above, the friction coefficient of PTFE *for low loads* become lower at increasing loads [28] which, together with the reduced contact speed, makes the inner touchdown bearing approach preferable from a life-time and friction point of view.
- The main disadvantage of this configuration is the mechanical coupling of the position sensor and the touchdown bearing, both being positioned within the inner rotor diameter. This means that a very stable mechanic pin needs to be provided.

5.2.1.4. Rotor components

As shown in Figure 5.2, the rotor consists of an inner aluminum sensor target, an inner back iron made from St37 steel, a diametrically magnetized N48SH NdFeB ring and a bandage. Different bandage materials have been investigated as described in Chapter 4. That

chapter also describes the mounting of the rotor components since the high centrifugal forces demand special attention to that point.

5.2.1.5. Sensors

Rotor angle detection The prototypes use a set of analogue HALL¹ sensors for the detection of the rotor angle. This is achieved by placing five sensors below the stator core, with their sensitive HALL surfaces facing the rotational axis. This means that, actually, only the stray field of the permanent magnet is detected but due to the high sensitivity of the sensors, the obtained signal is clear. Additionally, the special placement causes the sensors to be insensitive to the magnetic fields produced by the currents in the toroid windings as their conductors are perpendicular to the sensing plane. Figure 5.2 shows that, in the 5pd design, the sensors have been placed by inserting them into small rectangular pockets inside a plastic sensor carrier. For the 6ps prototype, they were mounted freely on the sensor PCB.

Radial displacement sensor By having sensors based on the eddy current principle monitor the distance to the aluminum target ring on the inner rotor surface, the radial rotor displacement can be measured without influence from the drive currents. This is a significant advantage over most bearingless drives presented in the literature which typically feature eddy current sensors placed between the stator coils on the outside of the rotor. However, this advantage is bought dearly by the fact that the rotor is only accessible from one axial side and that, in the case of the 6ps prototype, the sensors are mechanically coupled to the touchdown bearing as mentioned in Section 5.2.1.3. In order to provide the necessary mechanic rigidity, the sensor carrier was manufactured out of magnetically non-conductive steel for the 6ps design. Nevertheless, the placement on the inside of the rotor has shown to provide acceptable signals.

The research on eddy current displacement sensors is intense ([61], [84], [122], [93]) however, their detailed design and signal analysis is, to put it mildly, treated rather confidentially. In the course of this work, three sensor principles have been adapted for use in the prototype drives but as there was no scientific research connected to this process, the topic will not be embraced further.

5.2.1.6. Housing and in-machine PCBs

In order to provide good cooling qualities, the housing of the stator is milled out of a solid aluminum block. In combination with the epoxy pouring mentioned in Section 5.2.1.2, the housing construction was sufficient for the tests conducted with the prototype, yet it leaves the possibility of milling additional cooling fins if higher output power and, thus, higher losses are expected.

Below the stator core with the toroid windings, the housing further holds the PCB for connecting the coil endings to the connector on the side of the housing. Additionally, the sensor signal treatment components which need to be kept close to the sensor coils in order to ensure sufficient signal quality are placed on a PCB, mounted in the housing below the stator.

¹EDWIN HALL, * 1855 in Gorham, Maine, USA, † 1938 in Cambridge, Massachusetts, USA

5. Prototypes

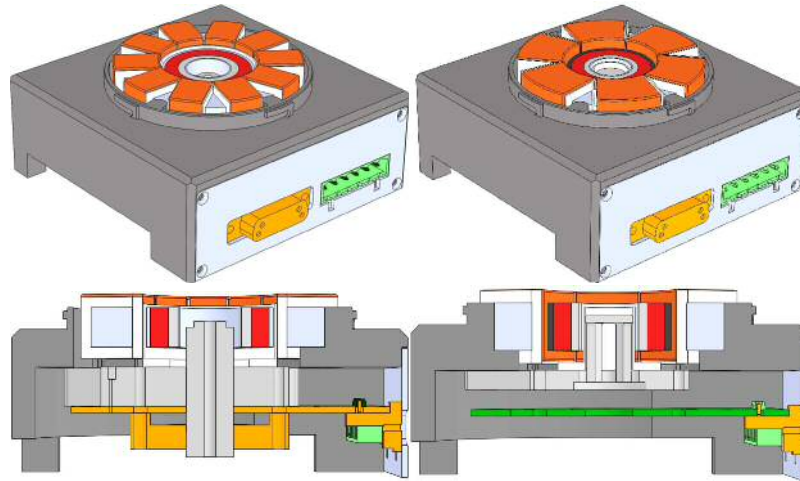


Figure 5.1.: Prototype 3D construction and cross section of 5pd (left) and 6ps (right).

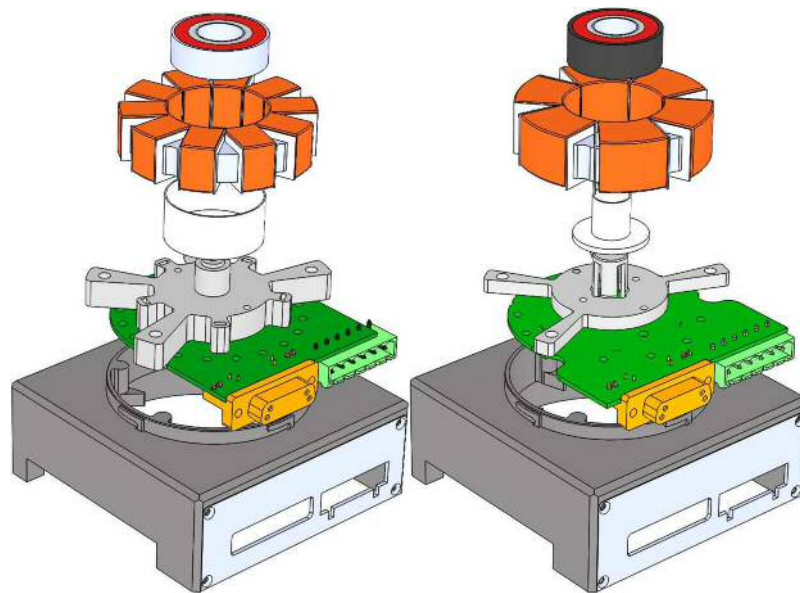


Figure 5.2.: Exploded view of 5pd (left) and 6ps (right). From top down: rotor with sensor target, back iron, magnet, and bandage; stator with core, coil carriers, and windings; touchdown bearing; sensor carrier (also carrying touchdown bearing in 6ps arrangement); PCB for power and signal connection; housing.



Figure 5.3.: Photos of actual prototypes

5.2.2. Prototype data

The following section gives the 3D construction and real prototype images of the two most recently realized high-speed bearingless disk drives. While several other prototypes using the 5pd design have been constructed over the years, the 6ps topology was only realized in this last series. Table 5.2 lists the geometric data of the two designs and Table 5.3 gives the measured performance values. When compared to the results of the optimization conducted in Chapter 2, given in Table 2.4, it becomes clear that the optimization, which became available only after the construction of the prototypes, is a very useful step in the design process. For instance, the coil width and the rotor length were designed too conservatively in the initial prototypes. The result of the optimization later on showed that also with larger coil volume and, hence, larger radial magnetic air gap, the specification for the stiffness values would be fulfilled while higher torque and forces could be produced.

	5pd	6ps
Dimension	Value	Value
$d_{o,S}$	60 mm	60 mm
h_S	10.5 mm	10.5 mm
h_{insul}	0.5 mm	0.5 mm
h_{Coil}	2 mm	2 mm
h_{TB}	0.5 mm	-
$d_{i,S}$	33 mm	34 mm
δ	0.5 mm	1.4 mm
$d_{o,B}$	32 mm	31.2 mm
h_B^2	1 mm	1.5 mm
$d_{o,M}$	30 mm	28.2 mm
h_M	4.5 mm	4.5 mm
h_Y	2.5 mm	2 mm
h_{Al}	0.5 mm	0.5 mm
$d_{i,R}$	15 mm	14.2 mm
δ_{TB}	-	0.5 mm
h_{TB}	-	0.5 mm
l_S	10 mm	12 mm
$I_{\alpha,\beta}$	3992 g mm ²	3411 g mm ²
I_φ	7230 g mm ²	5782 g mm ²
m_R	47.7 g	43.4 g

Table 5.2.: Mechanical dimensions of the constructed prototypes

5. Prototypes

Parameter	5pd	6ps
$c_{r,min}$	4.77 N/mm	4.73 N/mm
$c_{r,max}$	8.37 N/mm	7.56 N/mm
c_z	2.20 N/mm	1.84 N/mm
$F_{x,min}$ (6 A/mm ²)	1.29 N	1.27 N
$k_{startup}$	3.24	2.97
\bar{T}_z (6 A/mm ²)	22.4 mN m	37.3 mN m

Table 5.3.: Measured drive parameters. The air gap used for the calculation of $k_{startup}$, defined in (2.65) is the physically relevant one, i.e., δ for the 5pd design and δ_{TB} for the 6ps design.



Figure 5.4.: Prototype demonstrator equipped with impeller head and housing as well as speed display and power electronic circuit

5.3. Control

5.3.1. Power electronics unit

All realized prototypes are driven with the general purpose laboratory power electronic unit LCM-ECU-10HB-10A designed by LCM which is illustrated in Figure 5.4. It is highly customizable, is equipped with one current sensor for each half bridge, and is controlled by a Microchip ®TMS320F28335 digital signal processor (DSP), featuring a broad range of communication possibilities. Table 5.4 provides the most important data.

5.3.2. Control software

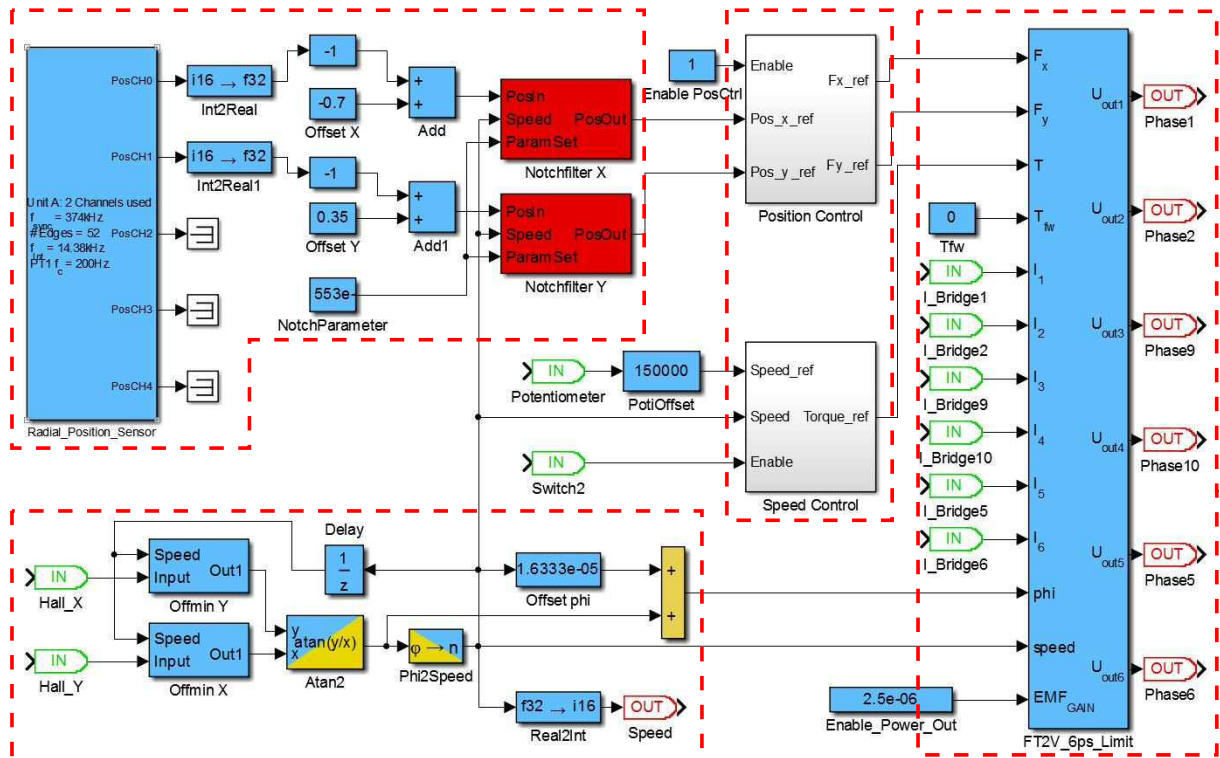
The hardware provides a comfortable platform for testing and configuration with the visual control tool X2C developed by LCM. X2C is available as open source software at www.mechatronic-simulation.org. The control scheme presented in Figure 5.5 displays the four principle parts of the control circle.

Parameter	Value
DC supply voltage	8–80 V
Power outs	10 half bridges
PWM frequency	up to 80 kHz
Max. phase current	up to 20 A (short-time)
Max. output power	1 kW

Table 5.4.: Technical data of the LCM-ECU-10HB-10A power electronics unit

Radial position signal treatment

Position and Speed dependent transformation and current control



Rotor angle and speed signal treatment

Figure 5.5.: Control scheme

5.3.2.1. Radial position signal treatment

The signal for the radial rotor position is created by the eddy current sensors in the inner rotor space and preprocessed on the signal treatment PCB which is also placed directly inside the drive. This signal consists of an x-channel and a y-channel which still contain offsets through improper sensor placement or part tolerances and a certain amount of white noise. Parts of the necessary signal treatment which must be done in software were described in a previous publication [70] of which only the notch filters as the key elements for making the control insensitive to unbalance signals, shall be treated here.

As the rotor speed passes the rigid body mode for the radial degree of freedom, the axis of rotation shifts from the geometric rotor center to the center of gravity causing an orbit movement. This shift occurs due to imperfections in the rotor balancing which, in a

real system, are always present. High values for controller-induced stiffness and damping reduce the influence of this unbalance-caused orbit and minimize rotor deflections. Unfortunately, this renders the system prone to sensor noise which will be amplified just like the desired signals and worse, calls for increased bearing currents. While this might not be a problem when crossing the relatively low radial resonance frequency, the maximum allowed current can quickly be reached when unbalance-caused deflections need to be corrected at higher speeds. The demanded bearing forces, necessary for keeping the rotor spinning around its axis of geometry, increase as the square of the rotational frequency.

A different approach takes advantage of the adjustable rotor support offered by an active magnetic bearing. Allowing the rotor to spin around its new axis of rotation avoids spending a lot of bearing power on forcing it back to the old one. This, however, can only be done if the orbiting movement of the rotor can be tolerated in the respective application. The idea of this approach is to either suppress the sensor signals which are synchronous to the current rotor speed or to inject reference position signals describing this very orbit. The method is known as “Unbalance Force Rejection Control”, “Adaptive Feedforward Compensation” or “Automatic Vibration Rejection” and has been thoroughly examined in the literature (e.g. [55], [60], [119]). For the present control, the design of a narrow band filter for the position sensor input according to the investigations of [51] has been chosen. HERZOG proposes a generalized notch filter characterized by its transfer function

$$H(s) = \frac{s^2 + \omega_{notch}^2}{s^2 - 2\xi \cdot \cos(\phi)s + \omega_{notch}^2 + 2\xi \cdot \sin(\phi)\omega_{notch} + \xi^2} \quad (5.1)$$

where s stands for the Laplace parameter $s = \sigma + \mathbb{j}\omega$, ω_{notch} is the notch frequency and the coefficients ϕ and ξ are defined as

$$\phi = \arg(T_R + \mathbb{j}T_J) + \pi \quad (5.2)$$

$$\xi = \frac{1}{2}\epsilon|T_R + \mathbb{j}T_J|. \quad (5.3)$$

The pole placement is achieved by varying the parameters T_R and T_J whereas ϵ regulates the filter bandwidth. The ideal desired filter has an infinitely sharp notch at the exact rotor frequency in order not to influence the remaining signal spectrum. In the real control however, a certain band gap needs to be assured in order to reduce sensitivity to position signal noise and constrain the negative effects of quantization noise due to the digital filter implementation. Of the three evaluated filters shown in Figure 5.6, the narrowest one with $\epsilon = 0.5$ shows the best results and was used to obtain the experimental results presented in Section 5.4.

Implementation with soft switching The discrete filter coefficients are calculated *a priori* for a certain number of discrete rotor frequency values and are then stored in a lookup-table on the DSP of the LCM-ECU-10HB-10A. In order not to run into quantization problems, the frequency step size needs to be matched to the notch filter bandwidth as stated above.

The justifying argument for using the described notch filter - the change of the rotational axis - applies only to the supercritical operation range. Therefore, the position sensor signal must not be filtered in the frequency range up to resonance. Implementing a hard turn-on or turn-off as the rotational speed passes a certain threshold level results in a sudden change of the position error signal. Even worse, the filter state might start

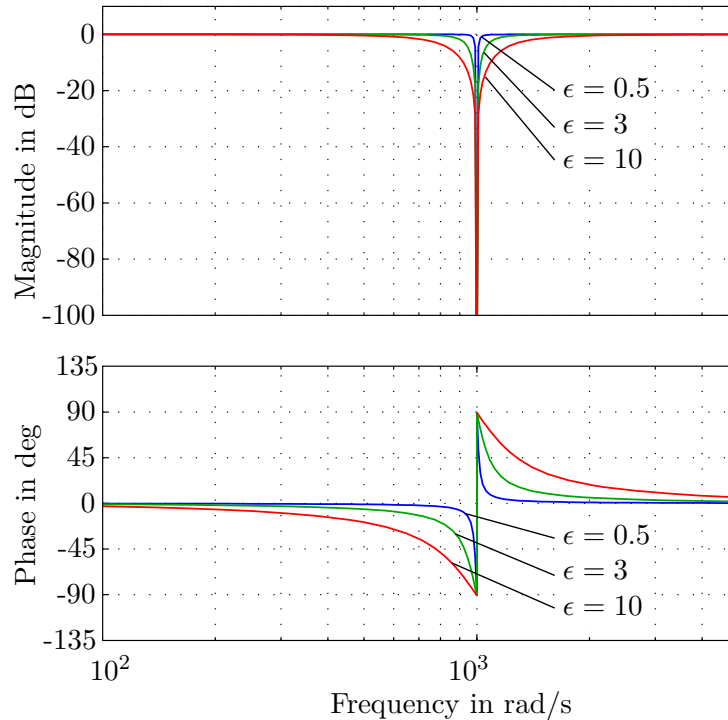


Figure 5.6.: Bode diagram of position signal notch filter for $T_R = 50$, $T_J = 0.5$ and different bandwidth parameters

toggleing if the rotor reference speed is set close to the threshold speed. This sudden variation of bearing forces can lead to high rotor deflections and destabilize the rotor movement as it touches the touchdown bearing. The toggleing problem could be solved using frequency hysteresis but the reaction to the hard switching cannot be avoided with this method.

A simple yet effective workaround has been found in constantly applying the filter to the position signal and varying the notch frequency as a consequence of the current rotor speed. Before the threshold speed has been reached, the filter is currently left at that very frequency. Figure 5.7 shows the decision taken in each computational cycle of the DSP.

The resulting position signal without the rotor synchronous frequency components causes a significant reduction in the necessary bearing currents as shown in Figure 5.10.

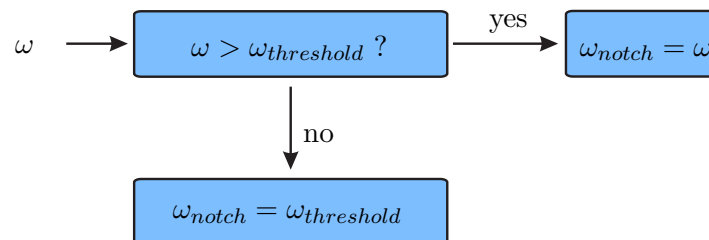


Figure 5.7.: Notch frequency determination depending on the actual speed ω_{act} .

5.3.2.2. Rotor angle and speed signal treatment

The rotor angle is calculated from the x- and y-hall sensor signals delivered by the sensor PCB inside the bearingless drive by using the $\arctan()$ function. The DC-offset of the

signals needs to be filtered before that in order not to obtain an discontinuous angle signal. Since the current drive is intended to achieve high rotational speeds, it is also important to note that a rotor angle correction is used. This correction compensates the fixed calculation time of the DSP between sampling the new HALL sensor signals and setting the new output voltages to the driver stage. While negligible at low speeds, this time delay needs to be translated into a speed-dependent angle error which needs to be added to the result of the $\arctan()$ function. The respective multiplication can be seen in Figure 5.5. Equally visible is the differentiation block labeled *Phi2Speed* which calculates the rotational speed used in several parts of the control scheme.

5.3.2.3. Position and speed control

Controlling the radial position and the rotational speed is the central duty of the control of a bearingless drive, yet technologically, this is not exciting. A PD-controller is used for the radial position and a PI-controller is applied to the speed loop. While the latter is tuned by intuition during the testing phase, the starting values for the first were calculated as described in [70]. The main challenge during the controller tuning is the correct setting of the mentioned notch filter coefficients, the back-EMF compensation described below, and the position offsets for the radial position which change when the drive unit is disassembled and reassembled for inspection or physical maintenance. Apart from the actual control issues, most errors during the prototype commissioning process came from mechanical shocks and vibration due to touchdown events: Broken soldering connections, deformed sensor supports, broken touchdown bearings, broken sensor wires, etc.

5.3.2.4. Speed dependent transformation and current control

The last missing piece in the control puzzle is the speed dependent transformation and current control block, where the output voltages are calculated according to the target radial forces and torques

$$\begin{bmatrix} F_x^* \\ F_y^* \\ T_z^* \end{bmatrix} \quad (5.4)$$

specified by the position and speed controllers. The asterisk notation * denotes the target character.

Figure 5.8 shows the sub-structure of this block. The speed dependent transformation realizes the inverse relationship described in 2.44. In addition to the resulting target currents, the P-controller used for the current control is fed with the measured current values and the current rotor angle. Before feeding the controller output to the inverter stages, the back-EMF is added as a feed-forward signal in order to minimize the control effort. In order to transform the currents and voltages from the four-dimensional d-q space (two dimensions for torque and force creation, each) to the six-dimensional phase space, a quasi-CLARKE³ transformation and its inverse are applied. More on this subject is detailed in [38].

³EDITH CLARKE, * 1883 in Howard County, Maryland, USA, † 1959, ibidem

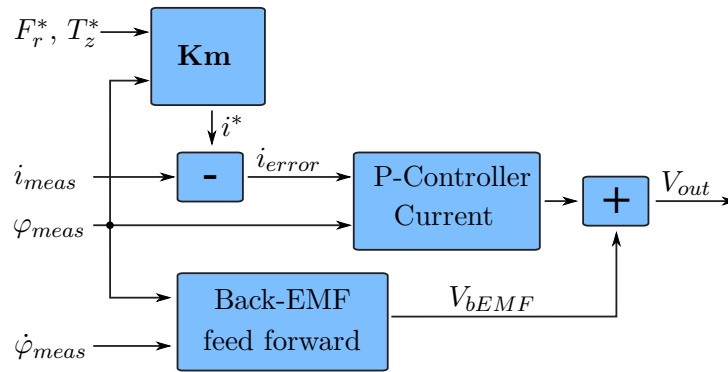


Figure 5.8.: Speed dependent transformation and current controller as last stage of control sequence

5.4. Prototype test results

The control scheme shown in Figure 5.5 was implemented and many tests have been conducted. The rapid control tool X2C mentioned above again offered a very comfortable setup for these tests as it allows online communication, not only for changing control parameter values but also for storing and visualizing any of the processed values.

5.4.1. Control verification tests

In order to evaluate the effectiveness of the notch filter, four different cases (a)-(d) are considered. Figure 5.9, Figure 5.7 and Figure 5.11 show the corresponding orbit radius, a phase current and the 3D-orbit for each case up to 20 krpm, respectively.

Case (a) The calculated minimum values for stiffness and damping are applied to the PD-position controller. The resulting rotor movement does not show stable behavior. In the 3D-orbit plot in Figure 5.11(a) it can clearly be seen that the rotor never starts to levitate but is instead bounced from one side of the touchdown bearing to the other. Since these parameter values represent the minimum necessary stiffness and damping in the ideal, theoretical case, this behavior is not surprising for the practical experiment.

Case (b) The same control structure as in (a) is used but more damping and higher stabilizing stiffness is applied. A sudden increase in both the rotor orbit radius as well as the drawn phase current marks the onset of the region surrounding the resonance frequency at approximately 5 krpm. According to the 3D-orbit plot in Figure 5.11(b) and the trace of the orbit radius in Figure 5.9(b), stable operation has been achieved. In Figure 5.10(b) however, the increasing phase current shows the drawback of a fixed axis of rotation as unbalance effects gain importance with rising speed.

Case (c) In case (c), the notch filter is added as given in (5.1). Up to 15 krpm, the plots resemble the results of case (b) since the same control parameters are used. As the threshold value is crossed, the phase current in Figure 5.10(c) is dramatically reduced since the bearing forces for keeping the rotor spinning around its axis of geometry are no longer needed. The sudden change in the position error, however, provokes a disturbance of the rotor's orbit at around 15 krpm.

Case (d) The last case uses the same configuration as (c) but here, the proposed soft switching algorithm is implemented. Regarding the phase current in Figure 5.10(d), the transient region from unfiltered to filtered position signal is clearly visible shortly before the threshold value is reached. As a consequence, the small disturbance in the rotor orbit which can be observed in case of hard switching does not occur in this case.

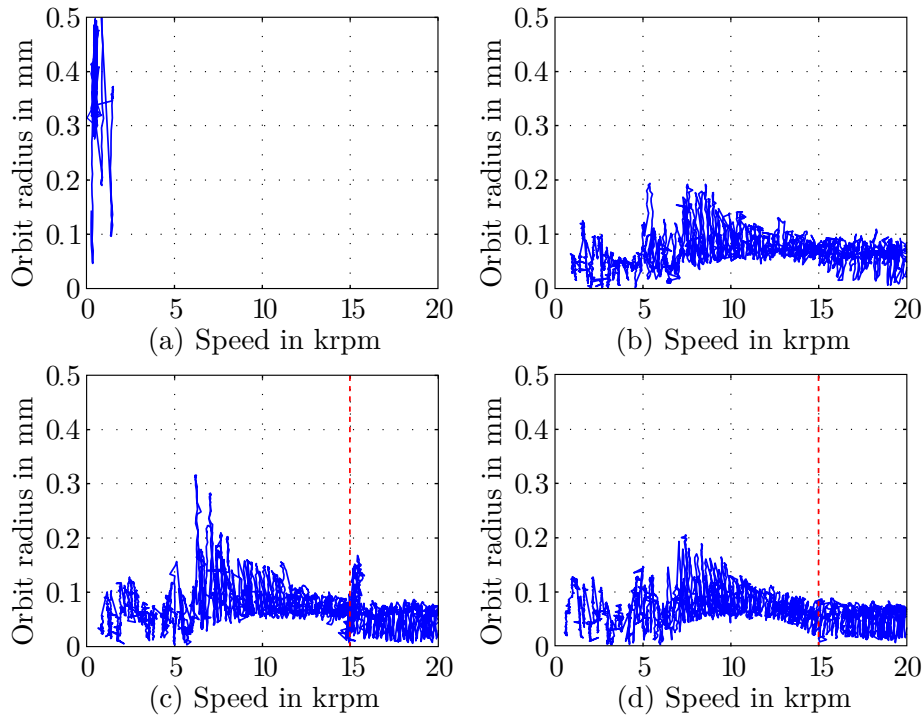


Figure 5.9.: Orbit radius for case (a)-(d)

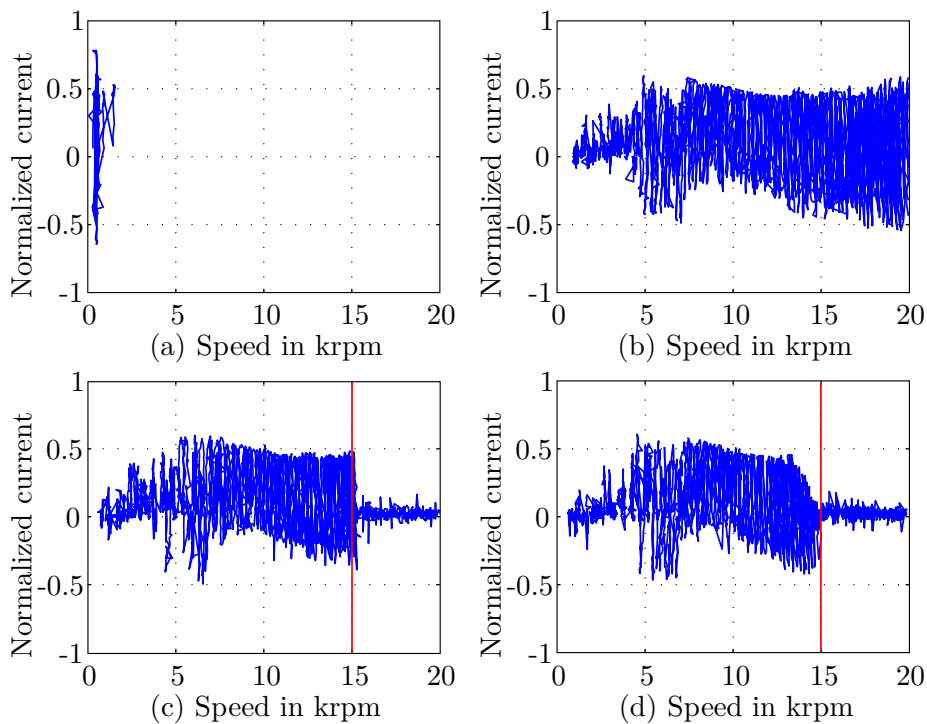


Figure 5.10.: Phase currents for case (a)-(d)

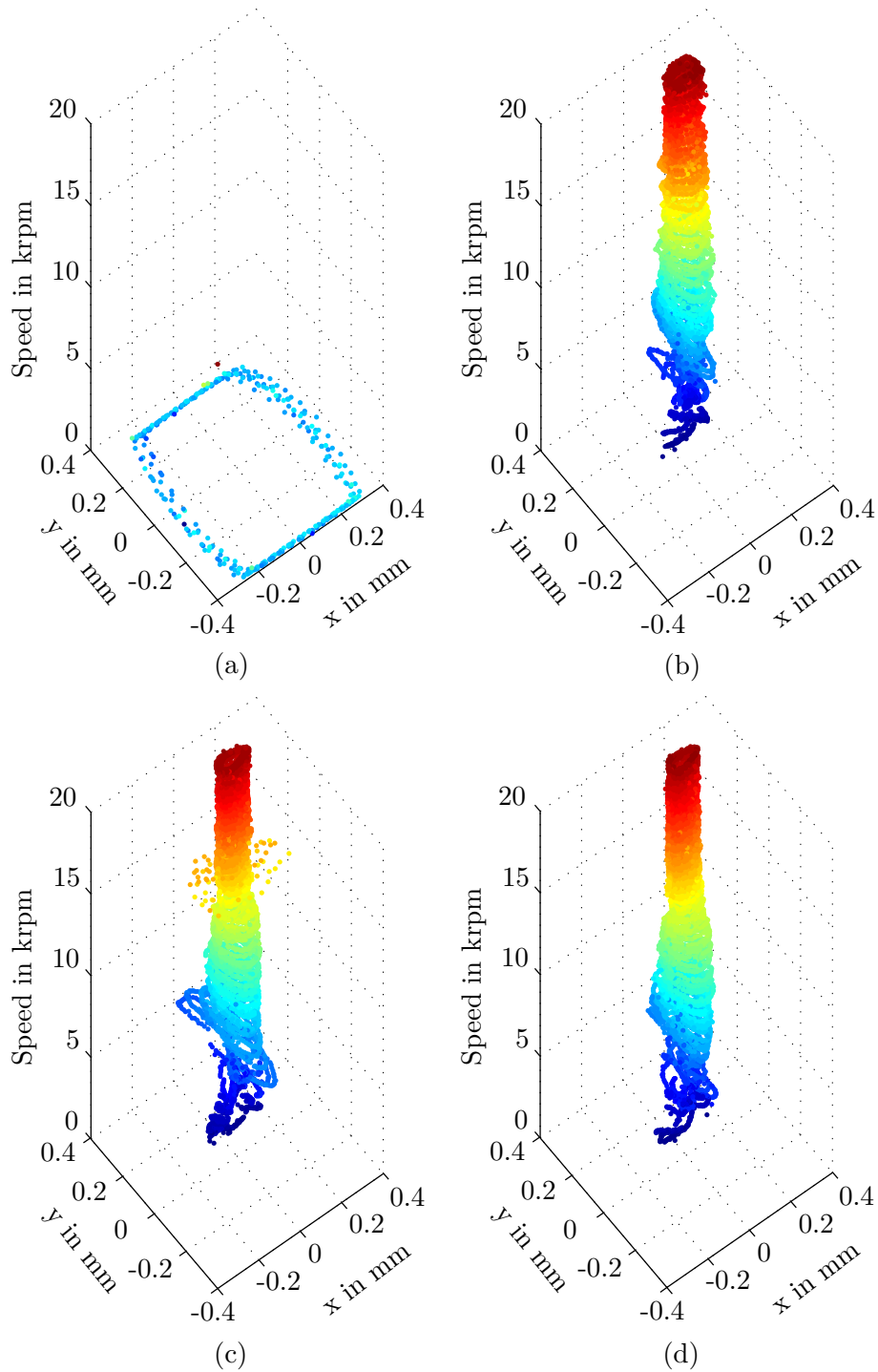


Figure 5.11.: 3D-orbit plot for case (a)-(d)

5.4.2. Turbine and compressor tests

The scope of possible applications of a high-speed drive contains the area of gas handling, ranging from compression, expansion, and transport of gaseous fluids. Therefore, polyamide rapid prototyping parts shown in Figure 5.12 for testing the potential use as turbine and compressor have been constructed.

The results of these tests have been presented in [78] and will be presented here in extracts, only. Key arguments in favor and against the use of magnetically levitated

5. Prototypes



Figure 5.12.: Housing and rotor equipped with compressor wheel (top) and housing and turbine wheel ready for mounting on the same rotor (bottom)

rotors in turbines and compressors are rather evident:

- Turbines and compressors typically have to be designed for long uptimes. Combined with the high rotational speeds necessary, this poses a very demanding requirement for the lifetime of mechanical bearings, favoring abrasion-free magnetic levitation.
- High temperatures of the gas flow in turbines renders the use of lubrication oil difficult or sometimes even impossible. This also speaks for the use of lubrication-free magnetic bearings.
- Unfortunately, these high temperatures are also a limiting factor for rotors with permanent magnet material due to impending demagnetization.
- Magnetic bearings provide a rather soft support in a sense that the axis of rotation is not as strictly constrained as in mechanical bearings. While favorable for the reaction to unbalance (cf. Section 5.3.2.1), this can be problematic as small air gaps between a compressor or turbine wheel and its respective housing can strongly affect the efficiency of a turbine.

Turbine operation One of the main criteria for successful operation is this tight tolerance in the axial direction. The passive stabilization in that degree of freedom does not allow controlling the process forces in direction, making it a hard constraint for the testing. As shown in Figure 5.13, the deflection during the turbine tests when the levitated rotor was driven by compressed air increases nearly linearly with speed and amounts to 2.25 mm at 70 krpm. This is, therefore, much more severe than during compressor operation, where the rotor is only deflected by 0.12 mm at 75 krpm. Additionally, it has to be mentioned that the rigid body modes could not be crossed without altering the control

parameters when the turbine was driven with compressed air. This means that the rotor had to be accelerated to between 20 krpm and 30 krpm in motor mode and was only then driven by air. This seems unorthodox but would probably not be a great problem in practical use because the power used to drive the rotor to this “starting speed” is only around 25W. After this acceleration, the tilting movement introduced by the non-symmetrically injected compressed air was sufficiently stabilized by the passive support and the gyroscopic forces so that no tilt problem was noticed during measurement. The massive axial shift, however, makes proper turbine operation impossible. The experiments had to be conducted with a wide air-gap-housing but still the rotor touched the housing at 70 krpm (visible in Figure 5.14), damaging the turbine wheel. At this point, the measurement was stopped as the axial shift poses a problem that cannot be influenced except by aerodynamic modeling of the turbine geometry which is not in the scope of this work. For future research, an axial bearing such as the modified TSC concept presented in Section 3.2 could be tested for turbine operation.

Compressor operation The drive has also been accelerated to 80 krpm in motor mode with the polyamide compressor wheel mounted on the rotor. Active as well as passive stabilization forces sufficiently supported the rotor up to that speed, however, at the top speed, the axial deflection also lead to contact between the rotor and its cover as the axial clearance was tighter than with the turbine housing. The housing inlet was connected to a mass flow sensor and a differential pressure sensor. The achieved flow rate and pressure levels are displayed in Figure 5.15. The resulting mechanical output power is shown in Figure 5.16. The different curves were obtained by manually setting a valve at the outlet to six different positions from completely closed to completely open and then running the drive at the distinct speed levels.

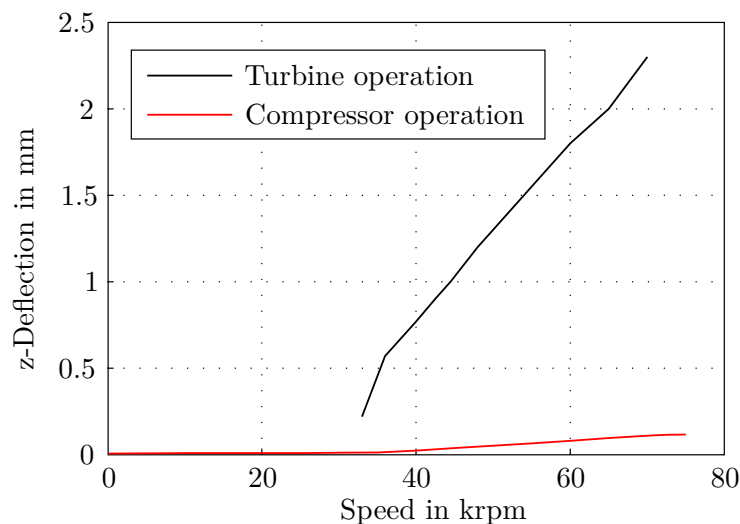


Figure 5.13.: Axial rotor deflection in turbine and compressor operation

5.4.3. High-speed test

In order to verify the research achievements, the prototype drives were accelerated to high rotational speeds. These test results have been published in [74] and are presented here in order to complete the experimental section. While conducting the tests, the

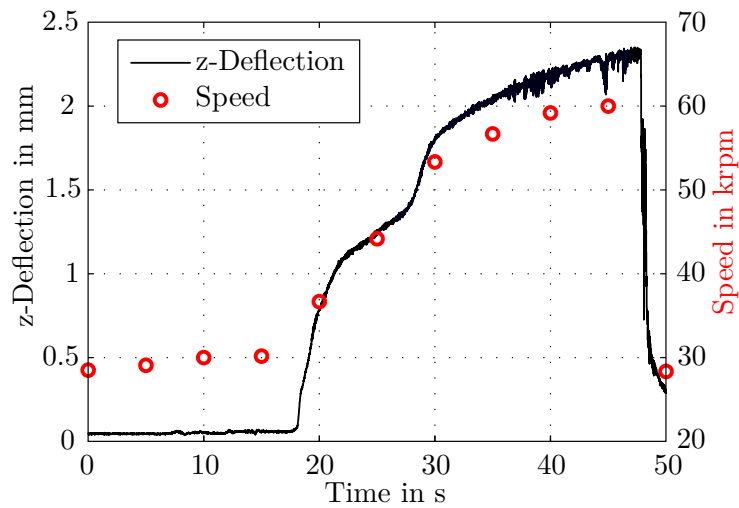


Figure 5.14.: Axial deflection and rotor speed over the experiment time

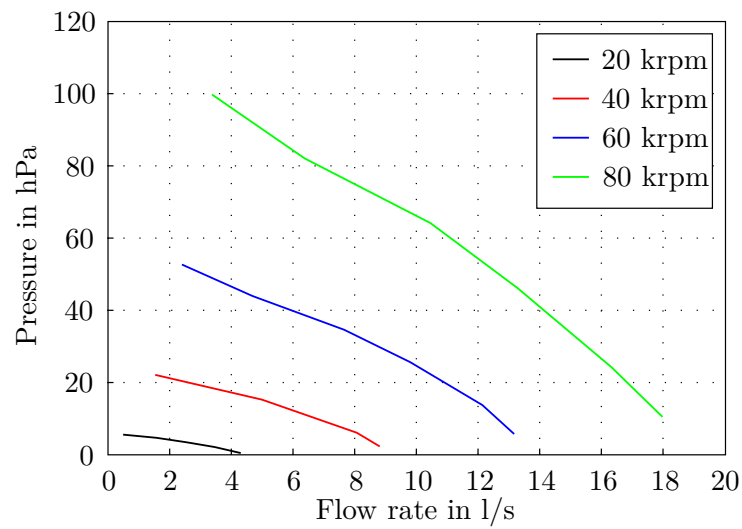


Figure 5.15.: Flow and pressure measurement during compressor operation

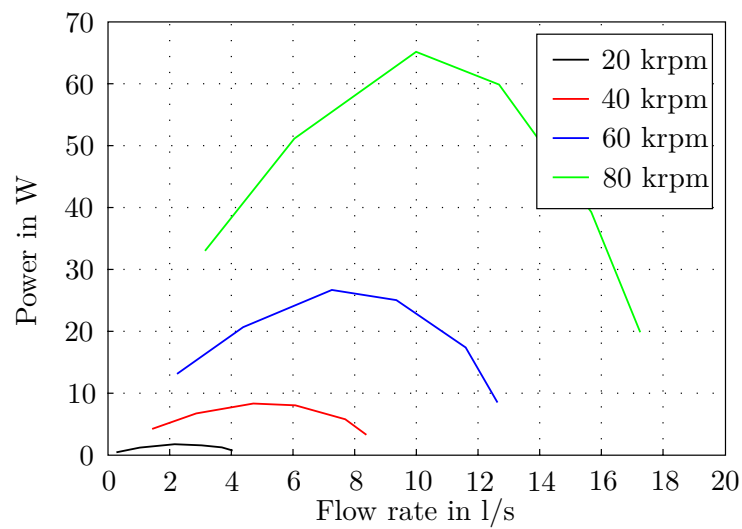


Figure 5.16.: Resulting mechanical output power during compressor tests

online connection to the control board in the power electronics board allowed tracing the radial position of the rotor. The plot in Figure 5.17 shows the orbital tube of the rotor during such a run-up where the initial goal of reaching 100 000 rpm was achieved and surpassed. In this figure, the rigid body resonance frequencies can be recognized by the increased orbit. Due to the low stiffness values and the flat rotor geometry, the resonance frequencies are passed at speeds below 5000 rpm. Since this speed region is not very interesting here, no significant effort was made to constrain the deflections more than necessary for preventing the rotor from contacting the touchdown bearing. Higher controller stiffness would reduce the orbit but would also shift the resonance frequencies to higher values.

As the rotational speed increases, the elliptical orbit is formed into a circular cross section due to self-centering. The remaining orbit is a consequence of the rotor unbalance. Due to the notch filter, the position controller no longer aims to reduce this orbit but permits the rotor to spin around its axis of inertia. The achieved reduction of the bearing currents then permits stable operation without surpassing the current limit of the power electronics. The limit of operation was reached well above 100 000 rpm when the rotor was mechanically destroyed by the centrifugal forces (Figure 5.17). The obtained speed maxima with a high-strength steel bandage, a carbon fiber bandage and an unsupported rotor are listed in Table 5.5. The predictions based on analysis presented in Chapter 4 were within a 10 % range for the unbandaged rotor and the rotor with the hot-work steel bandage. The fiber bandaged rotors, however, were destroyed significantly below the predicted tolerable speed maximum. The reason for this can very likely be found in the production and mounting of the fiber bandages: Due to the high stiffness of the fiber material, only few microns of increased press fit push the resulting stress in the bandage above the tolerable level. It is practically impossible to predict the precise inner bandage diameter without extensive experimental trials since aspects as the matrix compression, the initial fiber stretch, the exact fiber to resin ratio, etc. would have to be taken into account. Additionally, the axial movement between the magnet and the bandage during the press fitting process may destroy fibers at the inner radius of the bandage. As this represents the location of maximum stress, any damage will have severe influence on the bandage stability.

Table 5.5.: Achieved maximum speeds and calculated maximum speeds (in parentheses) with different bandages

Bandage type	Maximum speed 5pd	Maximum speed 6ps
Unbandaged	72 krpm (68.7 krpm)	
0.5 mm UMS-CFK	96 krpm (112.3 krpm)	
1.5 mm UMS-CFK		105 krpm (167.3 krpm)
0.5 mm Hot-work steel	115 krpm (106.2 krpm)	

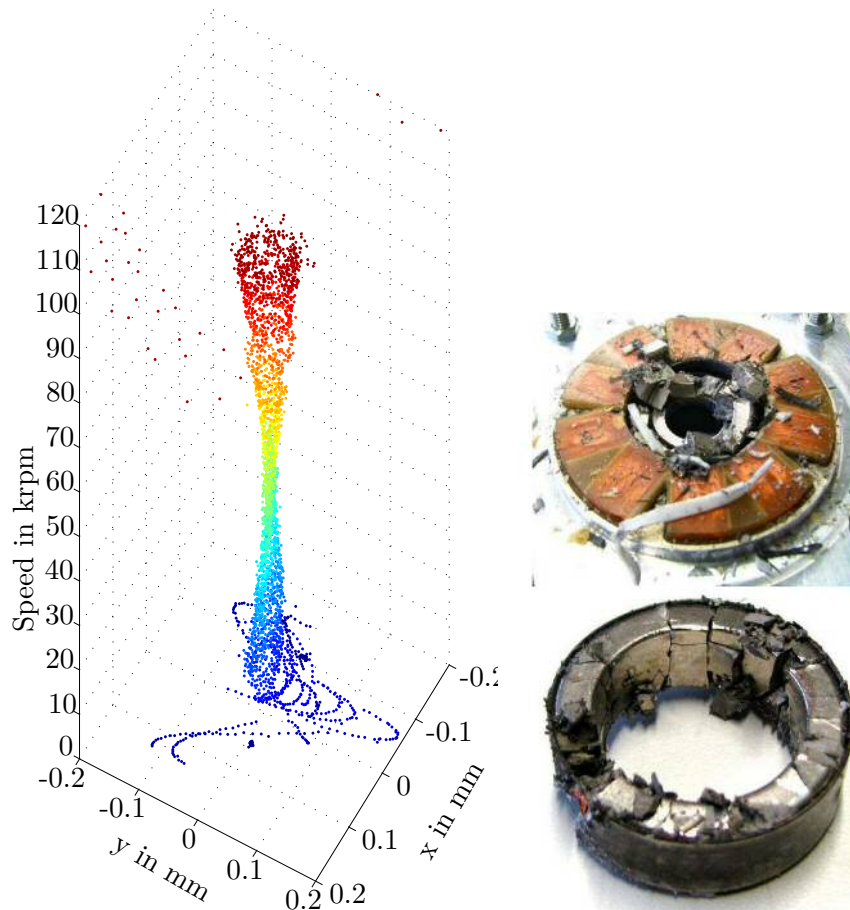


Figure 5.17.: Rotor orbital tube for acceleration from 0 to 115 000 rpm (left) and mechanical failure of a steel (bottom right) and a carbon fiber bandage (top right) due to centrifugal forces at maximum speeds given in Table 5.5

5.5. Conclusion

After the theoretical work presented in the first four chapters, the prototype chapter presents the key components of the constructed samples and the main test results obtained with them. It shall be mentioned that there have been multiple prototypes which were built and operated, the 5pd and 6ps drives represent only the last two which have been realized before the completion of this documentation. Several conclusions can be drawn from the manufacturing which has largely been done at LCM and from the conducted tests.

- As mentioned earlier in Chapter 2, it is very helpful to conduct an optimization before the construction of a prototype in order to receive better results in any possible way. Nevertheless, getting one's hands on a prototype, constructing, assembling and putting it into operation is, after thorough planning, an instructive and inspiring supplement to the development process.
- Speed dependent control features such as the angle correction and the position signal notch filter including their soft switching algorithm are helpful additions to the standard control concept.
- The suitability tests for turbine and compressor operation of the bearingless high-

speed disk drive have shown that the axial degree of freedom will very likely have to be controlled actively in order to succeed in these applications. The passive stabilization alone will keep the rotor in stable movement but the control of the axial impeller clearance which largely determines the efficiency for radial turbines and compressors cannot be achieved with the current setup.

- Resonance frequencies have not been a very large concern since the rigid body modes are located at very low frequencies where they can be passed quickly and the flexible body modes are located at very high frequencies which are clearly out of the rotational frequency scope.
- Mechanical stability is the main issue when driving a disk rotor to high rotational speeds. Due to the large diameter compared to elongated shafts, bandages need to be placed onto the rotor, influencing the air gap and, thus, the drive performance as well as the rotor design possibilities.

6. Drive losses

Contents

6.1. Introduction	120
6.2. Measurement setup and results	120
6.2.1. Measurement system	120
6.2.2. Loss measurement results	122
6.3. Loss component description	123
6.3.1. Analytical rotor field description	123
6.3.2. Comparison of FE and analytical calculation	125
6.3.3. Armature reaction field	127
6.3.4. Stator losses	127
6.3.5. Copper losses	131
6.3.6. Air drag losses	135
6.3.7. Thermal measurement	138
6.3.8. Efficiency measurement	140
6.4. Design variation	141
6.4.1. Increased speed	141
6.4.2. Wire selection	143
6.4.3. Variation of the radial air gap	146
6.4.4. Increased pole number	147
6.5. Conclusion and criticism	148

The loss components occurring in a high-speed bearingless disk drive are partly different from the losses occurring in standard motors in their nature and importance. After giving the motivation for why this aspect is covered in a separate chapter, the measurement setup is described in detail. The resulting experimental measurements are then compared to analytic models for the iron losses, the copper losses and the air drag losses.

Before concluding the chapter in a critical retrospective, the derived models are applied to estimate the losses for different relevant design modifications such as increased rotational speed, alternative wire selections, different radial air gap widths and an increased rotor pole number.

6.1. Introduction

With soaring carbon dioxide emissions due to the use of fossil fuels and overall rising energy prices, efficiency targets need to be met in many fields of the industry. As one of the main groups of electrical devices in terms of consumption, this especially applies to electrical drives. Needless to say that this has heavily influenced both the rise of efficient motor topologies such as permanent magnet synchronous motors as well as the growing trend towards smaller motor units running at higher speed, thus saving on material cost and weight. It goes without saying, that this demands a detailed consideration of the loss components in the high-speed drive considered here since many of these components increase with rising rotational speed.

However, the target of this chapter is not to predict something that *can* already be measured and then be satisfied or dissatisfied with the resulting agreement between analytical model and measurement. The target is rather to obtain a model that can be qualitatively verified and quantitatively adjusted by measurement in order to predict something that *cannot* be measured yet. This especially concerns the losses occurring in certain design variations of the presented drive.

First, Section 6.2 deals with the description of the measurement system and presents the experimental loss measurement results. In Section 6.3, the respective loss components are identified, analyzed and analytical models are created and compared to the measurement results. Finally, the feasibility of several proposed design variations from a loss-related point of view is discussed in Section 6.4.

6.2. Measurement setup and results

The 5pd¹ prototype was used for measuring the losses. A detailed description of this prototype can be found in Chapter 5 with all relevant system data.

Measuring the losses of a magnetically levitated disk which does not feature an output shaft is not trivial. Even if a torque sensor could be connected without disturbing the rotational behavior of the spinning permanent magnet and without putting additional loads on the shaft, torque values of only a few mNm would have to be clearly resolved for the unloaded case at rotational speeds of up to 100 krpm. Since this is a very demanding challenge for existing sensors, different techniques for measuring the motor losses have been investigated.

6.2.1. Measurement system

Continuously measuring the speed over the deceleration time of a freely running system usually gives excellent information about the occurring loss torque. Unfortunately, this so-called *free-wheel* operation of a bearingless drive using a combined winding system requires flawless winding manufacturing and ideal knowledge of the rotor angle at any time in order not to produce any torque when applying the bearing forces. Due to sensor noise, quantization noise and small imperfections in the winding, this cannot be guaranteed. Additionally, the air drag and bearing power is always present and, therefore, such a testing method is not suitable.

Instead, a high-precision reaction torque measuring test rig as shown in Figure 6.1 has been constructed. A similar method applied in [130] in order to measure cogging torque

¹5 phases, double coil arrangement, see Chapter 2 for the complete terminology

has been adapted to meet the present challenge. The rotor (b) is mounted on and driven by a separate machine (a) whereas the stator (c) is mounted on a rotatable shaft. The two ball bearings used for this purpose feature very low sticking friction. A lever (d) mounted on the shaft pulls on a string attached to a mass (e) which exerts a gravitational force F_g on a high precision scale. This pull reduces the force on the scale according to

$$F_{scale} = F_g - \frac{T_S}{l_{lever}} \quad (6.1)$$

with T_S being the torque transmitted from the rotor onto the stator and l_{lever} being the distance from the shaft axis to the string attachment point.

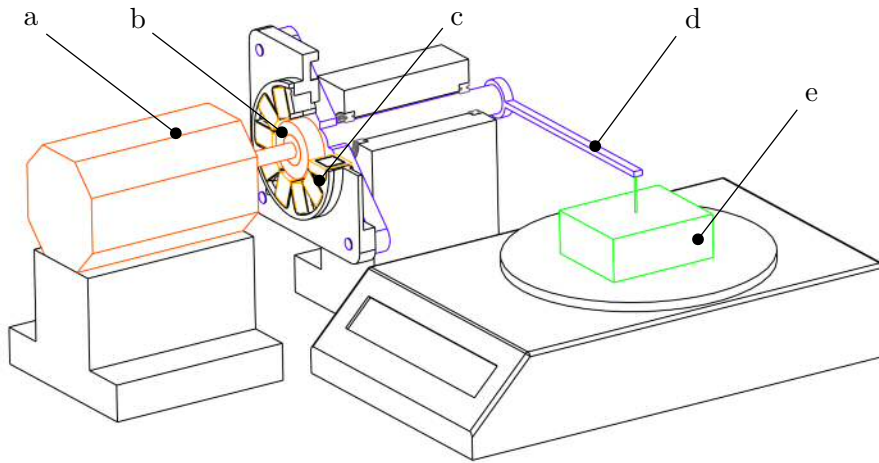


Figure 6.1.: Laboratory measurement setup

The torque T_S is the Newtonian reaction to the torque on the stator which, for a certain rotor speed, varies according to the transmitted power. This power is an equivalent for the losses acting on the mounted stator such as iron losses inside the stator core, eddy current losses in the winding system or air drag. The method has the advantage of being completely independent of the driving machine (a) and its internal losses or efficiency, which would have to be known if the losses were determined by measuring the input power of that machine.

With a scale resolution of 0.01 g and a lever length of 10 cm, a torque resolution of just below $10 \mu\text{Nm}$ can be achieved. Multiplying the torque with the rotor speed which can easily be measured separately gives a power resolution ranging from 0.01 W at 10 krpm to 0.1 W at 100 krpm.

The driving machine (a) is worth a few comments. The machine shown in Figure 6.1 is only an idealized image. There are a lot of problems when a machine shaft supported by conventional bearings is supposed to run at 100 krpm - which is one of the main reasons why this project exists. Things become even more difficult with a relatively large mass (the test rotor (b)) attached to one shaft end, protruding far beyond the last bearing point. This is especially true in this configuration because the entire rotor is difficult to balance since the test rotor should be easily mountable, cannot be shrink-fitted on the shaft due to mechanical limitations (see Chapter 4) and must not be placed near any ferromagnetic part. A first attempt using a milling spindle, running at a maximum speed of 30 krpm, and a two-stage belt transmission system failed due to the ball bearings of the fastest stage failing after several minutes and due to the belts not supporting the necessary pretension.

Another attempt succeeded, using a KP31 automotive turbocharger by Borg Warner which is used amongst others in a three-cylinder Smart Turbodiesel car engine, specified to run at a maximum speed of 280 krpm. The compressor wheel of the turbocharger was removed and replaced with the test rotor. As the device usually operates in a car, the necessary environment comprising a motor oil circuit and the adjustable compressed air connection for driving the turbocharger had to be established. This turned the whole setup into a cumbersome system, however, measurement of the required loss components was possible.

6.2.2. Loss measurement results

Test rig First, the experiments using the test rig shown in Figure 6.1 have been conducted. The speed was increased in steps of 5 krpm and then held constant during the actual measurements in order to avoid acceleration effects. Also, the air drag created between the spinning rotor and the respective stator configuration was obtained prior to the run-up by measuring the transmitted power in a separate run-up with a plastic “dummy” stator of the same size and with similar surface properties as the actual stator under test. This value was later on subtracted from the respective test result.

The first component measured with the test rig was the combined iron loss P_{Fe} consisting of eddy current and hysteresis losses which occur in the stator iron. This was achieved by inserting a stator core without windings and deducting the loss values due to the air drag which were measured before with a plastic stator core of the same dimensions. Secondly, the eddy current losses in the copper winding due to the permanent magnet field, $P_{Cu,M}$, were obtained by inserting a stator with a complete winding system, deducting the iron losses and the previously determined air drag losses. The detailed description below explains that these eddy current losses in the winding are very small in the chosen wire configuration and are, therefore, hardly visible in the measurement depicted in Figure 6.2.

Power meter In addition to the losses acquired with the test rig, the consumed power at the DC-input of the power electronics and at the interface between power electronics and the bearingless unit was measured using a high-resolution power meter. This allows determining the power consumption of the power electronics for both standby $P_{PE,0}$ and switching operation $P_{PE,s}$ by measuring the input and output power during both, standstill with inactive bearing function, and bearingless motor operation. The resistive copper losses $P_{Cu,i}$ were also identified with this power meter by measuring the five phase currents in the winding system and calculating the losses using the resistance values of the respective five coils. In the detailed description in Section 6.3.5, the frequency influence on the resistance value is also taken into account.

Vacuum chamber The exact air drag losses P_{Air} could not be obtained at the test rig mentioned above because the shaft of the external machine disturbs the true air flow in the motor. Therefore, this loss component had to be determined by comparing the power consumption of the bearingless drive (not the test rig) running under ambient pressure to the one where the system was placed in a vacuum chamber.

Cumulative loss illustration In order to display the complete loss measurement result in a well-arranged image, the measured individual losses were summed up. The bearing power consumption was eventually determined by deducting these individually measured

losses from the total motor power consumption. This method means, of course, that all measurement errors and unknown excess loss components are included in the bearing losses. Therefore, this component is titled $P_{Bearing} + P_{Ex}$. Figure 6.2 shows the total accumulated drive losses in the unloaded case during a run-up in ambient temperature from standstill to 100 krpm. A detailed description of the separated components follows in Section 6.3. Two particularities shall, however, be mentioned directly: First, the rapid increase of the bearing power consumption at around 15-20 krpm can be explained by the onsetting effect of the rotor unbalance which causes large bearing forces. When the notch filter described in Chapter 5 is activated at 25 krpm, this component is reduced. Second, the copper losses due to the rotating magnetic field $P_{Cu,M}$ shall be commented here, since they appear only as a hardly visible, thin line which will be explained in Section 6.3.5.

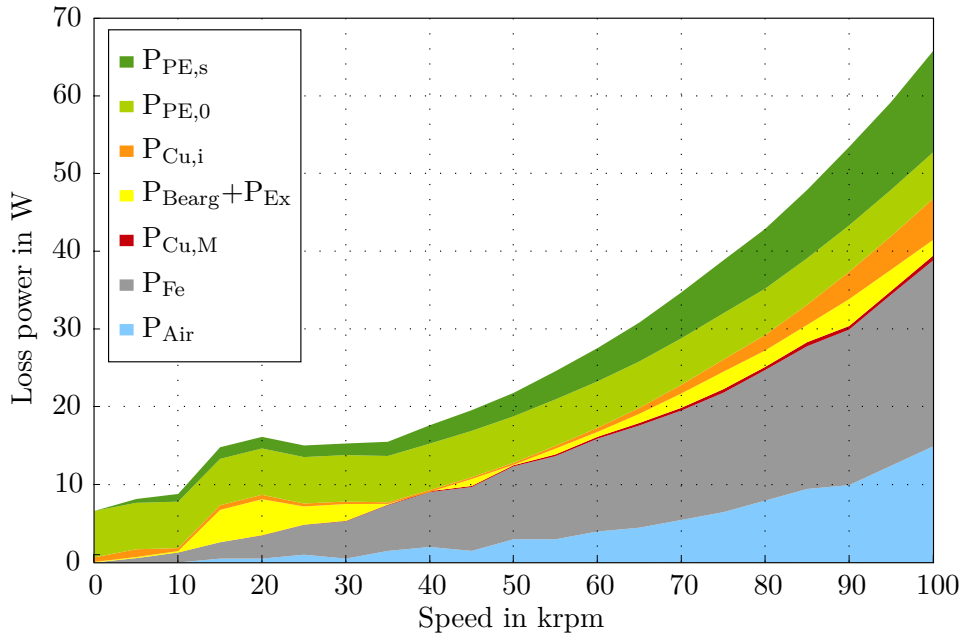


Figure 6.2.: Losses occurring during a run-up to 100 krpm in steps of 5 krpm.

6.3. Loss component description

The different loss components in Figure 6.2 depend on various operational parameters. Of course, the geometric dimensions and the material parameters play an important role but the focus of interest shall be put on the variable parameters such as the current amplitude \hat{i} and its fundamental frequency f_i , the amplitude \hat{B} and frequency f_B of the magnetic flux density, and the rotational frequency Ω . As the motor operates in synchronous mode and since the rotor has only two poles, Ω and f_i are basically identical but since the current $i(t)$ may also include frequency components other than the fundamental frequency as well, the two variables are introduced separately. Table 6.1 shows the respective relationships.

6.3.1. Analytical rotor field description

At first, the loss components related to the magnetic field characteristics are investigated. In the case of ferromagnetic stator parts, the changing magnetic rotor field causes losses

6. Drive losses

Loss component	Variable	Dependency
Power electronics, standby	$P_{PE,0}$	const.
Power electronics, switching losses	$P_{PE,s}$	\hat{I}, f_i
Copper losses, due to current	$P_{Cu,i}$	\hat{I}, f_i
Copper losses, due to magnet	$P_{Cu,M}$	\hat{B}, f_B
Combined iron losses (eddy currents + hysteresis)	P_{Fe}	$\hat{I}, f_i, \hat{B}, f_B$
Air drag losses in air gaps	P_{Air}	Ω

Table 6.1.: Loss components with their respective dependencies

due to eddy currents and the hysteresis effect. In conventional stators, stator teeth increase these losses because they typically represent the zones of the highest flux density and also because they provoke higher field harmonics causing additional losses in both stator and rotor. A slotless design does not show these increased losses and it has been pointed out in several publications such as [10] and [6], that especially for high-speed drives, slotless stator cores are advantageous. The remaining stator core losses will be discussed in Section 6.3.4.

As a consequence of the slotless topology, the air gap winding is also permeated by the rotor field. Even though hysteresis losses only occur in ferromagnetic materials, the copper conductors are subject to losses provoked by induced eddy currents. In addition to the losses provoked by the conducted current, this component will be analyzed in Section 6.3.5.

Before modeling these two loss components, the flux density distribution in the concerned areas (the stator for P_{Fe} , the air gap for $P_{Cu,M}$) needs to be known. Different methods can be used for obtaining the relevant field data and since it is by far the largest contribution, the permanent magnet's field will be regarded first.

Even though finite element methods are very advanced and allow obtaining the magnetic field in a relatively straight-forward approach, calculating the field analytically seems tempting because of the enormous savings concerning computation time. Since the slotless stator and air gap region have a cylindrical shape, an analytical model can be obtained with moderate effort. Additionally, the rotor is modeled as a full cylinder disk. The theoretical background for this purpose can be found in numerous works in the literature such as [47], [15], [129] or [64] and is detailed for the given geometric situation in the Appendix.

Following this approach leads to a compact model of which only the key result shall be repeated here, being the 2D radial (index r) and tangential (index φ) flux density equations for the magnet (index M), the air gap (index δ) and the stator (index S) region, given by

$$B_{r,M}(r, \varphi) = K_{B,M} \cos(\varphi), \quad (6.2)$$

$$B_{\varphi,M}(r, \varphi) = K_{B,M} \sin(\varphi), \quad (6.3)$$

$$B_{r,\delta}(r, \varphi) = K_{B,\delta} \left(1 + \left(\frac{r_{i,S}}{r} \right)^2 \right) \cos(\varphi), \quad (6.4)$$

$$B_{\varphi,\delta}(r, \varphi) = -K_{B,\delta} \left(1 - \left(\frac{r_{i,S}}{r} \right)^2 \right) \sin(\varphi), \quad (6.5)$$

$$B_{r,S}(r, \varphi) = K_{B,S} \left(-1 + \left(\frac{r_{o,S}}{r} \right)^2 \right) \cos(\varphi), \quad (6.6)$$

and

$$B_{\varphi,S}(r, \varphi) = -K_{B,S} \left(1 + \left(\frac{r_{o,S}}{r} \right)^2 \right) \sin(\varphi). \quad (6.7)$$

As mentioned, the mathematical derivation and explanation of these terms as well as the assumed coefficients and boundary conditions can be found in Section A.1 in the Appendix. The equations (A.17)-(A.22) show that the field distribution in the motor can be decomposed to the sinusoidally oscillating radial flux components and the tangential flux components. In case of the ideal rotor magnet, they have equal amplitude in the magnet region and thus, produce a constant air gap flux density magnitude

$$|B_\delta| = \sqrt{B_{r,\delta}^2 + B_{\varphi,\delta}^2}. \quad (6.8)$$

In both the air gap and the stator region, this flux density magnitude is elliptical with the radial and tangential flux density having different amplitudes.

6.3.2. Comparison of FE and analytical calculation

In order to validate the result of the analytical field calculation, a finite element simulation of a diametrically magnetized disk within a stator cylinder was conducted. Regarding the stator and air gap dimensions as well as the materials used for all motor parts, the simulation setup was chosen just as in the real prototype, let aside the uncertainties and imprecisions of the applied material models. At first, a 2D setup with linear B-H characteristics was calculated in order to reproduce the conditions of the analytical model. In a next step, the idealized model was evaluated in a 3D simulation with a flat rotor, now taking into account stray flux and edge effects which may be significant since the ratio of axial length to outer rotor diameter is only

$$\frac{l_R}{d_{o,R}} = \frac{1}{3} \quad (6.9)$$

and the magnetic air gap of 4.5 mm is large compared to the rotor diameter. Eventually, the last simulation assumed non-linear characteristics for the stator material in order to approach the real circumstances. Figure 6.3 compares the three simulation results to the analytically calculated flux density magnitude values for each of the regions of interest: the rotor, the air gap and the stator².

²The results of the 3D simulation depend on the regarded axial position. The presented values are taken from the central plane in the axial middle of the motor.

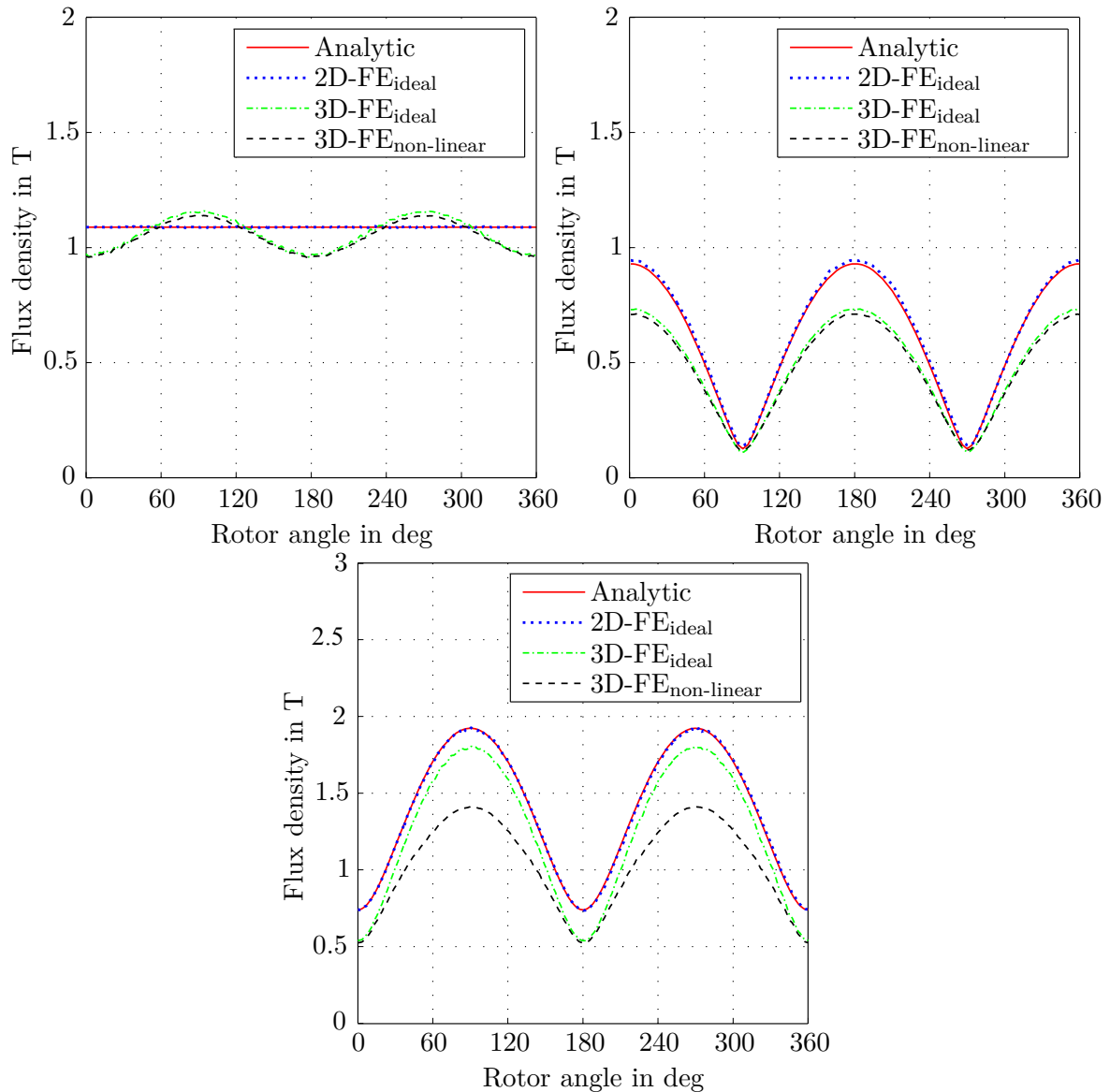


Figure 6.3.: Magnitudes of the flux density vectors in the rotor at the air gap boundary (top left), in the center of the air gap (top right) and in the stator at the air gap boundary (bottom)

The nearly perfect fit between analytical data (solid line) and the idealized 2D simulation (dotted line) in all three regions verifies the analytical model. The plot, however, also shows that the 2D field with its idealized materials - and, therefore, also the analytical model - is far off the 3D simulation with idealized materials (dash-dotted line) and even further off the actual, nonlinear 3D simulation (dashed line). The mean relative flux density values are summarized in Table 6.2. With the 3D values amounting to a mean value of only 73% of the analytical computation result, it becomes clear that using that analytical model for estimating the loss components in such a flat motor would lead to severe errors. This result should be seen as a reminder of how carefully idealized analytical flux density values must be used, even for such trivial geometric shapes as homogeneous concentric rings. Instead, a new 3D simulation with nonlinear material characteristics was conducted for the actual hollow rotor geometry, now also disposing of a back iron. The resulting flux density plot is given in Figure 6.4.

Type of result	Relative change of mean flux density in		
	rotor at air gap boundary	center of air gap	stator at air gap boundary
2D FE, ideal material	+0.1 %	+0.1 %	+0.1 %
3D FE, ideal material	-2.7 %	-21.1 %	-11.9 %
3D FE, non-linear material	-3.7 %	-22.5 %	-27.3 %

Table 6.2.: Comparison of simulated mean flux density values relative to analytical result

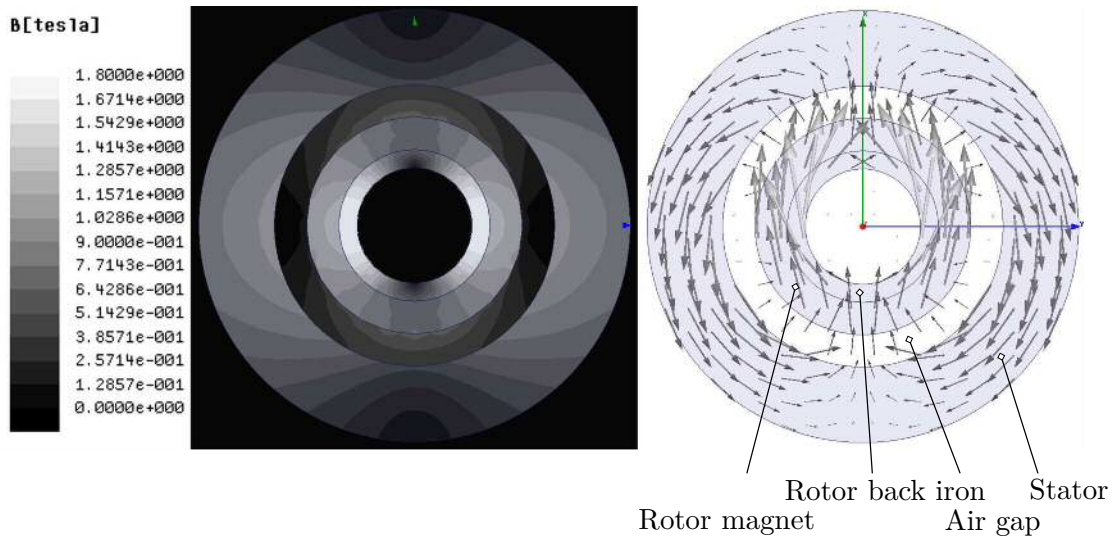


Figure 6.4.: FE-model of the permanent magnet field and the associated flux vector plot.

6.3.3. Armature reaction field

The effect of the coil currents on the magnetic field also needs to be analyzed. In order to simulate this armature reaction, a finite element analysis was carried out with one phase of a toroid winding, conducting 54.5 Aturns which equals a current density of 5 A/mm^2 in the actual winding. Figure 6.5 shows the resulting field in the stator, the air gap and the hollow rotor consisting of the permanent magnet ring and a magnetically conductive inner back iron. The permanent magnet's influence was neglected by setting its remanence flux density to 0 T while keeping its permeability unchanged. The field is drawn in the entire motor region and since the flux density peak value is just slightly above 0.02 T in the stator iron and below 0.02 T in the air gap, the magnetic fields due to the stator currents will be neglected in these regions. In the rotor back iron, a flux density of up to 0.04 T can be observed which seems to be relevant for eddy current losses in the first moment since the back iron is not manufactured as a laminated or SMC part but as a solid steel ring. However, as the principal field frequency is synchronous with the rotor speed, the local flux change rate is very small.

6.3.4. Stator losses

In order to model the stator iron losses per mass unit, p_{Fe} , which combine hysteresis and eddy current losses provoked by the rotating permanent magnet field, well-known

6. Drive losses

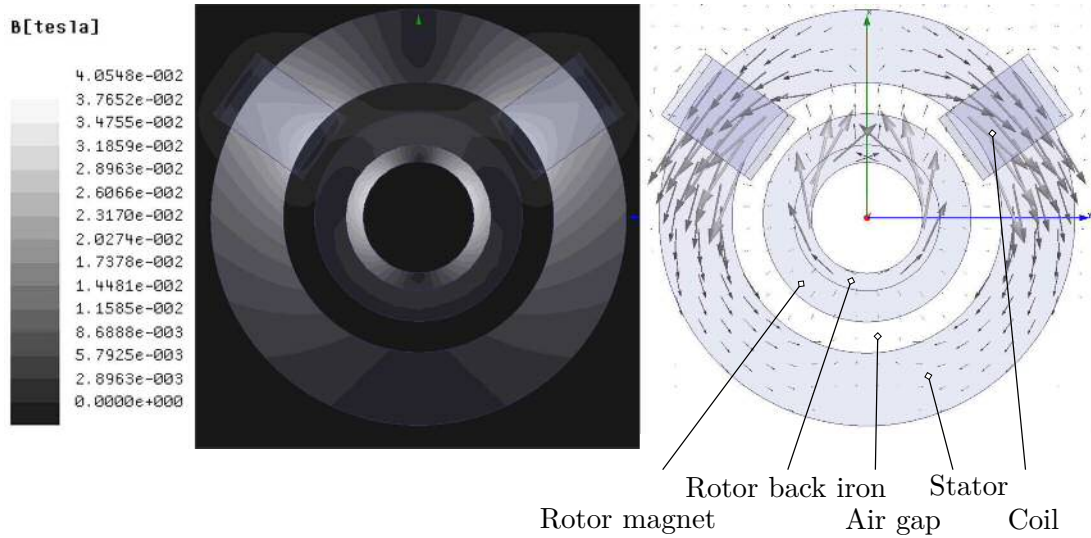


Figure 6.5.: FE-model of the armature reaction field and the associated flux vector plot.

approaches such as the STEINMETZ model

$$p_{Fe} = K_{Fe} \left(\frac{f}{f_0} \right) \left(\frac{\hat{B}}{B_0} \right)^2 \quad (6.10)$$

or the more detailed version in JORDAN'S formulation for one homogenous region

$$p_{Fe} = K_h \left(\frac{f}{f_0} \right) \left(\frac{\hat{B}}{B_0} \right)^{\beta_{Fe}} + K_{ec} \left(\frac{f}{f_0} \right)^2 \left(\frac{\hat{B}}{B_0} \right)^{\beta_{Fe}} \quad (6.11)$$

can be applied. For a region with inhomogeneous flux distribution, as in the given stator cylinder with inner radius $r_{S,i}$, outer radius $r_{S,o}$ and axial length l_R , (6.11) can be integrated to form

$$P_{Fe} = \int_{r_{i,S}}^{r_{o,S}} \left[K_h \left(\frac{f}{f_0} \right) \left(\frac{\hat{B}(r)}{B_0} \right)^{\beta_{Fe}} + K_{ec} \left(\frac{f}{f_0} \right)^2 \left(\frac{\hat{B}(r)}{B_0} \right)^{\beta_{Fe}} \right] 2r\pi l_R \rho_{Fe} dr, \quad (6.12)$$

giving the total stator iron losses. The material-specific loss coefficients K_{Fe} for the combined losses in (6.10) and K_h and K_{ec} for separated hysteresis and eddy current components in (6.11) and (6.12) are used along with the regarded magnetic field frequency f and the peak flux density value \hat{B} . The latter two are set in relation to the values f_0 and B_0 under which the loss coefficients were determined. Finally, the exponent β_{Fe} is used to weight the flux density dependency. The material specific parameters need to be obtained with an alternating flux material testing apparatus because these models assume an alternating flux situation in the concerned motor parts. While this assumption holds true for most conventional, slotted stators, it does not in the present, slotless stator, where most parts are subject to rotating flux consisting of oscillating radial and tangential flux components. As the amplitudes of the radial and tangential flux components are not equal, the flux vector describes an elliptical path. Literature proposes the use of vector orientated models such as the Jiles-Atherton model [62] or the dry friction-like hysteresis model [9], [8]. However, for evaluating these models, several other material

specific parameters need to be known which can only be determined with a rotating flux material testing apparatus. As such an apparatus was not available and since the necessary parameters for the SMC material used in the prototype stator could also not be found in the literature or manufacturer datasheets, the mentioned models cannot be applied directly for calculating the losses.

A different way of taking the elliptical rotating flux characteristic into account is given in a model first presented in [127]. This publication is based on the idea that the elliptical rotating flux can be decomposed into and treated as a combination of alternating and rotating flux. While the original work targeted steel sheet material, two later publications [45] and [46] focus on SMC materials. The parameters for Somaloy 500 SMC material³ and the detailed calculation are presented in Section A.2 in the Appendix.

Comparison of analytic models and measurement

Figure 6.7 compares the standard approach $P_{Fe,Jordan}$, the elliptical rotating flux model $P_{Fe,rotating}$ and the measured values $P_{Fe,measured}$. Two sets of material coefficients for $P_{Fe,Jordan}$ according to (6.11) have been determined. The first one was obtained using an alternating flux testing apparatus at the Institute of Electrical drives and Power Electronics at JKU ($P_{Fe,Jordan-JKU}$). The second one was provided by the manufacturer of the SMC material, *Höganäs AB* in Sweden, whose customer support team offered to measure the machined stator components ($P_{Fe,Jordan-HÖG}$). The parameters from both measurements are listed in Table 6.3. The coefficients for the rotating flux model were obtained from [45] and are listed in Section A.2. The iron loss plot reveals that the three differ-

Table 6.3.: Stator loss coefficients

Parameter	$P_{Fe,Jordan-JKU}$	$P_{Fe,Jordan-HÖG}$
K_h	5.58 W/kg	5.3 W/kg
K_{ec}	0.09 W/kg	0.073 W/kg
β_{Fe}	1.75	1.9

ent analytical models predict slightly different values, with $P_{Fe,Jordan-JKU}$ indicating the highest losses, followed by $P_{Fe,Jordan-HÖG}$ and, finally, $P_{Fe,rotating}$. However, the curve characteristics of all three models, specifying the ratio of linear (hysteresis) to nearly quadratic (eddy current) influence of the frequency are similar. The large deviation from the measured loss values is irritating and can be explained by a problem in the measurement apparatus. The turbocharger driving machine for the iron loss measurement has a bearing shield consisting of an inner aluminum part and an outer ferromagnetic steel part shown in the photograph in Figure 6.6. As the shaft of the turbocharger is thin (4 mm in diameter), the rotor had to be placed close to the oil bearing in order to prevent bending of the shaft at high speeds. Due to the proximity of the bearing shield to the rotating permanent magnet, eddy currents are induced and the field amplitude and its distribution are influenced. In order to quantify the effect on the iron losses, a transient 3D stator core loss simulation was conducted with and without the bearing shield, comparable to the measurement or ideal model situation, respectively.

³According to the website of the Somaloy manufacturer Höganäs AB, Somaloy 500 is close to the used prototyping material in terms of iron losses.

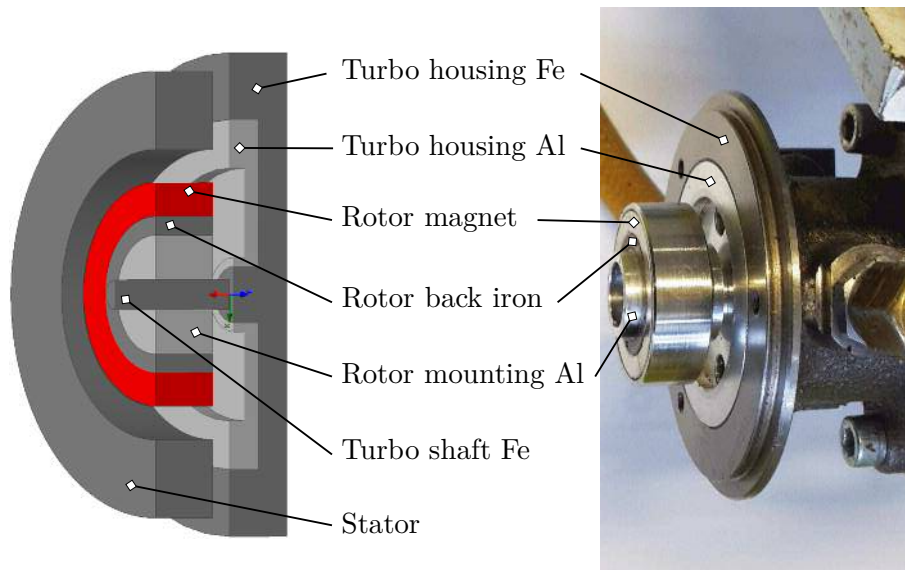


Figure 6.6.: Turbocharger drive end with mounted test rotor (right) and corresponding simulation model (left) for quantification of the bearing shield effect on the stator losses.

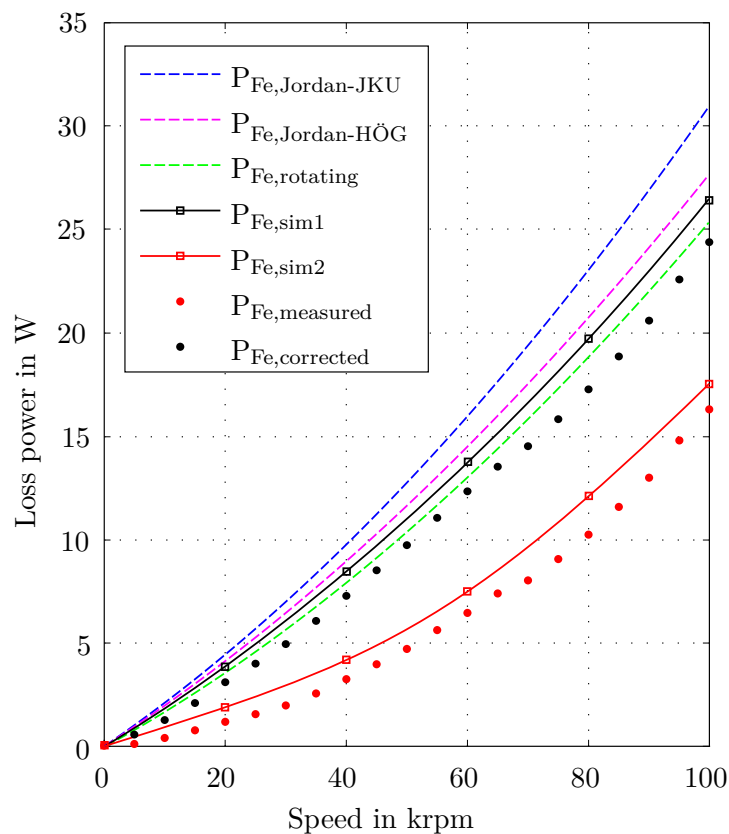


Figure 6.7.: Comparison of iron loss models with measured points. The additional simulation values without turbocharger (Sim1) and with turbocharger (Sim2) allow quantifying the influence of the bearing shield on the measurement and adding it to the measurement for correction.

For the SMC loss characteristic in the simulation, the values provided by *Höganäs AB*

have been used. The resulting iron loss curves have been added to Figure 6.7, explaining the large discrepancy between measurement and analytical model. This flaw practically makes the measurement rig useless. However, as no other driving machine was available, the iron loss measurements have been corrected by adding the difference between the two simulated curves. These *corrected* measurement points shown in Figure 6.7 produce an acceptable fit with the analytical rotating flux model. It is clear that this is not the preferred method of obtaining the iron losses in the prototype stator, however, due to the lack of options, the method seems acceptable.

The small deviation of the other two analytical predictions is within the range of variation for iron loss analysis: A closer look into the literature reveals that especially for SMC materials, there are large variations and uncertainties of loss coefficients and thus, a large deviation of the losses and loss characteristics due to manufacturing (e.g. pressing direction [53] and applied pressure [126], milled surface properties [58], micro structure inhomogeneity [24] due to temperature, etc.).

The rotating flux model with its coefficients given in Section A.2 are used for the loss extrapolation in Section 6.4.1.

6.3.5. Copper losses

The losses produced in the winding system have several different origins. First of all, the conductive copper losses $P_{Cu,i}$ reflect the ohmic losses due to a certain current through a conductor with a certain resistance. These losses depend, however, not only on the current amplitude and the conductor's DC resistance but also on the current's frequency since the effective cross section is influenced by two effects which are discussed in the following sections.

6.3.5.1. Skin effect

The effective cross section within a conductor is reduced due to the changing magnetic field produced by its "own" current. As a consequence of this magnetic field, eddy currents i_{ec} are induced inside the conductor, reducing the current density in its center and increasing it in its edge or *skin*. This well-known *skin effect* is explained in Figure 6.8.

The described current displacement results in a lower effective conductor cross section which in turn leads to higher resistance and, thus, higher ohmic losses. While the effect itself is well known, the consequent analytical loss calculation is rather complex. For the detailed analysis of transformer windings, several approaches have been published in [32, 121, 117, 33]. Based on a frequently cited approach by Ferreira [33], Biela deduces analytic terms for the copper losses including the skin effect P_{skin} in different wire configurations such as foil or litz wires [12]. For the latter type with insulated strands, the total skin effect related losses are simply the sum of the losses in the individual strands and can be calculated as

$$P_{skin} = n_s R_{DC,s} l_w G_{skin} \left(\frac{\hat{i}}{n_s} \right)^2 \quad (6.13)$$

with n_s , $R_{DC,s}$ and l_w standing for the number of litz strands per bundle, the DC resistance per meter of one single strand and the total wire length, respectively. The amplitude of the conducted current is directly entered as \hat{i} , while the current's frequency is indirectly included via the coefficient G_{skin} which is detailed in Section A.3 in the Appendix.

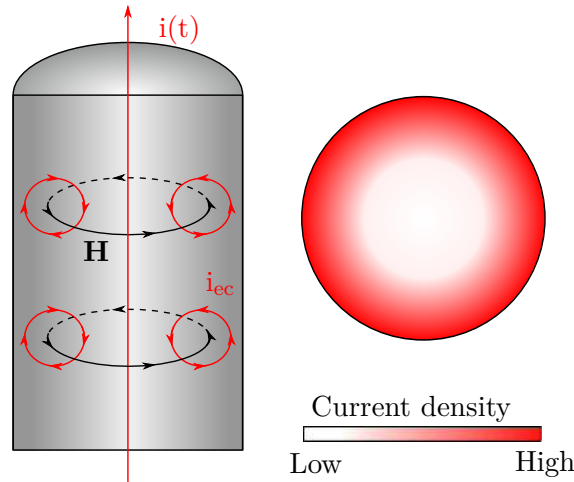


Figure 6.8.: Wire cross section showing the principle of the skin effect with the conducted high-frequency current $i(t)$, the produced magnetic field \mathbf{H} and the induced eddy currents i_{ec} . The right image gives the qualitative current density in the conductor cross section.

6.3.5.2. Proximity effect

Apart from the current through the regarded conductor itself, also the current in the neighboring conductors needs to be taken into account. There are, for one, the currents in the insulated strands of the same wire bundle in case of litz wire, and secondly, also the neighboring wire bundles as a whole. Other than for the skin effect consideration, the eddy current causing field is not concentric in the conductor and, thus, the resulting current displacement also shows a different form than in the above case. Figure 6.9 shows the principle of the proximity effect.

As with the skin effect, the conductor's cross section is reduced and the resulting loss component P_{prox} , given for litz wire windings, can be found in [12] as

$$P_{prox} = n_s R_{DC,slw} G_{prox} \left(\frac{\hat{i}^2}{2\pi^2 d_{bundle}^2} + \hat{H}_{bundle}^2 \right) \quad (6.14)$$

where d_{bundle} represents the diameter of the entire litz bundle, \hat{i} stands for the peak value of the applied sinus current in one strand of the litz wire and \hat{H}_{bundle} is the peak value of the accumulated magnetic field strength due to the neighboring wire bundles. As for the skin effect coefficient F_{skin} , the formulation of G_{prox} is given in Section A.3 in the Appendix. It is worth noticing that the two additive terms of (6.14) target the same effect but describe two different sources - the *internal* current in the conductor itself and an *external* magnetic field. This distinction is made since the wires within a bundle are assumed to be arranged in a circular cross section and also, to hold the same current density, whereas the neighboring wire bundles may be situated quite differently, e.g., in layers. The Appendix gives the derivation of (6.14) regarding the internal proximity effect which was presented in the original publication [12] for litz wire bundles.

The calculation of the *external* field due to the neighboring wire bundles, however, is strongly dependent on the winding form and the wire distribution and is, therefore, described separately in Section A.4 in further detail.

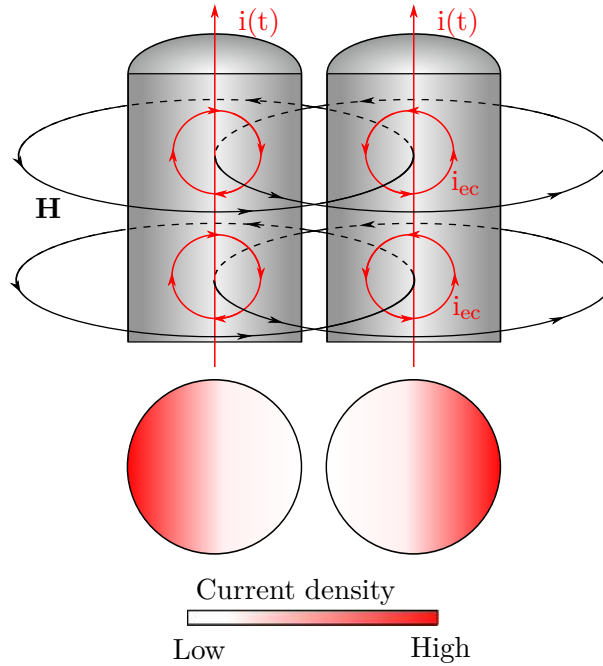


Figure 6.9.: Two neighboring wire cross sections showing the principle of the proximity effect with the conducted high-frequency currents $i(t)$, the produced magnetic fields \mathbf{H} and the induced eddy currents i_{ec} . The image below gives the qualitative current density in the conductors' cross sections.

6.3.5.3. Comparison to measurement

The total losses due to the skin effect and proximity effect

$$P_{Cu,i} = P_{skin} + P_{prox} \quad (6.15)$$

cannot be obtained directly from the power meter measurement displayed in the overall loss diagram in Figure 6.2 as the component $P_{Cu,i}$ changes significantly with the current value but shows only very small changes due to the frequency-related effects described above. Therefore, an additional measurement was carried out in order to reflect the losses due to the mentioned effects. Instead of directly obtaining the losses, the resistance of one coil pair was measured with a frequency-variable *Instek LCR-816* LCR-meter over a frequency range of 0 to 5 kHz. Figure 6.10 shows the increase of the measured values and compares them to the increase of the analytically calculated values by evaluating (6.15) and dividing it by the squared current value used for the calculation. The experiment values show an offset of 0.4 m Ω (measured 32.1 m Ω versus calculated 31.7 m Ω) compared to the calculated resistance values but this is related to small differences in the actual wire length. The resistance increase shown in the figure due to frequency for both curves is about 0.3 m Ω which is close to the LCR-meter resolution. Nevertheless, the resulting agreement between measurement and analytic result is an acceptable validation of the chosen model. Figure 6.10 clearly shows that, for the chosen litz wire configuration (225 strands, diameter 0.071 mm), the frequency dependency of the copper losses is absolutely negligible since the total increase for all five windings is below 0.1 W at nominal speed. However, the model becomes relevant if different wire configurations are to be analyzed.

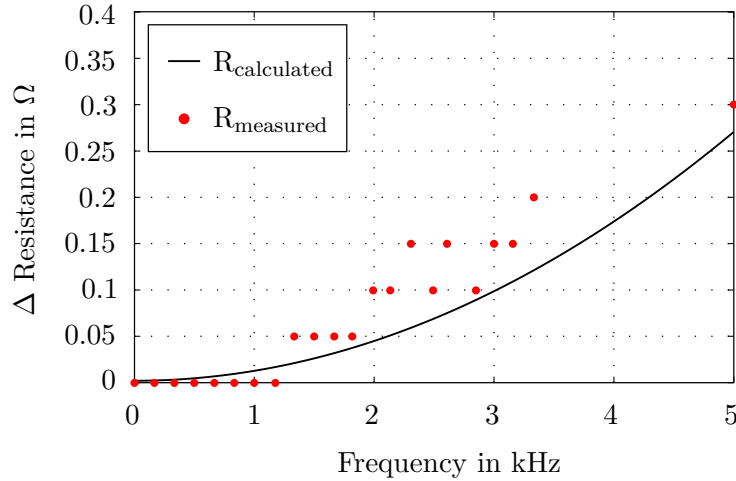


Figure 6.10.: Copper resistance increase over current frequency as a measure for the loss increase with frequency.

6.3.5.4. Losses due to permanent magnet field

Other than the loss components above, the remaining copper losses do not depend on the conducted current but on the rotating permanent magnet field. The analytical model for this component $P_{Cu,M}$ spawns from the same idea as the description of the external proximity effect losses since that formulation can be used to model the influence of a general external magnetic field. That field can be taken into the model as long as it is uniform within the regarded conductor, a condition which is presumed to be fulfilled as the radial winding space is rather small and the field amplitudes do not vary tremendously in the radial direction. Using (6.14) with the external permanent magnet peak field strength

$$\hat{H}_\delta = \frac{\hat{B}_\delta}{\mu_0} \quad (6.16)$$

which is deduced from the peak air gap flux density of approximately $\hat{B}_\delta = 0.5$ T (c.f. Figure 6.4), the losses in all five windings due to the rotating permanent magnet field can be described as

$$P_{Cu,M} = 5 \cdot n_s R_{DC,s} \frac{l_w}{4} \cdot G_{prox} \hat{H}_\delta^2. \quad (6.17)$$

It has to be noted that only one fourth of the total wire length is taken into account since only the winding part at the inner stator diameter is actually permeated by the rotor's magnetic field. Of course, there is a certain error to this assumption since there are also stray fields permeating other parts of the winding. When (6.17) is compared to the measurement carried out at the high-speed test rig presented in Section 6.2, that error is reflected in the deviation of the measured and calculated loss values as shown in Figure 6.11. Again, the maximum resolution of the measurement apparatus (0.01 W at 10 krpm, 0.1 W at 100 krpm) is quite coarse which is recognizable in the significant value steps between the different measurement points at high speeds. However, the agreement is within an acceptable range and the curve characteristic of the analytic model reproduces the real circumstances acceptably.

Finally, all three main components - the skin effect related losses including the DC ohmic losses, the proximity effect related losses due to the conducted current, and the

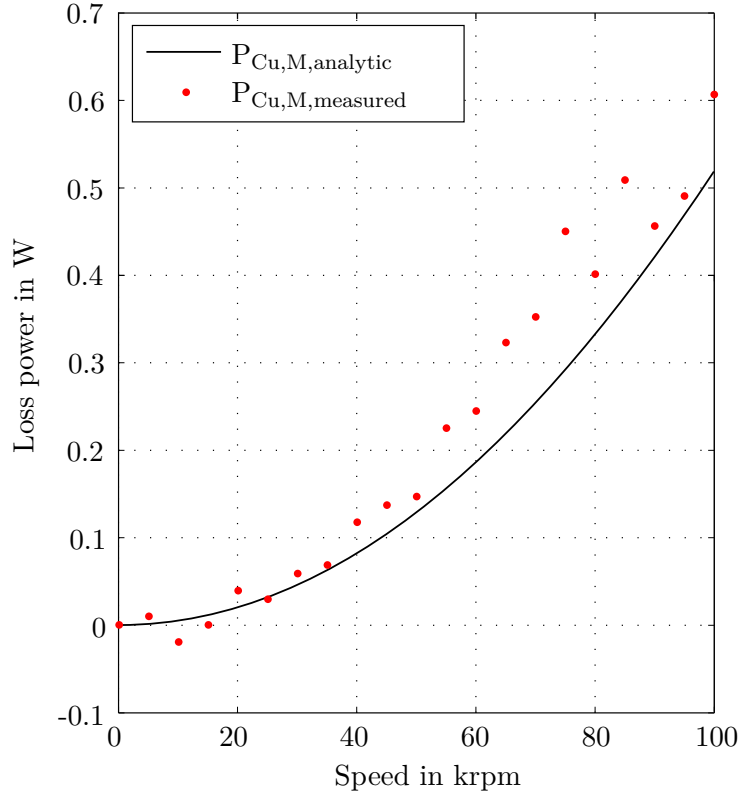


Figure 6.11.: Copper losses due to permanent magnet field. The negative value is due to a measurement imprecision and the differential measurement method.

losses due to the external permanent magnet field - can be summarized into

$$P_{Cu,total} = 5 \cdot n_s R_{DC,s} l_w \cdot \left(F_{skin} \left(\frac{\hat{i}}{n_s} \right)^2 + G_{prox} \left(\frac{\hat{i}^2}{2\pi^2 d_{bundle}^2} + \left(\hat{H}_{bundle} + \frac{\hat{H}_\delta}{2} \right)^2 \right) \right), \quad (6.18)$$

where all five phases of the motor are considered.

6.3.6. Air drag losses

Apart from the losses caused by the magnetic field in the various motor components, the air drag consumes considerable power. A lot of empirical data for certain geometries and experimental conditions are available from the first half of the 20th century. However, no experimental loss values could be found for the given rotor geometry and speed region, which is why we need to find an analytical model in order to estimate the occurring air drag losses. Since the typical speed range lies far above the speeds where laminar flow occurs, only turbulent behavior is regarded.

6.3.6.1. Rotor disk friction

The friction losses at the rotor faces can be modeled using an approach presented in [102, Chap. 12] to describing the friction due to axial flow against a rotating disk. The disk experiences the drag torque

6. Drive losses

$$T_{Air,z} = \frac{c_{drag,z}}{2} \rho_{Air} \Omega^2 r_{o,R}^5 \quad (6.19)$$

which rises with the temperature dependent mass density of air ρ_{Air} as well as with the considered rotor angular speed Ω and the outer rotor radius $r_{o,R}$. For the case of no forced axial flow, the drag coefficient $c_{drag,z}$ is implicitly defined in [102, Chap. 20], referencing [35], as

$$\frac{1}{\sqrt{c_{drag,z}}} = \frac{1}{\kappa\sqrt{8}} \ln(Re\sqrt{c_{drag,z}}) + 0.03, \quad (6.20)$$

where the empirical Kàrmàn constant is $\kappa = 0.41$. Re is the Reynolds number

$$Re = \frac{r^2\Omega}{\nu_{Air}} \quad (6.21)$$

with ν_{Air} being the kinematic viscosity of air. The drag coefficient in (6.20) is defined in order to consider both sides of a rotating disk. Therefore, the resulting losses for both rotor faces can directly be written as

$$P_{Air,z} = T_{Air,z}\Omega. \quad (6.22)$$

As mentioned above, the model describes the loss situation for no forced axial flow as it is the case in the drive considered here. However, the present hollow cylinder rotor is different from the full disk in the model. This model error will effect the analytical result but as mentioned later in Section 6.3.6.3, the discrepancy is small since the air drag losses depend heavily on the relevant radius.

6.3.6.2. Air gap friction

The losses in the thin air gap can be described using the turbulent Couette current model given in [102, Chap. 17]. The assumption of a turbulent flow might not be true for very low rotational speeds but due to the strong dependency of the air drag losses on the rotational frequency, only the regions of high speeds and thus, of turbulent flow, are of interest. Defining the shear stress at the cylindrical rotor surface A_δ as

$$\tau_\delta = \frac{c_{drag,\varphi} \rho_{Air} v_\delta^2}{2} \quad (6.23)$$

allows calculating the resulting load torque

$$T_{Air,\delta} = \tau_\delta A_\delta r_{B,o} \quad (6.24)$$

using the rotor outer radius $r_{B,o}$. The velocity v_δ in the middle of the air gap can be approximated easily for a given rotor speed since the fluid's speed is zero at the stator surface and equal to the rotor speed at the rotor surface. In the middle of the air gap, it is half of the rotor speed due to the symmetry of the air gap - even though there is no linear velocity distribution as in the laminar flow case. This becomes especially plausible if the situation between the inner stator surface and the outer rotor surface is imagined as two parallel plates whereof one is static and the other one is moving along the first one in a constant distance.

Finally, the drag coefficient is defined as

$$c_{drag,\varphi} = \frac{2\kappa^2}{(\ln(Re_\delta))^2} \quad (6.25)$$

where again, the Reynolds number is used. Other than with the loss calculation for the rotor faces, it is defined in the tangential flow case as

$$Re_\delta = \frac{v_\delta \delta}{2\nu_{Air}}. \quad (6.26)$$

for a certain air gap width δ . The air drag losses in the air gap can, hence, be written as

$$P_{Air,\delta} = T_{Air,\delta} \Omega. \quad (6.27)$$

6.3.6.3. Combined air drag losses

The proposed analytic model for the combined losses of the two rotor faces and the air gap is compared to the measurement data in Figure 6.12. According to the proposed model, 72 % of the losses are created by the disk friction at the rotor faces, only 28 % are being lost in the air gap at a speed of 100krpm. The radial air gap width in the test system at the time of the measurement was 0.5 mm whereas the axial air gap was 3 mm.

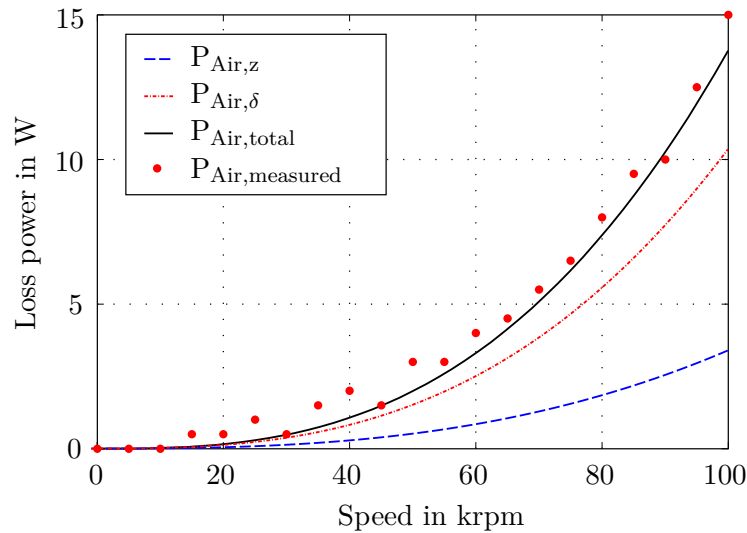


Figure 6.12.: Analytical air drag losses compared to measured data

The results in Figure 6.12 seem to suggest that the model is very accurate whereas they really should be regarded as a well estimated guess. This harsh verdict is based on the fact that the intense study of literature in this field showed how inaccurate and sensitive the predominant majority of analytic flow models are. The mentioned inaccuracy of the model describing a full disk, whereas the actual rotor is a hollow ring, also adds to that verdict even though the influence in the present case is negligible; When the sensor pin which is located inside the ring with an outer diameter of 11 mm is regarded as a rotor spinning at 100krpm while the actual rotor stands still, the model yields additional losses of 125 mW.

The air drag losses measured above produce an almost perfect fit with the proposed model but, nevertheless, the measurement can be challenged since the applied vacuum in

the vacuum chamber only reached pressures of 30 mbar (*fine vacuum*⁴). As a further loss reduction can be expected with decreasing pressure, another measurement was carried out where the pressure related drop in the complete power consumption of the disk drive spinning at 60krpm was monitored. Since this second measurement has been carried out separately from the original measurements, the vacuum chamber arrangement had to be set up again. The tightness of the cable-seal which was achieved in the original measurement could not be reproduced in the second one and, therefore, the minimum pressure reached was only 70 mbar, compared to 30 mbar in the first measurement. Nevertheless, Figure 6.13 clearly shows that the influence of the pressure reduction increases with stronger vacuum but it also makes clear that the error due to the imperfect vacuum does not completely overthrow the proposed model.

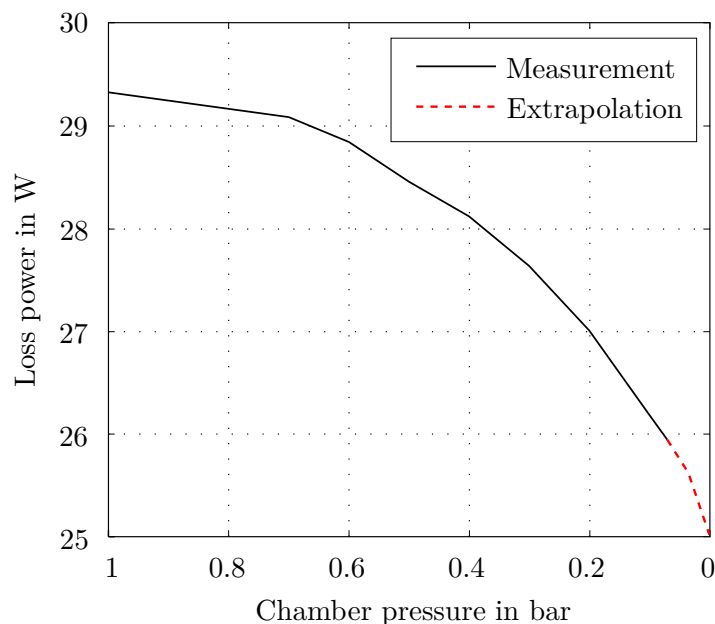


Figure 6.13.: Measured power consumption inside a vacuum chamber with an extrapolation to absolute vacuum.

Despite this criticism, the obtained relationship is of great value when seen within the strategy presented in the introduction to this chapter. The analytic model is suitable for reproducing the measurement results and should allow predicting the losses for other similar drive designs within a certain variation space.

6.3.7. Thermal measurement

In order to examine the thermal situation in the actual prototype, the motor was set to spin at 60krpm and was monitored with a thermographic camera until a stable thermal equilibrium was reached. There are several conclusions and remarks concerning the thermal image shown in Figure 6.14.

- The coils are the hottest spots since they are a main source of losses being dissipated in a smaller volume than, for instance, the stator core losses.

⁴“*Fine vacuum*” or “*Medium vacuum*” defines a pressure range of 30 mbar to 1 μ bar.

- The complete stator with the winding system is cast in a round epoxy form which protrudes axially out of the top plane of the housing. The two adjacent surfaces marked *stator* and *housing* in the figure are not directly in contact as they have different axial heights. This is the reason for the clear temperature difference between the housing and the epoxy-coil-block on the outer side of the stator ring and between the epoxy-coil-block and the air gap on the inside.
- The air gap temperature is actually the temperature of the housing below since the temperature of the air itself is not recognized by the thermal imaging camera. Being made of aluminum, the housing temperature is very evenly distributed.
- A numerical evaluation of the measured values states that the mean back iron temperature is only $0.35\text{ }^{\circ}\text{C}$ higher than the mean temperature of the permanent magnet ring while both range significantly below the surrounding temperatures. One reason for these lower temperature levels might be the slight draft of air due to the rotating ring. A second reason, however, is that the magnetic fields in the rotor parts are mostly synchronous to the rotational speed and, therefore, cause almost no eddy current losses. This assumption is supported by the fact that even though the sintered magnet material and the back iron steel have significantly different electrical conductivities, both parts have almost identical temperatures. If the magnetic field due to the stator currents shown in Figure 6.5 was not synchronous to the rotational speed, the solid steel back iron would be significantly hotter than the permanent magnet ring. This observation confirms that the loss influence of the back iron can be neglected.
- The loss power from the stator core is transferred to the housing since the core is directly contacted by the aluminum. This is not well visible in the image since these contacting notches are buried about 5 mm inside the epoxy block.
- The attentive reader has surely recognized the especially high temperature of one of the stator coils (mean value of $6.3\text{ }^{\circ}\text{C}$ above the mean value of the other coils). Thorough analysis showed that during the mounting procedure, several strands of the litz bundle of this coil were broken, thus limiting the effective cross section and increasing the conductive copper losses. Also the corresponding second coil half is clearly hotter than the average coil temperature.

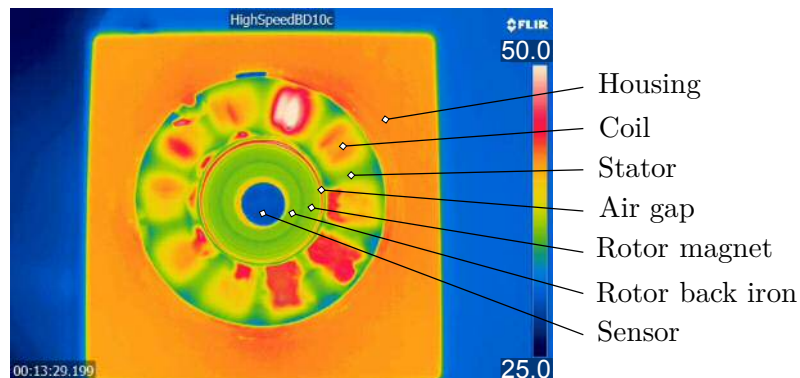


Figure 6.14.: Thermal image of the motor spinning at 60 krpm after the thermal equilibrium has been reached

6.3.8. Efficiency measurement

The determination of the drive efficiency in a classical, direct measurement approach is difficult due to several reasons.

- It is not possible to attach a torque sensor to the levitating rotor without heavily influencing the rotor movement.
- It is very hard to obtain a rotating torque sensor suitable for 100 krpm.
- It is a tempting method to spin the rotor and use an eddy current braking mechanism to draw output power. One possibility would be, e.g., a copper plate which is placed directly next to the spinning rotor's axial surface and which is attached to a non-rotating torque sensor. Unfortunately, this does not work well in the present case since the induced eddy currents have a backlash on the rotor field and, more importantly, the output power of this method amounts to several ten watts, only. Placing additional magnets on the rotor for an increased braking effect is equally impossible for weight, balancing and magnetic disturbance issues and so is the mounting of the eddy current brake on the rotor. This last possibility is even more problematic since the rotor-mounted conductive part would have to be very small and dissipate significant energy, e.g., around 200 W which would heat it beyond any tolerable temperature in a matter of seconds.
- The only plausible way of drawing significant output power is by attaching an impeller wheel to the rotor as presented in Chapter 5. Unfortunately, this output power cannot be measured appropriately since the aerodynamic losses inside the impeller housing are neglected when measuring output pressure and output volume as shown in Section 5.4.2. The deducted efficiency would characterize the drive - compressor - unit as a whole but this is neither the scope of this work, nor would it be representative due to the inability to control the axial impeller gap which needs to be as small as possible for high efficiency of radial compressors.

This leaves the field to indirect methods of efficiency determination. However, the necessary steps also have to be considered carefully:

- Measuring the AC power P_{AC} , provided by the power electronic circuit during compressor operation with a high-resolution power meter (here, a Yokogawa WT 1800 Power Analyzer) marks the starting point.
- The same power meter is used to determine the rms-currents I_{rms} in all m motor phases of the 5pd bearingless drive. Since the high-frequency influence on the coil resistance has shown to be negligible (cf. Section 6.3.5), the copper losses $P_{Cu,i}$ can be obtained from

$$P_{Cu,i} = \sum \left(R_m I_{m,rms}^2 \right) \quad \forall m \in [1, 5]. \quad (6.28)$$

- The difference between P_{AC} and $P_{Cu,i}$ still contains air drag, iron losses, and bearing and excess losses as shown in Figure 6.2. Even if the iron losses were precisely predictable, the bearing and excess losses could not be determined and deducted separately. Hence, a no-load run-up without impeller wheel is conducted over the same speed range as the load-measurement, giving $P_{AC,no-load}$ and $P_{Cu,i,no-load}$. By deducting the air drag losses P_{Air} for the no-load case which have been obtained in

Section 6.3.6.3, we end up with the sum of the speed-dependent iron and bearing and excess losses.

- The mechanical output power P_{out} of the compressor measurement, containing only the air power, can then be calculated as

$$P_{out} = P_{AC} - P_{Cu,i} - (P_{AC,noload} - P_{Cu,i,noload} - P_{Air}) \quad (6.29)$$

which, finally, allows to calculate the drive efficiency

$$\eta = \frac{P_{out}}{P_{AC}}. \quad (6.30)$$

Figure 6.15 shows the efficiency and the key power measurements with a measured maximum of 80%.

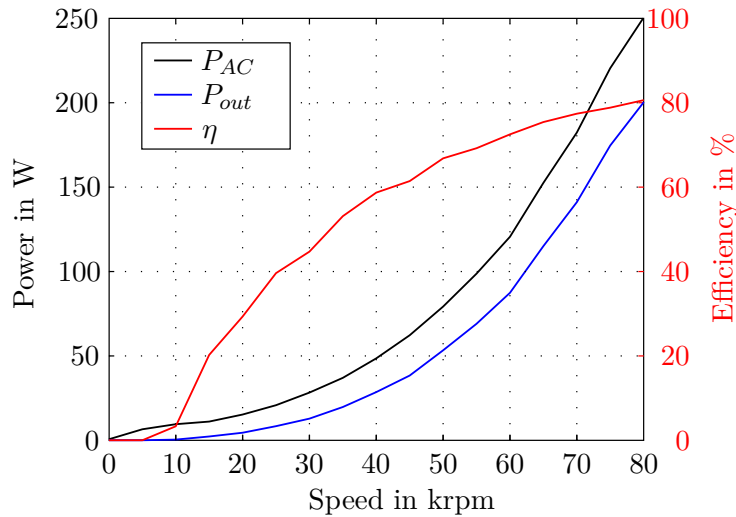


Figure 6.15.: AC power consumption, output power and resulting efficiency of the high speed bearingless drive unit.

6.4. Design variation

The models obtained in the previous section are now used to predict the losses which can be expected for certain design parameter variations such as

1. an increased rotational speed of up to 200 krpm,
2. a change of the used wire dimension for the stator winding,
3. a change of the physical air gap in radial direction or
4. an increase in the rotor permanent magnet pole number.

6.4.1. Increased speed

For the 5pd prototype, the rotational speed was limited to 115 krpm by the mechanical stability of the rotor which was vividly demonstrated in Chapter 5. As this limit could be

6. Drive losses

raised by various constructional measures as presented in Section 4.5, it is reasonable to project the loss models to an increased speed limit. Since this number was already used in the mentioned proposals for the possible mechanical design adaptations, the maximum speed for the projection shown in Figure 6.16 was set to 200 krpm.

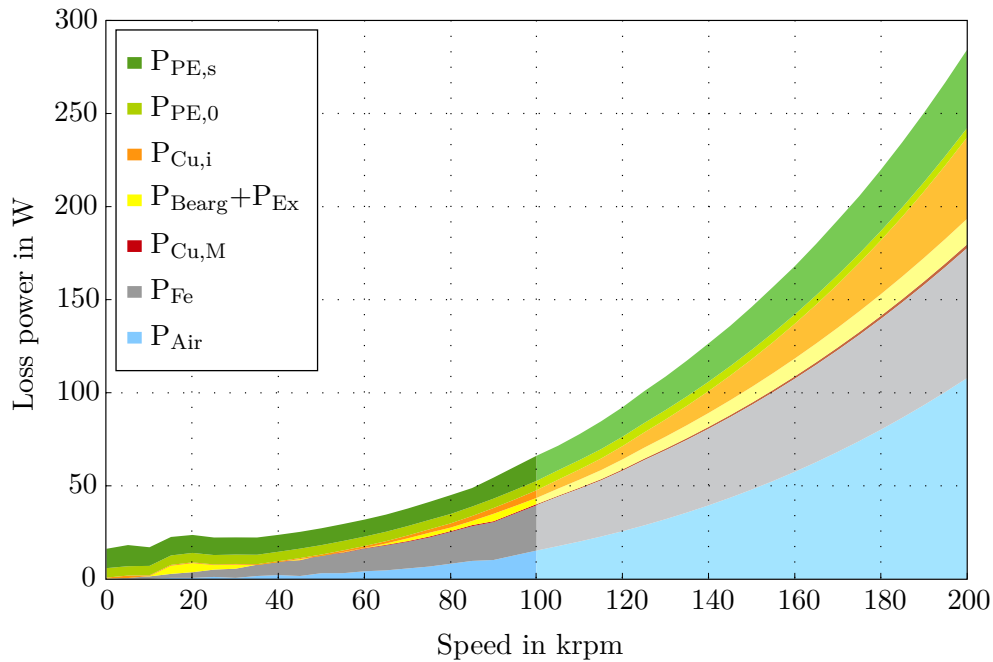


Figure 6.16.: Measured losses up to 100 krpm with analytical projection up to 200 krpm. Again, as in Figure 6.2, the copper losses due to the permanent magnet field are represented only by a thin line.

The projection shown in Figure 6.16 is based on the following assumptions:

Air drag losses The model presented in Section 6.3.6 was projected to a rotational speed of 200 krpm without changing the geometrical parameters such as the radial or axial air gap.

Iron losses Using the elliptical rotating flux model presented in Section (6.3.4) yields the projected iron loss curve. As the flux density amplitude is constant, the frequency of the magnetic field is the only changing parameter.

Bearing and excess losses As the excess losses P_{Ex} constitute an unknown component and since the bearing power $P_{Bearing}$ will not increase significantly with speed, the entire loss component is projected to the new maximum speed in the same linear manner as they increased from their minimum value at 40 krpm up to 100 krpm. Of course this may be a very coarse estimation because the unknown effects hidden in the excess losses may be non-linearly dependent on the rotational speed.

Copper losses In order to scale the copper losses, the expected power necessary to overcome the air drag, the iron losses, the bearing power and the excess losses needs to be calculated. The result allows calculating the expected phase currents when the induced

voltage is scaled linearly to the target speed. Additionally applying the increased frequencies of the phase currents and of the permanent magnet field with constant amplitude to the relationship described in (6.18) gives the estimated copper losses.

Power electronics The standby power demand $P_{PE,0}$ for the power electronics is held constant while the switching losses $P_{PE,s}$ are scaled with the projected phase currents. Of these, one part represents the conducting losses by multiplying the square of the projected currents with the MOSFET resistance $R_{DS,on}$. The other part, representing the actual switching losses, is extrapolated with a frequency dependent factor for the projected phase currents which was identified from the measurements by deducting $P_{PE,0}$ and the conducting losses from P_{PE} and dividing the result by the phase current.

6.4.2. Wire selection

Using litz wire does effectively reduce the field-related losses but also decreases the available copper cross section due to the strand insulation and the litz packing factor. There is, hence, an optimum between thick strands (high cross section for low DC-losses) and thin strands (low skin and proximity effect related losses). By using the model presented in Section 6.3.5, six different wire configurations (five litz wire types and one solid wire) have been analyzed for an enlarged operation range from 0 krpm–200 krpm in a loaded scenario with a magneto motive force of 220 ampereturns⁵ at maximum speed.

Theoretical comparison At first, theoretical litz wire configurations (wire types no. 1-5) with commercially available strand diameters from 0.05 mm to 0.355 mm were considered.

The solid conductor (wire type no. 6) was chosen with 1 mm diameter including 25 μm of insulation, allowing a rather dense wire packing as the available winding space in the regarded prototype was 2 mm in radial height. Filling the available winding space with type 6 wire yields a maximum of 20 turns. In order to obtain a solid basis for comparison, the same number of turns was fixed for the litz wires no.1-5 as well. This means that the induced voltage is identical and thus, the conducted current can also be set to the same value for all configurations.

The configurations are titled *theoretical* because only the strand diameters d_s and the number of winding turns N are fixed, whereas the number of strands n_s per bundle will be calculated in order to completely fill up the available winding space A_{WSpace} . This allows judging the basic influence of the strand diameter without being limited to commercially available wire bundle types which would distort the result. Therefore, the necessary area for one strand A_s which includes its insulation and its share of empty space inside the wire bundle was calculated using the wire bundle diameter d_{bundle} and strand number values from commercially available litz wire with identical strand diameter. When there is no external insulation or silk wrapping which keeps the litz bundle in its original shape, it can be deformed easily. We can, therefore, assume that the litz wire bundles can be evenly distributed into the available winding space. The possible number of strands per bundle was calculated as

$$n_s = \frac{A_{WSpace}}{N \cdot A_s} \quad (6.31)$$

⁵The magneto motive force was chosen to be 220 ampereturns in this loaded scenario since this equals a current density of 20 A/mm² in the winding configuration of the actual prototype.

6. Drive losses

Wire type no.	Theoretical wire type	No. of turns	$A_{Cu,Total}$	Fill factor
1	276.4x0.05 mm	20	11.07 mm ²	0.489
2	143.9x0.071 mm	20	11.62 mm ²	0.513
3	77.3x0.1 mm	20	12.39 mm ²	0.548
4	21.4x0.2 mm	20	13.39 mm ²	0.592
5	7.3x0.355 mm	20	14.48 mm ²	0.640
6	1x1.0 mm	20	14.78 mm ²	0.653

Table 6.4.: Wire characteristics for theoretical configurations

For the litz wire types in the theoretical case with non-whole strand numbers, the fill factor is equal to the internal litz fill factor.

by dividing the available winding space per coil by that necessary strand area. Of course, this means that for these theoretical configurations, the litz wire types have non-whole numbers of strands. Also, the resulting total copper cross sections $A_{Cu,Total}$ of the complete windings are quite different. Table 6.4 gives the calculated wire characteristics for the mentioned configurations.

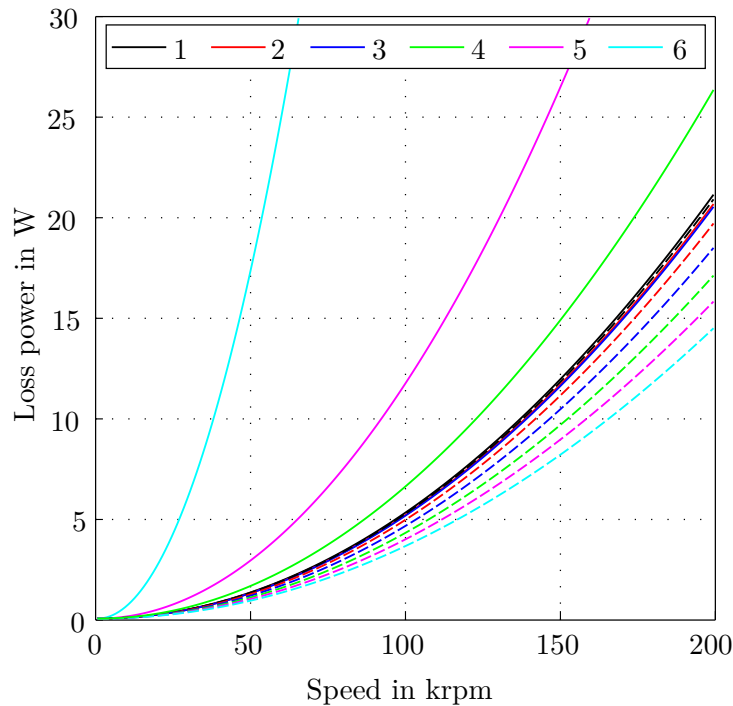


Figure 6.17.: Comparison of the DC-copper losses (dashed lines) and the total copper losses according to (6.18) (solid lines). The theoretical wire configurations are listed in Table 6.4.

Figure 6.17 shows the comparison between the ohmic DC-losses and the total copper losses according to (6.18) which take the frequency dependent effects due to the conducted current and due to the rotor's permanent magnet field into account. It becomes clear that the ohmic DC-losses alone are a very misleading criterion for selecting the best wire

configuration since the litz wires with the thickest strands and, especially, the solid wire seem to provoke the lowest losses because they provide the highest fill factor. When the additional effects described in Section 6.3.5 are taken into account, the configurations no. 6 and no. 5 appear as the worst choices and the thinly stranded wires no. 1 - 4 are preferable. For the enhanced target speed of 200 krpm, configurations no. 3 and no. 2 would look most promising if the strand number could be chosen freely.

Comparison of available wire types In order to help select the most suitable wire selection for a real drive, a comparison of available wire types was conducted. The compared wire configurations are listed in Table 6.5 and dispose of a copper cross section per wire $A_{Cu,Wire}$ similar to that of the 225x0.071 mm wire used in the prototype. All

Wire type no.	Wire type	No. of turns	$A_{Cu,Wire}$	$A_{Cu,Total}$	Fill factor
1	540x0.05 mm	9	1.09 mm ²	10.82 mm ²	0.478
2	225x0.071 mm	12	0.91 mm ²	10.90 mm ²	0.482
3	120x0.1 mm	12	0.96 mm ²	11.54 mm ²	0.510
4	30x0.2 mm	13	0.94 mm ²	13.16 mm ²	0.582
5	10x0.355 mm	13	0.99 mm ²	13.86 mm ²	0.613
6	1x1.0 mm	20	0.74 mm ²	14.78 mm ²	0.653

Table 6.5.: Characteristics for commercially available litz wire types (no. 1-5) and the solid conductor which was chosen above for the theoretical configuration comparison (see Table 6.4)

The fill factor contains the internal litz fill factor and the fill factor due to the specific wire area and the limited winding space.

configurations fill the winding space with as many winding turns as possible⁶ and conduct the same 220 ampereturns, equal to the theoretical comparison. Of course, the resulting current densities vary due to the different fill factors and achievable winding turns. Figure 6.18 clearly shows the advantage of the thinly stranded wire configurations no. 1 - 4 over the thickest litz version no. 5 and, especially, the solid wire. Like in the theoretical comparison, the additional frequency and external field related losses rise with increasing strand diameter. Since the bundle with no. 4 strands fits the available winding space quite well and, therefore, has a high fill factor, it achieves losses similar to those of the first three wire types. Configurations no. 3 and no. 2 with strand diameters of 0.1 mm and 0.07 mm, respectively, show the lowest losses at 200 krpm. Setting a different load point with a different number of ampere turns will of course change the ratio of DC to total copper losses and the ranking of the wire types may vary which means that the optimum needs to be found for the most relevant load scenario.

⁶The solid wire type no. 6 was again set to a diameter of 1 mm since otherwise, the entire second winding would have been eliminated which would have led to an unrealistic fill factor. The copper cross section per wire is, therefore, below the respective value of the litz wires.

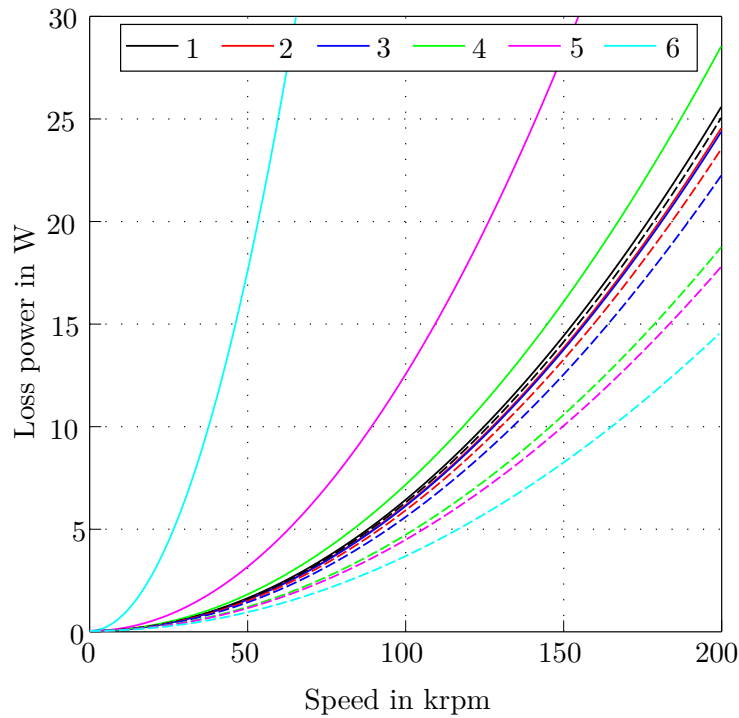


Figure 6.18.: Total copper losses of different actual wire types in loaded case for speeds from 0 krpm–200 krpm

6.4.3. Variation of the radial air gap

The proposed model allows comfortably varying the radial air gap dimension for the different variants presented in Figure 6.19. It is clearly visible, that the air drag losses increase quite significantly by 11 % when the air gap is reduced from 1 mm to 0.25 mm but only decrease by 4 % when the air gap is doubled to 2 mm. Even though the relative

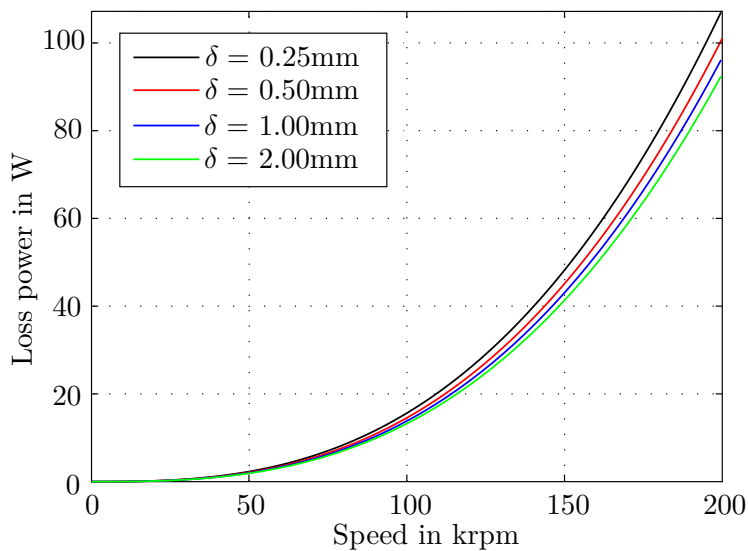


Figure 6.19.: Air drag losses due to different values for the radial air gap δ

change is impressive, this loss component should probably not gain too much weight in the design process. A promising approach which would demand a narrow air gap should surely not be dropped because of the expected air drag losses as the absolute change is

rather small.

6.4.4. Increased pole number

A 4-pole rotor does not feature the stiffness anisotropy of a diametrically magnetized rotor (see Chapter 2). However, also the stator loss situation is changed: On the one hand, a higher pole number results in higher field frequency at the same mechanical speed, on the other hand, the flux density in the stator yoke is lower due to the shorter pole distance. Nevertheless, the peak value in the air gap is practically identical. The iron losses according to the elliptical rotating flux model presented in Section 6.3.4 and the total winding copper losses according to (6.18) can be compared for the 2-pole and a 4-pole rotor. As for the wire selection and air gap variation, the comparison is extended to higher rotational speeds. Figure 6.20 shows that the expected iron losses are considerably

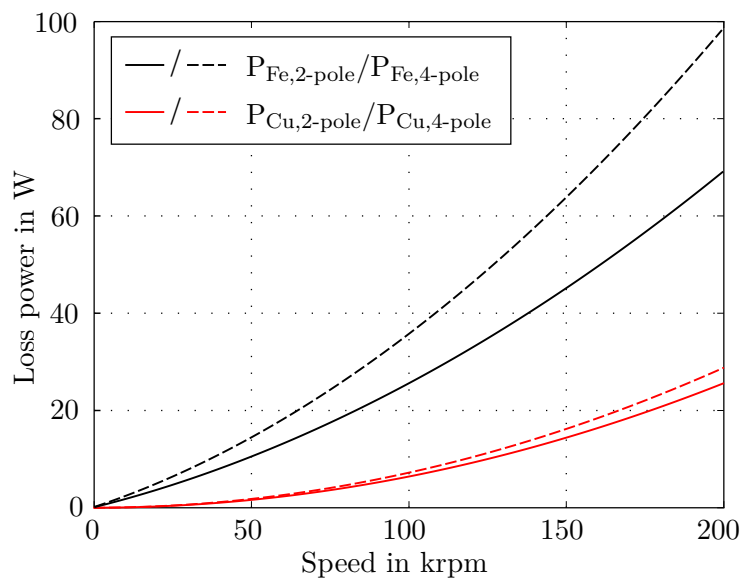


Figure 6.20.: Stator iron losses and total winding losses of 2-pole and 4-pole rotor design

higher for the 4-pole rotor design: +37% at 100 krpm and +39% at 200 krpm. Also the winding losses are higher but the increase is not significant for the 225x0.071 mm wire.

6.5. Conclusion and criticism

After the introduction at the beginning of this chapter, the measurement of losses at the 5pd prototype, together with the measurement techniques and a description of the occurring loss components are given in the second sub-chapter. The following analytical descriptions for explaining and modeling the iron, copper, and air drag losses conclude the first part of the chapter.

At this point, the strategy of presenting the obtained measurement results before building and evaluating analytical models shall be recapitulated. The primary motivation of this strategy is to use the measurement as a motivation and as a corrective guideline for the modeling process. In many works, the modeling and experimental verification process consists of the satisfied appraisal when the distance between a smooth analytic curve and a dotted measured curve is small. In the last part of this chapter, however, the obtained models are applied in various directions in order to estimate *what cannot yet be measured*. The increase of the target speed up to 200 000 rpm, the wire selection based on a different load situation, the change of the geometric air gap dimension and the change of the rotor pole number have been investigated in order to demonstrate the potential and, eventually, give the justification for the entire loss power modeling process.

Finally, some criticism needs to be conceded. Even though the measurements have been carried out as carefully and accurately as possible, some results, e.g., the measurement of the permanent magnet field related copper losses are imperfect as the bearingless motor setup and the necessary resolution are very demanding. Also, the iron loss measurement suffered from a flaw in the test rig as the bearing shield of the turbocharger substantially influences the magnetic field of the test rotor. The simulation approach for correcting the measurements in Section 6.3.4 presented the best available option, however, for future measurements, a new test rig should be acquired, providing:

- non-ferromagnetic shaft material,
- a shaft diameter of at least 8–14 mm which allows placing the test rotor at least 30–40 mm away from the last bearing point without running into flexible shaft bending problems,
- a free space around the rotor avoiding any electrically or magnetically conductive materials in the area of the rotor field,
- suitable mechanical bearings which, ideally, can be easily replaced, for the shaft support, and
- an electric drive for precise speed control.

7. Conclusion and outlook

This work has started out with a map of bearingless disk drives taken from realization examples presented in the literature (cf. Figure 1.5). At the end of this work, that figure is updated to Figure 7.1, now including the maximum rotational speed obtained with the presented prototypes which, to the knowledge of the author, constitutes a world record for bearingless disk drives. Apart from the personally satisfying aspect of this achievement, it would be rather useless were it not for the lessons to be learnt from the research and development process. As the roadmap of this process is outlined in Section 1.4 of the introduction and the individual results have been presented in the respective chapters and the conclusion sections at the end of each chapter, these final words shall not be invested into a summary with rather repetitive character but instead, be dedicated to a short conclusion combined with an outlook on the respective topic.

- As it is the case for the design of electrical machines with mechanical bearings and of stand-alone magnetic bearings, the design of bearingless drives also benefits strongly from an optimization process based on numerical simulation. However, for this optimization process, the proper definition and selection of optimization criteria is essential - especially the force and torque capacity of a bearingless drive can be difficult to assess since the independency of torque and force creation and the ability to provide forces in all radial directions at all possible rotor angles need to be regarded. The design criteria proposed in this work have been evaluated in the optimization suite MagOpt / SyMSpace, developed by LCM. As there are both rising requests from industry for such optimization tools on the one hand, and plans to intensify the development effort for the named tools at LCM, the developed algorithms may be implemented in simulation components or templates in the future.
- The prototype drives constructed in the course of this work have been presented at industrial fairs and at workshops or conferences with significant industry participation. The single most significant purpose where engineers confronted with this novel magnetic bearing approach would see a relevant application was the area of gas compression and expansion, notably, small turbines and compressors for steam, industrial gases, or air. Unsurprisingly, the lubrication-free operation promising extended lifetime is a reason for the interest in this development but not the key argument. These features are rather naturally expected since they are long-known from magnetic bearing technology. The main motivation why application engineers have shown interest is the compactness of the bearingless disk drive which is unmatched by machines with magnetically levitated elongated rotors.
- As mentioned in the turbine and compressor experiments which were not at all accompanied by sound aerodynamic engineering but must be seen as a quick shot, the axial deflection of the rotor in its passive magnetic support can be considerable. High process efficiency calls for controlling the axial impeller clearance, thus making

7. Conclusion and outlook

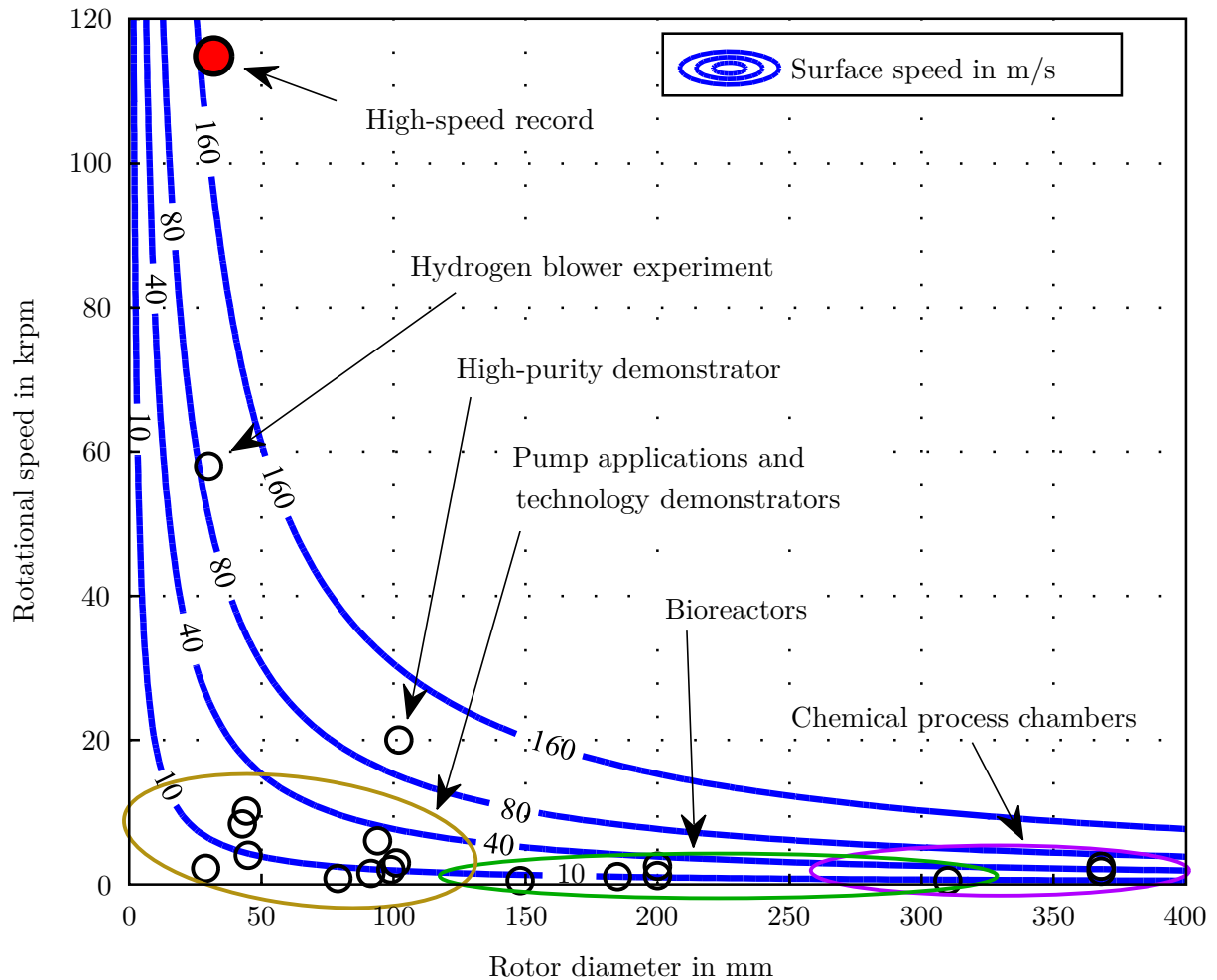


Figure 7.1.: Map of bearingless disk drives found in the literature, placed according to outer rotor diameter and documented rotor speed, also showing the resulting surface speed. The red spot marks the maximum speed attained in the presented work.

an active axial bearing and a careful aerodynamic design of the components indispensable. Section 3.2 has presented a method for how such active influence may be achieved while maintaining the high compactness of the drive. Future work will be necessary in this area in order to provide a true alternative to small compressors or turbines with high power density through high rotational speeds which run on conventional mechanical bearings. The demand is given and, even though the road may still be rocky, the task seems feasible from today's perspective.

- The passively stabilized degrees of freedom simplify the operation of a bearingless high-speed machine in a research project. For a machine in an industrial application, the active control or, at least, the restriction of the axial deflections is very likely among the required system features. Stabilization of the tilt degree of freedom may also be indispensable which is why the presented novel tilt stabilization coil can provide a valuable option. Future adaptations to the manner in which the stabilization coil is integrated in the stator core may allow an application in other drives with magnetically levitated rotors apart from disk drives. Generally speaking, the potential of electrodynamic bearings, compactly integrated into active or

passive magnetic bearing solutions, increases significantly as the rotational speed rises. Combinations of these two technologies seem very tempting.

- Measuring losses and testing the high-speed functionality of the constructed prototypes has been a challenging task. The non-balanced rotors which can be used in the proposed high-speed drive do not allow mounting them for test purposes on thin shafts which could be supported by small mechanical roller bearings which, for some limited time, could deal with the demanded rotational speeds. The use of thicker shafts which would provide sufficient rigidity is prevented by the fact that the necessary mechanical bearings do not support the rotational speeds. Additionally, non-ferromagnetic parts should be used in the test bench construction in order to avoid magnetic field deformation. Electrically conductive parts in the proximity of the rotating magnet are equally problematic due to the induced eddy currents which also influence the rotor field. Above all, the necessary prototype containment has to be provided when testing bearingless high-speed drives since failure of one single system component, e.g., the control, the power electronics circuit, the emergency bearings, the retaining bandage, etc. can lead to rotor destruction. At a surface speed of up to 192 m/s , parts of a shattered rotor turn into very dangerous projectiles.
- Of course, the relentless search for material improvement concerning mainly the iron losses in the stator back iron and the mechanical robustness of the rotor bandage must be followed in order to deliver the most attractive future solutions. Despite the importance of this fact, it is probably not electric or mechatronic engineers but rather material scientists who will contribute most to the advance of this field.
- A look at the shapes of the components used in the prototypes, above all, the stator cores, drive windings, and axial or tilt stabilization windings reveals that standard production processes may not be applicable. Significant work is necessary for adapting and improving the component production in higher numbers and with higher reliability. This is not required for the ongoing research but must absolutely be pursued in order to embrace industrial application.
- Last but not least, the aim of this work shall be reflected upon once more. The target speed of 100 000 rpm which was surpassed in this work touches the region where the life expectancy of mechanical bearings becomes a very critical aspect in applications with long uptimes. However, in order to truly put bearingless disk drives in the focus of application engineers, the speed region of 100 000 to 200 000 rpm must be conquered in research and secured with reliable, compact and highly efficient designs.

A. Appendix

A.1. Analytical magnetic field calculation

The theoretical background for the following approach can be found in numerous works in the literature such as [47], [15], [129] or [64].

Calculation approach

Before diving off into formulas, the objective shall be clarified: An equation for the entire region of interest needs to be found, which allows deriving the field characteristics in the relevant motor parts.

Such a relationship can be found in the magnetic scalar potential Ψ , a purely mathematical term, which is defined in analogy to the electrical potential ϕ . Starting with this analogy, Ψ is related to the field strength \mathbf{H} by

$$\mathbf{H} = -\nabla\Psi \quad (\text{A.1})$$

just as the electric potential ϕ is related to the electric field strength \mathbf{E} through

$$\mathbf{E} = -\nabla\phi. \quad (\text{A.2})$$

Definition (A.1), however, is only possible for the current free and displacement current free space. The reason for this can be found quickly in the fact that for every scalar field, the rotation of the gradient must be zero. In this case, this means for Ψ that

$$\nabla \times \nabla\Psi = \mathbf{0} \quad (\text{A.3})$$

which implies that AMPERE'S law needs to fulfill

$$\nabla \times \nabla(-\Psi) = \nabla \times \mathbf{H} = \mathbf{J}_m + \frac{\partial\mathbf{D}}{\partial t} = \mathbf{0} \quad (\text{A.4})$$

in order to permit the definition of a scalar field according to (A.1)¹. Armed with this knowledge, the analogy to the POISSON equation

$$\nabla \cdot \nabla\phi = \Delta\phi = -\nabla \cdot \mathbf{E} \quad (\text{A.5})$$

for the electric field can be used to find the counterpart

$$\nabla \cdot \nabla\Psi = \Delta\Psi = -\nabla \cdot \mathbf{H} \quad (\text{A.6})$$

for the magnetic field by applying the divergence operator. For the next step, the

¹The trivial case of cancelling current components $\mathbf{J}_m = -\frac{\partial\mathbf{D}}{\partial t}$ is also possible but shall not be regarded here, as a general formulation is needed.

solenoidal characteristic of the flux density

$$\nabla \cdot \mathbf{B} = 0, \quad (\text{A.7})$$

and the material dependent relation of flux density, field strength and magnetization

$$\mathbf{B} = \mu_0 (\mathbf{M}_0 + \mu_r \mathbf{H}) \quad (\text{A.8})$$

is used, with μ_0 , μ_r and \mathbf{M}_0 standing for the permeabilities of vacuum or a respective medium and the permanent magnetization, respectively. Replacing \mathbf{B} in (A.7) with (A.8) yields

$$-\nabla \cdot \mathbf{H} = \frac{1}{\mu_r} \nabla \cdot \mathbf{M}_0 \quad (\text{A.9})$$

which allows rewriting (A.6) into a LAPLACE equation

$$\Delta \Psi = 0 \quad (\text{A.10})$$

in the air gap and iron region, where the permanent magnetization \mathbf{M}_0 is constantly zero.

Within the permanent magnet however, this is not necessarily the case and equation (A.6) turns into

$$\Delta \Psi = \frac{1}{\mu_r} \nabla \cdot \mathbf{M}_0. \quad (\text{A.11})$$

This would result in a different solution approach for the differential equation system within the permanent magnet. However, after a look at the magnet in a Cartesian coordinate system, it becomes clear that this is not necessary. With x pointing in the direction of magnetization and y being perpendicular to it, the permanent magnetization $M_{0,x}$ is constant and $M_{0,y}$ is zero, resulting in $\nabla \cdot \mathbf{M}_0$ also being zero. This characteristic does not change with the change to a different, e.g. polar, coordinate system². This means that in all three regions - the permanent magnet, the magnetic air gap (also containing the winding space) and the stator iron - the magnetic scalar potential needs to satisfy the Laplace equation (A.10), written as

$$\frac{1}{r} \frac{\partial \Psi}{\partial r} + \frac{\partial^2 \Psi}{\partial r^2} + \frac{1}{r^2} \frac{\partial^2 \Psi}{\partial \varphi^2} = 0 \quad (\text{A.12})$$

in polar coordinates (r, φ) .

With equation (A.12), the described aim of finding an equation for the region of interest which allows deriving the loss-relevant field characteristics has been fulfilled.

Boundary conditions and solution

The set of Laplace equations for the three regions - permanent magnet (index M), air gap (index δ) and stator iron (index S) - can be solved by separation of variables which demands for adequate boundary and interface conditions to be defined. They can be

²The divergence can, of course, also be calculated directly in a polar coordinate system. For the example of e.g. radial magnetization, this seems tempting as in that case, the radial component would be constant and the tangential one would be zero. However, the divergence is not zero in that case since it is defined as $\nabla \cdot \Psi = \frac{1}{r} \frac{\partial(r\Psi_r)}{\partial r} + \frac{1}{r} \frac{\partial\Psi_\varphi}{\partial\varphi} + \frac{\partial\Psi_z}{\partial z}$ in cylinder coordinates and not as the sum of the gradients in each coordinate like in a Cartesian system.

found in the continuity of the normal (index r) flux component and of the tangential (index φ) magnetic field strength component at the region interfaces, described by

$$B_{r,M}(r) = B_{r,\delta}(r) \Big|_{r=r_{o,M}} \quad (\text{A.13})$$

$$B_{r,\delta}(r) = B_{r,S}(r) \Big|_{r=r_{i,S}} \quad (\text{A.14})$$

$$H_{\varphi,M}(r) = H_{\varphi,\delta}(r) \Big|_{r=r_{o,M}} \quad (\text{A.15})$$

$$H_{\varphi,\delta}(r) = H_{\varphi,S}(r) \Big|_{r=r_{i,S}}. \quad (\text{A.16})$$

Further, the radial flux density component is set to $B_{r,M}(r) = 0 \Big|_{r=r_{i,M}}$ at the inner magnet radius and to $B_{r,S} = 0$ at the outer stator rim, i.e. zero stray flux is assumed.

After solving the complete set of equations, the radial and tangential flux density can be expressed for all three problem regions as generally described in [129]. For a setup with a diametrically magnetized rotor, the solution can further be simplified as shown in [64] where the field of a slotless PM drive is modeled. Following the approach used in that work, the resulting flux density components in the three regions can be expressed as

$$B_{r,M}(r, \varphi) = K_{B,M} \cos(\varphi) \quad (\text{A.17})$$

$$B_{\varphi,M}(r, \varphi) = K_{B,M} \sin(\varphi), \quad (\text{A.18})$$

$$B_{r,\delta}(r, \varphi) = K_{B,\delta} \left(1 + \left(\frac{r_{i,S}}{r} \right)^2 \right) \cos(\varphi) \quad (\text{A.19})$$

$$B_{\varphi,\delta}(r, \varphi) = -K_{B,\delta} \left(1 - \left(\frac{r_{i,S}}{r} \right)^2 \right) \sin(\varphi) \quad (\text{A.20})$$

and

$$B_{r,S}(r, \varphi) = K_{B,S} \left(-1 + \left(\frac{r_{o,S}}{r} \right)^2 \right) \cos(\varphi) \quad (\text{A.21})$$

$$B_{\varphi,S}(r, \varphi) = -K_{B,S} \left(1 + \left(\frac{r_{o,S}}{r} \right)^2 \right) \sin(\varphi). \quad (\text{A.22})$$

The permanent magnet's remanence flux density $B_{rem,M}$ and the relative permeability of the stator material $\mu_{r,S}$ are taken into consideration in the coefficients K_B which are defined as

$$K_{B,M} = \frac{B_{rem,M}}{N} \left\{ \left[1 - \left(\frac{r_{i,S}}{r_{o,S}} \right)^2 \right] \cdot \left[1 + \left(\frac{r_{o,M}}{r_{i,S}} \right)^2 \right] + \frac{1}{\mu_{r,S}} \left[1 + \left(\frac{r_{i,S}}{r_{o,S}} \right)^2 \right] \cdot \left[1 - \left(\frac{r_{o,M}}{r_{i,S}} \right)^2 \right] \right\},$$

$$K_{B,\delta} = \frac{B_{rem,M}}{N} \left\{ \left[1 - \left(\frac{r_{i,S}}{r_{o,S}} \right)^2 \right] - \frac{1}{\mu_{r,S}} \left[1 + \left(\frac{r_{i,S}}{r_{o,S}} \right)^2 \right] \right\} \cdot \left(\frac{r_{o,M}}{r_{i,S}} \right)^2 \text{ and}$$

$$K_{B,S} = \frac{2B_{rem,M}}{N} \cdot \left(\frac{r_{o,M}}{r_{o,S}} \right)^2$$

using the coefficient

$$N = \left[1 - \left(\frac{r_{i,S}}{r_{o,S}} \right)^2 \right] \left[(\mu_{r,M} + 1) - (\mu_{r,M} - 1) \left(\frac{r_{o,M}}{r_{i,S}} \right)^2 \right] + \frac{1}{\mu_{r,S}} \left[1 + \left(\frac{r_{i,S}}{r_{o,S}} \right)^2 \right] \left[(\mu_{r,M} + 1) + (\mu_{r,M} - 1) \left(\frac{r_{o,M}}{r_{i,S}} \right)^2 \right].$$

The latter depends on the relative permeability of the permanent magnet $\mu_{r,M}$ as well as on the inner and outer radii of the magnet, $r_{i,M}$ and $r_{o,M}$, and the stator, $r_{i,S}$ and $r_{o,S}$, respectively.

A.2. Rotating field iron loss model

In the drive described in the present work, a slotless stator is used. As a direct consequence, the magnetic field orientation in most of the stator core is not alternating between a certain direction and the exact opposite direction but shows rotating behavior instead. This fact is considered in Section 6.3.4 by applying the iron loss model according to [45] and [127]. The elliptical rotating core loss in these works is composed of a circularly rotating component $P_{Fe,Rot}$ and an alternating component $P_{Fe,Alt}$ according to

$$P_{Fe,Elliptic} = R_B P_{Fe,Rot} + (1 - R_B)^2 P_{Fe,Alt} \quad (\text{A.23})$$

with the flux density ratio

$$R_B = \frac{B_{min}(r)}{B_{maj}(r)} \quad (\text{A.24})$$

between the minor axis flux density $B_{min}(r)$ and the major axis flux density $B_{maj}(r)$ of the elliptical flux orbit. The two loss components of (A.23) are defined as

$$P_{Fe,Rot} = P_{Fe,Rot,h} + K_{Rot,e} \cdot (fB(r))^2 + K_{Rot,a} \cdot (fB(r))^{1.5} \quad (\text{A.25})$$

for the circular rotating part with

$$P_{Fe,Rot,h} = a_1 f \left(\frac{\frac{1}{s_{sat}}}{\left(a_2 + \frac{1}{s_{sat}} \right)^2 + a_3^2} - \frac{\frac{1}{(2-s_{sat})}}{\left(a_2 + \frac{1}{(2-s_{sat})} \right)^2 + a_3^2} \right) \quad (\text{A.26})$$

where

$$s_{sat} = 1 - \frac{B(r)}{B_{sat}} \sqrt{1 - \frac{1}{a_2^2 + a_3^2}} \quad (\text{A.27})$$

and as

$$P_{Fe,Alt} = K_{Alt,h} \cdot fB(r)^{h_{Alt}} + K_{Alt,e} \cdot (fB(r))^2 + K_{Alt,a} (fB(r))^{1.5} \quad (\text{A.28})$$

for the alternating part. Table A.1 gives the coefficients mentioned in [45] for Somaloy 500 SMC material from Höganäs AB.

A final note of criticism shall be placed here: The description of iron losses in steel sheet and SMC materials is among the most delicate parts of an electrical actuator concerning analytical modeling. This verdict is supported by the numerous models presented in the

A.3. Skin and proximity effect related loss coefficients

Parameter	Value
$K_{Rot,e}$	$2.303e - 4$
$K_{Rot,a}$	0
$K_{Alt,h}$	0.1402
$K_{Alt,e}$	$0.1233e - 5$
$K_{Alt,h}$	$3.645e - 4$
h_{Alt}	1.548
a_1	6.814
a_2	1.054
a_3	1.445
B_{sat}	2.134

Table A.1.: Parameters of Somaloy 500 SMC material

literature and by the fact that they predict significantly different results. What makes this even worse is the statements of people working in the measurement of electrical actuators, saying that being wrong with the iron loss estimation by a factor of 2 is already considered a *decent fit* since the material parameters vary strongly depending on production process parameters and tooling steps. In this light, an analytic model with 9 different numerical parameters seems, to a certain extent, inappropriate. Nevertheless, the model and the coefficients found in the literature were applied here to give an overview of the different existing approaches.

A.3. Skin and proximity effect related loss coefficients

Based on the works [32, 121, 117, 33] and, consequently, [12] - Chapter 7.5 which focus on the loss calculation in transformer windings, Chapter 6 presents the used loss models (A.29) and (A.30) which take into account the skin and proximity effect, respectively.

$$P_{skin} = n_s R_{DC,s} l_w G_{skin} \left(\frac{\hat{i}}{n_s} \right)^2 \quad (\text{A.29})$$

$$P_{prox} = n_s R_{DC,s} l_w G_{prox} \left(\frac{\hat{i}^2}{2\pi^2 d_{bundle}^2} + \hat{H}_{bundle}^2 \right) \quad (\text{A.30})$$

This section gives a detailed formulation for the used parameters. As mentioned before, n_s and $R_{DC,s}$ give the number of strands and their individual resistance per unit length. Further, d_{bundle} and l_w represent the diameter of the entire litz bundle and the wire length. \hat{i} stands for the peak value of the applied sinus current and \hat{H}_{bundle} is the peak value of the accumulated magnetic field due to the neighboring wires. The exact formulation of

A. Appendix

G_{skin} and G_{prox} in this form is only possible for round conductors. They yield

$$G_{skin} = \frac{\xi}{4} \cdot \frac{\varkappa_r(0,\xi) \cdot \varkappa'_i(0,\xi) - \varkappa_i(0,\xi) \cdot \varkappa'_r(0,\xi)}{\varkappa'_r(0,\xi)^2 + \varkappa'_i(0,\xi)^2} \quad (\text{A.31})$$

$$G_{prox} = -\frac{\xi \pi^2 d_s^2}{2} \cdot \frac{\varkappa_r(2,\xi) \cdot \varkappa'_r(0,\xi) + \varkappa_i(2,\xi) \cdot \varkappa'_i(0,\xi)}{\varkappa'_r(0,\xi)^2 + \varkappa'_i(0,\xi)^2} \quad (\text{A.32})$$

with the relative conductor thickness

$$\xi = \frac{d_s}{\sqrt{2} \delta_{skin}} \quad (\text{A.33})$$

where d_s and δ_{skin} represent the strand diameter and the skin depth of the concerned strand. The symbols \varkappa_r and \varkappa_i stand for the real and imaginary part of the Kelvin differential equation describing a Bessel function of the first kind, sometimes also called *Ber* and *Bei*. The mentioned skin depth is calculated as

$$\delta_{skin} = \frac{1}{\sqrt{\pi f(i) \mu_0 \mu_{Cu} \kappa_{Cu}}} \quad (\text{A.34})$$

with μ_{Cu} and κ_{Cu} being the material specific permeability and conductivity of copper and $f(i)$ holds the frequency of the applied sinus current.

A.4. External field due to neighboring wire bundles

For the external field due to the neighboring wire bundles of the litz wire winding, the mean value of the field strength in the winding needs to be calculated. In good approximation, the wire bundles can be seen as quadratic blocks since the bundles deform when being wound onto the stator. The edge length of each quadratic block is

$$l_e = \sqrt{\frac{d_{bundle}^2 \pi}{4}} \quad (\text{A.35})$$

in order not to alter the cross section of the originally round wire bundle. Figure A.1

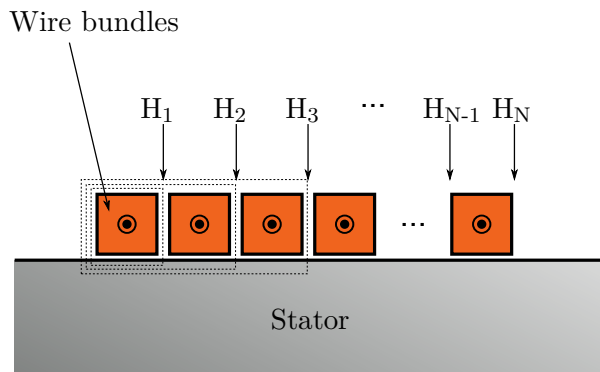


Figure A.1.: External field due to neighboring wire bundles in one winding side of the slotless winding configuration

shows the situation for the conductors of one coil side at the inner stator diameter. As

the present stator has a slotless design, the conductors face a ferromagnetic material on only one side. Applying Ampere's circuital law, the magnetic field strength H_1 between the first and the second bundle can be expressed as

$$H_1 = \frac{n_s \hat{i}}{3l_e} \quad (\text{A.36})$$

when the total permeability of the stator material is seen to be significantly higher than the permeability of air in the winding space. Integrating along the second dashed line, the field strength H_2 between the second and the third bundle would then be

$$H_2 = \frac{2n_s \hat{i}}{4l_e} \quad (\text{A.37})$$

which could be generalized for the field strength between the j -th and the $(j + 1)$ -th bundle as

$$H_j = \frac{jn_s \hat{i}}{(j + 2)l_e}. \quad (\text{A.38})$$

Assuming that the field strength within the bundle is homogeneous, it can be calculated as the mean value between the field strength to its left and its right. Averaging over all wire bundles with N being the number of winding turns, the average field strength in one bundle is

$$H_{avg} = \frac{1}{N} \left(\frac{0 + H_1}{2} + \frac{H_1 + H_2}{2} + \dots + \frac{H_{j-1} + H_j}{2} \right) = \sum_{j=1}^N \left(\frac{H_j}{N} \right) + \frac{H_N}{2N} \quad (\text{A.39})$$

B. Index of symbols

Abbreviations

Symbol	Description
TSC	Tilt Stabilization Coil
back-EMF	back-Electro Motive Force, also: induced voltage
DPNV	Dual-Purpose No-Voltage winding
MMF	MagnetoMotive Force

Notation

\mathbf{X}	Vector or matrix
\dot{x}	Time derivative
\ddot{x}	Second time derivative
\hat{x}	Peak value or variation ratio
\bar{x}	Mean value
x^{\parallel}	Parallel component
x^{\perp}	Normal component

Variables

The table below does not list all used symbols as many variables are distinguished by the use of additional indices.

Symbol	Description
A	Area
$\mathbf{A}_{\S\S}$	Transformation matrix from \S to \S
B	Magnetic flux density
c	Stiffness value
$c_{drag,z}$	Air drag coefficient for axial disk surface
$c_{drag,\varphi}$	Air drag coefficient for cylindrical surface
\mathbf{C}	Stiffness matrix
C_0, C_1	Calculation coefficients
d	Diameter
D	Damping parameter
\mathbf{D}	Damping matrix
$\tilde{\mathbf{D}}$	Extended damping matrix
E	YOUNG's modulus
\mathbf{E}	Electric field strength

B. Index of symbols

Symbol	Description
f	Frequency
F	Force
\mathbf{F}_g	Gravitational force vector
f_i	Frequency of the current
f_B	Frequency of the magnetic field
G_{prox}	Proximity effect loss coefficient
G_{skin}	Skin effect loss coefficient
\mathbf{G}	Gyroscopic matrix
h	(Radial) height
\mathbf{H}	Magnetic field vector
H	Transfer function
i	Current
\mathbb{j}	Complex number
I	Moment of inertia
\mathbf{I}	Moment of inertia matrix
j	Counting variable
J	Current density
k_F	Inverse force criterion parameter
k_T	Inverse torque criterion parameter
K_B	Flux density coefficient
K_{Fe}	Iron loss coefficient
K_{ec}	Eddy current loss coefficient
K_h	Hysteresis loss coefficient
\mathbf{K}_m	Bearing forces / torque to current relationship
l	(Axial) length
L	Inductance
\mathbf{L}	Angular momentum vector
m	Phase number
$m_{\#}$	Mass of #
\mathbf{M}	Magnetization
N	Winding turns
n_{slots}	Number of winding slots
n_s	Number of litz strands per bundle
p	Relative (loss) power
P	(Loss) power
q	Minimum coordinate
\mathbf{Q}	Forces and torque vector
r	Radius
R	Electric resistance
Re	REYNOLDS number
R_m	Tensile stress

Symbol	Description
$R_{p0,2}$	Yield stress
s	Laplace parameter $s = \sigma + j\omega$
s_{slots}	Slot step
t	Time
t_F	Direct force criterion parameter
t_T	Direct torque criterion parameter
T	Torque
T^{\parallel}	Torque about axis of magnetization
T^{\perp}	Torque perpendicular to axis of magnetization
T_{ex}	External torque
T_J	Notch filter parameter
\mathbf{T}_m	Current to bearing forces / to torque relationship
T_R	Notch filter parameter
u	Mechanical displacement
V	Voltage
$W_{m,co}$	Magnetic co-energy
x	Radial deflection in direction of rotor magnetization at $\varphi = 0$
y	Radial deflection in direction perpendicular to rotor magnetization at $\varphi = 0$
z	Axial deflection
α	Tilting angle about x -axis
β	Tilting angle about y -axis
β_{Fe}	Iron loss exponent
δ	Physical air gap width
δ_m	Magnetic air gap width
Δ_r	Interference fit related to radius
ϵ	Notch filter bandwidth factor
$\xi_{\bar{T}z}$	Mean torque factor
η	Efficiency
ζ	Safety factor
κ	VON KÁRMÁN constant
μ	Permeability
μ_0	Permeability of vacuum: $4\pi \cdot 10^{-7}$
ν	POISSON'S ratio
ν_{Air}	Kinematic viscosity of air
ξ	Ratio of polar to diametral moment of inertia
ρ	Density
σ	Stress component
τ_{δ}	Shear stress at the cylindrical air gap surface
φ	Rotational angle about z -axis
ϕ	Notch filter coefficient

B. Index of symbols

Symbol	Description
χ	Calculation variable
Ψ	Linked flux
ξ	Notch filter coefficient
θ	Phase angle between coil current and linked flux
ω	Electrical angular frequency
Ω	Mechanical angular frequency
Ω_{limit}	Mechanical speed limit

Indices

Unless the indices speak for themselves (l_{lever} , F_{scale}), the following table gives the used indices or combinations of indices which are annotated to the variables in the above table. The expression of variables in a certain coordinate system is denoted by an index placed in front of the respective variable.

Index	Variable # related to
$\#_0$	Idle condition
$\#_B$	Rotor bandage
$\#_{bEMF}$	Back-EMF
$\#_c$	Critical frequency (e.g. resonance frequency, cut-off frequency, etc.)
$\#_{Cu}$	Copper windings
$\#_d$	Diametral direction
$\#_{DC}$	Direct current
$\#_F$	Bearing force or bearing force system
$\#_{Fe}$	Stator iron
$\#_g$	Gravity
$\#_i$	Inner (e.g. radius)
$\#_M$	Rotor magnet
$\#_o$	Outer (e.g. radius)
$\#_p$	Polar direction
$\#_{PE}$	Power electronics
$\#_r$	Radial direction
$\#_R$	Rotor
$R\#$	Rotor bound coordinate system
$\#_{rel}$	Reluctance effect
$\#_S$	Stator
$\#_s$	Litz strand
$s\#$	Stator bound coordinate system
$\#_T$	Torque or torque system
$\#_{TSC}$	Tilt stabilization coil
$\#_x$	Radial x-direction
$\#_y$	Radial y-direction

Index	Variable # related to
$\#_Y$	Rotor yoke
$\#_w$	Wire
$\#_z$	Axial direction
$\#_\alpha$	Tilting direction about x-axis
$\#_\beta$	Tilting direction about y-axis
$\#_\delta$	Air gap
$\#\Delta$	Rotor deflection
$\#\mathcal{T}$	Tilting direction
$\#\varphi$	Tangential direction

Bibliography

- [1] W. Amrhein and S. Silber, "Bearingless single-phase motor with concentrated full pitch windings in interior rotor design," *Proc. 6th International Symposium on Magnetic Bearings*, 1998.
- [2] J. Asama, D. Kanehara, T. Oiwa, and A. Chiba, "Development of a compact centrifugal pump with a two-axis actively positioned consequent-pole bearingless motor," *IEEE Transactions on Industry Applications*, vol. 50, pp. 288–295, 2014.
- [3] D. Atherton and A. R. Eastham, "Flat guidance schemes for magnetically levitated highspeed guided ground transport," *Journal of Applied Physics*, vol. 45, 1973.
- [4] K. Bachovin, J. Hoburg, and R. Post, "Stable levitation of a passive magnetic bearing," *IEEE Transactions on Magnetics*, 2013.
- [5] N. Barletta and R. Schoeb, "Design of a bearingless blood pump," *Proc. 3rd International Symposium on Magnetic Suspension Technology*, 1995.
- [6] T. I. Baumgartner, A. Looser, C. Zwysig, and J. W. Kolar, "Novel high-speed, lorentz-type, slotless self-bearing motor," *Proc. Energy Conversion Congress and Exposition*, 2010.
- [7] R. Baumschlager, R. Schoeb, and J. Schmied, "Bearingless hydrogen blower," *Proc. 8th International Symposium on Magnetic Bearings*, 2002.
- [8] A. Bergqvist, "Magnetic vector hysteresis model with dry friction-like pinning," *Physica B: Condensed Matter*, vol. 233, pp. 342–347, 1997.
- [9] A. Bergqvist, A. Lundgren, and G. Engdahl, "Experimental testing of an anisotropic vector hysteresis model," *IEEE Transactions on Magnetics*, vol. 33, no. 5, pp. 4152–4154, 1997.
- [10] N. Bianchi, S. Bolognani, and F. Luise, "Potentials and limits of high-speed PM motors," *IEEE Transactions on Industry Applications*, vol. 40, no. 6, pp. 1570–1578, Nov. 2004.
- [11] J. Bichsel, "Beitraege zum lagerlosen Elektromotor," Ph.D. dissertation, ETH-Zurich, 1990.
- [12] J. Biela, "Wirbelstromverluste in Wicklungen induktiver Bauteile," *Online available: <https://www.hpe.ee.ethz.ch>*, 2011.
- [13] A. Binder, T. Schneider, and M. Klohr, "Fixation of buried and surface-mounted magnets in high-speed permanent-magnet synchronous machines," *IEEE Transactions on Industry Applications*, vol. 42, no. 4, pp. 1031–1037, 2006.

- [14] H. Bleuler, H. Kawakatsu, W. Tang, W. Hsieh, D. Miu, Y. Tai, F. Moesner, and M. Rohner, "Micromachined active magnetic bearings," *Proc. 4th International Symposium on Magnetic Bearings*, 1994.
- [15] E. Bolte, *Elektrische Maschinen*. Springer-Verlag, Berlin Heidelberg, 2012.
- [16] R. Bosch, "Development of a bearingless electrical motor," *Proc. ICEM International Conference on Electrical Machines*, pp. 331–335, 1988.
- [17] G. Bramerdorfer, G. Jungmayr, W. Amrhein, W. Gruber, E. Marth, and M. Reisinger, "Bearingless segment motor with halbach magnet," *Proc. 20th International Symposium on Power Electronics, Electrical Drives, Automation and Motion*, 2010.
- [18] W. Braunbeck, "Freischwebende Koerper im elektrischen und magnetischen Feld," *Zeitschrift fuer Physik*, vol. 112, pp. 753–763, 1939.
- [19] W.-R. Canders and D. Huelsmann, "Analysis and classification of bearingless machines with symmetric 3-phase concentrated windings," *Proc. 19th International Conference on Electrical Machines*, 2010.
- [20] A. Chiba, K. Chida, and T. Fukao, "Principles and characteristics of a reluctance motor with windings of a magnetic bearing," *Proc. International Power Electronics Conference, Tokyo*, pp. 919–926, 1990.
- [21] A. Chiba, T. Fukao, O. Ichikawa, M. Ooshima, M. Takemoto, and D. Dorell, *Magnetic Bearings and Bearingless Drives*. Elsevier, 2005.
- [22] A. Chiba, D. T. Power, and M. A. Rahman, "Characteristics of a bearingless induction motor," *IEEE Transactions on Magnetics*, vol. 27, no. 6, pp. 5199–5201, 1991.
- [23] A. Chiba, S. Horima, and H. Sugimoto, "A principle and test result of a novel bearingless motor with motor parallel winding structure," *Proc. Energy Conversion Congress and Exposition*, 2013.
- [24] C. Cyr, P. Viarouge, S. Clenet, and C. J., "Methodology to study the influence of the microscopic structure of soft magnetic composites on their global magnetization curve," *IEEE Transactions on Magnetics*, vol. 45, no. 3, pp. 1178–1181, 2009.
- [25] K. Davey, A. Filatov, and R. Thompson, "Design and analysis of passive homopolar null flux bearings," *IEEE Transactions on Magnetics*, vol. 41, no. 3, pp. 1169–1175, 2005.
- [26] K. Davey, T. Morris, J. Shaaf, and D. Rote, "Calculation of motion induced eddy current forces in null flux coils," *IEEE Transactions on Magnetics*, vol. 31, no. 6, 1995.
- [27] J. G. Detoni, F. Impinna, N. Amati, and A. Tonoli, "Rotordynamic stabilization of rotors on electrodynamic bearings," *INTECH Open Publishing*, vol. Advances in Vibration Engineering and Structural Dynamics, pp. 51–66, 2012.
- [28] Dupont, "Teflon ptfе properties handbook," *Tech.Rep. H-37051-3*, 1996.

- [29] S. Earnshaw, “On the nature of the molecular forces which regulate the constitution of the luminiferous ether,” *Transactions of the Cambridge Philosophical Society*, vol. 7, pp. 97–112, 1839.
- [30] EMT, “Allgemeine Informationen zu Elektroblechen,” <http://www.emt-net.de/elektrobleche/Allgemeine-Informationen-zu-Elektroblechen.pdf>, June 2012.
- [31] J. Fang, Y. Le, J. Sun, and K. Wang, “Analysis and design of passive magnetic bearing and damping system for high-speed compressor,” *IEEE Transactions on Magnetics*, vol. 48, no. 9, pp. 2528–2537, 2012.
- [32] J. A. Ferreira, “Analytical computation of AC resistance of round and rectangular litz wire windings,” *IEE Proceedings - B*, vol. 139, no. 1, pp. 21–25, 1992.
- [33] —, “Improved analytical modeling of conductive losses in magnetic components,” *IEEE Transactions on Power Electronics*, vol. 9, no. 1, pp. 127–131, 1994.
- [34] A. Filatov and E. Maslen, “Passive magnetic bearing for flywheel energy storage systems,” *IEEE Transactions on Magnetics*, vol. 37, no. 6, pp. 3913–3924, 2001.
- [35] S. Goldstein, “On the resistance to the rotation of a disc immersed in a fluid,” *Proc. Cambridge Phil. Soc.*, vol. 31, pp. 232–241, 1935.
- [36] H. Grabner, “Dynamik und Ansteuerkonzepte Lagerloser Drehfeld-Scheibenlaufermotoren in Radialer Bauform,” Ph.D. dissertation, JKU, 2007.
- [37] H. Grabner, W. Amrhein, S. Silber, and W. Gruber, “Nonlinear feedback control of a bearingless brushless DC motor,” *IEEE/ASME Transactions on Mechatronics*, vol. 15, no. 1, pp. 40–47, 2010.
- [38] H. Grabner, H. Bremer, W. Amrhein, and S. Silber, “Radial vibration analysis of bearingless slice motors,” *Proc. 9th International Symposium on Magnetic Bearings*, 2004.
- [39] H. Grabner, S. Silber, and W. Amrhein, “Bearingless torque motor - modeling and control,” *Proc. 13th International Symposium on Magnetic Bearings*, 2012.
- [40] W. Gruber, W. Amrhein, T. Stallinger, and H. Grabner, “Bearingless segment motor with buried magnets,” *Journal of System Design and Dynamics*, vol. 3, pp. 704–716, 2009.
- [41] W. Gruber, W. Amrhein, and T. Stallinger, “Bearingless segment motor with buried magnets,” *Proc. 11th International Symposium on Magnetic Bearings*, 2008.
- [42] W. Gruber, W. Briewasser, M. Rothboeck, and R. Schoeb, “Bearingless slice motor concepts without permanent magnets in the rotor,” *Proc. IEEE International Conference on Industrial Technology*, 2013.
- [43] W. Gruber, T. Nussbaumer, H. Grabner, and W. Amrhein, “Wide air gap and large-scale bearingless segment motor with six stator elements,” *IEEE Transactions on Magnetics*, vol. 46, no. 6, pp. 2438–2441, 2010.

- [44] W. Gruber, S. Silber, W. Amrhein, and T. Nussbaumer, “Design variants of the bearingless segment motor,” *Proc. International Symposium on Power Electronics, Electrical Drives Automation and Motion*, 2010.
- [45] Y. Guo, J. G. Zhu, J. Zhong, and W. Wu, “Core losses in claw pole permanent magnet machines with soft magnetic composite stators,” *IEEE Transactions on Magnetics*, vol. 39, no. 5, pp. 3199–3201, 2003.
- [46] Y. Guo, J. Zhu, Z. Lin, and J. Zhong, “3d vector magnetic properties of soft magnetic composite material,” *Journal of Magnetism and Magnetic Materials*, vol. 302, pp. 511–516, 2006.
- [47] B. Hague, *The Principles of Electromagnetism Applied to Electrical Machines*. Dover, 1962.
- [48] B. Han, S. Zheng, X. Wang, and Q. Yuan, “Integral design and analysis of passive magnetic bearing and active radial magnetic bearing for agile satellite application,” *IEEE Transactions on Magnetics*, 2012.
- [49] Y. Heng-Xiu, D. Yong, and S. Zhen-Iun, “The analysis of adhesion failure between Ni-coating and sintered NdFeB substrate,” *Proc. 2nd International Symposium on Advanced Magentic Materials and Applications*, 2010.
- [50] P. K. Hermann, “Radially-active magnetic bearing with rotary drive - has air-gap monitors modulating control field superimposed on drive field,” German Patent DE19 742 406 790, 1975.
- [51] R. Herzog, P. Buhler, C. Gahler, and R. Larsonneur, “Unbalance compensation using generalized notch filters in the multivariable feedback of magnetic bearings,” *IEEE Transactions on Control Systems Technology*, vol. 4, no. 5, pp. 580–586, 1996.
- [52] M. Hofer and M. Schroedl, “Statistic properties of a sensorless control method for a three phase permanent magnet biased radial active magnetic bearing,” *Proc. European Conference on Power Electronics and Applications*, pp. 1–8, 2009.
- [53] K. Ikeda and H. Dohmeki, “Study on improvement in the motor property by the difference in the fabrication density of the soft magnetic composite,” *Proc. 20th Int. Conf. on Electrical Machines*, pp. 784–788, 2012.
- [54] F. Impinna, “Electrodynamic bearings,” Ph.D. dissertation, Politecnico di Torino, 2010.
- [55] ISO14839-1, *Mechanical vibration - Vibration of rotating machinery equipped with active magnetic bearings - Part 1: Vocabulary*. ISO, 2002.
- [56] G. Jungmayr, E. Marth, W. Amrhein, H.-J. Berroth, and F. Jeske, “Analytical stiffness calculation for permanent magnetic bearings with soft magnetic materials,” *IEEE Transactions on Magnetics*, 2014.
- [57] P. Karutz, T. Nussbaumer, W. Gruber, and J. W. Kolar, “The bearingless 2-level motor,” *Proc. 7th International Conference on Power Electronics and Drive Systems*, pp. 365–371, Nov. 27–30, 2007.

- [58] M. A. Khan, P. Pillay, R. Guan, N. R. Batane, and D. J. Morrison, “Performance assessment of a pm wind generator with machined smc cores,” *Proc. International Electric Machines & Drives Conf.*, vol. 2, pp. 1049–1053, 2007.
- [59] V. Kluyskens and B. Dehez, “Dynamical electromechanical model for magnetic bearings subject to eddy currents,” *IEEE Transactions on Magnetics*, vol. 49, pp. 1444–1453, 2013.
- [60] R. Larsonneur and R. Herzog, “Feedforward compensation of unbalance: New results and application experiences,” *Proc. Symposium on the Active Control of Vibration*, 1992.
- [61] R. Larsonneur and P. Bühler, “New radial sensor for active magnetic bearings,” *Proc. 9th International Symposium on Magnetic Bearings*, 2004.
- [62] J. V. Leite, M. V. Ferreira da Luz, N. Sadowski, and P. A. da Silva, “Modelling dynamic losses under rotational magnetic flux,” *IEEE Transactions on Magnetics*, vol. 48, no. 2, pp. 895–898, 2012.
- [63] T. Lembke, “Design and analysis of a novel low loss homopolar electrodynamic bearing,” Ph.D. dissertation, KTH Stockholm, 2005.
- [64] J. Luomi, C. Zwysig, A. Looser, and J. W. Kolar, “Efficiency optimization of a 100W 50000r/min permanent-magnet machine including air-friction losses,” *IEEE Transactions on Industry Applications*, vol. 45, no. 4, pp. 1368–1377, Jul. 2009.
- [65] K. Magnus and H. Müller, *Grundlagen der technischen Mechanik*, 3rd ed. B.G. Teubner, 1982.
- [66] E. Marth, G. Jungmayr, and W. Amrhein, “Influence of viscoelastic elements on magnetically passive stabilized degrees of freedom,” *Proc. 13th International Symposium on Magnetic Bearings*, 2010.
- [67] —, “A 2-d-based analytical method for calculating permanent magnetic ring bearings with arbitrary magnetization and its application to optimal bearing design,” *IEEE Transactions on Magnetics*, 2014.
- [68] M. Minn and S. Sinha, “The lubrication of poly(etheretherketone) by an aqueous solution of nattokinase,” *Wear*, vol. 296, pp. 528–535, 2010.
- [69] H. Mitterhofer and W. Amrhein, “Design aspects and test results of a high speed bearingless drive,” *Proc. 9th Power Electronics and Drive Systems Conference*, 2011.
- [70] —, “Motion control strategy and operational behaviour of a high speed bearingless disc drive,” *Proc. IET Power Electronics, Machines and Drives Conference*, 2012.
- [71] H. Mitterhofer, D. Andessner, and W. Amrhein, “Analytical and experimental loss examination of a high speed bearingless drive,” *Proc. International Symposium on Power Electronics Electrical Drives Automation and Motion*, 2012.
- [72] H. Mitterhofer, H. Grabner, and W. Amrhein, “Comparison of two and four pole rotors for a high speed bearingless drive,” *Proc. 13th International Symposium on Magnetic Bearings*, 2012.

- [73] H. Mitterhofer, W. Gruber, and W. Amrhein, “Towards high speed bearingless drives,” *Proc. 12th International Symposium on Magnetic Bearings*, 2010.
- [74] —, “On the high speed capacity of bearingless drives,” *IEEE Transactions on Industrial Electronics*, vol. 61, no. 6, pp. 3119–3126, 2014.
- [75] H. Mitterhofer, “Elektrische Maschine,” European Patent EP16 173 200.3, pending.
- [76] H. Mitterhofer and W. Gruber, “Effizienzsteigerung durch die und in der magnetlagertechnik,” *e&i Elektrotechnik und Informationselektronik*, vol. 134, no. 2, pp. 191–196, 2017.
- [77] H. Mitterhofer and G. Jungmayr, “Stability improvement of passively stabilized degrees of freedom in magnetically levitated systems,” *Proc. 15th International Symposium on Magnetic Bearings*, 2016.
- [78] H. Mitterhofer, B. Mrak, and W. Amrhein, “Suitability investigation of a bearingless disk drive for micro turbine applications,” *Proc. Energy Conversion Congress and Exposition*, 2013.
- [79] H. Mitterhofer, B. Mrak, and W. Gruber, “Comparison of high speed bearingless drive topologies with combined windings,” *Proc. International Power Electronics Conference*, 2014.
- [80] —, “Comparison of high-speed bearingless drive topologies with combined windings,” *IEEE Transactions on Industry Applications*, vol. 51, no. 3, pp. 2116–2122, 2015.
- [81] H. Mitterhofer and M. Rakov, “On the direct use of electromagnetic field information for magnetic rotor position control,” *Proc. 14th International Symposium on Magnetic Bearings*, 2014.
- [82] H. Mitterhofer and S. Silber, “Comprehensive design and optimization of high-speed bearingless drives,” *Proc. Advances in Magnetics Conference*, 2016.
- [83] G. Munteanu, A. Binder, T. Schneider, and B. Funieru, “No-load tests of a 40kW high-speed bearingless permanent magnet synchronous motor,” *Proc. International Symposium on Power Electronics, Electrical Drives Automation and Motion*, 2010.
- [84] A. Müsing, C. Zingerli, I. Ph., and J. Kolar, “PEEC-based numerical optimization of compact radial position sensors for active magnetic bearing,” *Proc. 5th International Conference on Integrated Power Systems*, 2008.
- [85] M. Neff, N. Barletta, and R. Schoeb, “Bearingless centrifugal pump for highly pure chemicals,” *Proc. 8th International Symposium on Magnetic Bearings*, 2002.
- [86] T. Nussbaumer, P. Karutz, F. Zuercher, and J. Kolar, “Magnetically levitated slice motors—an overview,” *IEEE Transactions on Industry Applications*, vol. 47, no. 2, pp. 754–766, 2011.
- [87] T. Nussbaumer, “Bearingless electric rotary drive,” US Patent US8 581 462B2, 2013.

- [88] R. Oishi, S. Horima, H. Sugimoto, and A. Chiba, "A novel parallel motor winding structure for bearingless motors," *IEEE Transactions on Magnetics*, vol. 49, no. 5, pp. 2287–2290, 2013.
- [89] Y. Okada, T. Ohishi, and K. Dejima, "Levitation control of permanent magnet (pm) type rotating motor," *Proc. Magnetic Bearings, Magnetic Drives and Dry Gas Seals Conference and Exhibitions*, pp. 157–165, 1992.
- [90] M. Ooshima, A. Chiba, T. Fukao, and M. A. Rahman, "Design and analysis of permanent magnet-type bearingless motors," *IEEE Transactions on Industrial Electronics*, vol. 43, no. 2, pp. 292–299, 1996.
- [91] M. Ooshima, S. Kobayashi, and H. Tanaka, "Magnetic suspension performance of a bearingless motor/generator for flywheel energy storage systems," *Proc. IEEE Power and Energy Society General Meeting*, 2010.
- [92] M. Ooshima and C. Takeuchi, "Magnetic suspension performance of a bearingless brushless DC motor for small liquid pumps," *Proc. 12th International Conference on Electrical Machines and Systems*, pp. 1–4, 2009.
- [93] J. Passenbrunner, G. Jungmayr, M. Panholzer, S. Silber, and W. Amrhein, "Simulation and optimization of an eddy current position sensor," *Proc. International Conf. on Power Electronics and Drive Systems*, 2015.
- [94] K. Raggl, T. Nussbaumer, and J. Kolar, "Comparison of winding concepts for bearingless pumps," *Proc. International Conference on Power Electronics*, 2007.
- [95] K. Raggl, B. Warberger, T. Nussbaumer, S. Burger, and J. W. Kolar, "Robust angle-sensorless control of a PMSM bearingless pump," *IEEE Transactions on Industrial Electronics*, vol. 56, pp. 2076–2085, 2009.
- [96] T. Reichert, T. Nussbaumer, and J. W. Kolar, "Bearingless 300-W PMSM for bioreactor mixing," *IEEE Transactions on Industrial Electronics*, vol. 59, no. 3, pp. 1376–1388, 2012.
- [97] J. A. Rice, K. R. Gall, and G. Voss, "Enhanced adhesive shear strength of cyanate ester electrical insulation for fusion magnets," *IEEE Transactions on Applied Superconductivity*, vol. 13, no. 2, pp. 1476–1479, 2003.
- [98] M. Sagawa, S. Fujimura, N. Togawa, H. Yamamoto, and Y. Matsuura, "New material for permanent magnets on base of nd and fe," *Journal of Applied Physics*, vol. 55, pp. 2083–2087, 1984.
- [99] A. Salazar, A. Chiba, and T. Fukao, "A review of developments in bearingless motors," *Proc. 7th International Symposium on Magnetic Bearings*, 2000.
- [100] A. O. Salazar, W. Dunford, R. Stephan, and W. E., "A magnetic bearing system using capacitive sensors for position measurement," *IEEE Transactions on Magnetics*, vol. 26, 1990.
- [101] A. Schammas, R. Herzog, P. Buehler, and H. Bleuler, "New results for self-sensing active magnetic bearings using modulation approach," *IEEE Transactions on Control Systems Technology*, vol. 13, no. 4, 2005.

- [102] H. Schlichting and K. Gersten, *Grenzschicht-Theorie*, 9th ed. Springer, Berlin, 1996.
- [103] T. Schneeberger and J. W. Kolar, “Novel integrated bearingless hollow-shaft drive,” *Proc. 41st IEEE IAS Annual Meeting Industry Applications Conference*, vol. 1, pp. 70–75, Oct. 8–12, 2006.
- [104] R. Schoeb and N. Barletta, “Principle and application of a bearingless slice motor,” *Proc. 5th International Symposium on Magnetic Bearings*, 1996.
- [105] R. Schoeb, J. Hugel, and M. N., “Rotary machine with an electromagnetic rotary drive,” International Patent WO96/31 934, 1996.
- [106] E. Severson, R. Nilssen, T. Undeland, and N. Mohan, “Dual-purpose no-voltage winding design for the bearingless AC homopolar and consequent pole motors,” *IEEE Transactions on Industry Applications*, vol. 51, no. 4, pp. 2884–2895, 2015.
- [107] E. Severson, S. Gandikota, and N. Mohan, “Practical implementation of dual purpose no voltage drives for bearingless motors,” *Proc. IEEE Applied Power Electronics Conference and Exposition*, 2015.
- [108] S. Silber, “Beitraege zum lagerlosen Einphasenmotor,” Ph.D. dissertation, Johannes Kepler University Linz, 2000.
- [109] —, “Power optimal current control scheme for bearingless PM motors,” *Proc. 7th International Symposium on Magnetic Bearings*, 2000.
- [110] S. Silber, W. Amrhein, H. Grabner, and R. Lohninger, “Design aspects of bearingless torque motors,” *Proc. 13th International Symposium on Magnetic Bearings*, 2012.
- [111] S. Silber and W. Amrhein, “Design of a bearingless single-phase motor,” *Proc. Power Conversion and Intelligent Motion*, 1998.
- [112] Sintex, “Know-how - Sintex permanent magnets,” <http://sintex.com/Permanente-magneter.2206.aspx>, June 2012.
- [113] D. Smith, B. Mecrow, G. Atkinson, A. Jack, and A. Mehna, “Shear stress concentrations in permanent magnet rotor sleeves,” *Proc. 19th International Conference on Electrical Machines*, 2010.
- [114] T. Stallinger, W. Gruber, and W. Amrhein, “Bearingless segment motor with a consequent pole rotor,” *Proc. IEEE International Electric Machines and Drives Conference*, pp. 1374–1380, May 3–6, 2009.
- [115] D. Steinert, T. Nussbaumer, and J. Kolar, “Concept of a 150krpm bearingless slotless disc drive with combined windings,” *Proc. International Electric Machines and Drives Conference*, 2013.
- [116] —, “Slotless bearingless disk drive for high-speed and high-purity applications,” *IEEE Transactions on Industrial Electronics*, vol. 61, 2014.
- [117] C. R. Sullivan, “Optimal choice for number of strands in a litz-wire transformer winding,” *IEEE Transactions on Power Electronics*, vol. 14, no. 2, pp. 283–291, 1999.

- [118] Surahammar, “Typical data for SURA M400-50A,” <http://www.sura.se>, June 2008.
- [119] V. Tamsier and S. Font, “Optimal vibration control of a milling electrospindle,” *Proc. 9th International Symposium on Magnetic Bearings*, 2004.
- [120] S. P. Timoshenko, *Theory of Elasticity*, 3rd ed. McGraw-Hill Publishing Company, 1987.
- [121] F. Tourkhani and P. Viarouge, “Accurate analytical model of winding losses in round litz wire windings,” *IEEE Transactions on Magnetics*, vol. 37, no. 1, pp. 538–543, 2001.
- [122] N. Tsukada, T. Onaka, J. Asama, A. Chiba, and T. Fukao, “Novel coil arrangement of an integrated displacement sensor with reduced influence of suspension fluxes for a wide gap bearingless motor,” *Proc. Energy Conversion Congress and Exposition*, 2009.
- [123] H. Wang, Y. Wang, X. Liu, and J.-W. Ahn, “Design of novel bearingless switched reluctance motor,” *IET Electric Power Applications*, vol. 6, pp. 73–81, 2012.
- [124] B. Warberger, R. Kaelin, T. Nussbaumer, and J. Kolar, “50Nm / 2500W bearingless motor for high-purity pharmaceutical mixing,” *IEEE Transactions on Industrial Electronics*, vol. 59, pp. 2236–2247, 2012.
- [125] Z. Xu, D.-H. Lee, and J.-W. Ahn, “Modeling and control of a bearingless switched reluctance motor with separated torque and suspending force poles,” *International Symposium on Industrial Electronics*, 2013.
- [126] J. Zhu, Y. Guo, Z. Lin, and Y. Huang, “Low cost high performance smc motors: From material to application,” *Proc. International Conf. on Applied Superconductivity and Electromagnetic Devices*, pp. 385–391, 2009.
- [127] J. Zhu and V. Ramsden, “Improved formulations for rotational core losses in rotating electrical machines,” *IEEE Transactions on Magnetics*, vol. 34, pp. 2234 – 2243, 1998.
- [128] Y. Zhu, Q. Li, D. Xu, and M. Zhang, “Modeling of axial magnetic force and stiffness of ring-shaped permanent-magnet passive vibration isolator and its vibration isolating experiment,” *IEEE Transactions on Magnetics*, 2012.
- [129] Z. Q. Zhu, D. Howe, E. Bolte, and B. Ackermann, “Instantaneous magnetic field distribution in brushless permanent magnet DC motors. i. open-circuit field,” *IEEE Transactions on Magnetics*, vol. 29, no. 1, pp. 124–135, 1993.
- [130] Z. Zhu, “A simple method for measuring cogging torque in permanent magnet machines,” *IEEE Power and Energy Society General Meeting*, 2009.
- [131] F. Zuercher, T. Nussbaumer, and J. W. Kolar, “Motor torque and magnetic levitation force generation in bearingless brushless multipole motors,” *IEEE/ASME Transactions on Mechatronics*, vol. 17, no. 6, pp. 1088–1097, 2012.
- [132] F. Zuercher, T. Nussbaumer, W. Gruber, and J. Kolar, “Novel bearingless fractional slot motor,” *IEEE Intermag 2009 Motors and Actuators II, GG-02*, 2009.

Curriculum Vitae

Personal

Name	DI Dr. Hubert Mitterhofer
Born	June 11th, 1983 (St.Pölten, Austria)
Citizenship	Family
Family	Unmarried
Languages	German (native), English (fluent), French (fluent), Czech (intermediate), Spanish (basic), Russian (basic)

Education

2009-2017	Doctoral Program in Engineering Sciences, Johannes Kepler University, Linz, Austria PhD thesis: <i>Towards high-speed bearingless disk drives</i> Research visit, ETH Zurich, Switzerland, (Sept.-Dec. 2009)
2002-2008	Diploma studies of mechatronics, Johannes Kepler University, Linz, Austria Diploma thesis: <i>Entwicklung und Ansteuerung eines Robotergreifarms mit Linux-RTAI</i> Mechatronic exchange studies , Université Pierre et Marie Curie, Paris, France (2005-2006) Project thesis: <i>A robotic system guided by ultrasound - Application to intracardiac surgery</i>
1992-2001	Stiftsgymnasium Melk
1989-1992	Volksschule Hafnerbach

Other interests

Application and development of renewable energy generation, electric vehicle propulsion, energy storage systems

Technology impacts on sociopolitical development in fields of energy, resources and communication media

Farming and technological advances in agriculture

Experience

- | | |
|-----------------|---|
| 2013 to
date | Researcher at Linz Center of Mechatronics GmbH, Area Drives
Technical development of electric drives and magnetic bearings, project management including activities in acquisition and project planning, co-organization and co-chairing of magnetic bearings conference ISMB14, creation and operation of web portal <i>magneticbearings.org</i> , frequent publication in scientific context, co-authoring of several research proposals including four EU-funded (FP7, H2020) and one FFG-funded (Comet K2) projects, development coordination of system model suite <i>SyMSpace</i> , supervision of academic student works (three master theses, one project thesis). |
| 2009-2014 | Research assistant at the Institute of Electrical Drives and Power Electronics, JKU
Research activities in the field of magnetic bearings, electrical drives, high-speed bearingless drives, and magnetic gears, lecturer in mechatronic master course <i>Elektrische Schaltungen in der Antriebstechnik</i> , researcher in diverse industry-funded projects, database development for optimization suite <i>MagOpt</i> , diverse scientific publications and presentations. |
| 2007-2008 | University tutor at the Institute of Mechatronic Design and Production |
| 1999-2007 | Diverse internships, amongst others: VoestAlpine (steel plant), Senco (switch gear manufacturing), Voith Hydro (hydro power plant supplier), Raiffeisen Informatikzentrum (computer services) |
-

Publications and Patents

- H. Mitterhofer and W. Gruber, “Effizienzsteigerung durch die und in der Magnetlagertechnik”, Springer e&i Journal, 2017.
- H. Mitterhofer and W. Gruber, “Crucial Parameters and Optimization of High-Speed Bearingless Drives”, Journal of the Applied Computational Electromagnetics Society (ACES), 2017. (accepted for publication)
- H. Mitterhofer, “Elektrische Maschine,” European Patent EP16173200.3, pending.
- H. Mitterhofer and G. Jungmayr, “Stability improvement of passively stabilized degrees of freedom in magnetically levitated systems,” Proc. 15th International Symposium on Magnetic Bearings, 2016.
- H. Mitterhofer and S. Silber, “Comprehensive design and optimization of high-speed bearingless drives,” Proc. Advances in Magnetics Conference, 2016.

- H. Mitterhofer, B. Mrak, and W. Gruber, "Comparison of high-speed bearingless drive topologies with combined windings," *IEEE Transactions on Industry Applications*, vol. 51, no. 3, pp. 2116–2122, 2015.
- H. Mitterhofer, W. Amrhein, S. Silber, W. Kappelmüller, A. Prokesch, "Formgebungsmaschine und Verfahren zum induktiven Erhitzen", Pending patent AT517241 (A1), 2016
- H. Mitterhofer and M. Rakov, "On the Direct Use of Electromagnetic Field Information for Magnetic Rotor Position Control", *Proc. 14th International Symposium on Magnetic Bearings*, 2014.
- H. Mitterhofer, W. Gruber, and W. Amrhein, "On the high speed capacity of bearingless drives," *IEEE Transactions on Industrial Electronics*, vol. 61, no. 6, pp. 3119–3126, 2014.
- H. Mitterhofer, B. Mrak, and W. Amrhein, "Suitability investigation of a bearingless disk drive for micro turbine applications," *Proc. Energy Conversion Congress and Exposition*, 2013.
- H. Mitterhofer and W. Amrhein, "Motion control strategy and operational behaviour of a high speed bearingless disc drive," *Proc. IET Power Electronics, Machines and Drives Conference*, 2012.
- W. Amrhein, W. Bauer, H. Grabner, W. Gruber, H. Mitterhofer, and S. Silber, "Bearingless Permanent Magnet Motors: Trends and Technical Advancements", *Actuator 12, International Conference and Exhibition on New Actuators and Drive Systems*, 2012.
- H. Mitterhofer, D. Andessner, and W. Amrhein, "Analytical and experimental loss examination of a high speed bearingless drive," *Proc. International Symposium on Power Electronics Electrical Drives Automation and Motion*, 2012.
- H. Mitterhofer, H. Grabner, and W. Amrhein, "Comparison of two and four pole rotors for a high speed bearingless drive," *Proc. 13th International Symposium on Magnetic Bearings*, 2012.
- H. Mitterhofer and W. Amrhein, "Design Aspects and Test Results of a High Speed Bearingless Drive", *Proc. International Conference on Power Electronics and Drive Systems*, 2011
- H. Mitterhofer, W. Amrhein, and W. Gruber, "Towards High Speed Bearingless Drives", *Proc. 12th International Symposium on Magnetic Bearings*, 2010.
- M.-A. Vitrani, H. Mitterhofer, G. Morel, and N. Bonnet, "Robust Ultrasound-Based Visual Servoing for Beating Heart Intracardiac Surgery", *Proc. IEEE International Conference on Robotics and Automation*, 2007.
-